Deliverable 5.5: FUTuRE Final technical report on radionuclide mobility in crystalline systems

Work Package WP5 FUTURE

This project has received funding from the European Union's Horizon 2020 research and innovation programme under grant agreement N°847593.

http://www.ejp-eurad.eu/

Document information

Project Acronym	**EURAD**
Project Title	**European Joint Programme on Radioactive Waste Management**
Project Type	**European Joint Programme (EJP)**
EC grant agreement No.	**847593**
Project starting / end date	**1st June 2019 – 30 May 2024**
Work Package No.	**5**
Work Package Title	**Fundamental understanding of radionuclide retention**
Work Package Acronym	**FUTURE**
Deliverable No.	**5.5**
Deliverable Title	**Final technical report on radionuclide mobility in crystalline systems**
Lead Beneficiary	**FZJ**
Contractual Delivery Date	
Actual Delivery Date	
Type	
Dissemination level	
Authors	**Filip Jankovský (ÚJV), Milan Zuna (ÚJV), Karol Kočan (ÚJV), Susan Britz (GRS), Artur Meleshyn (GRS), Marja Siitari-Kauppi (U Helsinki), Xiaodong Li (U Helsinki), Francesca Quinto (KIT), Johannes Kulenkampff (HZDR), and Cornelius Fischer (HZDR)**

To be cited as:

F. Jankovský, M. Zuna, K. Kočan, S. Britz, A. Meleshyn, M. Siitari-Kauppi, X. Li, F. Quinto, J. Kulenkampff, C. Fischer (2024): Final version as of 26.02.2024 of deliverable D5.5 of the HORIZON 2020 project EURAD. EC Grant agreement no: 847593.

Disclaimer

Acknowledgement

This document is a deliverable of the European Joint Programme on Radioactive Waste Management (EURAD). EURAD has received funding from the European Union's Horizon 2020 research and innovation programme under grant agreement No 847593.

Status of deliverable		
	By	Date
Delivered (Lead Beneficiary)	Cornelious Fischer (FZJ)	27.10.2023
Verified (WP Leader)	Sergey Churakov (PSI)	12.11.2023 / 06.02.2024
Reviewed (Reviewers)	Rainer Daehn PSI	15.12.2023
Approved (PMO)	Bernd Grambow	26.02.2024
Submitted to EC	Andra (Coordinator)	27.02.2024

Executive Summary

For the FUTURE work package, a number of research topics focussing on crystalline rock were combined. The work package addressed the connected pore network and surface topography, transport and sorption processes as well as the impact of surface potential, water chemistry, pore size and grain boundaries. Overarching goals covering all the latter topics were formulated such as the quantitative and mechanistic understanding of the impact of site-specific mobility of species; the impact of specific surface properties of materials (diffusive double layer, surface potential), the role of grain boundaries, the effect of water saturation, content and chemistry (pH, ionic strength) as well as the impact of pore size variability (nanometer pore scale: meso-/ macropores). The various objectives are addressed in individual subchapters dealing with sorption processes and the impact of surface charge (Chapters 1-4), addressing transport processes in fractures (Chapter 5), and illustrating a long-term in situ experiment (Chapter 6) in crystalline host rocks.

Major findings and conclusions include: Chapter 2 presents sorption data from experiments with Ni, Cs, Se, Ba, and Ra on fracture-filling calcite and chlorite and on site-specific host rocks (migmatite, granite). PHREEQC speciation calculations of Ni, Cs, Se, Ba, and Ra and synthetic groundwater data accompany the experimental data. Distribution coefficients show the effect of impurities/compositional heterogeneity of fracture-filling minerals on sorption variability and allow comparisons with previous data based on pure minerals. Chapter 4 reports effective diffusivity and distribution coefficients for Sr, Co, and Cs in the Grimsel Granodiorite and relates them to porosity (e.g., PMMA technique) and structural (e.g., CT) data sets. The roughness and mineralization of the fracture walls are not negligible for the prediction of advective transport. A quantitative influence on fluid residence times and on the development of flow path localization (channelization) has been demonstrated (chapter 5).

Subchapters 1-3 are dedicated to investigating the roles played by specific calcite fracture fillings in sorption processes. The primary objective was to conduct a detailed comparison between fracture fillings and the surrounding rock matrix, or additional significant minerals such as biotite. This comparative analysis aimed to elucidate the impact of their distinct characteristics on the uptake of essential elements. The mineral composition of rocks and their structural characteristics are vital in assessing the ability of fractures and rocks to efficiently retain the elements under study.

According to the proposed work plan, the following steps were carried out:

- Batch sorption experiments were conducted on carefully selected fracture infills and rock matrices from both Bukov URF and Onkalo, Finland. Selected rocks reflect a comprehensive representation of geologically diverse formations. These experiments involved a wide range of radionuclides (RNs) (e.g. Cs, Ni, Ra, Se, Ba) categorized according to their distinct sorption characteristics (e.g. strongly/weakly sorbing RNs, pH dependence, ionic strength (IS) dependence, etc.). In addition, surface complexation models were developed for radium and selenium sorption on biotite based on titration, sorption and pH isoterms data.
- XCT was used to obtain the three-dimensional structure of a core scale Bukov sample. The C-14-PMMA autoradiography was used to obtain the porosity of different minerals and scanning-micro X-ray fluorescence (µXRF) was used to obtain elemental maps from the same sample, which are then converted into mineral maps using the Bruker AMICS automated mineralogy software. The mineral maps and XCT data are then combined using an in-house modified version of the deep learning method to obtain 3D mineral maps. When the porosity map and mineral map are combined to calculate mineral-specific porosities a 3D porosity map suitable for diffusion simulations and modeling was obtained.
- Calcite infills were investigated in detail fostering the collaborative research within the work package involving multiple institutes. Calcite infills from each sample site were distributed to all participating partners to facilitate a comprehensive analysis with comparable samples, encompassing not only standard batch sorption studies but also intricate desorption analyses.
- Bukov and a commercially obtained cleaned calcite sample were used for surface charge investigations. Different IS, CO_2 partial pressures and electrolyte compositions were applied to investigate the effect on surface charge development which vice versa most likely has large influence on retardation properties of calcite fracture infills.

The focus of our investigations reported in subchapter 5 is on specific characteristics of transport behavior in fractures of crystalline host rocks. This concerns the coupled influence of fracture aperture

and wall topography/roughness on fluid residence time and preferred flow paths, e.g., channelling. Furthermore, these questions are related to the influence of fracture mineralization. Different mineralization types, such as calcite and phyllosilicates are dominant in the investigated host rocks from Czech Republic and Finland. Such fracture fillings further alter the advective flow field by a local increase in fluid residence time and a more pronounced heterogeneity of the fluid-rock interface.

In accordance with the proposed work plan, the following steps have been carried out:

- The connected pore network and surface topography of fractured crystalline rock samples and mineral infills (provided by SURAO and POSIVA) were analyzed using µCT and confocal/ interferometry microscopy prior to flow, diffusion, and sorption experiments. After the transport experiments, random studies of potential changes in the flow paths were performed. This ensured that no unwanted changes occurred during the long-term flow experiments.
- Batch type and flow-through experiments utilized the reference pore water of the specific host rock to allow comparison with existing studies and direct applicability for subsequent practical use. We analyzed the impact of pore size variability of fracture infills and intact rock.
- Additional objectives included the analysis of the fluid velocity field (diffusive vs. advective transport) in and close to fractures by using PET techniques. We utilized flow-through tracer tests to analyse the mobility of non-sorbing tracers within rock fractures.

The experimental and analytical results were prepared to provide a basis for rigorous uncertainty and sensitivity studies thus providing an interface to numerical work. Due to the specific situation with laboratory closures during the project period, we used a PET flow field data set as well as CT and surface data for own extensive numerical studies to quantitatively understand the coupling between fracture aperture widths and mineralization affecting surface roughness variability.

Generally, the results contribute to a more realistic view on radionuclide migration in complex systems to overcome the current over-conservative consideration of heterogeneities, such as fracture planes, mineral infills, and porosity networks. All activities have been performed under close cooperation of the participating institutions.

Keywords

- Synthetic granitic water (SGW2)
- Batch sorption experiments
- Desorption experiments
- Leaching experiments
- Fracture filling
- RN Speciation calculations
- Crystalline hostrocks
- Advective transport of radionuclides
- Flow field analysis
- Positron emission tomography (PET)
- Fracture aperture
- Fracture surface roughness
- Transport modelling

Table of content

List of figures

List of Tables

1 Introduction to transport controlling processes in crystalline host rock

Transport by advection in fractured rocks is usually evaluated from the simplistic aspect that the fractures are not filled with minerals. However, a large number of fractures, whether in unsaturated, saturated or hydrothermal regimes, are partially or completely filled with minerals. This includes both hydrothermal precipitates or transported infiltrations. The mineralogy of fracture fillings is diverse: Clay minerals such as illite, chlorite, and kaolinite as well as carbonates (calcite, siderite) were frequently observed. Therefore, the modification of the fluid-host rock interface to a fluid-infill interface is an important boundary condition for predicting transport and retention of radionuclides. A deeper knowledge of these boundary conditions does contribute significantly to improving the understanding of radionuclide migration in crystalline rocks and enables a realistic safety assessment. Our studies on non-simplified geomaterials provided insight into the role of interface topography, pore network variability, and fracture aperture heterogeneity, as well as the effects of chemical boundary conditions on radionuclide migration.

1.1 Motivation

The focus of this task is the experimental analysis of the role of microstructures and the influence of chemical boundary conditions on radionuclide transport pathways in crystalline rocks. Objectives include a quantitative and mechanistic understanding of the effects of site-specific mobility of species, the effects of specific surface properties of materials (diffusive double layer, surface charge of minerals), the role of grain boundaries, the effects of water saturation, content and chemistry (pH, ionic strength), and the effects of pore size variability (nanometer pore scale: meso-/macropores). Additional objectives include the connection between the fractures and the pores and micro-fissures in the rock matrix, and the feedback of mineral reactions (precipitation, clogging) on pore structure and connectivity.

The first part of the study focuses on the behavior of radionuclides (RN) in the host rock and its minerals. Mainly the batch sorption method was used to determine the partition coefficients for used RNs. RN transport in intact rock cores was evaluated based on heterogeneous pore structures in crystalline rock. The mineral reactions (coupled dissolution-precipitation processes, clogging, mineral content, etc.) and the associated pore network are an important basis for the evaluation of matrix diffusion and permeability/fluid mobility. The investigations included rock samples from crystalline rock sites, from the Bukov URL (SURAO) and from Onkalo, Finland at the depth of the potential repository. The combined analysis of pore structures and mineralogy and the sorption behavior of RNs focused on understanding the Ra retention in the intact rock using C-14-PMMA autoradiography combined with µCT method and the sorption of Ra on thin sections determined by autoradiography.

The project partners at Helmholtz-Zentrum Dresden-Rossendorf (HZDR) investigated the influence of pore size and its variability (nm scale: meso- and macropores) on transport properties. The variability of the flow field measured by positron emission tomography (PET) is analyzed as a function of pore size variability and gradients in the host rock samples. In parallel to conservative tracers for flow field analysis, reactive PET tracers have been used to study the behavior of strongly/intermediately-weakly sorbing actinide homologues. The partners at the Nuclear Research Institute of Czech Republic (UJV) studies were directly linked to a tracer test using different types of radionuclides to describe the influence of the above properties on fracture flow. Differently sorbing radionuclides (^{3}H and non-radioactive I^- - non-sorbing, ^{22}Na, ^{134}Cs, ^{63}Ni and ^{133}Ba as sorbing radionuclides) were investigated.

The complementary study targets retention processes on the intact crystalline rock and fracture filling materials. Comparative diffusion sorption studies as a support of prognostic tools for radionuclide migration through complex systems. These studies were outlined in collaboration with the partners Gesellschaft für Anlagen- und Reaktorsicherheit (GRS), HZDR and UJV Rez and Univ. of Helsinki (UH).

The studied materials originated from Czech Republic (granite,migmatized gneiss), most preferably from the depth of potential DGR (provided in joint effort of SURAO and UJV). This includes fissure infill minerals, mainly calcite, with well-defined mineralogical composition, as well as surface properties and connective heterogeneous pore space characterization.

HZDR focused on the analysis of the flow field by positron emission tomography (PET) and the cross-scale surface roughness of the open fractures (interferometry, confocal microscopy, µCT) and provided quantitative data for this purpose.

UJV supported rock characterization with respect to sample mineralogical composition, pore space characteristics and surface properties (XRD, SEM/TEM, SIMS, CEC, BET) altogether with description of the real geological conditions of the rock formation (groundwater conditions namely). Furthermore, in collaboration with other entities, UJV will conduct flow-through experiments and be responsible for batch sorption studies of sorbing radionuclides (with a primary focus on ^{63}Ni) on diverse types of fracture infills originating from the Bukov Underground Research Facility (URF).

The project partner UH studied the behaviour of Ra on selected rock samples from Onkalo, Finland (gneisses and granite pegmatoids) by batch sorption method and the mechanisms are evaluated by PHREEQC modelling. Also, Se sorption is studied on Grimsel granodiorite and surface complexation modeling is developed to interpret the results for biotite. For transport, namely for matrix diffusion of cations in Grimsel granodiorite electromigration through diffusion method is developed. For characterizing the rock cores heterogeneous connected pore network C-14-PMMA autoradiography and CT tomography were used. Surface charge of calcite (Bukov) was studied experimentally to explain the sorption of Ni and Ba on it.

GRS contributed by studying leaching behavior of crystalline rock and fracture filling from the Bukov URF in batch experiments at 10 and 80 °C and determining in-situ desorption distribution ratios for non-radioactive rare-earth elements and yttrium (REEY), as chemical analogues of radioactive lanthanides and trivalent actinides, as well as Cs, Sr, Ba, Th, U, Ni, and I. The motivation behind this desorption studies is that during the interaction between waters flowing or residing in the fracture and wall rock, on one hand, or fracture minerals, on the other hand, which occurred in the geological past, these materials documented the retention of the studied elements at in-situ conditions. The scientific aim of the work is to establish a method to extract this information from the natural materials. To carry out surface complexation modeling of the sorption-desorption processes occurring upon contact of pore waters with calcitic fracture filling, a derivation of necessary parameters is carried out based on experimental studies of its surface charge by UH.

1.2 Organisation of the work

1.2.1 Sorption

Sorption experiments were conducted under precisely defined conditions, employing a diverse set of radionuclides that were categorized based on their sorption characteristics into strongly sorbing, sorbing, and non-sorbing groups. The selected radionuclides represent a range of elements with varying affinities for the materials, and their inclusion allows for a comprehensive evaluation of the sorption processes. The rock matrices utilized in these experiments were carefully chosen from Bukov URF and Onkalo, ensuring a wide representation of geological diverse formations. The diversity of rock matrices provides valuable insights into the influence of mineralogical composition, pore structure, and surface properties on the radionuclide sorption behavior.

At UJV, the focus of our research entailed conducting batch sorption experiments exclusively on materials acquired from the Bukov URF. In alignment with prior discussions and with the objective of collaborative endeavor between institutes, we deliberately opted to investigate calcite infills, which were provided by us to the GRS and UH. In pursuit of a comprehensive analysis of calcite infills, we also

explored various other materials exhibiting diverse mineralogical compositions and distinct sorption properties. The primary element of interest, employed in the batch experiments, as mutually agreed upon by the collaborating institutes, was Ni (in the radionuclide isotope ^{63}Ni at UJV), chosen for its prominent attributes and sorption behavior. Additionally, we further examined the element Cs (in the radionuclide isotope ^{134}Cs) due to its specific characteristics and unique sorption behavior.

At GRS, sorption of stable Ni on calcitic fracture infill and migmatite was studied in a subset of batch experiments. The main focus of the other experiments was on studying the release of REEY (amongst others, Sm, Eu), Cs, Sr, Ba, Th, U, Ni, and I from these materials, the radioactive analogues of which can be of relevance for safety cases of potential or licensed repositories in crystalline rocks.

At UH, the sorption behaviour of Se(IV) on Grimsel granodiorite and its main minerals, plagioclase, K-feldspar, quartz and biotite, were investigated in Grimsel groundwater simulant in a large Se concentration range. To provide quantitative predicts of Se(IV) sorption in groundwater conditions, a surface complexation model of Se(IV) sorption on biotite with one type of strong sorption sites and two types of weak sorption sites were developed based on experimental data obtained from titration, sorption edge and sorption isotherm experiments. The sorption of Ni and Ba on calcite were studied with batch sorption method (sorption isotherm, sorption as a function of pH, titration). To better illustrate the sorption data, zeta potential measurements of calcite surface were also performed. The sorption of Ra on Olkiluoto biotite in four different Olkiluoto reference groundwaters with salinity types ranging from fresh to saline was studied with batch sorption experiments.

1.2.2 Matrix diffusion

At UH, the matrix diffusion was studied with three cationic tracers, Sr^{2+}, Co^{2+} and Cs^{+} by electromigration technique over an intact Grimsel granodiorite rock sample. The traditional electromigration device was updated by the introduction by potentiostat to impose a constant voltage difference. To interpret the experimental results with more confidence, an advection-dispersion model was developed by accounting for the most important mechanisms governing the movement of the tracer ions, i.e. electromigration, electroosmosis and dispersion. In addition, a reactive transport model was developed based on the consideration that the effects of aqueous chemistry should not be neglected in the former models. The newly developed models, compared to the traditionally used ideal plug-flow model, can provide more precise diffusion parameters. The advection-dispersion model gives nearly the same estimations of parameters as the reactive transport model, with only minor differences in the mean values and uncertainties ideal plug-flow model and an advection-dispersion model were applied to analyze the breakthrough curves. To understand the diffusion processes in heterogneous rock samples, matrix characterization by C-14-PMMA autoradiography, XCT and µXRF or scanning electron microscopy were applied with centimetre scale Grimsel granodiorite and Bukov metamorphic rock samples, revealed the interconnected diffusion paths.

1.2.3 Flow analysis

Geometry of and flow field on fractures were investigated on different fracture types with different fracture fillings in host rocks from Finland and the Czech Republic (Table 1-1). Investigations included quantification of fracture geometries, aperture widths, and fracture wall roughness. Mineralization types were determined. Resulting 3D data on complex fracture geometries, some of which include multiple fracture planes and identify fracture plane connectivity. Questions of spatial resolution relevant to the use of geometry data in transport models were answered. A case study was used to demonstrate the optimization of µCT geometry data with high spatial resolution roughness data and to show its application in transport models, with respect to sensitivity analyses. Application-related motivation was to test the impact on flow field changes in the combined analysis of fracture aperture and surface roughness of the fracture wall. A large amount of flow field data was collected using PET analytics and is available for validation of transport models**.**

Table 1-1: Overview of sample names, origin, material specifications and comments on the data sets for transport analysis

Sample Name	**Provenance**	**Specifications / Purpose**	**Analytical**
MSVJ2	Mrakotin quarry (CZ)	open fracture, no infills	Fracture geometry, surface topography, advective flow, transport modeling
BZ8_1 (BZ-XII-38.8 - 3 -11)	Bukov URL (CZ)	tight fractures with precipitates	Fracture geometry, advective flow/ diffusive flux
SS36_5	Bukov URL (CZ)	simple fracture geometry, no fracture-filling materials	Fracture geometry, advective flow
OLKR5	Onkalo (FI)	filled fracture (mica gneiss rock core: sheet silicates and calcite)	Fracture geometry, surface topography, advective flow

1.3 Material characterization

1.3.1 Material from Onkalo (POSIVA)

The Olkiluoto deep geological disposal site lies on an island in western Finland, on the coast of the Baltic Sea. The Palaeoproterozoic bedrock in Olkiluoto consists of variably migmatised supracrustal high-grade metamorphic rocks: migmatized meta-pelites, meta-arenites and intermediate, pyroclastic metavolcanites. They are intruded by Paleoproterozoic felsic, granitic–tonalitic plutonic rocks and granitic pegmatoids, and diabase dikes. The rocks were metamorphosed simultaneously with the different phases of ductile deformation. Hydrothermal alteration at Olkiluoto can be subdivided into two different modes on the basis how the fluids have proceeded in the rock mass: fracture- or veinlet-controlled alteration and pervasive or disseminated alteration. The brittle deformation history of Olkiluoto can be reconstructed through paleostress inversion of fault-slip data from outcrops and drill cores and from K-Ar ages if fault gouge illites: seven distinct paleostress states can be identified, spanning in time from ca. 1.7 Ga to 1.0 Ga. The disposal facility is under construction at a depth of over 400 m below the surface. The disposal site lies in the Southern Svecofennian complex area in an area where the postglacial land uplift is still present, approximately 6 mm per year (Aaltonen et al., 2016). At the Olkiluoto site, metatexitic gneiss, is the main rock type (67 vol%) with notable amounts of diatexitic gneiss (22 vol%), and granitic pegmatoid (6 vol%), with mica gneiss making up a minor species of the total volume (1 vol%) (Mattila et a., 2022). To achieve a balanced and representative selection of the various rock types of Olkiluoto at the disposal facility level, four different rock types were chosen for this study: veined gneiss or metatexitic gneiss (VGN), diatexitic gneiss (DGN), granitic pegmatoid (PGR), and mica gneiss (MGN) (Figure 1-1). The phyllosilicate mineral biotite is one of the main minerals in veined gneiss, and can make up to 40% of the total mass of the host rock (Kärki and Paulamäki, 2006).

DGN

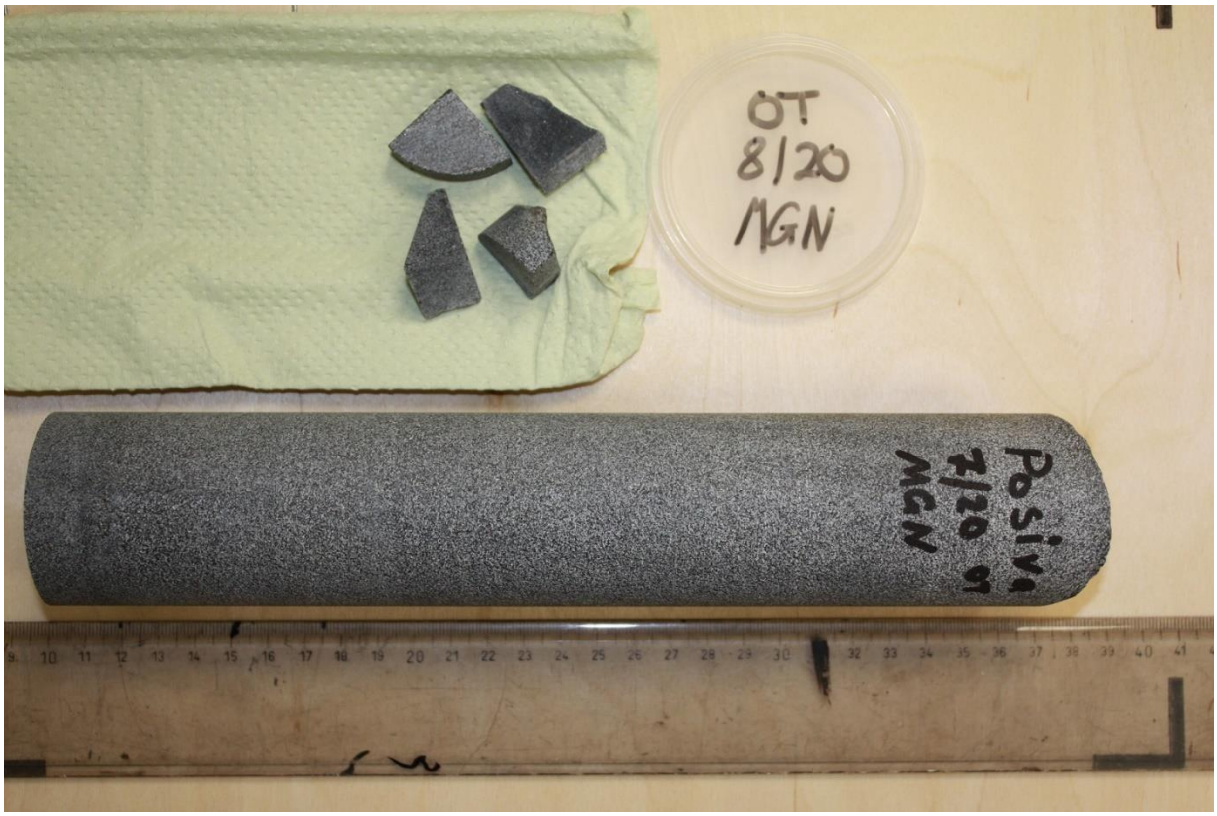

MGN

VGN

PGR

Figure 1-1 Initial photos of the Olkiluoto rock samples

Rock samples from Olkiluoto, received from Posiva Oy, were obtained in the form of drill core samples. The drill core samples were photographed and marked before sawing them into smaller and more manageable cylinder shapes. Selected sample cylinders were then crushed, milled, and sieved to the desired size fraction of 0.071–0.3 mm. Part of the prepared sample powders was reserved for background analyses: X-ray Diffraction (XRD) at the Geological Survey of Finland (GTK), Specific Surface Area (SSA) at the Chalmers University of Technology with the Kr-BET method using gas adsorption analyzer (Micromeritics ASAP2020), and Cation Exchange Capacity (CEC) using the ammonium acetate method at pH 7 (van Reeuwijk, 2002). The XRD, SSA, and CEC results are important parameters in the geochemical modeling of sorption. Mineralogical XRD results (Pasi Heikkilä, Geological Survey of Finland) of the studied rock samples, along with the corresponding SSA and CEC results, are presented in Table 1-2. The SSA of the experimented biotite was determined to be 0.6675 ± 0.0147 m^2 g^{-1} with the Brunauer-Emmett-Teller theory (BET) method. Li and group (2020) have previously reported the Cation Exchange Capacity (CEC) of the biotite (as phlogopite in the studied samples) also used in this study as 12.64 ± 0.42 meq kg^{-1}, obtained with the ammonium acetate method (van Reeuwijk, 2002).

Table 1-2 X-ray diffraction normalized quantitative phase compositions (%) of the rock samples. XRD work done by Pasi Heikkilä at the Geological Survey of Finland, and the SSA and CEC of the studied rock samples. SSA was determined with Kr BET method (Stellan Holgersson, Chalmers University of Technology). CEC was determined with the ammonium acetate method (van Reeuwijk, 2002). Uncertainties (± 1σ) of CEC obtained with propagation of error. Sample ID legend: VGN veined gneiss or metatexitic gneiss; PGR granitic pegmatoid; DGN diatexitic gneiss; and MGN mica gneiss

	Olkiluoto			
Mineral	VGN	PGR	DGN	MGN

Quartz	41	29	18	26
Microcline	0.6	45	23	1
Albite	1.8	22	6.1	1.2
Oligoclase	6.5	1.5	6.3	1.4
Andesine	35	0.6	9.7	45
Muscovite	1.6	1.5	15	1.4
Phlogopite	12	-	19	19
Annite	0.7	-	1.8	2.3
Hornblende	-	-	-	-
Clinochlore	0.6	0.1	0.8	0.6
Hematite	-	-	-	-
Magnetite	-	-	-	-
Apatite-CaF	-	0.2	-	1.1
SSA (m^2 g^{-1})	0.53 ± 0.01	0.19 ± 0.01	1.30 ± 0.04	0.24 ± 0.01
CEC (meq kg^{-1})	19 ± 2	45 ± 9	16 ± 1	6 ± 1

1.3.2 Groundwaters from Onkalo (POSIVA)

As the Olkiluoto site lies on the coast of the Baltic Sea, the hydrogeochemical conditions of the site have been influenced by repeated transgressions and regressions in the past in addition to several glacial events during the Quaternary. The effects of the ancient Littorina Sea (8,000–2,500 BP) can be observed in modern day: anoxic redox conditions in the groundwaters and a band of high sulfate levels (up to 500–600 mg l^{-1}) in the depth of 100–300 m below the surface (Partamies and Pitkänen, 2014). At the same depth, groundwaters with varying degrees of glacial meltwater influence have been discovered. The Na, Ca, and Cl based salinity of the ground and fracture waters rises steadily as a function of depth: 2–9.8 g l^{-1} in 60–500 m to 10–70 g l^{-1} at 800 m, and 130 g l^{-1} at 900 m (Vuorinen and Snellman, 1998; Posiva, 2012). In the natural groundwaters of the disposal depth of the Olkiluoto site, Ba and Ra levels of 5.9×10^{-7} to 1.9×10^{-5} M and 10^{-14} to 10^{-9} M, respectively, have been observed (Vaaramaa et al., 2003; Hellä et al., 2014). The groundwater chemistry at depth below 300–400 m is characterized by brackish to saline waters of non-marine type (Posiva, 2012).

Due to the varying groundwater types of the Olkiluoto site area, multiple types of reference groundwater solutions were selected for the Ra batch sorption experiments of this study. As the salinity of the surrounding sorption solution has been established as one of the key parameters when assessing the magnitude of Ra and Ba sorption onto crystalline rock (Sajih et al., 2014; Muuri et al., 2018; Söderlund et al., 2019; Fabritius et al., 2022), groundwater types of different salinities were chosen for the sorption

experiments of the Olkiluoto rock samples. All of the tested reference groundwaters have been based on natural groundwaters from Olkiluoto. For the four Olkiluoto rocks, three reference water types were tested: fresh Modified Allard (ALLMR); saline reference Olkiluoto Saline Reducing (OLSR); and glacial meltwater simulant Olkiluoto Glacial Anoxic (OLGA) (Hellä et al., 2014; Söderlund et al., 2019). The chemical recipes of the groundwater simulants prepared for the experiments have been presented in Table 1-3. Note that only the reference water preparation recipes are presented here – since the experiments were conducted in ambient atmospheric conditions, all tested waters are bound to contain HCO_3^-.

Table 1-3 The ionic compositions (mg l^{-1}) of the Olkiluoto and Forsmark reference groundwaters (ALLMR, OLSR, and OLGA, and OLBA) prepared for the experiments, along with the initially set solution pH

	Concentration of the ion or compound (mg l^{-1})			
Ion	ALLMR	OLSR	OLGA	OLBA
Na^+	52.5	4,800	0.66	1,750
K^+	3.9	21	0.6	18.9
Mg^{2+}	0.7	54.6	0.3	26.5
Ca^{2+}	5.1	4,000	0.52	84.5
Sr^{2+}	-	35	-	0.1
$B(OH)_3$	-	0.92	-	3.5
HCO_3^-	165	-	-	111
Cl^-	48.8	14,500	3	2,540
Br^-	-	104.7	-	13.1
F^-	-	1.2	-	0.3
I^-	-	0.9	-	-
SO_4^{2-}	9.6	4.2	0.2	458
SiO_3^{2-}	17	-	0.1	6.1
pH	8.8	8.3	5.8	7.6

1.3.3 Material from Bukov (SURAO)

1.3.3.1 Selection of the material and the extraction of samples for the sorption experiments

Natural Calcite Fracture Filling Samples

The selection of samples for the experimental work conducted in Task 2.2 was based on the outcomes of meetings held between 2019 and spring 2020. ÚJV Řež was assigned the responsibility of identifying and acquiring fracture core samples from the Bukov Underground Research Facility (URF) for subsequent use in the experimental research, subject to permission from SÚRAO. The ÚJV team conducted a visit to the drill core archive to identify suitable drill cores containing calcite or other fillings such as chlorite and clay minerals. Several drill cores were chosen to be utilized in the flow through experiments. However, due to the poor quality of samples with calcite fracture fillings, calcite filling samples were directly extracted from the Bukov URF. Two suitable collection points, BZXIIJ (219.4 m) and BZXII (38.8 m), were identified within the Bukov URF (as depicted in Figure 1-2). From the BZXIIJ (219.4 m) collection point, two drill cores with diameters of 79 mm and lengths of 60 cm and 30 cm were obtained (see Figure 1-3). The calcite veins within these cores had an approximate thickness of 3 cm. In addition to the calcite fillings, sections of the surrounding rock material containing varying proportions of calcite filling (approximately 1 kg each) were also collected. These materials were subsequently processed for use in the sorption experiments. From the BZXII (38.8 m) collection point, one drill core measuring 79 mm in diameter and 50 cm in length was obtained. This core contained a complex vein system that was denser compared to the other samples (see Figure 1-5).

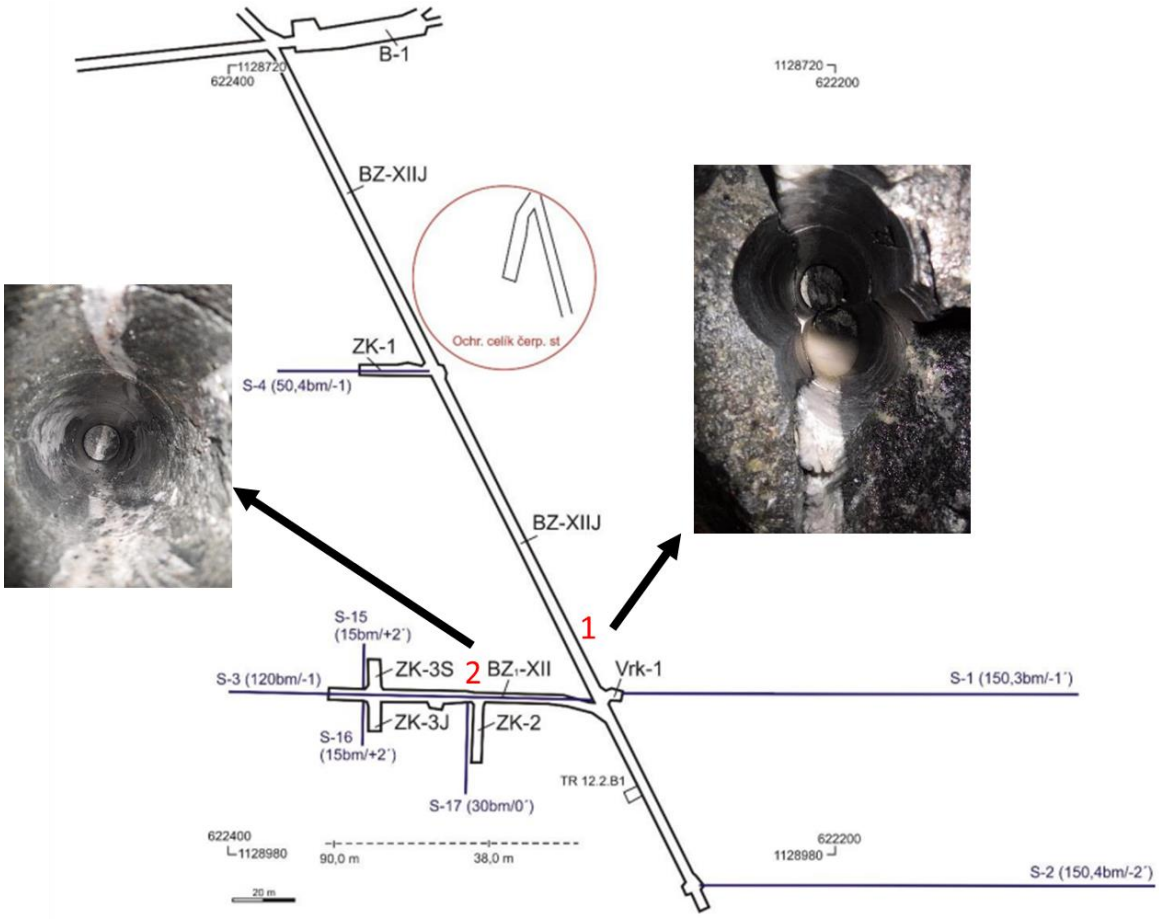

Figure 1-2 Schematic drawing of the Bukov URF with the locations from which the cores with the calcite fillings were extracted

Figure 1-3 Extraction of a sample of a calcite filling in the Bukov URF (sampling point BZJXIIJ 219.4 m)

Figure 1-4 Samples of fracture fillings extracted from sample collection point BZJXIIJ (219.4 m)

Figure 1-5 Sample of a fracture filling extracted from sampling point BZJXII (38.8 m)

Some of the fracture filling samples were prepared wrt. to size and shape according to specifications provided by the co-researchers (HZDR, GRS, KIT and Helsinki University) and were sent to them for use in the experimental programme (see Figure 1-7).

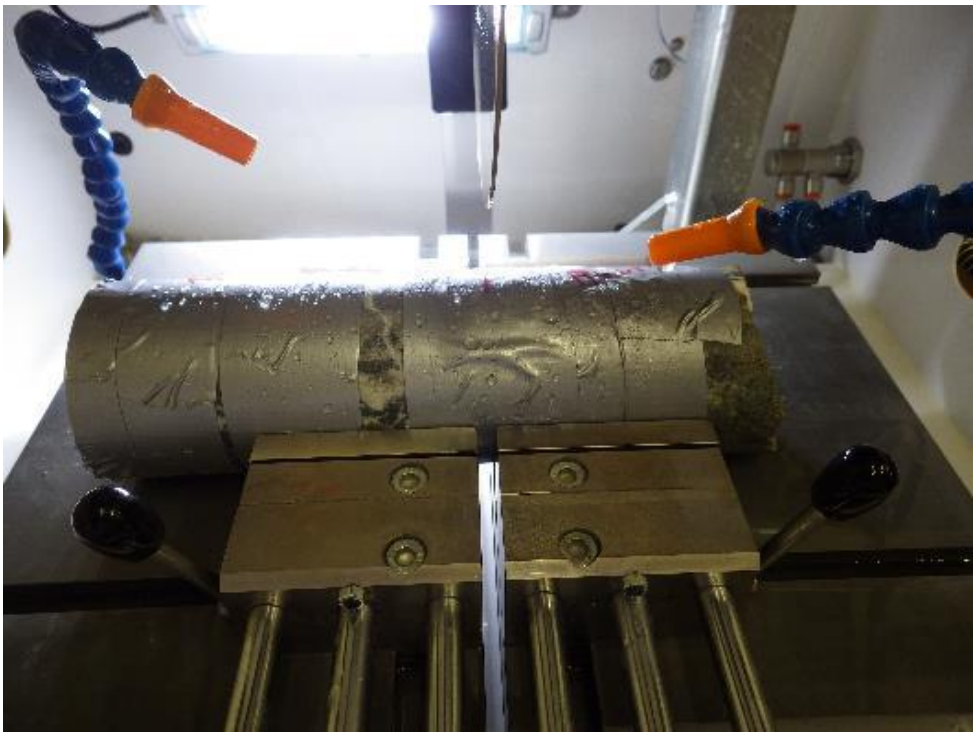

Figure 1-6 Formatting of rock core samples from BZJXII (38.8 m)

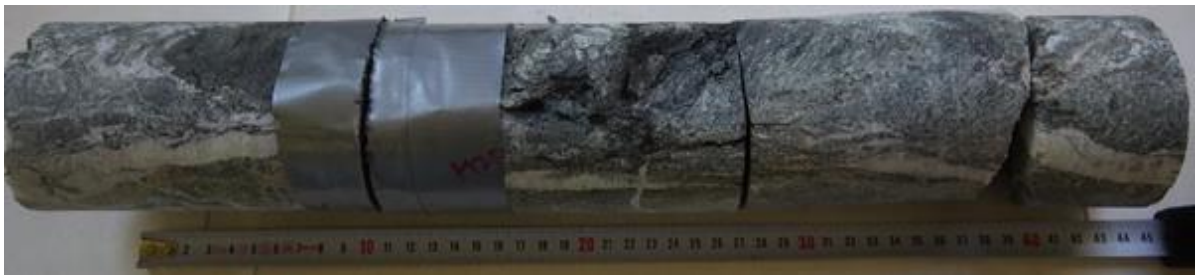

Figure 1-7 Scheme of the division of a rock core from BZJXII (38.8 m)

Approximately 560 g of Bukov calcite infill was extracted from the BZJXIIJ (219.4 m) samples. The calcite material was further fragmented into fractions with a maximum grain size of 1 cm and subsequently quartered to create batches of approximately 100 g each (refer to Figure 1-8). These batches were then sent to the co-researchers for further analysis. The surrounding rock material underwent a similar processing method, as shown in Figure 1-9. Both the calcite filling and the surrounding rock were subjected to grinding and sieving processes to obtain various grain fractions (A-E). For the sorption experiments, fractions C (0.63-0.125 mm) and D (0.80-0.63 mm) were selected. Additionally, a type of calcite referred to as "Bukov calcite infill with rock admixture" which contained a higher proportion of the surrounding rock material, was also separated.

Furthermore, samples of the parent rock (BZJXII, 250 m; migmatized gneiss) were processed specifically for experimental purposes.

Figure 1-8 Separated calcite material (left) and the quartering of the crushed material for distribution among the research partners (right)

Figure 1-9 Separated “Bukov calcite infill with adrock mixture” (left) and the same material following crushing (right)

Plagioclase, Biotite, and Amphibole-rich-bearing Samples (UJV)

Rich-bearing rock samples were selected to investigate the contribution of specific minerals in the sorption process of the studied elements. Biotite, plagioclase, and amphibole were chosen due to their prevalence and potential significance in granite-type rocks. These minerals exhibit unique structural and chemical properties that can influence their sorption capabilities. Biotite is known for its high cation exchange capacity (CEC) and large surface area, making it an important sorbent in geological systems. Plagioclase, a group of minerals within the feldspar family, possesses ion-exchange properties that can affect sorption behavior. Amphibole minerals, rich in cations, contribute to the overall sorption capacity of the rock samples.

The selected samples for the study include Bukov host rock with high biotite content (V18), which contains approximately 21% biotite, Bukov host rock with high plagioclase content (2S3-3), enriched with about 45% plagioclase, and Bukov host rock with high amphibole content (2S4-4), which contains approximately 41% amphibole. By examining these enriched samples, we aim to investigate the sorption characteristics and potential contributions of these minerals to the overall sorption process. Understanding the sorption mechanisms and behavior of specific minerals in complex geological systems is crucial for comprehending the fate and transport of elements in the environment.

Natural Chlorite Infill Samples (UJV)

Samples of chlorite infill were located in the corridor BZ-XIIJ (chainage 218 m) at Bukov URF (Figure 1-10). In Bukovská et al. (2018) are described several types of fillings of tectonic disorders in Bukov URF. One of them is also tectonic clay, which has similar characteristics to our material. The sampling of this material was carried out in two separate campaigns. During the first excavation period in 2020, sample of clay infill material was extracted from the site no. 1 (Figure 1-11). The second sampling period took place in March 2022 and material from the site no. 2 was excavated (Figure 1-11). In both cases ca 1 kg of material was collected.

The processing of the clay material was similar as previously described. The material was dried, then crushed and milled before it was divided by sieving into different grain fractions.

Figure 1-10 Fracture with chloritic infill material located in the corridor BZ-XIIJ (chainage 218 m) with indicated sampling sites (red circles 1 and 2)

Figure 1-11 Left: sampling site no. 1, right: samplig site no. 2

Figure 1-12 Processing stages of the clay infill (from left: drying, crushing and sieving)

Synthetic Material (UJV)

The sorption experiments involved the use of synthetic calcite, specifically calcium carbonate precipitated from p.a. EMSURE® (Merck) with a calcium carbonate content exceeding 98.5%. To ensure uniform crystal size, the synthetic calcite was prepared using the ageing method, following the procedure outlined in Alvarez (2019). A total of 150 g of synthetic calcite was exposed to a 0.02 mol/L $NaHCO_3$ solution (5 L) with intermittent stirring for a duration of one month. Subsequently, the suspension underwent filtration using a 0.45 µm MF-Millipore membrane filter. The resulting solid phase was subjected to washing with acetone and distilled water, followed by a two-day drying period at 50°C. This processed solid phase was referred to as "aged" calcite throughout the experiments.

1.3.3.2 Sample Preparation for Experiments with Rock Materials at UJV

Prior to conducting the sorption experiments, the rock materials were subjected to a crushing process to achieve the desired particle size. The use of a jaw crusher BB 200 (Retsch) (Figure 1-13) ensured uniformity and homogeneity of the crushed rock samples. Subsequently, sieving with different-sized sieves on a sieving machine AS 300 (Retsch) (Figure 1-13) was performed to obtain specific particle size fractions, with fraction C selected for the sorption experiments (Table 1-4). The choice of crushed rock offers several advantages in the context of these experiments. Firstly, it promotes sample homogeneity, ensuring consistent composition and particle size distribution, which is crucial for accurate and reproducible results. Secondly, the use of crushed rock increases the available surface area, allowing for enhanced interactions with the experimental environment and facilitating sorption and chemical processes. Moreover, crushed rock allows for precise control over particle size fractions, enabling comprehensive investigations into the material's properties.

The preparation of crushed rock samples for various experiments followed standardized procedures to ensure reliable and accurate results. To eliminate fine dust produced during grinding, the crushed samples underwent multiple washes using demineralized water or were treated in an ultrasonic bath. This washing process was repeated until the solution became clear. A final rinse with SGW2 water was conducted, and the samples were allowed to air dry. For XRD analysis, the washed and crushed samples were finely ground using a Planetary Ball Mill PM 200 (Retsch). These meticulous sample preparation steps are crucial for minimizing potential contamination with fine particles with higher specific surfaces and optimizing the suitability of the samples for subsequent experimental analyses.

It has to be noted that in addition to evident advantages, sample crashing can midify the effective properties of the initially consolidated rocks. In particular, the crushing can increase reactive surface area. Further the freshly cleaved surfaces may have different reactivity or expose surface tipes not available in mature rocks due to alteration or deposition of secondary minerals. These aspects have different relative importance for various minerals in terms of reactivity and also the effect of mass to volume ratio depends strongly on grain size and available surface for each contributing mineral. These aspects have to be taken into account when extrapolating the laboratory result to the natural systems.

Table 1-4 Size fractions of rock for mineralogical analysis and sorption experiments

Fraction name	Particle size (mm)
A	< 0,063
B	0,125−0,063
C	0,63−0,125
D	0,8−0,63
E	> 0,8

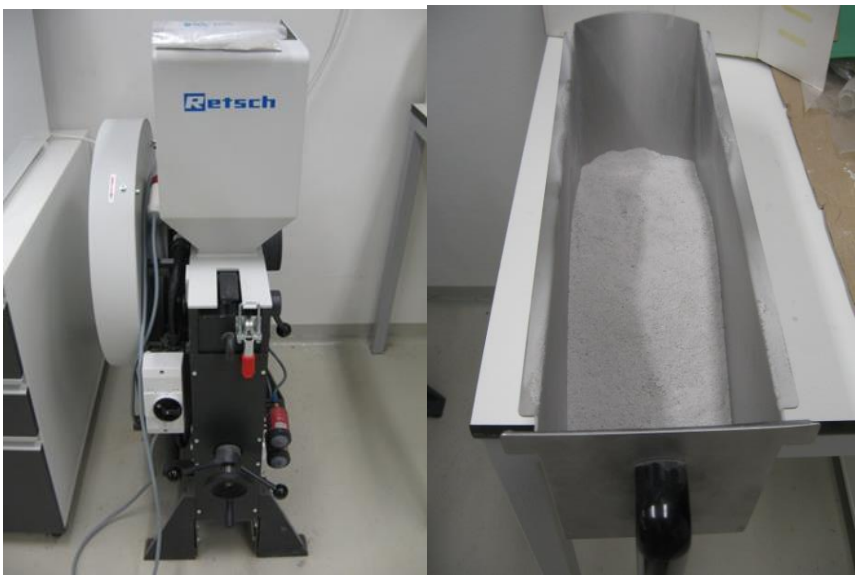

Figure 1-13 On the left: Jaw crusher BB 200 (Retsch), on the right: Crushed rock sample

Figure 1-14 Planetary Ball Mill PM 200 (Retsch), Sieving Machine AS 300 (Retsch), and UV Bath for Cleaning Sieves (description of the image from right to left)

1.3.3.3 Advanced Characterization Methods Employed at UJV

Prior to initiating the experimental investigations focusing on sorption-related properties, a comprehensive analysis was performed on both the fracture fillings and the rock material samples. The objective of this analysis was to assess and characterize the properties that might have an impact on sorption processes. We present the comprehensive mineralogical characterization achieved through X-ray diffraction (XRD) analysis, the determination of specific surface area using the BET (Brunauer-Emmett-Teller) analysis technique, the assessment of cation exchange capacity employing medium Cu(II)-triene methodology, and the evaluation of the potential for radiocesium interception (RIP). These scientifically rigorous methods have provided valuable insights into the mineralogical composition, surface properties, ion exchange capabilities, and radiocesium capture potential of the studied materials.

XRD Analysis

The determination of mineral phase content was performed at CGS (Czech Geological Survey) (RNDr. F. Laufek, Ph.D.) using a Bruker D8 Advance X-ray powder diffractometer configured in the Bragg-Brentano arrangement (see Figure 1-16). CuKα radiation and a position-sensitive detector with a Lynx Eye XE detector were utilized in the analysis. The powdered samples were deposited onto a flat substrate made of diffraction-free silicon. Diffraction patterns were recorded over an angular range of 4 to 80° 2Θ, with a step size of 0.015° and a reading time of 0.8 seconds per step.

The obtained X-ray diffraction patterns were qualitatively evaluated using the Difrrac. Eva program (Bruker AXS, 2015) and the PDF 2 database. A subsequent semi-quantitative phase analysis was conducted employing the Rietveld method (Bish and Post, 1989) in the Topas 5 program (Bruker AXS, 2014). Crystal structure models for the individual phases were sourced from the ICSD database (FIZ, 2015). During the Rietveld analysis, scale factors, lattice parameters, and sizes of coherently diffracting domains were specified for each phase. A correction for preferred orientation was applied for selected mineral phases. The detection limit of the method ranges from approximately 0.2 to 0.5 wt.% depending on the phase's nature and crystallinity. The resulting compositions of the samples are presented in Table 1-5 and Figure 1-17. As an example, the diffraction pattern of the analyzed sample Host rock of Bukov Calcite Infill, is shown in Figure 1-15, highlighting the detected mineral phases.

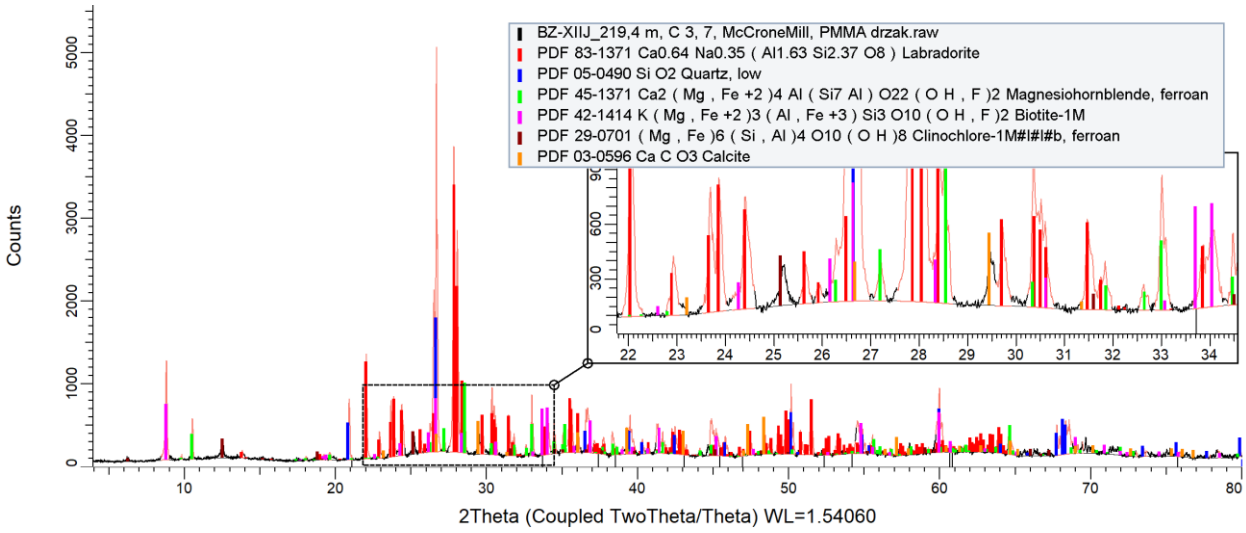

Figure 1-15 Powder X-ray diffraction analysis performed on the Host rock of Bukov Calcite Infill at CGS (by RNDr. F. Laufek, Ph.D.) XRD diffraction patterns were obtained, and prominent peaks corresponding to specific mineral phases were marked

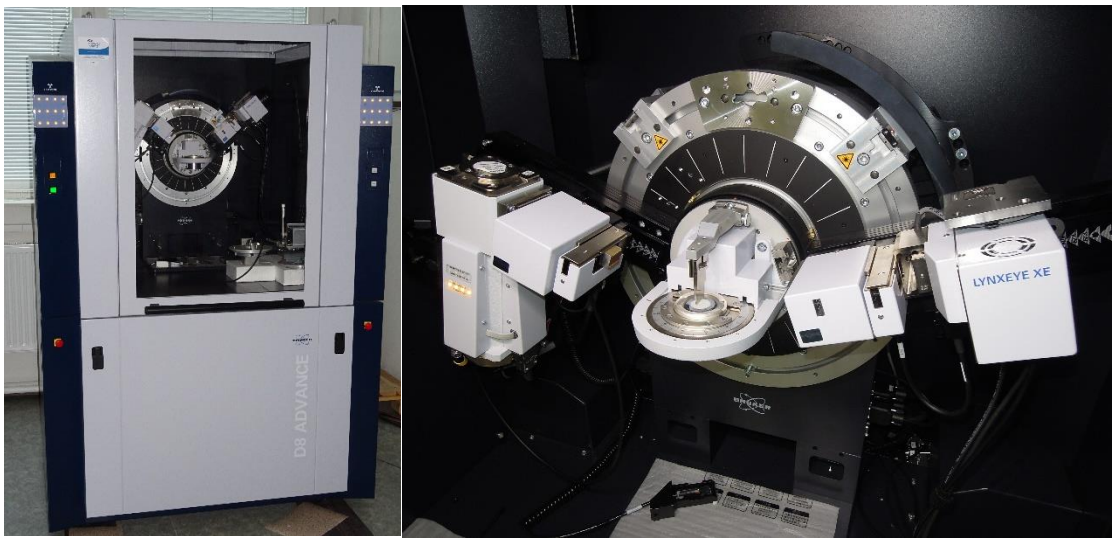

Figure 1-16 Powder X-ray diffractometer Bruker D8 Advance (left). Detailed description of the goniometer of the powder X-ray diffractometer Bruker D8 Advance (right)

Table 1-5 Contents of the mineral phases (wt.%) for the samples of Bukov Calcite Infill, Bukov Calcite Infill with rock admixture and surrounding rock from the BZJHXII (219.4 m) sample collection site. In addition, samples of the parent rock (BZJXII 250 m), Host rock with high biotite, plagioclase and amphibole contents, chlorite infills from the BZ-XIIJ_218 m and synthetic calcite were also processed for experimental purposes (preparation methodology according to Alvarez. 2019)

Sample	Calcite	Quartz	Chlorite	Plagioclase	K-feldspar	Dolomite	Amphibole	Biotite/Mica	Kaolinite	Note
BZJXIIJ_219.4 m_C **Bukov Calcite Infill**	89.5	10.5								
BZJXIIJ_219.4 m_D **Bukov Calcite Infill**	87.5	12.5								
BZJXIIJ_219.4 m_C **Bukov Calcite Infill with rock admixture**	74.5	20.5	1.5	2	1	0.5				the presence of dolomite is uncertain
BZJXIIJ_219.4 m_D **Bukov Calcite Infill with rock admixture**	70.5	23.5	1	2.5	2	0.5				the presence of dolomite is uncertain
BZJXIIJ_219.4 m_C Surrounding rock, **Host rock of Bukov Calcite infill**	4.5	15.5	3	53			13	11		Prehnite is probably present in an amount that is at the limit of detection; the presence of chalcopyrite, ilmenite (or apatite) in amounts at the limit of detection cannot be excluded
BZJXIIJ_219.4 m_D Surrounding rock, **Host rock of Bukov Calcite infill**	5.5	14	3.5	54.5			12	10.5		Prehnite is probably present in an amount that is at the limit of detection; the presence of chalcopyrite, ilmenite (or apatite) in amounts at the limit of detection cannot be excluded

Sample	Calcite	Quartz	Chlorite	Plagioclase	K-feldspar	Dolomite	Amphibole	Biotite/Mica	Kaolinite	Note
BZ-XIIJ-250 m_C Surrounding rock; migmatised gneiss (host rock), **PVP-2**		14.5	1.5	42	0.5		29	12.5		calcite in the amount of approx. 0.5 wt.%
BZ-XIIJ-250 m_D Surrounding rock; migmatised gneiss (host rock), **PVP-2**		15	1.5	49.5	0.5		26	7.5		
Synthetic calcite										EMSURE®, Merck
"Aged" calcite										prepared from synthetic calcite using the methodology according to (Alvarez 2019); ageing ensures a uniform crystal size
V18_C, **Bukov Host rock with high biotite contents**		35.3	2	41.3				21.4		
2S3-3_C, **Bukov Host rock with high plagioclase contents**	1.1	24.2	2.2	45.2			20.8	6.5		
2S4-4_C, **Bukov Host rock with high amphibole contents**	1	10.1	1.2	46.4			41	0.3		
BZ-XIIJ_218 m_C **Bukov Chlorite Infill extracted from 1.site**	21	48	5.5	4				7.5	14	

Sample	Calcite	Quartz	Chlorite	Plagioclase	K-feldspar	Dolomite	Amphibole	Biotite/Mica	Kaolinite	Note
BZ-XIIJ_218 m_C **Bukov Chlorite Infill extracted from 2.site**	19.5	34.5	7	7.5				11.5	9	

The Bukov calcite infill exhibits a high calcium carbonate content, reaching up to 89 percent, with a minor impurity in the form of low-reactive quartz. By dissecting the embedded filling material within the surrounding rock, we obtained a sample of calcite infill mixed with the surrounding rock. This mixture has a lower calcium carbonate content but higher silicon content, along with the presence of chlorite. The composition of the surrounding rock resembles tectonic granitic rocks, characterized by a high content of plagioclase, quartz, amphibole, as well as non-expanding phyllosilicates such as biotite and chlorite. The surrounding rock with a significant plagioclase content can be classified as amphibolitic migmatites containing biotite. The rock with a high amphibole content can be identified as fine-grained amphibolite with a substantial amount of biotite/mica (Havlová et al. 2018). Among all the samples used, only the Bukov Chlorite infill sample displays a high percentage of phyllosilicates, including kaolinite and chlorite, both exhibiting a distinct layered structure. For the mineralogy calculation of the Bukov Chlorite Infills, muscovite mineral data was utilized. However, it cannot be ruled out that both dioctahedral and trioctahedral micas may also be present. When considering the Bukov Chlorite Infills, it is important to acknowledge that the XRD calculations may not be entirely accurate, and therefore, the obtained results should be regarded as a reasonable approximation.

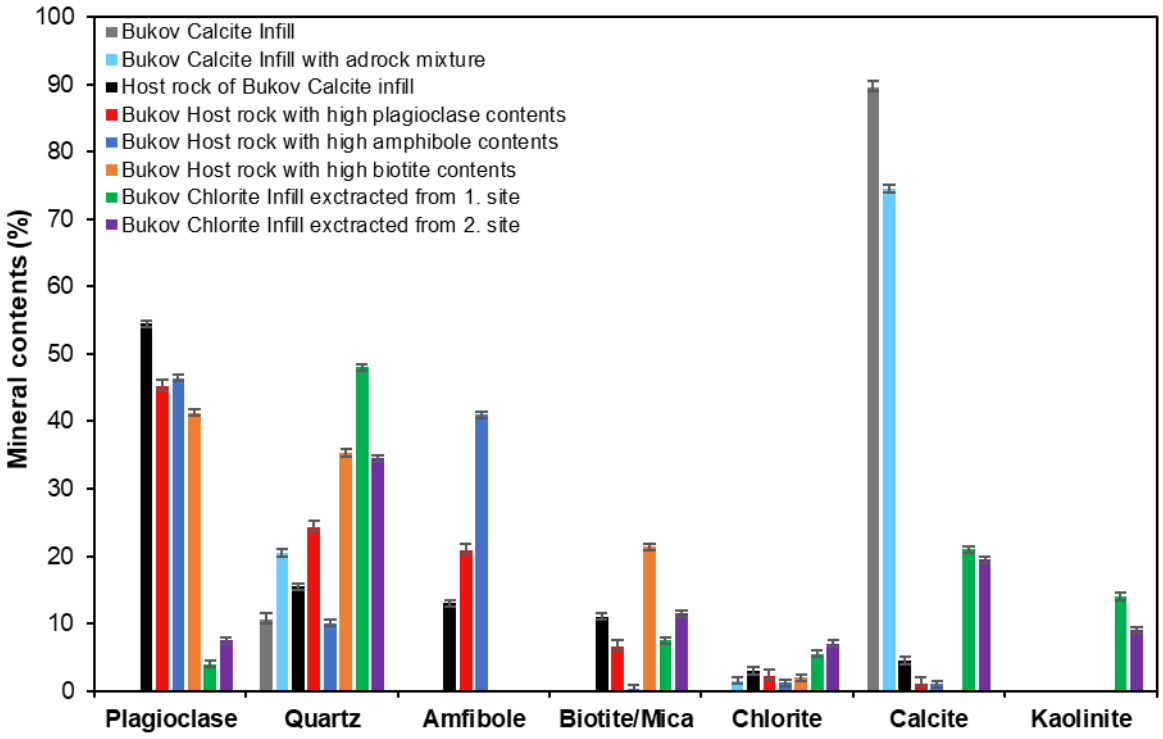

Figure 1-17 Contents of the mineral phases (wt.%) for the samples of Bukov Calcite Infill, Bukov Calcite Infill with rock admixture and surrounding rock from the BZJHXII (219.4 m) sample collection site. In addition, samples of the parent rock (BZJXII 250 m), Host rock with high biotite, plagioclase and amphibole contents, Chlorite infills from the BZ-XIIJ_218 m with detection limit (0.5%) as deviations

Specific BET Surface Area

The pore distribution and specific surface areas of the crushed samples were assessed at UCT Prague (University of Chemistry and Technology in Prague) (Doc. Ing. M. Lhotka, Ph.D.) using the Micromeritics 3Flex and ASAP 2020 devices (Figure 1-18). These instruments are multifunctional and capable of measuring the specific surface area of solid materials as well as the distribution of mesopores and micropores. The measurement process involves recording the adsorption isotherm of nitrogen or krypton, which depicts the relationship between the amount of adsorbed component and its pressure above the solid

material at a constant temperature. In cases where materials possess very low specific surface areas, krypton is preferred as the adsorptive. Based on the adsorption isotherm, the specific surface area of the mesopores was determined using the BET method, while the volume distribution and area of the mesopores were obtained using the BJH (Barrett-Joyner-Halenda) method. Before conducting each adsorption isotherm measurement, the samples underwent vacuum degassing at a temperature of 100°C for 2 hours (with a temperature ramp-up rate of 10 °C/min). Subsequently, the temperature was raised to 120°C at a rate of 10°C/min and maintained for 12 hours. The results of the specific surface area measurements determined by the BET isotherm are presented in Table 1-6. Due to the limited amount of gas adsorbed, it was not possible to determine the volume distribution or surface area of the pores. Consequently, it can be concluded that the calcite particles exhibited a non-porous nature.

Figure 1-18 Micromeritics 3Flex (left) and ASAP 2020 (right) adsorption analyzers: advanced instruments for adsorption analysis at UCT Prague (Doc. Ing. M. Lhotka, Ph.D.)

Despite Bukov Chlorite Infill exhibiting a lower specific surface area compared to typical clay minerals, the measurement of adsorption isotherms was conducted using nitrogen due to the limited applicability of krypton measurements to specific surface areas smaller than 1 m^2/g. The BET isotherm constant, denoted as 'C', falls within the range of 135 to 140, providing empirical evidence that the utilization of the BET isotherm for specific surface area calculations is justified.

Table 1-6 The specific BET surface area (m^2/g) and average particle size (nm) of all Bukov rock samples, as well as the synthetic and "aged" calcite, were determined using nitrogen (N2) and krypton (Kr) as the adsorptive medium, with standard deviations

Sample	Specific BET surface area (N_2), m^2/g	Specific BET surface area (Kr), m^2/g	Average particle size (N_2), nm	Average particle size (Kr), nm
Bukov Calcite Infill	0.1463 ± 0.0020	0.0956 ± 0.0071	15 267.3	23 370.9
Bukov Calcite Infill with rock admixture	0.1488 ± 0.0006	0.1318 ± 0.0017	15 129.5	17 074.3

Sample	Specific BET surface area (N_2), m^2/g	Specific BET surface area (Kr), m^2/g	Average particle size (N_2), nm	Average particle size (Kr), nm
Host rock of Bukov Calcite infill	0.4014 ± 0.0007	0.2878 ± 0.0006	5 332.1	7 436.6
Migmatized gneiss, PVP-2	0.1917 ± 0.0007	0.1687 ± 0.0008	11 001.0	12 502.7
Synthetic calcite	0.1616 ± 0.0010	0.1148 ± 0.0077	13 883.2	19 550.7
“Aged” calcite	0.1508 ± 0.0008	0.1140 ± 0.0039	14 821.1	19 598.5
Bukov Host rock with high biotite contents	-	0.1045 ± 0.0006	-	-
Bukov Host rock with high plagioclase contents	-	0.0999 ± 0.0004	-	-
Bukov Host rock with high amphibole contents	-	0.0994 ± 0.0003	-	-
Bukov Chlorite Infill extracted from 1.site	7.4247 ± 0.0096	-	796.4	-
Bukov Chlorite Infill extracted from 2.site	9.1673 ± 0.0174	-	612.9	-

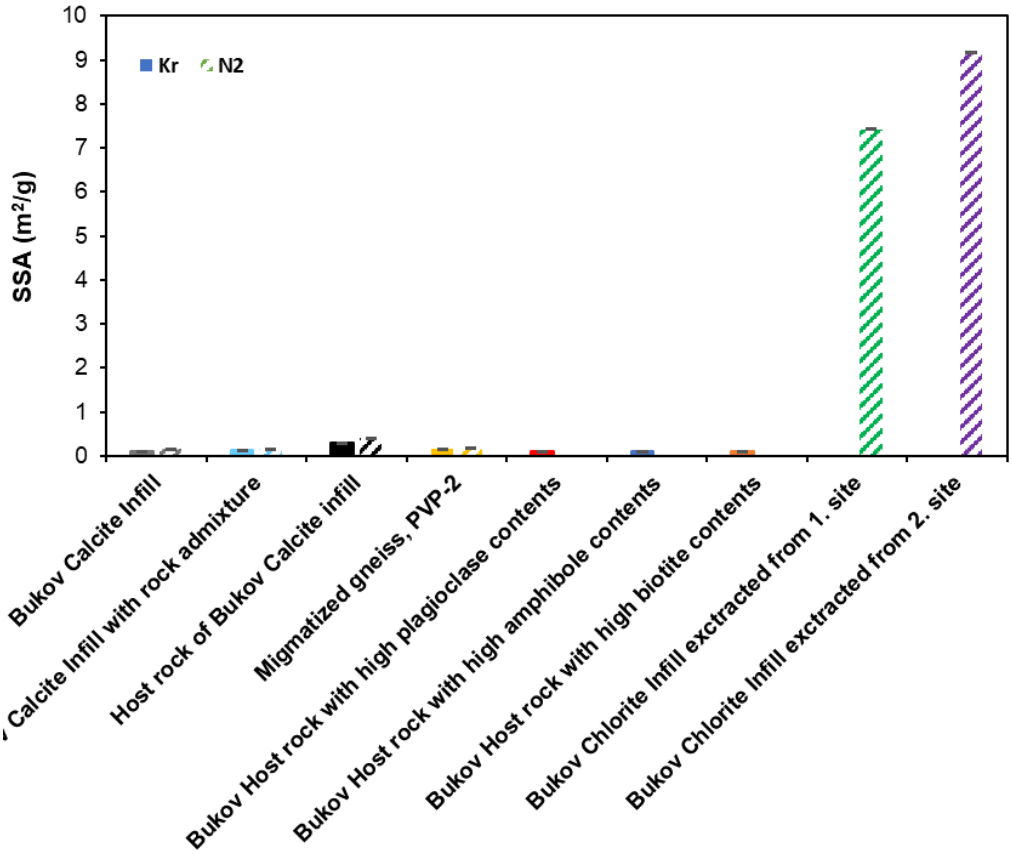

Figure 1-19 Specific surface area of all Bukov samples measured, nitrogen (N_2) and krypton (Kr) was used as the adsorptive medium with standard deviations

The specific surface area measured using N_2 was found to be greater than that achieved with Kr, which can be attributed to their disparate reactivity and subsequent sensitivity to the adsorbent surface. Kr demonstrates enhanced responsiveness to minor pressure variations, thereby enabling more accurate determination of specific surface area (Dubois 2011). Based on mineralogical analysis, the Bukov Chlorite Infills exhibit the highest specific surface area, primarily due to their elevated concentrations of layered phyllosilicates, chlorite, and kaolinite as rock-altered minerals with enhanced specific surface area compared to the Bukov Calcite Infill. Conversely, the host rocks associated with the Bukov Calcite Infill demonstrate a higher specific surface area in comparison to the Bukov Chlorite Infills. The lower specific surface area of the host rocks can be attributed to their abundant silicate minerals, such as quartz, aluminosilicates, and calcites, which possess structures with inherently lower specific areas for adsorption of adsorbates.

In the context of assessing larger specific surface areas, nitrogen is often employed as an adsorptive medium. However, when comparing it to nitrogen, krypton demonstrates diminished sensitivity to surface polarity effects owing to its lack of a quadrupole moment. Moreover, krypton exhibits reduced spatial orientation on the surface. As a consequence, when measuring specific surface areas below 1 m^2/g, krypton yields lower values compared to nitrogen, as we can see from the SSA in Table 1-6,Figure 1-19 and Figure 1-20.

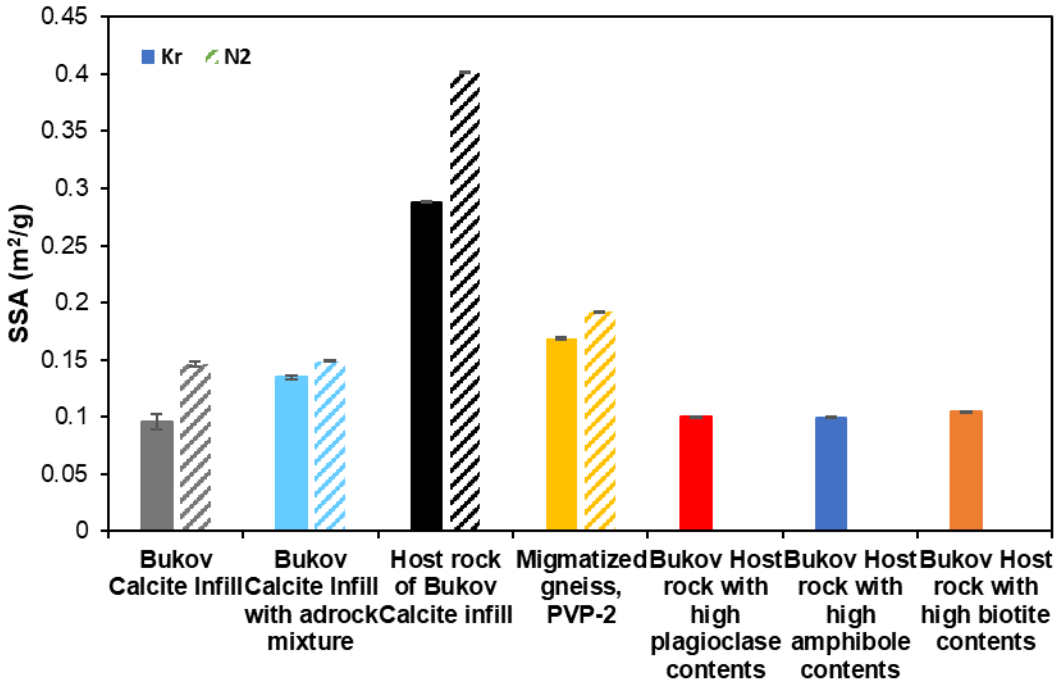

Figure 1-20 Specific surface area of all Bukov samples measured, nitrogen (N_2) and krypton (Kr) was used as the adsorptive medium with standard deviations

The analysis of the BET isotherms presented in Figure 1-20 reveals a distinct disparity in the quantity of nitrogen adsorbed, with the Bukov Chlorite Infill exhibiting a significantly higher uptake compared to the other samples under investigation. This observation is in alignment with the specific BET surface area measurements and mineral compositions of the respective samples. Based on the analysis of the adsorption isotherms of Bukov Chlorite Infills, it is evident that the adsorption isotherms conform to the Type IVa classification as per the IUPAC guidelines, indicating the presence of mesoporous materials. The absence of a steep adsorption uptake at the beginning of the isotherm suggests the lack of micropores. Notably, a pronounced hysteresis loop is observed, indicating the accessibility of the pores from both directions, which aligns with the characteristic layered structure typically associated with clay-like materials. The BJH examination further confirms the mesoporous nature of the sample, predominantly characterized by smaller mesopores.

The BET isotherms for the samples exhibiting lower nitrogen adsorption are depicted in Figure 1-21. The observed shape of the adsorption isotherms aligns with Type II isotherms according to the IUPAC classification, indicating a nonporous or macroporous material. In general, the adsorbed nitrogen quantities are minimal, corroborating the nonporous nature of the material. Significantly, an increase in adsorbed quantity is observed at relative pressures nearing 1, attributable to adsorption occurring on the external surface of the calcite particles. Hysteresis loops are also evident in the calcite adsorption isotherms, likely arising from capillary condensation between the particles. Nevertheless, the overall amount of adsorbed nitrogen remains exceedingly small, precluding the determination of pore volume or surface area distribution. Consequently, it can be inferred that the calcite particles lack significant porosity.

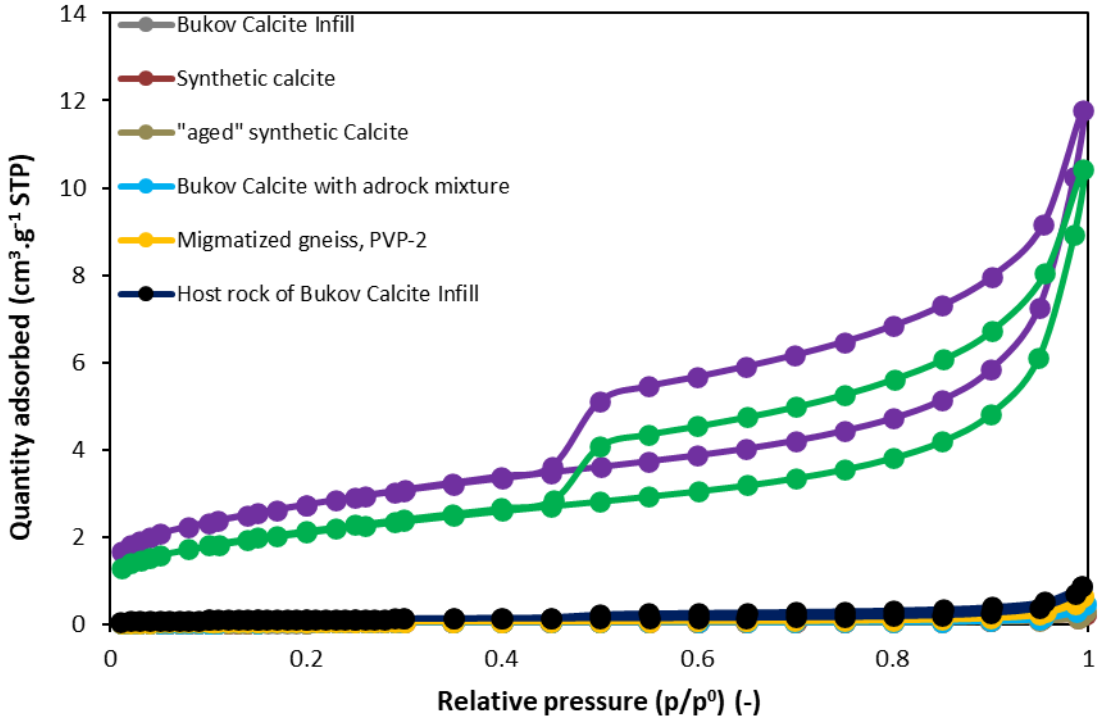

Figure 1-21 Adsorption isotherms were determined using nitrogen (N_2) as the adsorptive medium for Bukov Calcite Infill samples, synthetic calcite, migmatized gneiss, and Bukov Chlorite Infill

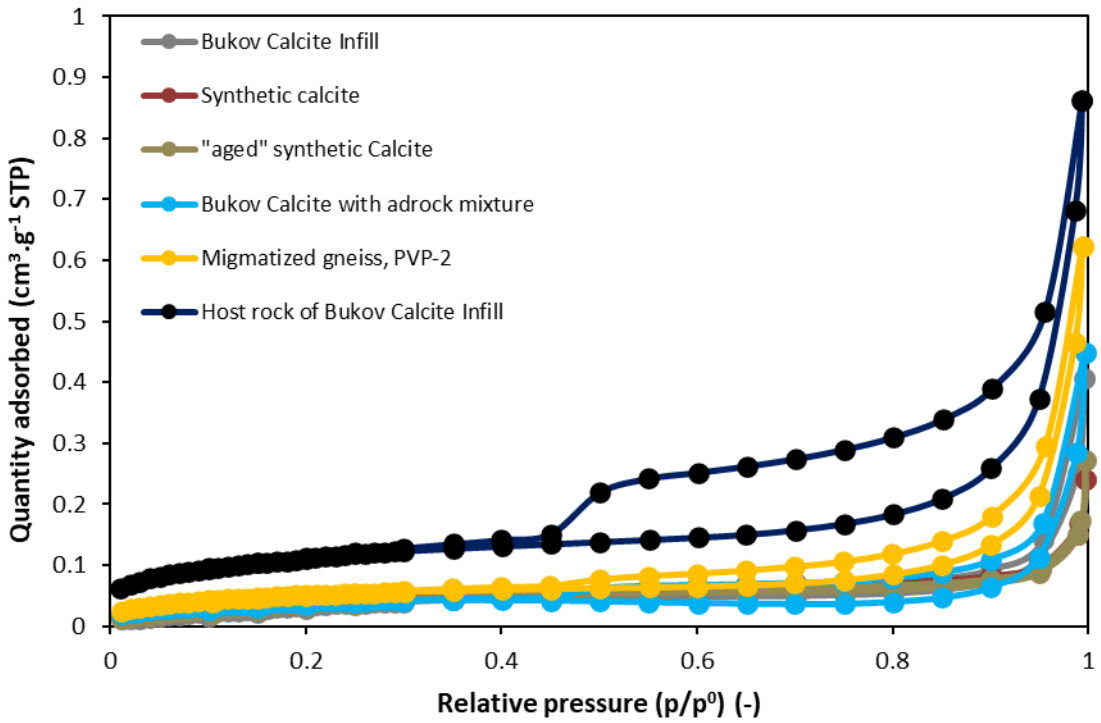

Figure 1-22 Adsorption isotherms were determined using nitrogen (N_2) as the adsorptive medium for Bukov Calcite Infill samples, synthetic calcite, migmatized gneiss

Krypton was employed as an adsorptive medium to measure the specific BET surface area, which was found to be lower than 1 m^2/g. The specific surface area of the rock samples was determined by measuring a section of the adsorption isotherm using krypton within a relative pressure range of 0.05 to 0.2 (Figure 1-23). The obtained low values for the specific surface area further support the nonporous nature of the rock samples.

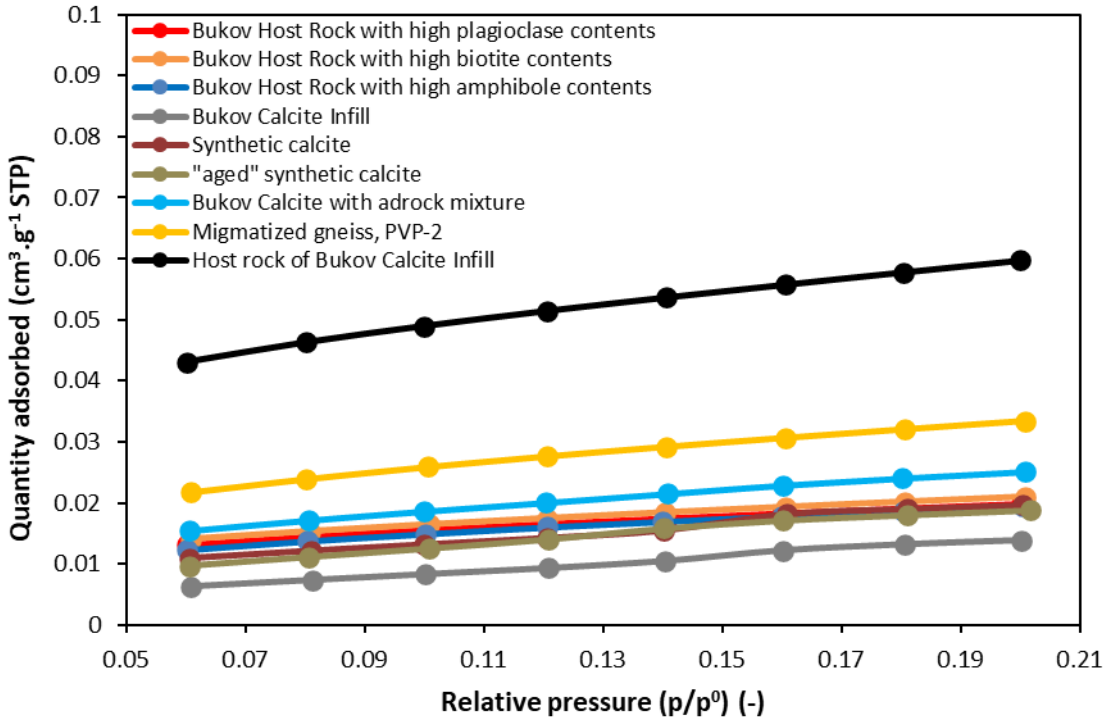

Figure 1-23 Adsorption isotherms were determined using Krypton (Kr) as the adsorptive medium for Bukov Calcite Infill samples, synthetic calcite, migmatized gneiss and enriched Bukov Host rocks with biotite, amphibole and plagioclase

After the utilization of Bukov Calcite Infill in sorption experiments (chapters **Erreur ! Source du renvoi introuvable.** and **Erreur ! Source du renvoi introuvable.**), where the entirety of the available sample was used due to its limited amount, a new Bukov Calcite infill was meticulously prepared from the same rock core to ensure consistency. Additionally, a calcite infill rock cube (see Figure 1-24) was specifically crafted from the identical core to enable a comprehensive comparison of the available surfaces (see Table 1-7). It is important to note that prior to measurement, the cube underwent a controlled crushing process to generate smaller fragments, ensuring that this fragmentation did not introduce significant bias in the final determination of the measured specific surface area. The separation and isolation of the calcite infill followed the same meticulous procedure employed previously. It is noteworthy that the newer sample exhibited a lower specific surface area, reflecting an improved separation from the surrounding host rock matrix. Intriguingly, the calcite infill rock cube displayed an approximate fourfold decrease in specific surface area, providing compelling evidence of its nonporous behavior when compared with the crushed rock samples. This is primarily due to the differences in particle size and surface roughness between the two types. Non-crushed rock consists of larger particles with irregular shapes and surfaces, resulting in a relatively smaller surface area. On the other hand, crushed rock undergoes a mechanical process that breaks it down into smaller fragments, increasing the total surface area by generating additional surfaces through fracturing (André et al., 2009).

The Bukov Calcite Infill samples, obtained through the quartering method, were uniformly distributed among all participating institutions. Each institution employed different preparation methods and utilized varying particle sizes in the treatment of the samples and for the sorption experiments. Subsequently, the prepared samples were exchanged between institutions for the express purpose of conducting comparative cross-sectional analyses and quantifying the specific BET surface areas. The results demonstrated that the natural calcite samples sourced from the University of Helsinki (UH) exhibited surface areas comparable to the calcite samples employed at ÚJV Řež. However, a discernible disparity was evident in the case of the Bukov Calcite Infill prepared by the University of Helsinki (UH), as it exhibited a significantly higher specific BET surface area. This dissimilarity can be attributed to the deliberate implementation of a smaller particle size in the preparation process, which resulted in an amplification of the available surface areas (Lehto et al. 2019). Furthermore, variations in the sample preparation protocol employed by UH may have contributed to the observed disparity. These findings underscore the substantial influence of pre-experimental preparation processes on the surface area and sorption capacities of crushed rock samples.

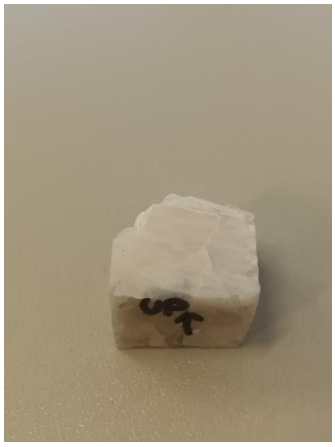

Figure 1-24 The Bukov Calcite Infill sample, in the form of a cube, was utilized for the determination of specific surface area

Table 1-7 The specific BET surface area (m^2/g) of Bukov Calcite Infill, Bukov Calcite Infill with adrock mixture, Bukov Calcite Infill_2022, Bukov Calcite Infill_2022_Cube and Bukov Calcite Infill, specifically prepared by the University of Helsinki for their sorption, were determined using krypton (Kr) as the adsorptive medium, with standard deviations

Sample	Specific BET surface area (Kr), m^2/g
Bukov Calcite Infill	0.0956 ± 0.0071
Bukov Calcite Infill with adrock mixture	0.1318 ± 0.0017
Synthetic calcite	0.1148 ± 0.0077
"Aged" calcite	0.1140 ± 0.0039
Bukov Calcite Infill_2022	0.0624 ± 0.0014
Bukov Calcite Infill_2022_Cube	0.0191 ± 0.0007
Natural Calcite_UH	0.1079 ± 0.0017

Sample	Specific BET surface area (Kr), m^2/g
Bukov Calcite Infill_UH	1.3001 ± 0.0355

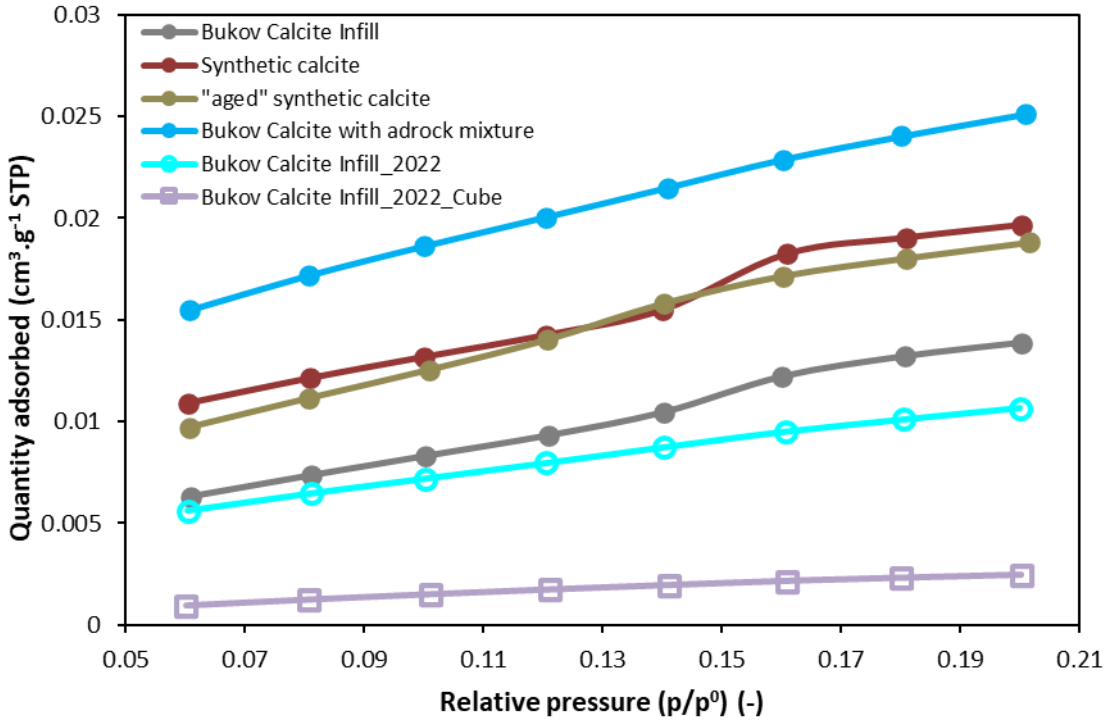

Figure 1-25 Adsorption isotherms were determined using Krypton (Kr) as the adsorptive medium for Bukov Calcite Infill samples, synthetic calcite, “aged” calcite, Bukov Calcite with adrock mixture, Bukov Calcite Infill_2022 as well as Bukov Calcite Infill_2022_Cube

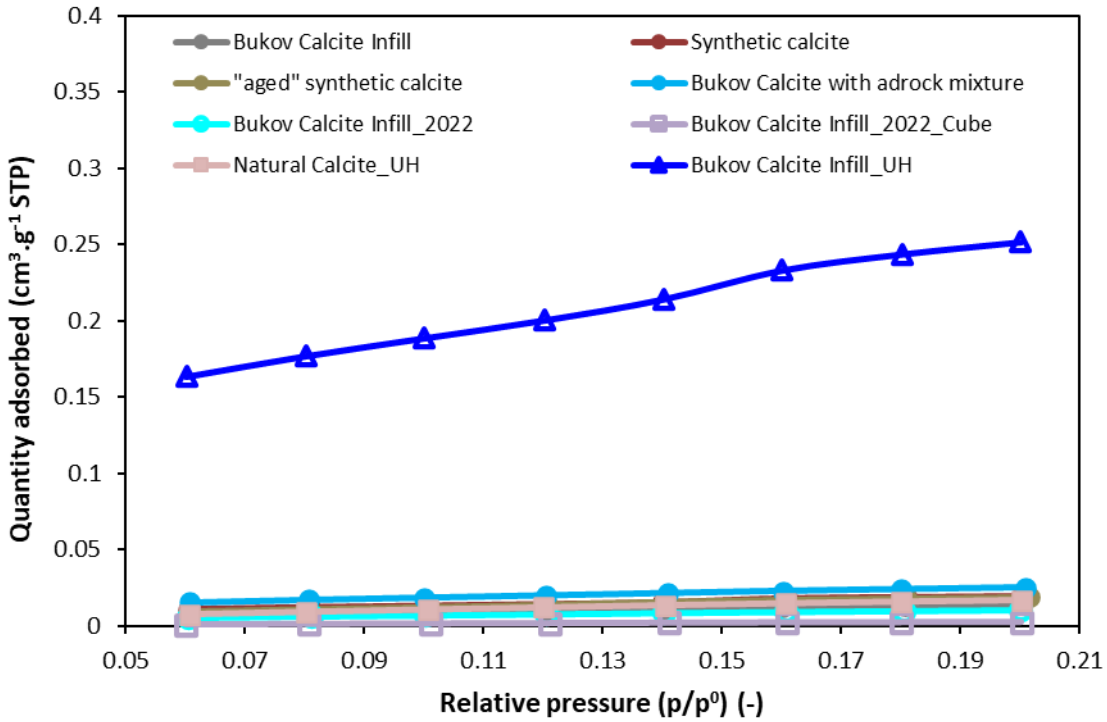

Figure 1-26 Adsorption isotherms were determined using Krypton (Kr) as the adsorptive medium for Bukov Calcite Infill samples, synthetic calcite, “aged” calcite, Bukov Calcite with adrock mixture, Bukov Calcite Infill_2022, Bukov Calcite Infill_2022_Cube, as well as Bukov Calcite Infill, specifically prepared by the University of Helsinki for their sorption experiments

Determination of the density using an He pycnometer

The densities of the analysed samples were determined using a "Pycnomatic" helium pycnometer (see Figure 1-27) provided by Thermo company at the UCT Prague (University of Chemistry and Technology in Prague) laboratory (Doc. Ing. M. Lhotka, Ph.D.). The obtained density values are presented in Table 1-8. In the context of sorption, a higher density suggests a potentially reduced accessibility of sorption sites within the particles, which could result in lower sorption capacity. However, it is crucial to consider other factors such as specific surface area, pore size distribution, and chemical composition of the samples. These factors can influence sorption behavior and may compensate for variations in density. Therefore, it is essential to evaluate density in conjunction with other parameters to gain a comprehensive understanding of the sorption capabilities of the samples.

Figure 1-27 "Pycnomatic" helium pycnometer at the UCT Prague (Doc. Ing. M. Lhotka, Ph.D.)

Table 1-8 Actual (helium) densities in form of g/cm^3 for the crushed samples of calcite Infill and surrounding host rock, with standard deviations

Sample	Bukov Calcite Infill	Bukov Calcite Infill with adrock mixture	Host rock of Bukov Calcite infill	Migmatized gneiss, PVP-2	Synthetic calcite	"aged" calcite
ρ, g/cm^3	2.686 ± 0.001	2.666 ± 0.001	2.8031 ± 0.003	2.845 ± 0.001	2.674 ± 0.001	2.685 ± 0.001

The measured densities demonstrate a consistent correlation with the average particle sizes observed in the samples. Notably, the Host rock of Bukov Calcite infill and migmatized gneiss PVP-2, exhibit higher densities coupled with smaller average particle sizes. This suggests a relationship between the mineralogical composition of these rock samples and the observed variations in density and particle size. These variations may be attributed to the presence of the specific minerals and their arrangement within the rock matrix.

Cation Exchange Capacity

The assessment of the cation exchange capacity of rock materials offers valuable insights into the sorption behavior of radionuclides on granitic rocks. It provides information on the sorption mechanisms and identifies the dominant sorbing minerals within the rock matrix (Havlová et al. 2018). Phyllosilicates (such as micas and clays), which possess layered structures, play a significant role as sorbents in rock materials, offering multiple sorption sites (Bradbury and Baeyens 1999). The high value of cation exchange capacity indicates the occurrence of ion exchange processes associated with these sorption sites.

Furthermore, the determination of cation exchange capacity (CEC) for rock samples lacks a standardized method, primarily due to variations in the number of exchange sites governed by the mineralogy. In a Technical Report by Neubeck (2016), multiple CEC methods involving $BaCl_2$, NH4Ac, and $CO(NH_3)_6^{3+}$ complexes were employed in column experiments using fracture coating rock samples from Äspö/Lasemar. The results indicated that the utilization of the $CO(NH_3)_6^{3+}$ complex yielded the most consistent outcomes, demonstrating an expected dependence on grain size.

The cation exchange capacity (CEC) and the occupancy of cations at exchange sites were determined following the certified methodology with registration number SÚJB/ONRV/15452/2014 (Červinka R. 2014). The methodology employed the Cu(II)triethylenetetramine complex (Cu(II)-triene) to facilitate the exchange

of cations in the interlayers of phyllosilicates with Cu^{2+} cations. The outcome of the analysis provided the CEC value (in meq 100 g^{-1}) of the rock material, which represents the quantity of copper that has been bound (i.e., exchanged for cations) to the rock material, along with the CEC_{sum} value (in meq 100 g^{-1}), representing the total amount of exchanged cations. The equilibrium between these two values is expected. This standardized procedure is commonly employed for determining the cation exchange capacity of clay materials, particularly bentonites, with CEC values typically ranging in the order of tens of meq 100 g^{-1}, contingent upon the specific characteristics of the bentonite. The CEC of selected bentonites, such as Rokle (80 meq 100 g^{-1}), B75 (56.8 meq 100 g^{-1}), and S65 (71.5 meq 100 g^{-1}) has been determined within projects such as TIP (Gondolli et al. 2013) for illustrative purposes (Havlová et al. 2018).

The Cu(II)-triene solution was prepared using the standardized procedure at UJV Řež, a.s.. The clay materials typically required a Cu(II)-triene concentration of 0.01 mol/L. However, based on the specific surface area analysis of the rock samples employed in this study, it was evident that the number of exchange sites would be considerably lower. Consequently, for these particular samples, the Cu(II)-triene concentration was reduced by one order of magnitude (0.001 mol/L). The rock samples, weighing approximately 1g, were carefully placed into 50ml polyethylene vials. The volume of Cu(II)-triene solution (10ml) added to the vials was adjusted to compensate for the anticipated decrease in concentration, which could be accurately determined using an atomic absorption spectrometer (AAS). Subsequently, the samples were subjected to agitation on an orbital shaker (IKA HS 260, IKA®-Werke GmbH & Co., DEU) for the desired duration. Upon completion of the predetermined time, the entire vials containing the samples were subjected to centrifugation at 9000 RPM for 15 minutes (MPW 352, MPW Med.Instruments, POL). The resulting solution was carefully collected, and the necessary volume was transferred to polyethylene vials. Nitric acid was added to these vials in the appropriate amount for the subsequent measurement of Cu, Na, Ca, Mg, and K cation concentrations using a dual-beam flame atomic absorption spectrometer (SavantAA Σ, GBC Scientific Equipment, Pty Ltd, Australia), equipped with a deuterium background correction lamp for enhanced accuracy. Each specific cation was analysed using a single-element hollow cathode lamp provided by Photron Pty Ltd, Australia, and an optimized measurement method was employed. This method encompassed fine-tuning the flame composition, optimizing burner positioning, establishing an appropriate calibration range, generating calibration curves and employing ionization buffers and sample acidification techniques. Sample acidification was carried out using 67% NORMATOM nitric acid for ultra-trace analysis. In cases where ionization buffering was required, a solution of potassium chloride (99.0-100.5% ACS) was used to ensure a final nitric acid concentration of 2% and a potassium concentration of 2000 mg/l in the sample matrix. The cation concentrations were determined using the integration method evaluated through linear least squares (LLS) analysis. Certified reference materials supplied by Analytika, spol. s.r.o., Czech Republic, were utilized as calibration standards.

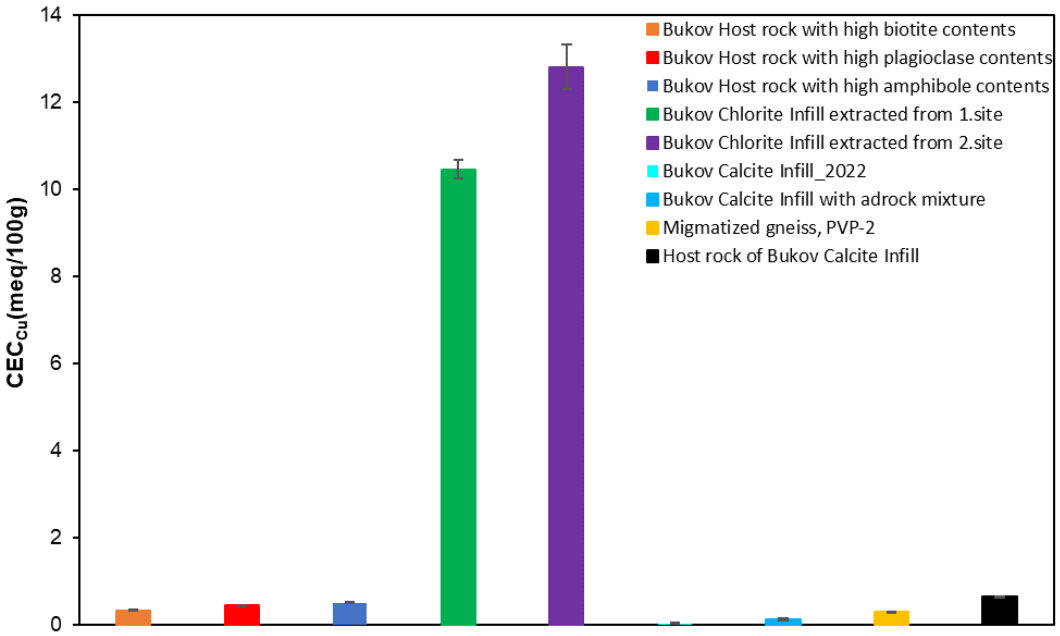

Figure 1-28 The CEC (cation exchange capacity) values in meq/100g were determined using the Cu(II)-triene method for the Bukov Host rock samples enriched with biotite, plagioclase, amphibole, Bukov Calcite Infill, Bukov Calcite infill with adrock mixture, migmatized gneiss PVP-2, and Host rock of Bukov Calcite Infill as well as for the Bukov Chlorite infills extracted from the 1st and 2nd sites with standard deviations

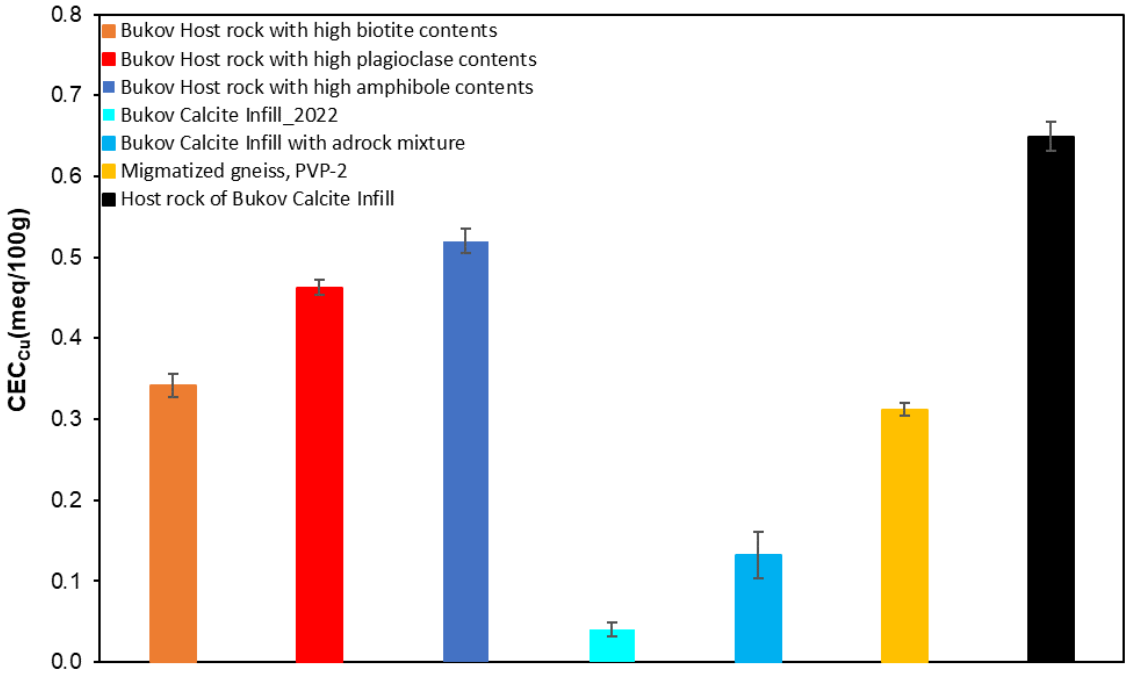

Figure 1-29 The CEC (cation exchange capacity) values in meq/100g were determined using the Cu(II)-triene method for the Bukov Host rock samples enriched with biotite, plagioclase, amphibole, Bukov Calcite Infill, Bukov Calcite infill with adrock mixture, migmatized gneiss PVP-2, and Host rock of Bukov Calcite Infill as well as for the Bukov Chlorite infills extracted from the 1st and 2nd sites with standard deviations

Consistent with expectations based on the specific surface area and mineralogical composition, the Bukov Chlorite Infill extracted from the 1st and 2nd sites exhibited the highest cation exchange capacity (CEC) values (see Figure 1-28, Figure 1-29 and Table 1-9). This can be attributed to the elevated levels of kaolinite, chlorite, and biotite present in these infills. Specifically, the 2nd site Bukov Chlorite Infill displayed the highest CEC, which can be attributed to its higher contents of biotite, chlorite, and other minerals compared to the Chlorite Infill from the 1st site. Interestingly, even though the 2nd site had a lower kaolinite content, it exhibited a higher CEC due to the presence of higher amounts of biotite/mica and chlorite, as well as a different mineralogical composition.

Table 1-9 The CEC (cation exchange capacity) values in meq/100g were determined using the Cu(II)-triene method for the Bukov Host rock samples enriched with biotite, plagioclase, amphibole, Bukov Calcite Infill, Bukov Calcite infill with adrock mixture, migmatized gneiss PVP-2, and Host rock of Bukov Calcite Infill as well as for the Bukov Chlorite infills extracted from the 1st and 2nd sites with standard deviations

Sample	CEC_{Cu}, meq/100g	Ca^{2+}, meq/100g	Mg^{2+}, meq/100g	Na^{+}, meq/100g	K^{+}, meq/100g	CECsum, meq/100g
Bukov Host rock with high biotite contents	**0.34 ± 0.01**	0.43 ± 0.01	0.030 ± 0.001	0.056 ± 0.003	0.051 ± 0.002	**0.57 ± 0.01**
Bukov Host rock with high plagioclase contents	**0.46 ± 0.01**	0.55 ± 0.02	0.068 ± 0.002	0.050 ± 0.001	0.041 ± 0.003	**0.71 ± 0.02**
Bukov Host rock with high amphibole contents	**0.52 ± 0.02**	0.62 ± 0.01	0.057 ± 0.002	0.052 ± 0.004	0.016 ± 0.001	**0.74 ± 0.02**
Bukov Chlorite Infill extracted from 1.site	**10.46 ± 0.22**	6.67 ± 0.15	1.94 ± 0.59	0.104 ± 0.001	0.208 ± 0.001	**8.92 ± 0.16**
Bukov Chlorite Infill extracted from 2.site	**12.81 ± 0.51**	8.69 ± 0.24	2.40 ± 0.05	0.106 ± 0.006	0.221 ± 0.007	**11.42 ± 0.24**
Bukov Calcite Infill_2022	**0.040 ± 0.009**	0.37 ± 0.014	0.018 ± 0.001	0.030 ± 0.002	0.003 ± 0.001	**0.42 ± 0.01**
Bukov Calcite Infill with adrock mixture	**0.13 ± 0.03**	0.433 ± 0.005	0.055 ± 0.005	0.059 ± 0.001	0.006 ± 0.001	**0.55 ± 0.01**
Migmatized gneiss, PVP-2	**0.31 ± 0.01**	0.48 ± 0.02	0.059 ± 0.002	0.050 ± 0.002	0.036 ± 0.001	**0.62 ± 0.02**
Host rock of Bukov Calcite Infill	**0.65 ± 0.02**	0.75 ± 0.04	0.116 ± 0.002	0.058 ± 0.002	0.068 ± 0.001	**0.99 ± 0.04**

The higher concentrations of Ca^{2+} and Mg^{2+} suggest the presence of more accessible exchange sites for bivalent cations. In contrast, the concentrations of monovalent cations exhibited similar levels, indicating

comparable accessibility of biotite/mica interlayers between both infills and their potential presence within other mineral structures.

Regarding the remaining host rock samples, their cation exchange capacity (CEC) was generally lower compared to the infills, which aligns with expectations based on their mineral compositions. However, it is worth noting that the Bukov Host rock, characterized by high biotite contents, exhibited the lowest measured CEC. This may be attributed to the specific interlayer structure of biotite/mica present in the sample. The interlayer structure of biotite/mica in the Bukov Host rock could result in reduced accessibility of cation exchange sites, leading to a lower CEC compared to the infills. In comparison of Chlorite infills they notable have lower CEC in comparison with the bentonite with majority of clay contents around

The Bukov Calcite Infill and adrock mixture displayed the lowest Cation Exchange Capacity (CEC) values as measured by Cu (II)-triene complex or from the sum of cations, indicating a limited presence of readily exchangeable sites due to the structural integrity of the calcite mineral and the overall composition of these samples (see Table 1-9, Figure 1-30 and Figure 1-31). However, the CEC measured from the sum of cations was notably higher due to the dissolution of calcite and subsequent release of Ca^{2+} cations during the sorption process of the complex. The host rock of the Bukov Calcite Infill exhibited the highest CEC among the tested samples, particularly after the inclusion of Chlorite Infills. This observation was consistent with the specific surface areas of the samples, where the size of Kr gas was comparable to the leaching cations. Consequently, the sorption behaviour and relative chemical affinities of the Cu (II)-triene complex influenced the CEC of the PVP-2 sample, resulting in a slightly lower value compared to the enriched host rock samples.

In terms of selective sorption sites for specific elements such as Cs, the CEC did not demonstrate significant values, challenging the prediction of sorption behaviour for these elements. The easily accessible cation exchange sites were predominantly observed in the Bukov Chlorite Infill due to the characteristic mineral structure of the infills.

Additionally, when considering the XRD mineralogy analysis, it was anticipated that higher biotite content would correspond to higher CEC and a greater BET specific surface area. Furthermore, more than 70% of the exchangeable cations in the examined rock samples were found in the form of Ca^{2+}. This suggests that calcium plays a significant role in the cation exchange processes within these rock samples, potentially influencing their overall sorption behaviour.

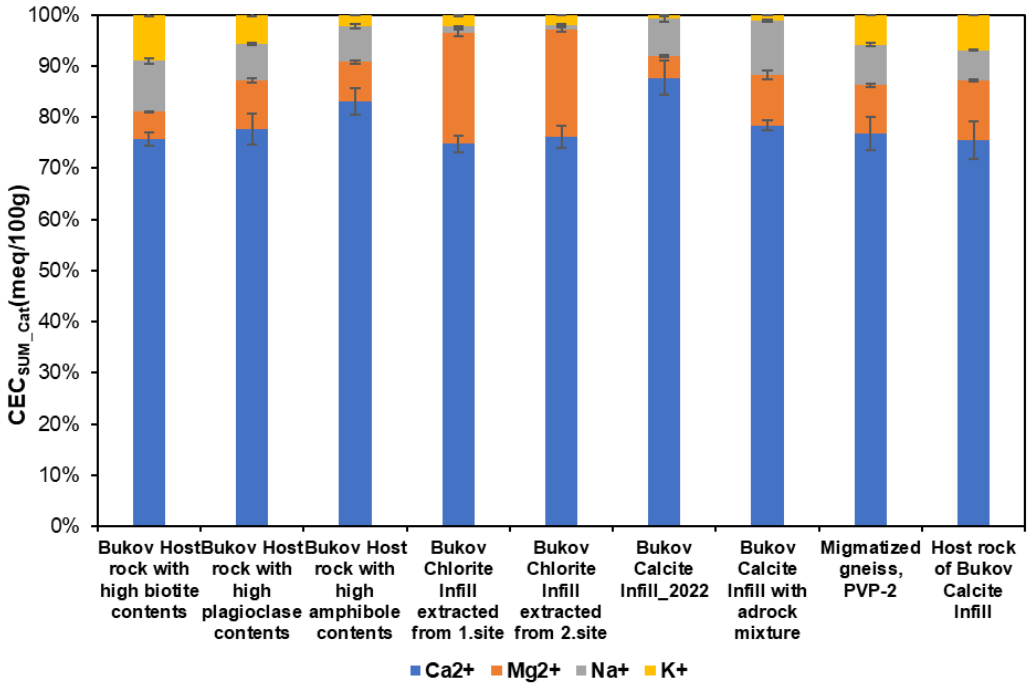

Figure 1-30 The CEC (cation exchange capacity) values in % for exchange cations were determined using the Cu(II)-triene method for the Bukov Host rock samples enriched with biotite, plagioclase, amphibole, Bukov Calcite Infill, Bukov Calcite infill with bedrock mixture, migmatized gneiss PVP-2, and Host rock of Bukov Calcite Infill as well as for the Bukov Chlorite infills extracted from the 1st and 2nd sites with standard deviations

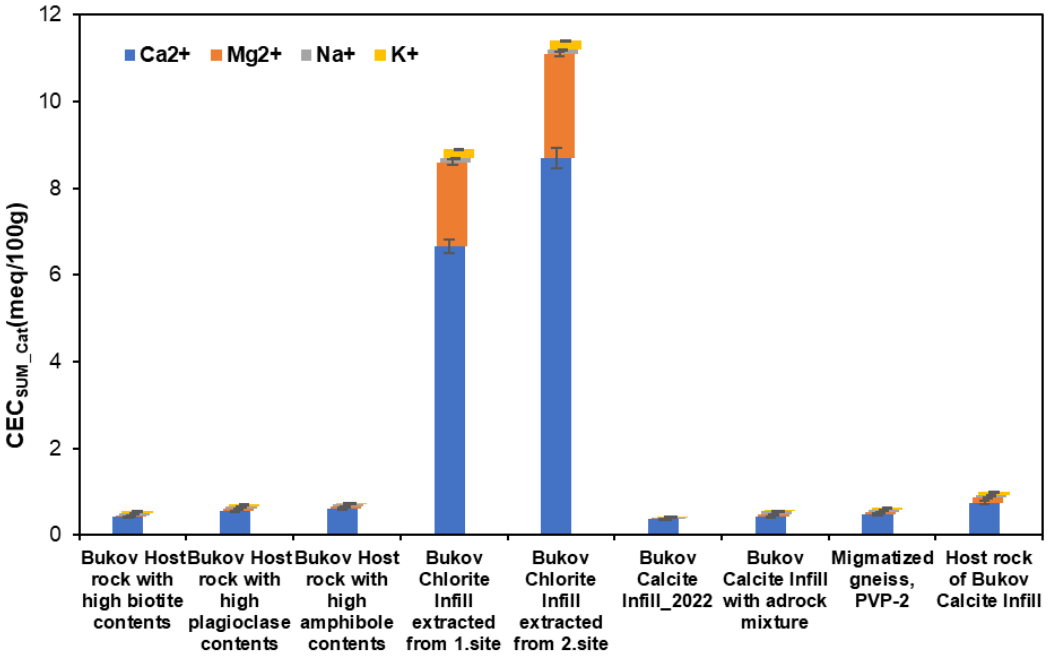

Figure 1-31 The CEC (cation exchange capacity) values in meq/100g for exchange cations were determined using the Cu(II)-trien method for the Bukov Host rock samples enriched with biotite, plagioclase, amphibole, Bukov Calcite Infill, Bukov Calcite infill with adrock mixture, migmatized gneiss PVP-2, and Host rock of

Bukov Calcite Infill as well as for the Bukov Chlorite infills extracted from the 1st and 2nd sites with standard deviations

Radiocesium Interception Potential (RIP)

Based on the XRD analysis, the Bukov samples exhibit higher levels of non-expandable phyllosilicates. These minerals, such as biotite and mica, may possess varying sorption capacities not only for higher concentrations of Cs, but also for lower concentrations below < 10^{-8} mol/L. In the lower concentration range, specific sorption sites known as frayed edge sites (FES) play a dominant role in Cs retention. The quantification of FES sites can be achieved through the analysis of radiocesium interception potential (RIP), which provides insights into the adsorption ability of Cs (Cremers et al., 1988; Wauters et al., 1996). RIP is defined as the product of the selectivity coefficient for Cs over K in the FES ($Kc_{(Cs\text{-}K)}^{FES}$) and the quantity of FES present (Wauters et al., 1996). This product is determined by the solid/liquid distribution coefficient for Cs (K_DCs) in a specific K-Ca ionic background and the concentration of K in the solution (mK) (Kitayama et al. 2019). The calculation is based on the following principles:

$$\mathrm{RIP} = \mathrm{Kc}_{(\mathrm{Cs\text{-}K})}^{\mathrm{FES}} * (\mathrm{FES}) = \mathrm{K}_{\mathrm{D}}^{\mathrm{Cs}} * \mathrm{mK}\ (\mathrm{mol/kg})$$

Where, K_D^{Cs} * mK is regarded to be proportional to the amount of the FES, because $Kc_{(Cs\text{-}K)}^{FES}$ is a constant. The hypothetical amount of FES can be calculated from the RIP divided by 1000 (i.e., a reference value of $Kc_{(Cs\text{-}K)}^{FES}$(Wauters et al. 1996, Kitayama et al. 2019).

To assess the radiocesium interception potential (RIP), 1 g of rock samples was introduced into 50 ml polyethylene vials, along with 50 ml of a solution containing 0.1 M $CaCl_2$ and 0.5 mM KCl. The vials were subjected to shaking twice a day for approximately 2 hours each, over a span of 5 days. Equilibrium was maintained by renewing 45 ml of the solution before each shaking cycle. Following the 5-day period, the vials were centrifuged at 5000 RPM for 5 minutes to separate the rock samples from the solution.

After achieving equilibrium, the solution was replaced with 45 ml of a Ca-K-^{137}Cs solution (0.1 mol/L $CaCl_2$ and 0.5 mmol/L KCl), spiked with 400 Bq of carrier-free ^{137}Cs, and continuously shaken for 1 day (Wauters et al. 1996). The activity of ^{137}Cs in the solution was quantified using a NaI scintillation counter (2480WIZARD^2, PerkinElmer, Waltham, MA). The distribution coefficient of Cs (K_D^{Cs}) was then calculated based on the reduction of ^{137}Cs concentration in the solution (see Figure 1-32 and Table 1-10).

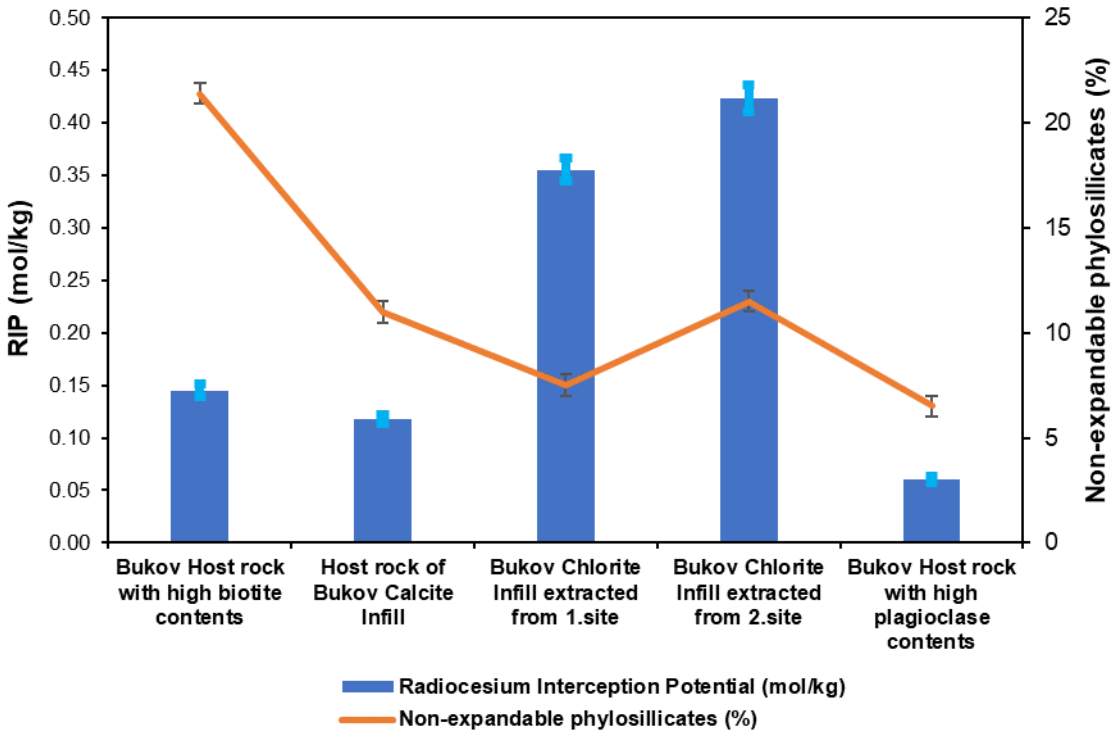

Figure 1-32 The radiocesium interception potential (RIP) values in mol/kg were determined for the Bukov host rock samples enriched with biotite, plagioclase, and the Bukov Host rock of Calcite Infill, as well as for the Bukov Chlorite Infill extracted from the 1st and 2nd sites. The RIP values were accompanied by their respective standard deviations. Additionally, the percentage contents of non-expandable phyllosilicates in these samples were also reported

The RIP analysis revealed that the Chlorite infills exhibited the highest values, which aligned with their elevated specific BET surface area and cation exchange capacity (CEC). The presence of numerous sorption sites suggested a higher abundance of frayed edge sites (FES), even though the concentration of non-expandable phyllosilicates was comparable. Intriguingly, the Bukov Host rock with high biotite contents displayed approximately twofold higher FES sites compared to the Bukov Host rock with higher plagioclase contents, despite similar specific surface area and CEC outcomes. This discrepancy may be attributed to the greater concentration of non-expandable phyllosilicates within the biotite sample. Notably, the FES sites in this sample surpassed those found in the Host rock of Bukov Calcite Infill, despite the latter possessing approximately twofold greater specific BET surface area. This discrepancy can be attributed to the higher abundance of non-expandable silicates within the biotite sample. Samples exhibiting a high number of exchange sites as measured by CEC and a substantial specific surface area for the adsorptive gas N_2 likely contain a significant amount of specific sites for Cs. This phenomenon was observed through the removal of K+ ions from non-expandable phyllosilicates, which resulted in higher CEC and RIP values (Kitayama et al., 2019). However, the measured results for rock samples were comparatively lower than those obtained from pure non-expandable phyllosilicates (Kitayama et al., 2019; Yamaguchi et al., 2017), indicating a reduced quantity of FES sites due to the complex composition of the samples.

Table 1-10 The radiocesium interception potential (RIP) values in mol/kg were determined for the Bukov host rock samples enriched with biotite, plagioclase, and the Bukov Host rock of Calcite Infill, as well as for the Bukov Chlorite Infill extracted from the 1st and 2nd sites. The RIP values were accompanied by their respective standard deviations. Additionally, the percentage contents of non-expandable phyllosilicates in these samples were also reported

Sample	Radiocesium Interception Potential (mol/kg)	Non-expandable phyllosilicates (%)
Bukov Host rock with high biotite contents	0.145 ± 0.006	21.4 ± 0.5
Host rock of Bukov Calcite Infill	0.118± 0.005	11 ± 0.5
Bukov Chlorite Infill extracted from 1.site	0.355 ± 0.011	7.5 ± 0.5
Bukov Chlorite Infill extracted from 2.site	0.423 ± 0.013	11.5 ± 0.5
Bukov Host rock with high plagioclase contents	0.060 ± 0.003	6.5 ± 0.5

1.3.3.4 Characterization of host rock materials

At GRS, the mineralogic composition of migmatite was determined by XRD analysis (X´Pert Pro, PANalytical) and revealed plagioclase and amphibole as its major components (Table 1-11). Carbonate content of migmatite of 5.9 ± 0.2 mass% was obtained from triplicate measurements by carbonate bomb method (Müller & Gastner 1971, Klosa 1994), in which 6 M HCl acid (Honeywell Fluka™ 37 % HCl, Puriss. p.a., Charlotte, North Carolina, US) was used to decompose solid carbonates whereby the pressure of the released CO_2 gas was measured using a high-precision pressure sensor (FDAD3302A, Ahlborn Mess- und Regelungstechnik GmbH, Holzkichen, Germany).

Table 1-11 Mineralogic composition of migmatite

	migmatite (ÚJV)	migmatite (GRS)
calcite		5.5
quartz		10.6
plagioclase		40.6
biotite		9.5
amphibole		24.1
chlorite		9.7

Specific surface area (multipoint BET) of the grain fraction of 1–2 mm of the unreacted migmatite sample and reacted migmatite samples was measured by TriStar II Plus 3030 Krypton Surface Area and Porosity Analyzer (Micromeritics Instrument Corporation, Norcross, GA, USA) using Kr as analysis gas.

1.4 References

Aaltonen, I., Engström, J., Front, K., Gehör, S., Kosunen, P., Kärki, A., Paananen, M., Paulamäki, S., Mattila, M. (2016) Geology of Olkiluoto (POSIVA 2016-16). Posiva Oy.

André, M., Malmström, M. E., & Neretnieks, I. (2009). Specific surface area determinations on intact drillcores and evaluation of extrapolation methods for rock matrix surfaces. *Journal of contaminant hydrology*, *110*(1-2), 1–8.

Bukovská, Z., Verner, K. et al. (2018). *Comprehensive geological characterization of URF Bukov. Final report*. SÚRAO TZ 247/2018, Radioactive Waste Repository Authority, Prague, Czech Republic.

Červinka R. (2014). Determination of cation exchange capacity (CEC) and exchangeable cations using the Cu(II)triethylenetetramine method. Certified methodology, Č.j. SÚJB/ONRV/15452/2014, in Czech.

Dubois, I. E., Holgersson, S., Allard, S., & Malmström, M. E. (2011). Dependency of BET surface area on particle size for some granitic minerals. *Proceedings in Radiochemistry*, 1(1), 75-82.

Fabritius, O., Puhakka, E., Li, X., Nurminen, A., Siitari-Kauppi, M. (2022) Radium sorption on biotite; surface complexation modeling study. *Applied Geochemistry*. 140, 105289. https://doi.org/10.1016/j.apgeochem.2022.105289.

Gondolli J., Brynych V., Drinová B., Hofmanová E., Večerník P., Videnská K., Vopálka D. (2013): Research on the interaction processes of selected radionuclides with engineering barrier materials. Report 14270, project *TIP FR-TI1/362*, SURAO, Prague, Czech Republic, in Czech.

Hellä, P., Pitkänen, P., Löfman, J., Partamies, S., Vuorinen, U., Wersin, P. (2014) Safety Case for the Disposal of Spent Nuclear Fuel at Olkiluoto - Definition of Reference and Bounding Groundwaters, Buffer and Backfill Porewaters (POSIVA 2014-04). Posiva Oy.

Kärki, A., Paulamäki, S. (2006) Petrology of Olkiluoto (POSIVA 2006-02). Posiva Oy.

Kelokaski, M., Siitari-Kauppi, M., Sardini, P., Möri, A., & Hellmuth, K. H. (2006). Characterisation of pore space geometry by 14C-PMMA impregnation—Development work for in situ studies. *Journal of Geochemical Exploration*, *90*(1–2), 45–52.

Kitayama, R., Yanai, J., & Nakao, A. (2020). Ability of micaceous minerals to adsorb and desorb caesium ions: Effects of mineral type and degree of weathering. *European Journal of Soil Science*, *71*(4), 641-653.

Lehto, J., Puukko, E., Lindberg, A., & Voutilainen, M. (2019). Batch sorption experiments of cesium and strontium on crushed rock and biotite for the estimation of distribution coefficients on intact crystalline rock. *Heliyon*, *5*(8).

Li, X., Puhakka, E., Ikonen, J., Söderlund, M., Lindberg, A., Holgersson, S., Martin, A., Siitari-Kauppi, M., 2018. Sorption of Se species on mineral surfaces, part I: Batch sorption and multi-site modelling. *Appl. Geochem*. 95, 147-157. https://doi.org/10.1016/j.apgeochem.2018.05.024.

Mattila, J., Suikkanen, J., Read, R., Valli, J., Hakala, M., Sjöberg, J., Figueiredo, B., Kiuru, R., Haapalehto, S. (2022) Rock Mechanics of Olkiluoto (POSIVA 2021-18). Posiva Oy.

Muuri, E., Matara-aho, M., Puhakka, E., Ikonen, J., Siitari-Kauppi, M., Martin, A., Koskinen, L. (2018) The sorption and diffusion of 133Ba in crushed and intact granitic rocks from the Olkiluoto and Grimsel in-situ test sites. *Appl. Geochem*. 89, 138–149. https://doi.org/10.1016/j.apgeochem.2017.12.004.

Neubeck, A. (2016). Comparative cation exchange capacity experiments on Laxemar fracture coating material using four different methods. *Technical Report TR-15-04*, Svensk Kärnbränslehantering AB/Swedish Nuclear Fuel and Waste Management Company.

Partamies, S., Pitkänen, P. (2014) Mass-Balance Modelling Results of Groundwater Data Collected at Olkiluoto over the Period 2004-2007 (POSIVA 2014-06). Posiva Oy.

Poinssot, C., Baeyens, B., & Bradbury, M. H. (1999). Experimental and modelling studies of caesium sorption on illite. *Geochimica et cosmochimica Acta*, *63*(19-20), 3217-3227.

Posiva (2012) Olkiluoto Site Description 2011 (POSIVA 2011-02). Posiva Oy.

Post, J. E., & Bish, D. L. (1989). Rietveld refinement of crystal structures using powder X-ray diffraction data. *Modern powder diffraction*, *20*, 277-308.

Vaaramaa, K., Lehto, J., Ervanne, H. (2003) Soluble and particle-bound 234,238U, 226Ra and 210Po in ground waters. *Radiochim. Acta*. 91, 21–27. https://doi.org/10.1524/ract.91.1.21.19015.

van Reeuwijk, L. (editor) (2002) Procedures for Soil Analysis, 6th ed. (ISRIC Technical Paper 9). International Soil Reference and Information Centre.

Vuorinen, U., Snellman, M. (1998) Finnish Reference Waters for Solubility, Sorption and Diffusion Studies (POSIVA 1998-61). Posiva Oy.

Sajih, M., Bryan, N.D., Livens, F.R., Vaughan, D.J., Descostes, M., Phrommavanh, V., Nos, J., Morris, K. (2014) Adsorption of radium and barium on goethite and ferrihydrite: a kinetic and surface complexation modelling study. *Geochem. Cosmochim. Acta* 146, 150–163. https://doi.org/10.1016/j.gca.2014.10.008.

Söderlund, M., Ervanne, H., Muuri, E., Lehto, J. (2019) The sorption of alkaline earth metals on biotite. *Geochem. J*. 53, 223–234. https://doi.org/10.2343/geochemj.2.0561.

Wauters, J., Elsen, A., Cremers, A., Konoplev, A. V., Bulgakov, A. A., & Comans, R. N. J. (1996). Prediction of solid/liquid distribution coefficients of radiocaesium in soils and sediments. Part one: a simplified procedure for the solid phase characterisation. *Applied Geochemistry*, *11*(4), 589-594.

Yamaguchi, N., Tsukada, H., Kohyama, K., Takata, Y., Takeda, A., Isono, S., & Taniyama, I. (2017). Radiocesium interception potential of agricultural soils in northeast Japan. *Soil Science and Plant Nutrition*, *63*(2), 119-126.

2 Sorption experiments on rock samples

2.1 Background

Fracture fillings of crystalline rocks (considered as potential natural barriers for deep repositories in multiple countries), serve not only as conduits for underground water flow but also as potential environments capable of sequestering migrating contaminants within the system. The intricate interplay of several factors within the rock mass can generate fractures fillings exhibiting diverse mineralogical compositions. While extensive studies have focused on the clays, it is equally crucial to investigate fillings predominantly comprised of high calcium content. The significance of such investigations lies in the association of calcium with the presence of cementitious components in deep repositories, which undergo degradation over time, resulting in the release of a substantial amount of calcium ions. These ions, in conjunction with carbonate anions present in groundwater, initiate the formation of calcite (Fernandes et al., 2008). Extensive studies exploring the sorption properties of calcite fillings are warranted, along with investigations into other potential filling materials. Existing research encompasses sorption studies involving a broad spectrum of elements, ranging from Sm, Eu, Np, Pu (Smith et al., 2018; Zavarin et al., 20042009), and divalent metal elements (Zachara et al., 1991). However, most of these studies have been conducted on synthetic or naturally occurring calcites. Hence, there is a pressing need to explore the sorption potential of fracture fillings present in the environment mirroring the conditions of deep repository environments. Batch sorption experiments have proven to be one of the widely utilized and recognized methods for assessing sorption properties. In addition to calcite fillings, other rock samples, characterized by their distinct compositions, have been employed in sorption experiments to gain deeper insights into their sorption capacities for the target elements.

2.2 Experimental methods

2.2.1 Methodological Approaches for Batch Sorption and Desorption Experiments

2.2.1.1 Leaching experiments

Samples and synthetic ground water

Grain fraction of 1–2 mm of fracture filling was obtained from the samples provided by UJV by a gently crushing using agate mortar, the migmatite grain fraction of 1–2 mm was prepared using a small jaw crusher Retsch BB50 (Haan, Germany) with crushing jaws and wear plates made of ZrO_2. These fractions were washed at least four times with ethanol to remove the adhering smaller particles and dried at 40 °C. For the measurements of the carbonate content of migmatite using carbonate bomb and for the digestion of migmatite and calcite grain fraction <0.063 mm was used.

The mineralogic composition of migmatite was determined by XRD analysis (X´Pert Pro, PANalytical) and revealed plagioclase and amphibole as major components of migmatite (Table 2-1). Carbonate content of migmatite of 5.9 ± 0.2 mass% was obtained from triplicate measurements by carbonate bomb method (Müller & Gastner 1971, Klosa 1994), in which 6 M HCl acid (Honeywell Fluka™ 37 % HCl, Puriss. p.a., Charlotte, North Carolina, US) was used to decompose solid carbonates whereby the pressure of the released CO_2 gas was measured using a high-precision pressure sensor (FDAD3302A, Ahlborn Mess- und Regelungstechnik GmbH, Holzkichen, Germany). Results of XRD analysis of fracture filling in the Table 2-1 were provided by UH.

Table 2-1 Mineralogic composition of studied samples

	migmatite	fracture filling

calcite	5.5	91.6 ± 4.6
quartz	10.6	8.2 ± 0.4
plagioclase	40.6	
biotite	9.5	
amphibole	24.1	
chlorite	9.7	0.2 ± 0.01

A synthetic groundwater of URF Bukov SGW2 (Table 2-2) was prepared from a ready-mix obtained from the UJV and had a pH of 8.0 ± 0.5 at 10 °C and 8.2 ± 0.2 at 80 °C. Content of major ions in SGW2 is given in Table 2-2. Sodium dithionite ($Na_2S_2O_4$, Natriumdithionit, Sigma-Aldrich Chemie GmbH, Taufkirchen, Germany) was added (2×10^{-4} M) to adjust E_h to the in-situ value of −470 ± 15 mV. Bidistilled water was used for preparation of all used solutions.

Table 2-2 Composition of SGW2 according to Bukovská et al. (2018)

	Ca^{2+}	Mg^{2+}	Na^{+}	K^{+}	Cl^{-}	SO_4^{2-}	HCO_3^{-}
mg/l	34.6	8.3	16.5	2.1	3.3	21	168.7

Aqueous leaching

Triplicate leaching batches with 600 mg migmatite or 300 mg fracture filling (grain size 1–2 mm) and 20 ml SGW2 were carried out for 1, 4, 10, 17, 24, 31 days at 10°C in a refrigerator and at 80 °C in an oven, which were equipped with a rocker providing a continuous rocking of batches at 12 rpm and a tilt angle of 9°. The batches were prepared in a glove box (MB-Labmaster Pro SP (1500/780), M. Braun Inertgas-Systeme GmbH, Garching, Germany) using glass vessels (25 ml DURAN® Original GL made of borosilicate glass 3.3, SCHOTT AG, Mainz, Germany) and transferred to air-tight flange vessels, which were flushed for 2–3 min with Ar before closing and contained 30 ml SGW2 to maintain pCO_2 of SGW2 (c. 1.4 or 5.3 mbar at 10 or 80 °C, respectively). Upon completion, the solution was decanted, filtered (0.45 µm, Minisart® NML plus syringe filter, Sartorius AG, Göttingen, Germany), and, after taking an aliquot for the measurement of iodine (see the section "ICP-OES and ICP-MS/MS analyses" below for the full list of measured elements), acidified with 2 % HNO_3 (nitric acid 67–69 % for trace analysis supra, Bernd Kraft GmbH, Duisburg, Germany). The solid was removed from the batch vessel, the acidified solution was given back into the batch vessel and shaken by hand to desorb the ions adsorbed on the vessel wall.

Extractions

In the first triplicate extraction at 10 °C and 80 °C, 600 mg of migmatite or 300 mg of fracture filling (grain size 1–2 mm) reacted for 24 h with 20 ml 0.1 M HCl (30% Suprapur®, Merck KGaA, Darmstadt, Germany), which also contained 1% tetramethylammonium hydroxide (tetramethylammonium hydroxide pentahydrate, Thermo Fisher Scientific Inc.) to prevent iodine loss from the acidic solution (pH = 1) (Tagami & Uchida 2005). Upon completion, the extractions were handled the same way as the solutions in the leaching batches with SGW2. The iodine measurement from extractions was carried out 1–2 hours after the extractions at the latest.

In the second triplicate extraction at 25°C, 600 mg of the migmatite or 200 mg of fracture filling (grain size 1–2 mm) reacted for 30 min with 20 ml or 5 ml 6 M HCl acid (Honeywell Fluka™ 37 % HCl, Puriss. p.a., Charlotte, North Carolina, US), respectively.

In the third triplicate extraction with aqua regia, 150 mg of the residual migmatite from the second extraction reacted for 30 min with 3 ml concentrated HCl (30% Suprapur®, Merck KGaA, Darmstadt, Germany) at 25°C and, after subsequent addition of 1 ml concentrated HNO_3 (nitric acid 67–69 % for trace analysis supra, Bernd Kraft GmbH, Duisburg, Germany), for 2 hours in a water bath at 80°C.

Total digestions

Reference materials AC-E (granite from Ailsa Craig Island, Scotland, UK: Govindaraju, 1987) and GS-N (granite from Senones, Vosges, France: Govindaraju 1984, Govindaraju and Roelandts 1989) were obtained from CRPG-CNRS / SARM (Vandoeuvre-les-Nancy, France). These materials were digested with HBF_4 (38% solution, ultra-pure, obtained from CHEM-LAB NV, Zedelgem, Belgium) according to the method by Zimmermann et al. (2020) adjusted to use the microwave oven ETHOS1 (MLS GmbH, Leutkirch, Germany) operating at an output of 1500 W, so that the digestion was carried out at 210 °C for 30 min following the initial heating for 8 min to reach 180 °C and further 4 min to reach 210 °C.

BET analyses

Specific surface area (multipoint BET) of the grain fraction of 1–2 mm of the unreacted migmatite sample and reacted migmatite samples was measured by TriStar II Plus 3030 Krypton Surface Area and Porosity Analyzer (Micromeritics Instrument Corporation, Norcross, GA, USA) using Kr as analysis gas.

ICP-OES and ICP-MS/MS analyses

K, Na, Mg, Ca, S, and Si were analysed with ICP-OES (Thermo iCAP 7400 DUO, Thermo Fisher Scientific Inc.). A triple quadrupole ICP-MS/MS (Agilent 8900 Triple Quad, Agilent, Santa Clara, USA) was applied to analyse Al, Fe, Mn, Ti, V, P, S, Cs, Rb, Sr, Ba, Ni, I, Th, U, Y, La, Ce, Pr, Nd, Sm, Eu, Gd, Tb, Dy, Ho, Er, Tm, Yb, and Lu in supernatant solutions. This instrument features mass filters before and after the collision reaction cell, which contained no gas for Th and U and O_2 as reaction gas for the other analysed elements. Concerning the typical operating conditions for the ICP-MS/MS, amongst others, flow rate of 0.30 ml/min, octopole bias of −15 V, and kinetic energy discrimination of −9 V were applied for REEY according to Zhu et al. (2021) and 0.35 ml/min, −5 V, and −7 V, respectively, for the other elements according to Sugiyama & Nakano (2014) (for Al, Rb, Th, and U), Nakano (2018) (for P), McCurdy (2020) (for Ti), Li & Li (2021) (for V, Mn, Ni), Chen et al. (2019) (for Fe), Fletcher et al. (2020) (for I), Wang et al. (2021) (for Cs), Liu et al. (2020) (for Sr), and Manard et al. (2020) (for Ba). The integration time of 1 s was applied for all elements.

Calculation of desorption distribution ratios

For sorption batch experiments with an element concentration in a liquid phase with a volume *V* decreasing from C_0 to *C* upon adsorption to a solid phase with a mass *M* and the element concentration increasing from zero to *A*, the sorption distribution ratio can be derived from $A = V/M \cdot (C_0 - C)$ as $K_d = A/C = V/M \cdot (C_0 - C)/C$.

For desorption batch experiments with an element concentration in a liquid phase with a volume *V* increasing from C_0 to *C* upon desorption from a solid phase with a mass *M* and the element concentration decreasing from A_0 to *A*, the desorption distribution ratio can be derived from $A - A_0 = V/M \cdot (C_0 - C)$ as $K_{ds} = A/C = \big(A_0 - V/M \cdot (C_0 - C)\big)/C$. To calculate K_{ds} according to this formula, A_0 for studied elements was estimated by the extraction with 0.1 M HCl, following the finding by Igarashi et al. (1998) that for Sr in granites K_{ds} estimated in this way corresponds to K_d.

2.2.1.2 Sorption of Ra, Ba, Ni and Se on gneisses, pegmatite granite, granodiorite, biotite and calcite (UH)

Sample preparation

The Grimsel granodiorite used in batch sorption experiments was provided by an underground research laboratory in Grimsel test site, Switzerland. It is a medium grained and slightly foliated granite. The main

minerals, according to the results of XRD analysis shown below, are plagioclase (40%), potassium feldspar (25%), quartz (20%) and biotite (10%). The porosity of Grimsel granodiorite varies from 0.5% to 1.5% (Kelokaski et al., 2006) and permeability is $(1.3 \pm 0.3) \times 10^{-17}$ m^2 (Ikonen et al., 2016).

Batch sorption experiments were also performed with single main minerals of Grimsel granodiorite to study the effects of sorption by each single minerals. The main minerals, plagioclase, biotite and K-feldspar, were provided by the Geological Survey of Finland. Quartz used in this work was bought from UKGE, a geological and expedition supplier in UK.

The types of calcites, Bukov calcite and pure calcite, were used in the batch sorption experiments to study the radionuclides sorption on calcite. The Bukov calcite was provide by Bukov underground laboratory in Czech Republic. The sample was taken from the research facilities that are located 550 m below the earth's surface. The pure calcite sample was commercially bought from UKGE, same as the quartz sample mentioned above.

The mineralogy of all the samples were characterized by X-ray diffraction (XRD) before further handling. The results are summarized in Table 2-3. All the samples were also characterized with Kr-BET method to check the specific surface area using gas adsorption analyzing instrument (Micromeritics ASAP, 2020). The samples were kept in a vacuum oven at room temperature until constant weight before measuring (the drying time was about 1 month). The cation exchange capacities of Grimsel granodiorite and its main minerals (plagioclase, biotite, quartz, K-felspar) were determined by extracting crushed samples with 1 M ammonium acetate (NH_4Ac) which can buffer the pH of the solutions contacting with different minerals at about pH 7. For the CEC measurements of Bukov calcite and pure calcite, a modified hexamminecobalt(III) chloride method was used based on former research performed by Dohrmann et al. (2009). The main purpose of utilizing the hexamminecobalt(III) chloride method is to minimize the dissolution of calcite which might cause large errors for the CEC measurements. The results of SSA and CEC are also summarized in Table 2-3.

Table 2-3. Summary of the minerology analysis of samples with XRD measurements, specific surface areas measured by Kr-BET method, and cation exchange capacities measured by ammonium acetate and haxamminecobalt chloride.

Rock/mineral	XRD	SSA (m^2/g)	CEC (meq/kg)
Grimsel granodiorite	40% plagioclase, 25% K-feldspar, 20% quartz, 10% biotite and 5% chlorite	0.1268	3.32
Plagioclase	75% plagioclase, 5% biotite, 5% K-feldspar, 5% amphibole; chlorite, quartz, magnetite, ilmenite altogether < 10%	0.115	22.69
Biotite	100%	1.0323	12.64
Quartz	100%	0.0486	0.01
K-feldspar	90% K feldspar, 8% plagioclase and 2% quartz	0.1084	1.68
Bukov calcite	91.6% magnesian calcite, 8.2% quartz, 0.2% clinochlore	2.418	5.87
Pure calcite	100%	0.1136	1.38

All the rock and mineral samples were crushed by ball-milling method, and the part with particle sizes between 0.075 mm and 0.3 mm was sieved for the following titration and sorption experiments. In order to remove the impurities that are attached on the mineral surface (such as pure biotite), a purifying procedure was applied to the crushed biotite sample to convert them into a mono-potassium form containing only K^+ at the exchange sites as far as possible. A cation exchange column was used for this conversion work. Ten

grams of the crushed biotite sample was packed into a glass column, and 0.1 M $KClO_4$ and 0.01 M $KClO_4$ solutions were pumped through the column with a peristaltic pump at a flow rate of 4 mL/h. The equilibrium time was about one month to ensure that the accessible sorption sites were in the desired potassium form. The effluent samples were analyzed by Microwave Plasma – Atomic Emission Spectrometer (MP-AES 4200, Agilent). The conversion procedure ended when the concentrations of Mg^{2+}, Ca^{2+}, and Al3+ ions were under detection limits (< 0.01 ppm) and the concentration of Na+ was 0.06 ppm.

Titration and backtitration experiments

Biotite and calcite titration experiments was carried out in a batch-wise manner in an inert N_2 atmosphere glovebox. Standard 0.1 M HCl and NaOH solutions of analytical reagent level were used to adjust the pH. At first, 0.5 g mineral samples were equilibrated with 25 mL 0.01 M $KClO_4$ while stirred in a 50 mL Sorvall polypropylene centrifuge tube for 3 days. Aliquots of standard acid or base were added to the preequilibrated biotite suspensions to give a series of initial pH. For biotite, initial pH is from 3 to 11, and for calcite from 7 to 11. Then the centrifuge tubes were shaken end-over-end for 24 h. Additional acid or base solutions were added into the centrifuge tubes to get the final wanted pH. After shaking, the tightly closed centrifuge tubes were transferred out of the glovebox and centrifuged followed by returning into the glovebox for sampling. Two samples were made from each single vial for different measurement purposes. Firstly, 5 mL of supernatant was taken from each vial and the pH were measured, after which the concentrations of Na, K, Ca, Mg, Al, Mn and Si were determined by Microwave Plasma Atomic Emission Spectroscopy MP-AES. Secondly, 15 mL of the supernatant was sampled for the subsequent backtitration. The backtitration was carried out by adding aliquots of standard base or acid solutions to each sample until the pH value was returned to the initial pH 7. The samples were stirred constantly and the time intervals of adding each aliquot of base or acid standard solution were > 5 min to achieve complete backtitration reactions.

Sorption measurements as a function of pH (sorption edge) experiments

Sorption edge measurements were carried out with different tracers (Se, Ba, Ni) in a controlled N_2 atmosphere glovebox. The total concentration of tracers (radioactive + stable forms) used in the sorption edge experiments was 10^{-9} M. For Se, radiotracer Se-75 added was 52.8 Bq/ mL, corresponding $1.66*10^{-10}$ M, while the radiotracer Ni-63 added was 35.335 Bq/mL, and the radiotracer Ba-133 was 31.91 Bq/mL. Firstly, 0.5 g minerals was first equilibrated with 25 mL background solution in a 50 mL polypropylene centrifuge tube for 3 days. Aliquots of standard acid or base were added to the vials together with proper amount of tracers, resulting in the final concentration of each total tracer was 10^{-9} M in a pH series. The vials were then closed tightly and shaken end-over-end for 7 days. Subsequently the vails were transferred out of the glovebox and centrifuged. After returning to the glovebox, the pH of the supernatant was checked and sampled for radioactive measurement. Radioactive Se-75 was measured by a Hidex-AMG gamma counter in 8 mL background solutions with counting time setting to be 30 min. Radioactive Ni-63 was measured with liquid scintillation counting (LSC) by Tri-carb 2010 TR, Perkin Elmer for 2 hours. Radioactive Ba-133 was measured with HPGe detector (Canberra XtRa; Extended Range Coaxial HPGe Detector with spectral analysis program Gamma Acquisition & Analysis Genie/Canberra) for 10 hours.

Sorption measurements as a function of concentration (sorption isotherm) experiments

Sorption isotherm measurements were performed in a controlled N_2 atmosphere glovebox to obtain the sorption data of different tracers on mineral samples with initial concentrations between 10^{-10} M to 10^{-3} M. Firstly, the mixture of 0.5 g mineral samples was stabilized with 10 mL background solutions for 2 weeks. After stabilization, the batch sorption experiments were conducted in two different ways according to the tracer concentrations added. For the samples with tracer concentrations from 10^{-6} M to 10^{-3} M, stable tracers were added into the vials, causing a series of selenium concentration from10^{-6} M to 10^{-3} M; for the samples with tracers concentrations from 10^{-10} M to 10^{-7} M, both radioactive and stable tracers were added and the total tracer concentrations in the background solution was ranged from 10^{-10} M to 10^{-7} M. After the addition

of tracers, all the vials were agitated for two weeks followed by centrifuging and sampling. For stable tracers, the concentrations were determined with ICP-MS and MP-AES while the determination of radioactive tracers were performed the same way as indicated in the sorption edge experiments.

The sorption properties of different tracers are expressed in two ways, distribution coefficient K_d (L/g) and sorption efficiency (%). The distribution coefficient K_d can be determined as,

$$K_d = \frac{C_0 - C_e}{C_e} \times \frac{V}{m}$$

where C_0 (mol/L) is the initial total concentration of tracers in the solution), C_e (mol/L) is the final concentration of tracers in the background water, V (L) is the volume of solution and m (Kg) is the mass of the solid phase. The sorption efficiency can be determined as,

$$\% = \frac{C_0 - C_e}{C_0} * 100$$

Sorption modelling

The main purpose of the modelling is to find a set of parameters that can fit all the experimental data. If a set of modelled parameters were reached, it is believed to have great constraints for errors and can reasonably reflect the real properties of Se sorption processes (Bradbury & Baeyens, 1995, 1997, 2000).

Titration results can give information of site capacities and acid/base constants of the site protonation and deprotonation reactions, which are basic parameters for further sorption result simulations. Thus, the titration results were considered first. The sorption results can provide information about the constants of reactions between different tracer species and sorption sites. Two types of sorption sites were assumed in the developed surface complexation model, the strong sorption sites (≡S^SOH) and weak sorption sites (≡S^WOH). This approach is supported by the existence of multiple sites on the surface of phyllosilicates (Bradbury and Baeyens, 1997; Dähn et al., 2011; Zheng et al., 2003). The strong sorption sites (≡S^SOH) are considered having small capacities but strong complexes with sorbate. Strong sorption sites (≡S^SOH) will dominate the sorption when the sorbate is in a trace amount. The weak sorption sites (≡S^WOH), on the contrary, have much larger capacities, but much weaker complex abilities. The weak sorption sites (≡S^WOH) are believed to have dominant effects when the solution ions are in large concentrations.

Two types of weak sorption sites (≡S^{W1}OH and ≡S^{W2}OH) and one type of strong sorption sites (≡S^SOH) were assumed to exist on the studied biotite surfaces based on molecular modelling results (Puhakka et al., 2019). The molecular modelling results show that two types of weak sorption sites exist on biotite surfaces (base (001) surface and edge (110) edge surface) with the site densities of 3.2 sites/nm^2 and 1.4 sites/nm^2, respectively.

For all the fitting and optimization processes, a code that coupled PHREEQC with Python was developed (Charlton and Parkhurst, 2011; Liu et al., 2014; Wissmeier and Barry, 2011). To facilitate interaction between PHREEQC and Python, a Microsoft COM (component object model) and COM version of PHREEQC called Iphreeqc were used. The Microsoft COM provides a server that allows PHREEQC to be used by any software that can interface with a COM server – for example, Excel, Visual Basic, Python and MATLAB. Iphreeqc is a version of PHREEQC that is specially designed for coupling to other programming codes andhere it is coupled with Python for the fitting and optimization of the modelling results. While it retains all of PHREEQC reaction capabilities, Iphreeqc provides additional methods for data manipulation and communication to the host application (Charlton and Parkhurst, 2011; Wissmeier and Barry, 2011).

The modelling was performed by fitting titration, sorption edge and sorption isotherm data in an iterative procedure. Any parameter fitted in the present step will be fixed in all the subsequent steps. The iterative procedure breaks out if no satisfying fitting result can be reached. Then the modelling process returns to

the first step with different parameters and begin the iteration again. The iteration ends when a group of parameters is found to be able to describe all the experimental results successfully (the squares of the difference between experimental data and simulated data < 10^{-4}).

2.2.1.3 UJV (Methodology and Procedural Modifications for Conducting Sorption Experiments at UJV)

Preliminary Sorption Experiments for Determining Batch Sorption Method for Bukov Calcite, Chlorite Infills and Host Rocks Samples

The initial experimental procedures involved the careful selection of an appropriate setup to establish the necessary parameters for determining the distribution coefficients of rock samples. The methodology employed by UJV, based on the solid-liquid equilibrium (SE) approach, was utilized within the VPBHU project to investigate the sorption behaviour of Cs, Sr, Se, I, and U (Bukovská et al., 2017; Havlová et al., 2018). The solid phase and liquid phase, both containing the target tracer, were brought into contact in triplicate samples, maintaining a sample-to-volume ratio of 1:10. In this configuration, the volume of the liquid phase (5 ml) corresponded to a solid phase mass of 0.5 g. The liquid phase consisted of SGW2 water supplemented with an inactive carrier at a concentration of 2×10^{-5} mol/l, along with a specific radioisotope (e.g., ^{134}Cs, ^{85}Sr). The suspensions were agitated using an orbital shaker at a controlled speed of 120 rpm for a designated contact time. Experiments were terminated at specific time intervals (0.04, 0.31, 1, 2, 4, and 7 days), allowing for the determination of tracer concentration changes in the liquid phase and the corresponding distribution coefficients (R_d). Detailed modifications to this methodology will be discussed in subsequent paragraphs.

For these experiments, migmatized gneiss samples (specifically PVP-2) extracted from the Bukov Underground Research Facility (URF) were employed. The liquid phase used in the experiments was SGW2 water. The experimental setup encompassed several critical factors, including the careful preparation of rock samples prior to sorption experiments, the precise duration of the sorption experiments, the influence of controlled agitation during the process, the equilibration period before initiating sorption, the inclusion of non-radioactive tracers, variations in initial concentration levels, different ratios of solid to liquid phases, and the influence of ambient air. Consequently, experiments were conducted under controlled ambient atmospheric conditions and also within an argon atmosphere, ensuring the necessary precautions were taken within a glove box setting.

Further details regarding the specific selection of experimental setups can be found in the Kočan (2022).

Sorption Studies Following Preliminary Investigations on Bukov URF Materials

After conducting preliminary studies, it was determined that a methodology utilizing different solid-to-liquid ratios would be suitable for the rock sample. Subsequently, batch sorption experiments were performed using Bukov materials, specifically Bukov Calcite Infills, rich host rocks, and Bukov Chlorite infills material. The forthcoming chapters provide comprehensive descriptions of the methods employed in the preliminary sorption experiments as well as subsequent sorption experiments involving Bukov materials.

Characterization and Preparation of Liquid Phases for Sorption Experiments

The commonly employed liquid phase in sorption experiments, similar to the methodology described by UJV, consisted of SGW2 with an added inactive carrier. Liquid phase was prepared by pipetting an aliquot of 1×10^{-3} mol/L $NiCl_2$ or CsCl solution, resulting in a final carrier concentration of 1×10^{-5} mol/L. Subsequently, an aliquot of 63Ni or ^{134}Cs solution was added to achieve a volume activity of approximately 50000 Imp/min for ^{63}Ni and 10000 Imp/min for ^{134}Cs in the stock solution of liquid phase. After each preparation of KF, the pH was checked using pH paper to monitor any potential acidification resulting from the addition of the ^{63}Ni solution. In the experiments without a carrier, no aliquot of $NiCl_2$ or CsCl solution was added to the liquid phase. In experiments with varying initial carrier concentrations, an aliquot of 1×10^{-2}/1×10^{-3}/1×10^{-5} mol/L

$NiCl_2$ or CsCl solution was added to achieve final concentrations of 1×10^{-7}, 1×10^{-6}, 1×10^{-5}, 1×10^{-4}, and 1×10^{-3} mol/L, respectively.

In order to faithfully replicate the conditions prevailing in deep geological repositories, our experimental approach encompasses not only the selection of rocks obtained from the underground laboratory corresponding to the depth at which deep geological repositories are typically envisioned, but also the utilization of representative groundwater from the surrounding environment. The chosen groundwater sample serves as an accurate representation of the deep groundwater circulation within the crystalline rock setting of the Bohemian Massif. It exhibits characteristic features consistent with Ca-HCO_3 type groundwater, exhibiting a notable concentration of carbonate ions. The composition of the selected groundwater sample was based on the average composition of water samples collected from the Bukov site at a depth of approximately 600 m (see Table 2-4). The ionic strength of the water sample is estimated to be around 0.005 mol/L. For detailed information on the sample preparation protocol, refer to the study conducted by Červinka and Gondolli (2016). Designated as SGW2, this specific groundwater sample was chosen as one of the reference samples for the SURAO Research Support for the Safety of Deep Geological Repositories research project (Havlová et al., 2018). Building upon previous sorption experiments conducted with crushed rock samples, SGW2 was employed as the foundational liquid phase in conjunction with all solid phases in the present study.

Table 2-4 Composition of synthetic groundwater SGW2 prepared following the protocol in Červinka and Gondolli (2016)

Ions	concentration [mg/l]
Na^+	16.5
K^+	2.1
Mg^{2+}	8.3
Ca^{2+}	37.3
Cl^-	3.5
NO_3^-	0.0
SO_4^{2-}	21.9
HCO_3^-	168.7
pH	**8.2**

Solid Phase Contacting Procedure in Sorption Experiments

The solid phase samples were subjected to a well-defined contacting procedure to ensure controlled experimental conditions. Firstly, 5 ml of the stock liquid phase solution was precisely pipetted into polyethylene ampoules along with the pre-weighed PF. Blank samples were prepared by pipetting only the liquid phase solution into separate ampoules. The ampoules containing solid phase and liquid phase, including the blank samples, were accurately weighed and placed on an orbital shaker operating at 120 rpm for the designated contact duration. Triplets of samples were prepared to assess the influence of interaction time, agitation, equilibration, and carrier presence. For samples investigating the dependence of sorption

capacity (q) on initial concentration (C), a single sample mass was employed, maintaining a specific mass-to-volume ratio. In the absence of agitation, the suspensions were left undisturbed, with periodic manual mixing (at a frequency of 2-3 times per week) to ensure homogeneity.

Establishing Concentration Equilibrium through Repeated Phase Interactions: A Method for Attaining Equilibrium in PVP-2 and SGW2 Systems

In order to attain concentration equilibrium between the phases, the PVP-2 samples underwent a rigorous equilibration process with SGW2. The method involved a cyclic procedure of contacting the PVP-2 samples with SGW2. Precisely weighed samples (0.5 g) were initially brought into contact with 5 ml of SGW2 and placed on an orbital shaker. After a week of continuous agitation, the samples were carefully removed from the shaker, and following the sedimentation of the solid phase, 4 ml of the supernatant was meticulously exchanged with fresh SGW2 (4 ml). Subsequently, the samples were reintroduced to the shaker for further phase interactions. This cyclic process was meticulously repeated three times over a span of three weeks to ensure optimal equilibration. On the 28th day of the interaction period, specifically after three successive exchanges of SGW2, the supernatant was not collected. Instead, an aliquot of ^{63}Ni or ^{134}Cs was introduced to the suspension, meticulously adjusting the activity level of the supernatant to align with that of the other solid-liquid interactions. Furthermore, an inert carrier substance was added to the supernatant to maintain a concentration level of 1×10^{-5} mol/l. Both additions were meticulously implemented to minimize any significant alterations in the mass-to-volume ratio. Following these steps, the samples were carefully weighed and reintroduced to the shaker for continued phase interactions. This specific solid-liquid interaction procedure lasted for a duration of 14 days.

Activity Measurement Procedures for Evaluating Sorption Coefficients in Experimental Setups

After the designated phase interaction time, in nearly all experiments, the samples were subjected to double centrifugation. The original polyethylene ampoules were centrifuged at 9000 rpm for 15 minutes, and then 2 ml of the supernatant were transferred to microcentrifuge Eppendorf tubes and further centrifuged at 12000 rpm for 5 minutes. This procedure was chosen to remove turbidity and to separate any potential (radio)colloids that could affect the measurement of ^{63}Ni and ^{134}Cs activity. From the tubes, two aliquots were collected for the determination of the volumetric activity of the radioactive tracer. Three aliquots were taken from the blind samples for the activity determination. The obtained data were used to calculate the sorption coefficients for the respective sorption experiments. The volumetric activity of the radioisotope ^{63}Ni was quantified using an automated liquid scintillation counter Hidex 300 SL, Hidex Oy, FIN (Figure 2-1). The measurement procedure employed for the radionuclide ^{63}Ni closely followed the methodology, where 1 ml of supernatant was sampled and combined with 2 ml of scintillation cocktail (ROTISZINT® eco plus). Subsequently, the volumetric activity of the radioisotope ^{134}Cs in 1 ml of supernatant was determined utilizing an automated gamma counter Wizard2® 2480 (Figure 2-1), Perkin Elmer Inc., USA, for a duration of 5 minutes, adhering to the recommended protocol for precise ^{134}Cs measurements in range of the peaks with the highest yields. The volumetric activity was assessed in terms of counts per minute (or counts per measured time) within 1 ml of supernatant.

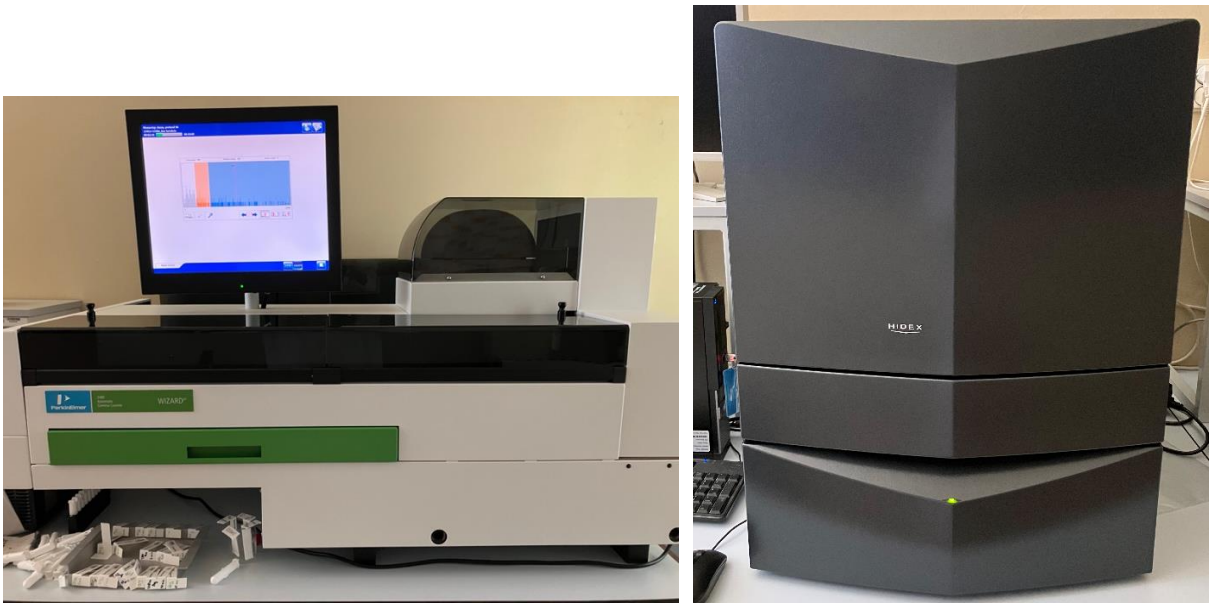

Figure 2-1 The gamma counting instrument used in the study was the automated gamma counter, model Wizard® 2480, Perkin Elmer Inc., USA (on the left), while the liquid scintillation counting system employed was the Hidex 300 SL, Hidex Oy, FIN (on the right) at UJV

Experimental Setup and Procedures for Anaerobic Conditions

In order to assess the impact of CO_2 on the distribution coefficient (K_d), sorption experiments were conducted within a glove box under an inert atmosphere. The sorption experiments, including supplementary interaction experiments, were performed using the PVP-2 sample with a liquid phase consisting of a $CaCl_2$ solution. The prepared samples, contained in ampoules, were combined with the liquid phase comprising a 0.00166 mol/l $CaCl_2$ solution and an inactive carrier with a concentration of 1×10^{-5} mol/l. Subsequently, they were introduced into the glove box via a vacuum chamber and left exposed for a minimum period of 14 days. This duration was deemed adequate for eliminating dissolved gases, particularly O_2 and CO_2, and for achieving a steady-state equilibrium between the liquid phase and the inert argon atmosphere. Furthermore, a precise volume of ^{63}Ni and ^{134}Cs in microcentrifuge Eppendorf tubes was introduced into the glove box to initiate the respective sorption experiments. Following this, the radioactive solutions were quantitatively transferred into pre-prepared scintillation vials. Notably, unlike the aerobic experiments, it was not feasible to weigh the samples, and instead, their approximate masses were estimated using a spoon within the glove box. The samples were subsequently agitated under the same conditions as the other sorption experiments. However, the termination of the sorption experiment varied slightly, aiming to minimize exposure of the collected anaerobic supernatant to external conditions. Consequently, after the completion of agitation, the supernatant was collected within the glove box following solid phase sedimentation (approximately 30 minutes). Subsequently, 2 ml of supernatant from the glove box were withdrawn through the vacuum chamber into well-sealed microcentrifuge Eppendorf tubes and centrifuged at 12000 rpm for 15 minutes. The collection of aliquots for volumetric activity measurement followed a similar procedure to the aerobic sorption experiments.

The sorption experiments investigating the interaction between Bukov Calcite Infill and the host rock of Bukov Calcite Infill, were conducted using a standardized experimental setup within a controlled glovebox environment. The experiments employed SGW2 water as the aqueous medium to facilitate the desired reactions and measurements.

2.2.2 Speciation modeling

This subchapter offers a brief overview of speciation calculations of Ni, Se, Ba, and Ra performed by UH, UJV, and GRS using geochemical boundary conditions which are relevant for this study. Details in terms of applied codes and databases are provided in the respective subchapters (Chapters 2.2.2.1 - **Erreur ! Source du renvoi introuvable.**).

2.2.2.1 Ni speciation in SGW2 with and without calcite under oxidizing and reducing conditions

In the following, geochemical solution speciation calculations of a **s**ynthetic **g**round**w**ater called **SGW**2 (see Chapter 2.2.1.3 and Table 2-4) with PHREEQC (version phreeqc-3.3.8-11728-x64, Parkhurst and Appelo (2013)) are illustrated. SGW2 was used in sorption experiments (Chapter 2) as well as surface charge measurements (Chapter 3). Solution speciation calculations were performed for ambient and reducing conditions (referring to an N_2 atmosphere with 1 ppm CO_2), with and without calcite. All calculations were carried out using the ThermoChimie TDB for PHREEQC (ThermoChimie_PHREEQC_eDH_v9b0.dat).

In Figure 2-2 results of Ni speciation calculations in SGW2 without solid influence are illustrated. As expected, Ni carbonate species gain influence at higher pH values under atmospheric conditions (Figure 2-2 b)), whereas $Ni(OH)_2$ is the dominant species at pH values > 9 in systems where an N_2-1ppm-CO_2 atmosphere was used for calculations (Figure 2-2 a)).

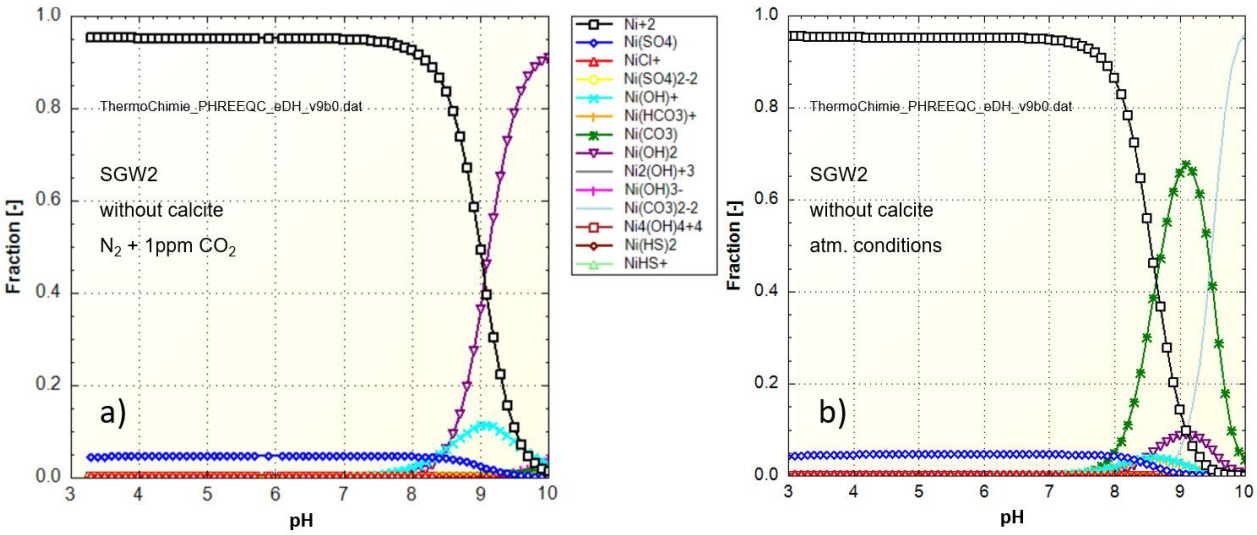

Figure 2-2 a) Ni speciation in SGW2 calculated with a N_2-atmosphere containing 1 ppm CO_2, without calcite. b) Ni speciation in SGW2 under atmospheric conditions without calcite.

An interesting picture was obtained repeating the same speciation calculations as illustrated in Figure 2-2 in equilibrium with calcite (50 g/L) (Figure 2-3 and Figure 2-4). Figure 2-3 a) shows the solution speciation of Ni in equilibrium with calcite under atmospheric conditions, b) illustrates the respective saturation indices (SI). The solid liquid ratio (SLR) of 50 g/L was chosen for the simulations since it is an acceptable overall representation of applied SLRs in the experiments. In both simulations the precipitation of calcite and $Ni(OH)_2(s)$ was allowed. Up to pH 7 calcite (50 g/L) dissolves completely. At pH > 7 calcite is in equilibrium with the solution which is illustrated by means of SI values = 0. The occurrence of a $NiCl^+$ species looses influence at pH > 7 (Figure 2-3 a), red triangles) is due to the reduced addition of NaCl for pH adjustment for pH values above pH 7. For basic conditions NaOH was used to adjust the system's pH in the simulations and experiments.

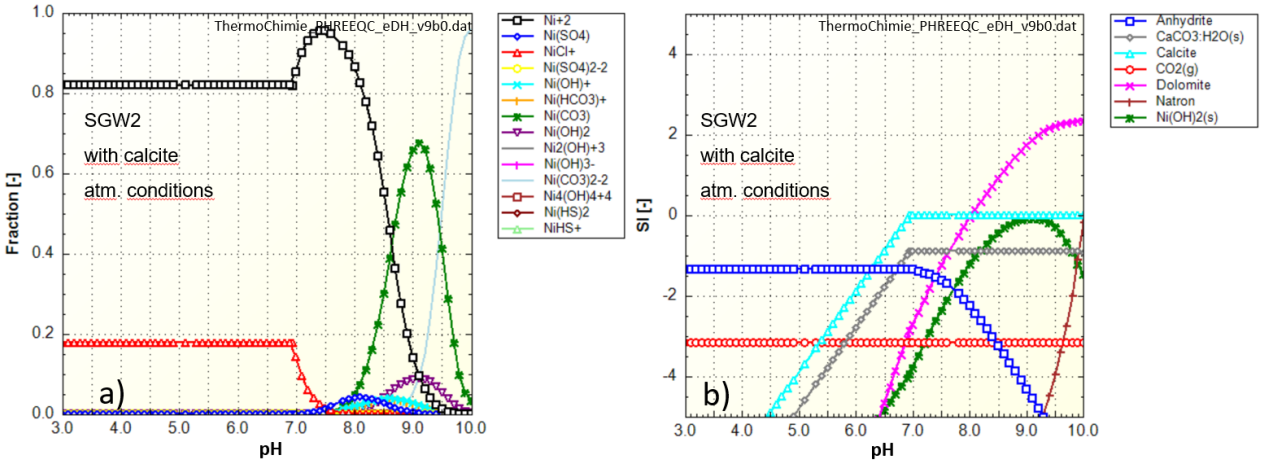

Figure 2-3 a) Ni speciation in SGW2 under atmospheric conditions in equilibrium with calcite. b) Respective saturation indices (SI) of speciation calculation shown in a) for relevant solids in SGW2 under atmospheric conditions. SI > 0 refers to solids (and gases) that may precipitate / leave the system (oversaturation); SI < 0 refers to undersaturated conditions and, hence, dissolution processes; SI = 0 shows solids that are in equilibrium with the system.

Figure 2-4 illustrates similar Ni speciation calculations as shown above with the only difference that a N_2 atmosphere containing 1 ppm CO_2 was applied. As a consequence of the almost negligible CO_2 influence speciation calculations change: Above pH 8 Ni^{2+}, $Ni(OH)_2$, and $Ni(OH)^+$ are the dominating species. In contrast to simulations carried out under ambient conditions there is no $NiCO_3$ species in the system and calcite seems to completely dissolve until pH 8.2. SI values indicate an equilibrium between the solid and the solution (SI = 0) for pH values > 8.2. This observation is reasonable since the missing atmospheric CO_2 influence results in an increased dissolution of calcite.

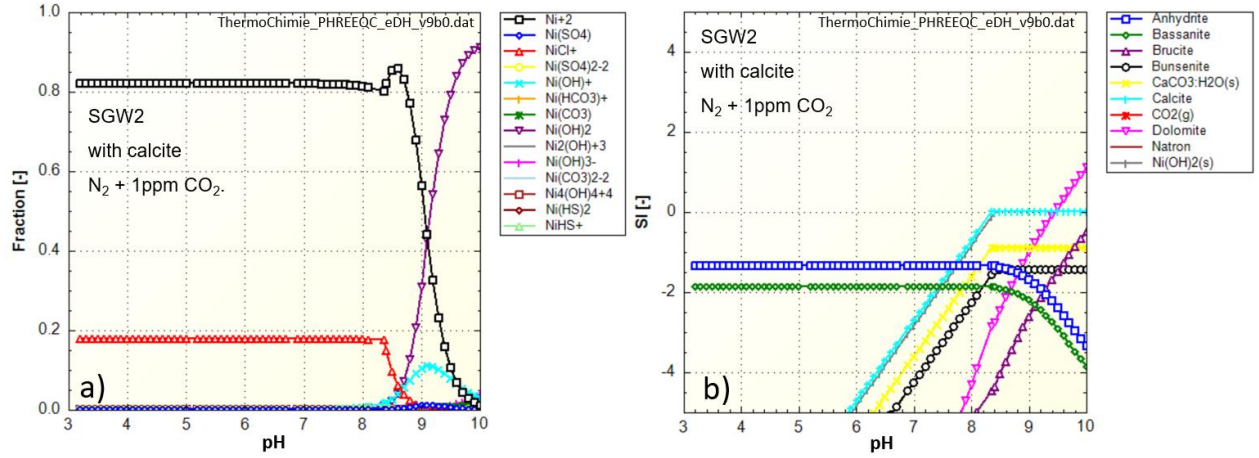

Figure 2-4 a) Ni speciation in SGW2 with a N_2 atmosphere including 1 ppm CO_2 in equilibrium with calcite. b) Respective saturation indices (SI) of speciation calculation shown in a) for relevant solids. SI > 0 refers to solids that may precipitate (oversaturation); SI < 0 refers to undersaturated conditions and, hence, dissolution processes; SI = 0 shows solids that are in equilibrium with the system.

In terms of planned experiments these calculations indicate that under equilibrium conditions no calcite is left for sorption processes up to pH ~ 8.2 under the chosen geochemical boundary conditions.

2.2.2.2 Se speciation modelling under atmosphere and reducing conditions

Similar to the Ni speciation modelling, the PHREEQC software was used for the speciation modelling of Selenium (Se). The speciation calculations were conducted using an artificial groundwater composition designed to simulate the Grimsel groundwater. The Se speciation modelling was performed under two sets of conditions: atmospheric conditions (with O_2 and CO_2) and reducing conditions (without O_2 and CO_2). However, the experimental data from previous investigations revealed that the transition between Se(IV) and Se(VI) species is a slow process. For example, a five-year-long experiment conducted by Ikonen et al. (2016) demonstrated that only 3.7% of Se(IV) was oxidized to Se(VI). Due to this slow transition rate, we considered only the influence of CO2 in the Se speciation modelling to differentiate between atmospheric and reducing conditions and avoid overestimation of O_2 effects.

Figure 2-5 illustrates the results of the Se speciation modelling under atmospheric conditions with the influence of CO_2. The total Se concentration in the system is 10^{-7} M. Figure 2-5 (a) shows the significant variation in Se speciation across different pH conditions. At pH values below 8.5, $HSeO^{3-}$ predominates as the primary Se species, while at pH values above 8.5, SeO_3^{2-} becomes more dominant. Additionally, it is noteworthy that the concentration of H_2SeO_3 increases with decreasing pH when pH is below 4. Furthermore, Figure 2-5 (right) demonstrates the influence of Se concentrations under atmospheric conditions. The model results indicate that the relative proportions of different Se species remain constant within the concentration range from 10^{-10} M to 10^{-3} M. Therefore, the results suggest that Se will not form precipitation species or complexation species until at least concentration reaches 10^{-3} M.

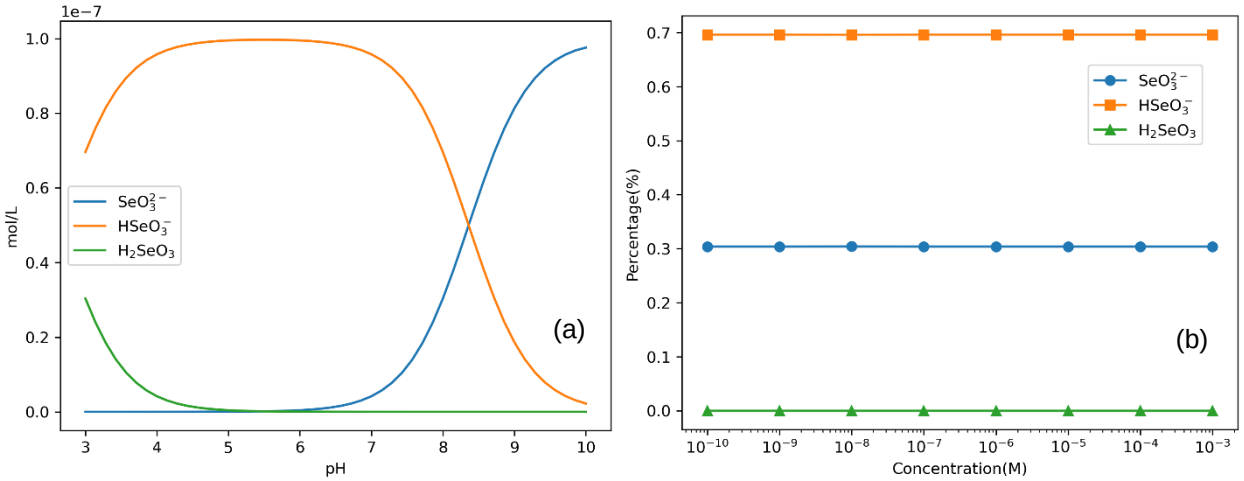

Figure 2-5 a) Se(IV) speciation as a function of pH in Grimsel groundwater simulant with atmospheric conditions. The concentration of total Se(IV) in the simulation was 10^{-6} M. b) Percentages of different Se(IV) species as a function of total aqueous Se(IV) concentrations at pH 8 in equilibrium with atmosphere CO_2.

Figure 2-6 presents the Se speciation modelling results without the influence of CO_2, simulating the experimental conditions of a N2 glovebox. The pH condition of the simulation is 8. Remarkably, the modelled speciation results under varying pH and concentration conditions are nearly identical to those obtained under the effects of CO_2. Thus, we can conclude that CO_2 has no significant impact on the Se aqueous species.

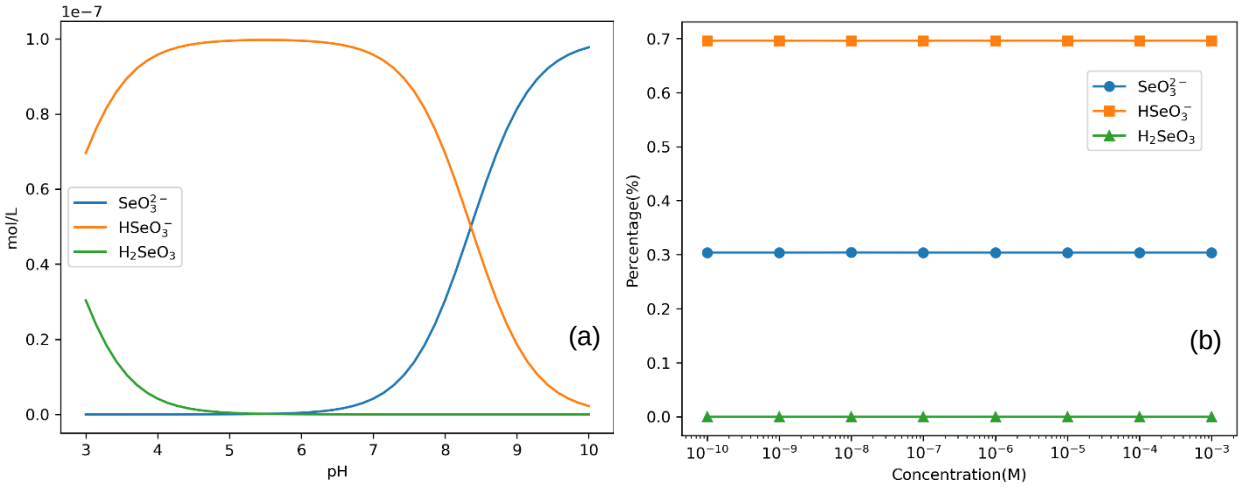

Figure 2-6 a) Se(IV) speciation as a function of pH in Grimsel groundwater simulant in inert atmosphere. b) Percentages of different Se(IV) species as a function of total aqueous Se(IV) concentrations at pH 8 in equilibrium conditions without atmosphere CO_2.

2.2.2.3 Ba speciation modelling under atmospheric and reducing conditions

Barium (Ba) speciation modelling was conducted using the PHREEQC software. The speciation calculations were performed in equilibrium with SGW2, as previously demonstrated in Section 2.2.2.1 for the Ni speciation modelling. The Ba speciation modelling was also carried out under two sets of conditions: atmospheric conditions (with O_2 and CO_2) and reducing conditions (without O_2 and CO_2).

The results of the Ba speciation modelling under atmospheric conditions are presented in Figure 2-7. Figure 2-7a illustrates the distribution of Ba aqueous species over a pH range from 3 to 10, with the total Ba concentration in the system set at 10^{-7} M. It is evident that the Ba species remain relatively constant until pH reaching 8.5. Below pH 8.5, Ba^{2+} dominates as the primary aqueous species, while the remaining fraction consists of $BaSO_4$(aq) at approximately 10%. As the pH exceeds 8.5, the concentration of $BaCO_3$(aq) rapidly increases and reaches around 90% at pH 10, due to the equilibrium with atmospheric CO_2(g). The amounts of Ba^{2+} and $BaSO_4$(aq) decrease accordingly. Additionally, a small amount of $BaHCO_3^+$ appears when pH is between 9 and 10.

In Figure 2-7 b, the percentages of Ba species are present as a function of the total Ba concentration, ranging from 10^{-10} M to 10^{-3} M, while maintaining a pH of 9 during the modelling. Same as shown Figure 2-7a, Ba^{2+} remains the dominant species at pH 9. However, Figure 2-7b also reveals that the percentages of all Ba species decrease when the aqueous Ba concentration exceeds 10^{-7} M. This decrease is attributed to the precipitation of barite ($BaSO_4$) due to the relatively high concentration of SO_4^{2-} in the background solution. The saturation index (SI) curve in Figure 2-7b indicates that barite SI reaches 0 when the Ba aqueous concentration is 10^{-6} M. Another possible Ba precipitation is witherite ($BaCO_3$), the SI of which reaching 0 when the Ba aqueous concentration reaches 10^{-3} M.

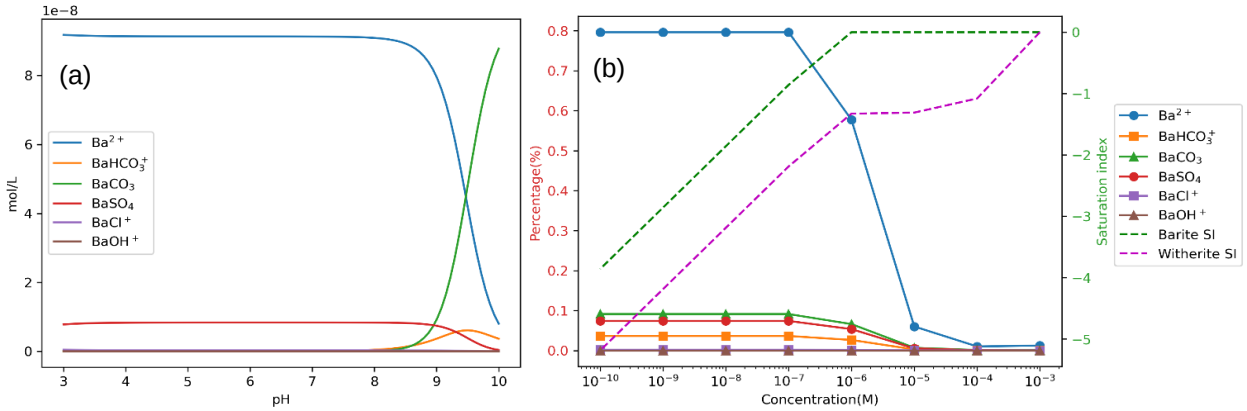

Figure 2-7 a) Ba speciation as a function of pH in SGW2 with atmospheric conditions. The concentration of total Ba in the simulation was 10^{-7} M. b) Percentages of different Se(IV) species as a function of total aqueous Se(IV) concentrations at pH 8 in equilibrium with atmosphere CO_2..

Figure 2-8 shows the Ba speciation modelling results without equilibrium with atmospheric conditions. Figure 2-8a demonstrates that Ba^{2+} remains the most dominant Ba species across the entire pH range from 3 to 10. Only in the pH region above 9, there is a slight decrease in the concentration of Ba^{2+} due to the increase of $BaCO_3$(aq). Similar to the modelling results with equilibrium with CO_2(g), $BaSO_4$(aq) is the second most abundant Ba species throughout the pH span.

Figure 2-8b presents the percentages of Ba species as a function of Ba concentrations, ranging from 10^{-10} M to 10^{-3} M, at a pH of 9. Same as the modelling results with equilibrium with CO_2, Ba^{2+} remains the dominant species, and the percentages of all Ba species are influenced by the formation of barite precipitation when the aqueous Ba concentration exceeds 10^{-7} M. The difference here is that the percentage of Ba^{2+} increases with Ba concentration over 10^{-4} M, caused by the sufficient presence of Ba^{2+} species remaining in the solution without equilibrium with CO_2(g).

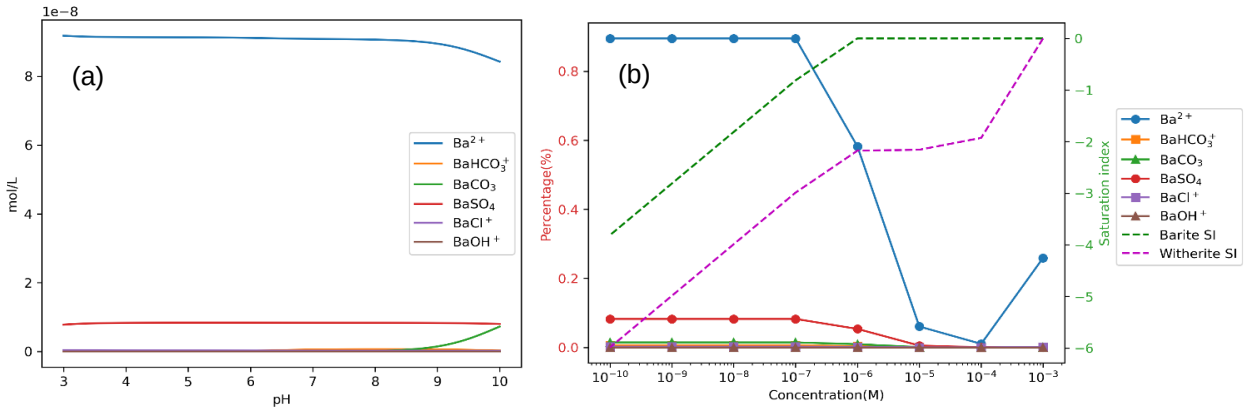

Figure 2-8 a) Ba speciation as a function of pH in SGW2 without atmospheric conditions. The concentration of total Ba in the simulation was 10^{-7} M. b) Percentages of different Se(IV) species as a function of total aqueous Se(IV) concentrations at pH 8 without equilibrium with atmosphere CO_2.

2.2.2.4 Ra speciation modelling

In the Ra batch sorption experiments, four different types of groundwaters were utilized to represent various salinities at varying depths of the Olkiluoto site. The compositions of these four groundwaters are presented

in Table 2-5. Thus, Ra speciation modeling was conducted for these four groundwaters to support the experimental data illustrations.

Table 2-5 The ionic compositions (mg/l) of the Olkiluoto reference groundwaters used in the experiments, along with the set pH and the reference ionic strengths (I).

Ion	Concentration of the ion or substance (mg/L)			
	ALLMR	OLSR	OLGA	OLBA
Na^+	52.5	4800	0.66	1750
K^+	3.9	21	0.6	18.9
NH_4^+	–	–	–	0.33
Mg^{2+}	0.7	54.6	0.3	26.5
Ca^{2+}	5.1	4000	0.52	84.5
Sr^{2+}	–	35	–	0.1
$B(OH)_3$	–	5.3	–	3.5
Cl^-	48.8	14,500	3	2530
HCO_3^-	165	–	–	111
SiO_2	17	–	0.1	6.1
SO_4^{2-}	9.6	4.2	0.2	458
F^-	–	1.2	–	0.3
I^-	–	0.9	–	–
Br^-	–	104.7	–	13.1
pH	8.8	8.3	5.8	7.6
I (mmol/l)	4.31	515	0.123	91.4

Figure 2-9 illustrates the Ra speciation calculated in equilibrium with ALLMR groundwater. The modelling was performed for both experimental conditions without CO_2 influence and in equilibrium with atmospheric CO_2, with a total Ra concentration set at 10^{-7} M. Figure 2-9A displays the Ra species under the absence of CO_2 influence, showing that Ra^{2+} is the dominant species from pH 3 to pH 10. Only at pH levels above 9, there is a slight decrease in the concentration of Ra^{2+} due to the formation of $RaCO_3$(aq) in high pH conditions. A small amount of $RaSO_4$(aq) is present consistently due to the presence of SO_4^{2-} in the groundwater. Figure 2-9B shows the Ra species in ALLMR groundwater in equilibrium with atmospheric CO_2. The notable difference compared to the Ra species without CO_2 influence is the rapid increase in $RaCO_3$(aq) concentration when pH exceeds 8.5, primarily due to the significant rise in CO_3^{2-} concentration in the solution. The amount of $RaCO_3$(aq) surpasses the amount of Ra^{2+} when pH rises above 9.5.

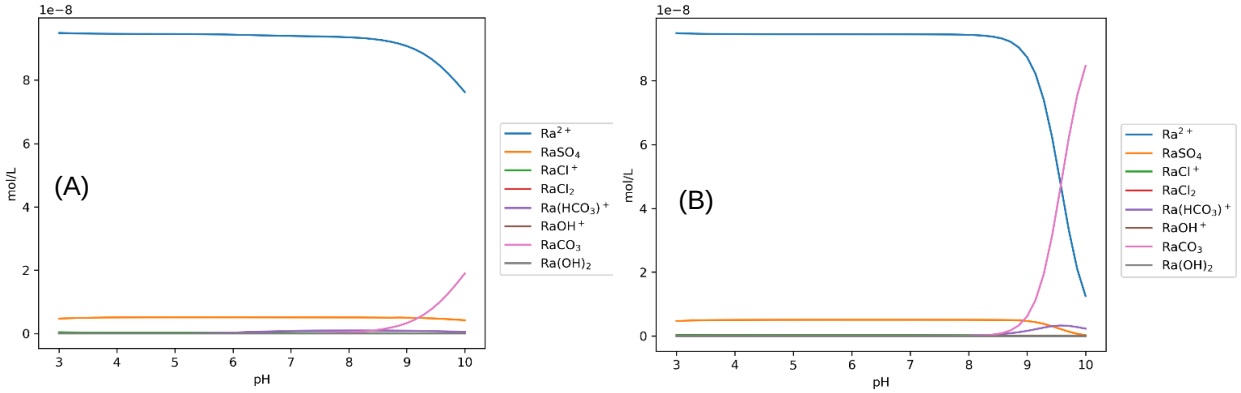

Figure 2-9 Ra speciation modelling in ALLMR groundwater. A) Modelled species without the effects of CO_2. B) Modelled results in equilibrium with atmospheric CO_2.

Figure 2-10 demonstrates the Ra speciation modelling results for OLSR groundwater. As indicated in Table 2-5, the salinity of OLSR groundwater is substantially higher than the other three types of groundwater, especially with a Cl^- concentration of 14500 mg/L. The Ra speciation modelling without CO_2 effects, shown in Figure 2-10A, reveals that Ra species remain unaffected by pH changes from pH 3 to pH 10. Ra^{2+} remains the dominant Ra species, accounting for more than 70% of the total amount. The second and third most abundant Ra species are $RaCl^+$ and $RaCl_2$(aq), respectively, due to the high Cl^- concentration in the groundwater. Figure 2-10B shows the Ra speciation modelling with atmospheric CO_2 influence. Similar to the Ra species in ALLMR groundwater, the concentration of $Ra(CO_3)$(aq) rises significantly after pH 8.5, becoming the most dominant Ra species after pH 9.5.

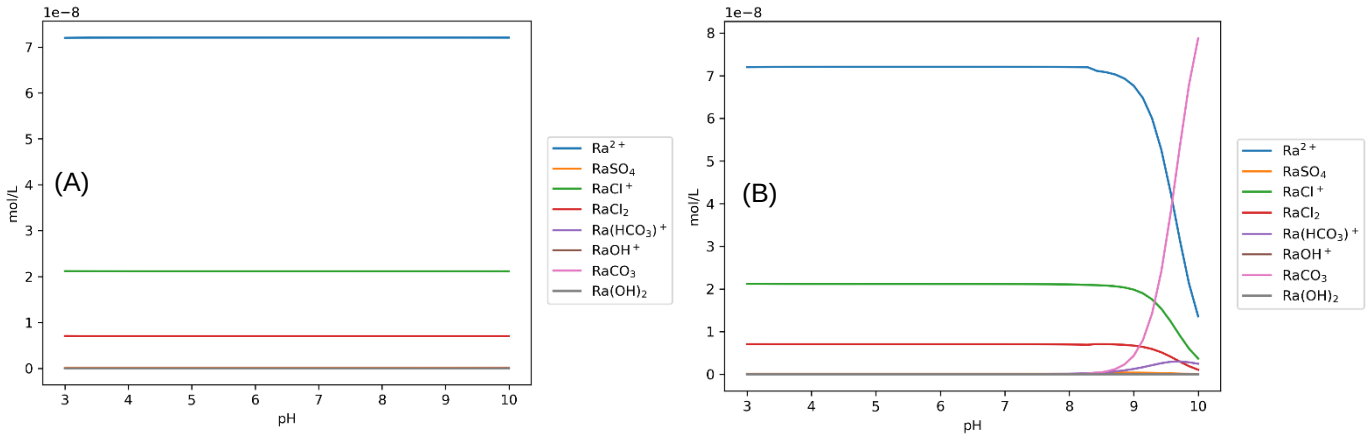

Figure 2-10. Ra speciation modelling in OLSR groundwater. A) Modelled species without the effects of CO_2. B) Modelled results in equilibrium with atmospheric CO_2.

Ra speciation modelling with OLGA groundwater is presented in Figure 2-11. OLGA groundwater is the freshest among the four types, with an ionic strength of only 0.123 mmol/L. Thus, the Ra species in OLGA groundwater closely resemble those in freshwater. As shown in Figure 2-11A, Ra^{2+} is the only Ra species present from pH 3 to pH 10 without CO_2 effects. However, when atmospheric CO_2 is in equilibrium, the concentration of $RaCO_3$(aq) increases after pH 8.5, surpassing the amount of Ra^{2+} when pH exceeds 9.5.

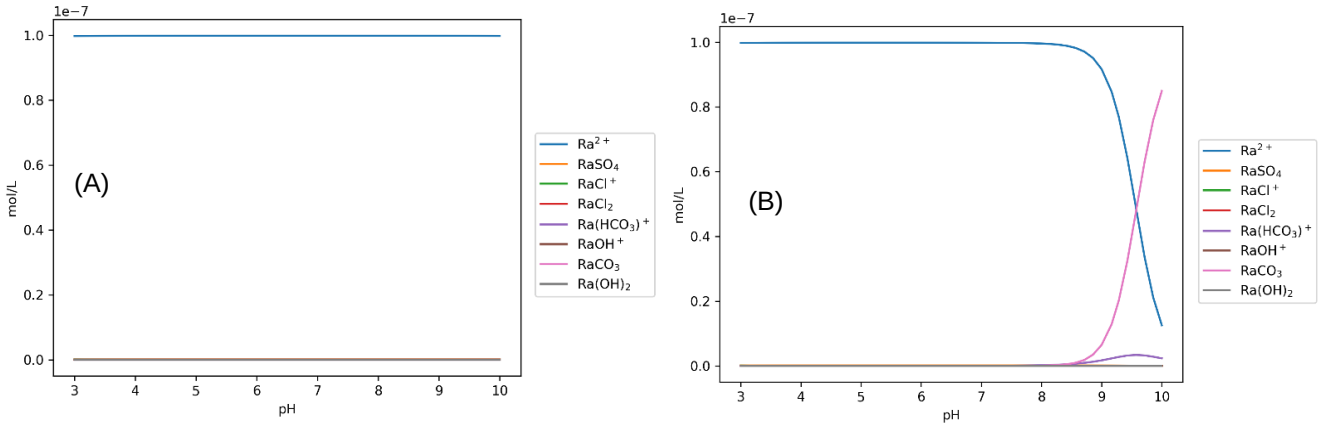

Figure 2-11. Ra speciation modelling in OLGA groundwater. A) Modelled species without the effects of CO_2. B) Modelled results in equilibrium with atmospheric CO_2.

Figure 2-12 shows the Ra speciation modelling results in equilibrium with OLBA groundwater. OLBA groundwater is the second most saline among the four types, with an ionic strength of 91.4 mmol/L. Notably, the concentration of SO_4^{2-}, which can precipitate RaSO4(s) with Ra^{2+}, is relatively high. The impact of SO_4^{2-} is clearly shown in Figure 2-12. In Figure 2-12A, the Ra species without CO_2 effects are shown, revealing that $RaSO_4$(aq) is the dominant Ra species, and its concentration remains constant. This is attributed to the precipitation of $RaSO_4$(s), and the constant concentration of $RaSO_4$(aq) represents the saturation concentration in the aqueous phase. The formation of $RaSO_4$(s) precipitation is also evident from the total concentration of Ra species in the solution, which remains below 10^{-7} M (the defined total Ra concentration in the model). The dissaperance of Ra in the solution is due to the formation of $RaSO_4$(s) precipitation. The amount of $RaSO_4$(s) precipitates increases after pH 7.5, leading to a decrease in the amount of Ra^{2+} in the solution. When in equilibrium with atmospheric CO_2, a transition from $RaSO_4$ to $RaCO_3$ in the solution is observed, as reflected by the rapid increase in $RaCO_3$(aq) species and the simultaneous decrease of $RaSO_4$(aq) in the solution. The total amount of Ra species in the solution also increases, indicating the dissolution of RaSO4(s) due to the increased amount of CO_3^{2-} formed in the solution.

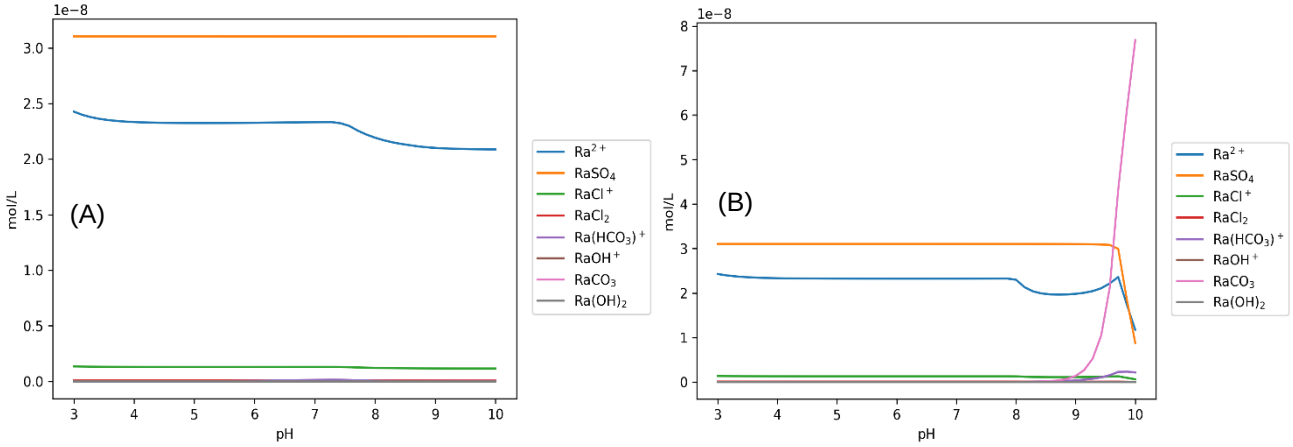

Figure 2-12. Ra speciation modelling in OLBA groundwater. A) Modelled species without the effects of CO_2. B) Modelled results in equilibrium with atmospheric CO_2.

2.3 Results and discussion

2.3.1 Preliminary Sorption Experiments for Determining Batch Sorption Method for Bukov Calcite, Chlorite Infills and Host Rocks Samples at UJV

Sorption studies encompass a range of methodologies, but the conventional and widely utilized approach, known as static batch sorption experiments, stands out due to its simplicity and well-established initial conditions. This method enables the quantitative analysis of adsorp contaminants, which is crucial for modelling studies aimed at comprehending their migration. By carefully selecting appropriate qualitative analysis techniques, valuable insights can be gained regarding the magnitude and underlying mechanisms of the sorption process. In intricate systems like rock formations, the distribution coefficient, a significant parameter, provides vital information for successfully describing the transport of contaminants across natural barrier systems in subsequent stages.

A subset of the conducted experiments has been included in the diploma thesis titled "Migration of Ni in barrier materials" authored by Kočan in 2022 at the Faculty of Nuclear Sciences and Physical Engineering, Czech Technical University in Prague. The thesis chapters, namely preliminary sorption experiments alongside the sorption data obtained for the Bukov calcite infill, were selectively utilized in the subsequent publication.

Phase 1 Factor Testing: Exploration of Variable Factors

The preliminary sorption experiments were conducted in three distinct phases. In the initial phase, modifications were made to the baseline methodology used by ÚJV to prolong the duration of phase contact. Furthermore, the impact of drilling, pre-equilibration of the phase fraction, and the presence of a carrier material were investigated. Throughout all the tested configurations, a consistent phase ratio of 1:10 (corresponding to a sample load of 0.5 g) was maintained under aerobic conditions. The obtained values of the distribution coefficient K_d for cesium and nickel are presented in detail in Table 2-6.

Table 2-6 Experimental design and distribution coefficient of cesium and nickel in the first phase of factor testing on the PVP-2_washed in ultrasonic bath in SGW2 environment. Any alterations made to the baseline methodology were denoted by green highlighting, providing clear distinction from the original approach, distribution coefficients with standard deviations

Variable parameter	**Previous UJV methodology**	**Contact time adjustment**	**Samples agitation**	**Solid phase equilibration**	**Presence of non-radioactive carrier**
Modification of solid phase	PVP-2_washed in ultrasonic bath	PVP-2_washed in ultrasonic bath	PVP-2_washed in ultrasonic bath	PVP-2_washed in ultrasonic bath, equilibrated with SGW2 (see chapter 2.2.1.3)	PVP-2_washed in ultrasonic bath
Presence of non-radioactive carrier	yes	yes	yes	yes	**no**
Samples agitation	yes	yes	**no**	yes	yes
Contact time adjustment, days	7	**14, 28**	**14**	**14**	**14**
K_d (Cs), m³/kg	0.014 ± 0.003	0.019 ± 0.002 (14 d)	0.008 ± 0.002	0.052 ± 0.003	0.530 ± 0.045

Variable parameter	Previous UJV methodology	Contact time adjustment	Samples agitation	Solid phase equilibration	Presence of non-radioactive carrier
		0.022 ± 0.003 (28 d)			
K_d (Ni), m^3/kg	0.794 ± 0.064	1.910 ± 0.055 (14 d) 2.825 ± 0.521 (28 d)	0.205 ± 0.045	1.747 ± 0.277	1.913 ± 0.374

The data presented in Table 2-6 demonstrates an increase in the distribution coefficient for nickel (Ni) with prolonged contact time. However, the observed increase is more pronounced for Ni. Notably, sorption equilibrium was not achieved within the investigated contact time for neither tracer. This phenomenon may be attributed to mechanical abrasion of particles, thereby potentially increasing the specific surface area of the rock grains. Following the interaction, the post-interaction solid phase was not subjected to network analysis or specific surface area determination; however, a slight increase in solution turbidity was observed. In a related interaction experiments involving PVP-2_washed with ultrasonic bath samples with SGW2 over drilling durations of 7, 14, and 28 days were conducted. The results revealed the release of nearly all ions except calcium, while potassium, magnesium, and bicarbonate concentrations exhibited a modest increase over time. This behavior could be attributed to the aforementioned particle abrasion and potential dissolution of minerals present in PVP-2. The increase in K_d over time has also been observed in previous studies, such as Cs sorption on crushed granite as reported by Huitti and Hakanen (1998). Among the tested factors, the non-agitated samples exhibited the lowest K_d, suggesting that diffusion processes (solution, surface, and intraparticle diffusion) govern the sorption mechanism in this particular setup, as described by Simonin and Bouté (2016). Furthermore, lower sorption compared to agitated samples was observed in non-drilled crushed granite samples during Cs and Sr sorption, as reported by Tsukamoto and Ohe (1991).

The equilibration of the PVP-2_UK sample with SGW2 resulted in a more than twofold increase in the distribution coefficient (K_d) for Cs compared to the non-equilibrated sample, whereas a slight decrease in K_d was observed for Ni. The sorption experiments were supplemented with an analysis of non-active chemical equilibrium. The progression of chemical reactions during equilibration was monitored using liquid phase chemistry. Starting from the third partial exchange of the liquid phase with fresh solution, ion concentrations, excluding potassium and calcium, approached the concentrations in SGW2. The enhanced K_d for Cs can be attributed to the replacement of potassium with calcium, leading to the expansion of biotite layers and the consequent enhanced cesium sorption on illite, as demonstrated in the studies by Benedicto et al. (2014) and Wauters et al. (1994). In contrast, equilibration of the PVP-2_washed with ultrasonic bath did not result in an increase in the sorption potential of Ni, as observed for Cs. This disparity may be attributed to distinct sorption mechanisms for Cs and Ni. Literature review indicated that the equilibration of granite and granodiorite had a limited impact on the sorption of the studied elements (Eu and U) (Holgersson, 2013, Stage et al., 2012), which aligns more closely with the results for Ni rather than Cs.

Further experiments did not involve equilibration. This decision was based on the fact that equilibration did not achieve potassium and calcium concentrations comparable to those in SGW2 water (see below). Moreover, considering that the crushed post-interaction phase represents a distinct sorption environment compared to intact rock in the deep geological repository, using equilibration as a means to approximate phase equilibrium, as in in-situ conditions, may not be suitable. This discrepancy in environments can likely be attributed to the varying phase ratios and the resulting different chemistries.

The dynamic changes in the chemistry of the liquid phase were meticulously monitored throughout the equilibration process. Commencing from the third partial replacement of the liquid phase with a fresh solution, the concentrations of Na^+, Mg^{2+}, Cl^-, SO_4^{2-}, and HCO_3^- progressively approached the concentrations determined for SGW2 water. However, the attainment of equilibrium with SGW2 groundwater remained elusive for K^+ and Ca^{2+}, as evidenced in Figure 2-13. Notably, even after three partial

exchanges, potassium persisted at concentrations 2.5 times higher than those observed in SGW2 water, while continuous depletion of calcium occurred. Thus, the employed equilibration procedure proved inadequate in achieving the desired equilibrium between the fragmented rock and SGW2 groundwater. The equilibration process engendered an augmented distribution coefficient for Cs and a diminished K_d for Ni. Moreover, this equilibration led to a discernible reduction in the concentrations of the majority of ions, effectively aligning them with the concentrations found in SGW2 water. Consequently, the competitive potential of ions in the sorption process experienced a decrease. The amplified K_d for Cs can plausibly be ascribed to the lower ionic strength witnessed in experiments involving the equilibrated material. However, the underlying mechanism governing the sorption of nickel remains enigmatic, thereby precluding a comprehensive explanation for the observed decline in K_d for Ni during the equilibration process.

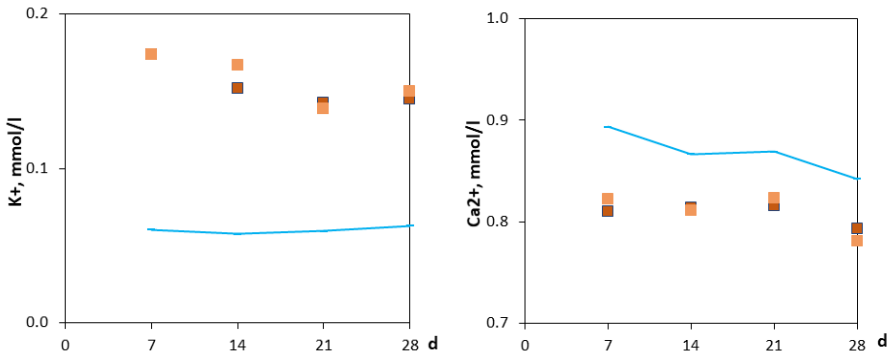

Figure 2-13 Development of the K^+ and Ca^{2+} concentrations (dots) in the liquid phase during the rock equilibration process with SGW2 (blue line)

When examining the influence of the added inactive carrier, divergent trends in K_d for Cs and Ni were observed. While the highest K_d value for Cs was observed in the experiment without the inactive carrier, the K_d value for Ni without the inactive carrier was similar to that with the carrier. The elevated K_d for Cs can be ascribed to the increased availability of sorption sites for $^{134}Cs^+$ in the absence of competitive inactive Cs^+ (similar trends were observed, for example, in the study by Muuri et al. (2016)). The K_d values for Ni indicate a sufficient number of sorption sites for this tracer, even in the presence of the inactive carrier.

Based on the K_d values for varying phase contact times and the K_d values for non-drilled samples, a drilling duration of 14 days was chosen for subsequent experiments. Additionally, a reasonably long experimental duration (14 days) was selected, allowing for meaningful observations even without achieving a steady-state sorption. The procedure of adding an inactive carrier from the UJV methodology was maintained for subsequent sorption experiments. The decision to include the inactive carrier was based on the assumption of higher stability of the respective element at higher concentrations (e.g., negligible sorption on ampoule walls), albeit deviating from similarity with potentially low radionuclide concentrations in the deep geological environment.

Phase 2 Factor Testing: Assessment of the Influence of Concentration Variations and Solid-to-Liquid Ratios

The second phase of factor testing aimed to investigate the impact of the phase ratio m/V and the initial carrier concentration C_0 on the sorption process. Altering these parameters allowed for a detailed examination of the adsorbed quantity q in relation to the equilibrium concentration C. If the data points for q and C exhibit a linear correlation without significant deviations, a linear sorption isotherm can be employed to model this relationship and determine the distribution coefficient K_d as a slope of the isotherm. Both experimental setups maintained a fixed contact time of 14 days under aerobic conditions. The phase ratio m/V was adjusted to a range of 1:20 to 1:3, with corresponding weights of 0.25-1.67 g, while the variation of initial C_0 spanned from $1x10^{-3}$ to $1x10^{-7}$ mol/L. The obtained results depicting the distribution of Cs and

Ni between PVP-2_washed with ultrasonic bath and SGW2 during the second phase of factor testing are presented in Figure 2-14 and Table 2-7.

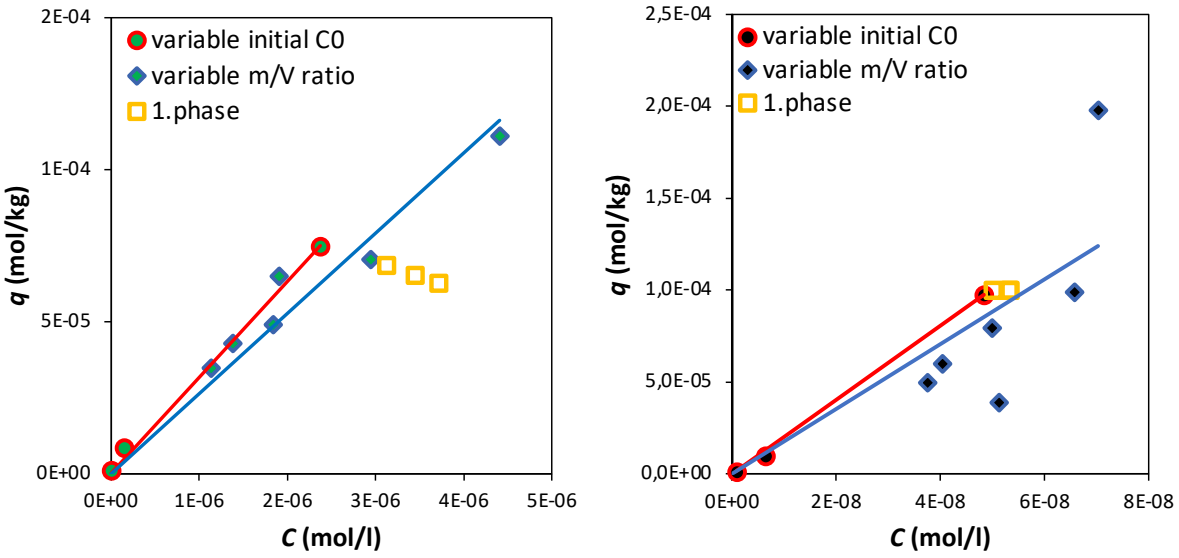

Figure 2-14 Distribution coefficient variation of cesium (left) and nickel (right) in the second phase of factor testing: impact of solid-to-liquid ratio and initial concentration variation on PVP-2_washed in an SGW2 environment

Sorption experiments with an initial carrier concentration of $1x10^{-5}$ mol/l for both elements and varying *m*/*V* ratios yielded linear *q* vs. *C* distributions across the entire concentration range, as clearly depicted in Figure 2-14. An outlier point was observed for nickel at a loading of 0.25 g. This observation suggests that the sample loading size, particularly in the case of heterogeneous samples such as crushed granite, may introduce variability in the *q* vs. *C* data. The linear regression analysis of the obtained data in the second phase effectively illustrates the high degree of similarity between the two SE methodologies employed, as presented in Table 2-7.

Table 2-7 Distribution coefficients of cesium and nickel: phase 2 factor testing with solid-to-liquid ratio and initial concentration variation on PVP-2_washed in SGW2 environment, Including standard deviations from the linear regression

Variable parameter	*m*/*V* ratio	Initial *C*
K_d (Cs), m³/kg	0.0264 ± 0.0014	0.0315 ± 0.0012
K_d (Ni), m³/kg	1.764 ± 0.318	2.007 ± 0.042

Additionally, Figure 2-14 presents data from the first phase (yellow cubes) to discuss the appropriateness of the UJV methodology and its modifications, specifically the implementation of sorption experiments in triplicates for a single phases ratio. This yields a single "calibrated" data point of the *q* vs. *C* distribution. However, this approach fails to provide information about the shape of the distribution, which can exhibit convex, linear, or concave behavior. Consequently, it is not valid to equate the value of the distribution coefficient K_d to the sorption coefficient K_d, from linear isotherm, which holds significance in safety calculations for deep geological repositories. Under the chosen conditions of the UJV methodology (excluding time), K_d for the one *m*/*V* ratio (K_d (*m*/*V*)) and K_d values from the linear isotherm (K_d (linear)) exhibit similarity for Ni, albeit to a lesser extent for Cs. Nevertheless, it should be noted that the UJV methodology does not investigate diverse sorption experiments conditions, as K_d (*m*/*V*) values are always contingent on the specific conditions employed. For Cs, the deviation between K_d (*m*/*V*) and K_d (linear)

values may be attributed to the potential lower mass (0.5 g) owing to variations in grain composition during the weighing process. Methodologies that provide K_d (linear) values demonstrate greater robustness by accounting for any deviations from ideality (e.g., sample heterogeneity, differing compositions in liquid phase during sorption experiments), which are encompassed within the K_d (linear) deviation. These deviations can surpass those observed for K_d (m/V). Despite larger deviations, K_d (linear) values possess greater weightage due to their derivation from a linear relationship. Thus, the approach involving the variation of m/V ratio appears more favorable compared to the alteration of initial C_0, as it permits the utilization of multiple m/V ratios and facilitates linear regression analysis for multiple q vs. C values, in contrast to the methodology relying on changes in initial C_0. Another advantage of the m/V ratio approach is its lower experimental complexity, as it entails working with a single radioactive solution, eliminating the need to prepare a series of solutions with different concentrations and thereby minimizing the generation of radioactive waste.

Based on the findings of the initial and subsequent phases investigating the impact of sorption experiments factors on the sorption of cesium and nickel on the PVP-2_washed in ultrasonic bath sample, the methodology involving the variation of the m/V ratio was selected as the preferred method for the ensuing phase.

Phase 3 Factor Testing: Phase 3 Factor Testing: Examination of the Impact of Anaerobic Conditions

The third phase of factor testing was dedicated to investigating the influence of inert conditions, characterized by the absence of oxygen (O_2) and carbon dioxide (CO_2), on the distribution coefficients (K_d) of cesium and nickel. The primary objective was to evaluate the feasibility and effectiveness of employing the sorption methodology within an anaerobic environment, facilitated by the utilization of an anaerobic box. To facilitate comparative analysis, sorption experiments were also conducted under aerobic conditions using the same liquid phase. The experimental procedure remained consistent across both environments, with the sole variation being the manipulation of the mass-to-volume ratio (m/V). The outcomes of the partitioning phenomenon, elucidating the distribution dynamics of Cs and Ni between the solid and liquid phases during the pivotal third phase of factor testing, are graphically represented in Figure 2-15.

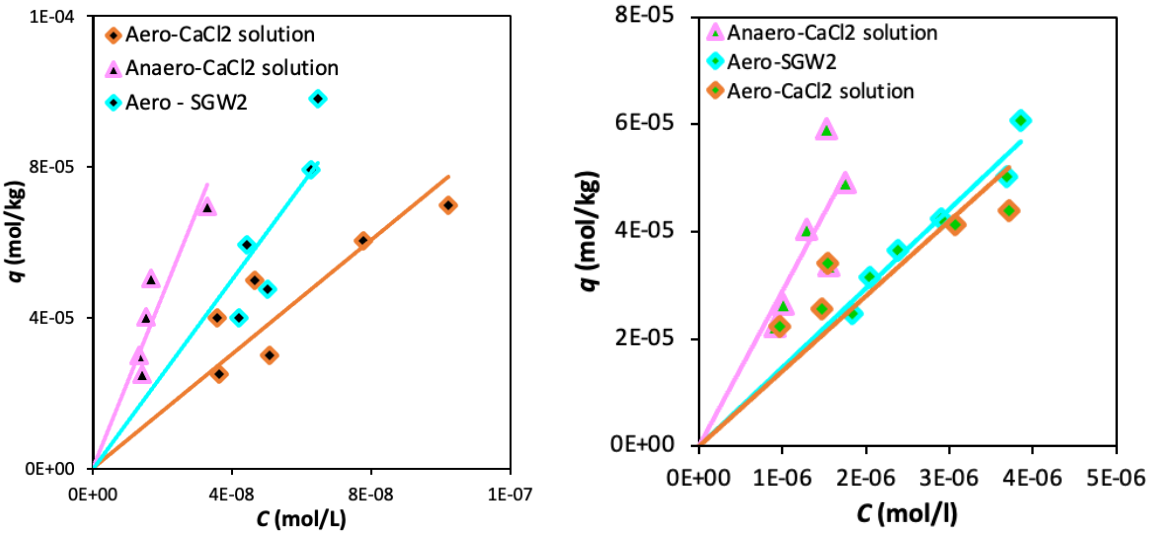

Figure 2-15 Distribution coefficient of cesium (left) and nickel (right) in phase 3 factor testing on PVP-2_washed in an SGW2 and $CaCl_2$ environment: investigating the influence of anaerobic conditions

The analysis of the linear sorption isotherms depicted in Figure 2-15 reveals that the sorption of both cesium and nickel exhibited higher affinity under anaerobic conditions than under aerobic conditions. The quantified values of the distribution coefficients, as tabulated in Table 2-8, indicate that the K_d values for both elements were more than twofold greater in the anaerobic environment compared to the aerobic counterpart.

Table 2-8 Distribution coefficient of cesium (left) and nickel (right) in phase 3 factor testing on PVP-2_washed in an SGW2 and $CaCl_2$ environment: investigating the influence of anaerobic conditions, including distribution coefficients with standard deviations

Conditions	Aerobic atmosphere (Air)		Anaerobic atmosphere (Ar)
Liquid phase	$CaCl_2$	SGW2	$CaCl_2$
K_d (Cs), m^3/kg	0.014 ± 0.002	0.015 ± 0.001	0.029 ± 0.003
K_d (Ni), m^3/kg	0.869 ± 0.059	1.256 ± 0.110	2.285 ± 0.184

The observed differential cesium uptake in presence of $CaCl_2$ solution between the two environments differ from the findings of Lee et al. (2006) and Stage et al. (2012), who did not observe significant differences in cesium sorption behavior on granite and granodiorite in their chosen synthetic waters under both aerobic and anaerobic conditions. Therefore, speciation calculations were performed for Cs as well. It was found that Cs exclusively occurs in the form of Cs^+ in both environments. The divergent cesium uptake could be related to the varying chemical conditions in these environments, which were investigated through interaction experiments, presented in Kočan (2022).

In the aerobic environment, the distribution coefficient of nickel was observed to be twofold lower compared to the anaerobic environment. One plausible explanation for this disparity could be attributed to changes in nickel speciation. However, a comprehensive evaluation of Table 2-9 reveals that the transition from aerobic to anaerobic conditions exerts negligible influence on nickel speciation. Extensive literature research (refer in Kočan (2022)) underscores the profound impact of pH on nickel sorption behavior. Elevated pH levels prompt the deprotonation of functional groups within the sorbent, consequently diminishing the concentration of H^+ ions (Yu and Nerentnieks, 1997). As a result, the sorption capacity of nickel exhibits a progressive increase as the liquid phase transitions towards alkaline conditions (Bradbury and Baeyens, 1995). Consequently, an alternative explanation arises from the differential pH characteristics of the $CaCl_2$ solution employed within the anarobic and aerobic environments. Consequently, a meticulous examination of the dissimilarities in sorption behavior was undertaken via interactive experiments, delineating the chemical interplay of the sorption system under both aerobic and anaerobic conditions, which are fully presented in Kočan (2022).

Table 2-9 The relative abundance (%) of nickel species at a concentration of c(Ni) = $1x10^{-5}$ mol/l in SGW2, calcium chloride solution with and without the presence of CO_2, calculated in PHREEQC with Andra Thermochimie v.10d database

Liquid phase	Ni^{2+}	$NiCO_3$	$Ni(HCO_3)^+$	$Ni(CO_3)_2^{2-}$	$Ni(OH)^+$	$Ni(OH)_2$	$NiSO_4$	$NiCl^+$
SGW2	77.9	13.1	3.9	< 1	2.2	< 1	2.0	< 1
$CaCl_2$ (without CO_2)	99.5	-	-	-	< 1	< 1	-	< 1
$CaCl_2$ (with CO_2)	99.7	< 1	< 1	< 1	< 1	< 1	-	< 1

The chemical aspects of interaction experiments and their methodology have been comprehensively described by Kočan (2022). The quantification of released ions likely arises from exchange reactions with calcium ions in liquid phase or the dissolution of minerals present in the analyzed samples. Differential concentrations of potassium ions and bicarbonate ions between the aerobic and the anaerobic experiments conducted in a calcium chloride medium have been observed. However, the observed more than twofold higher distribution coefficient values for both elements in the anaerobic environment compared to the

aerobic environment could not be satisfactorily explained through the conducted interaction experiments, thus leaving this discrepancy unaddressed.

Subsequently, the suitability of substituting complex water with a simple electrolyte in this phase of experiments is discussed. Under identical conditions, sorption experiments were carried out using aerobic conditions in the presence of simulated ground water SGW2 and 0.00166 mol/L $CaCl_2$. Cesium exhibited very similar K_d values in both liquid phase solutions, suggesting that the composition of the solution, including the presence of other ions and variations in pH, does not exert a significant influence on the sorption process of Cs. In contrast, distinct K_d values were determined for nickel, approximately 1.5 times higher in the SGW2 environment compared to $CaCl_2$ under identical ionic strength conditions. This indicates that the sorption of nickel is affected by the solution composition, encompassing the presence of other ions and pH variations.

The differing composition of SGW2 and $CaCl_2$ solutions, despite having the same ionic strength, implies variations in pH levels between these solutions. As previously discussed, the increased sorption of nickel in the more alkaline SGW2 solution may be attributed to the deprotonation of functional groups associated with the solid phase. In this context, it is expected that the disparate compositions of both liquid phase solutions have an impact on the speciation of nickel. Examination of Table 2-9 reveals that nickel exclusively exists as Ni^{2+} in $CaCl_2$, while the SGW2 model considers the presence of Ni^{2+}, $NiCO_3$, $Ni(HCO_3)^+$, $Ni(CO_3)_2^{2-}$, $Ni(OH)^+$, $Ni(OH)_2$, $NiSO_4$, and $NiCl^+$. Therefore, the higher sorption of nickel in the SGW2 environment is likely caused by the presence of carbonate, hydroxide, or sulfate complexes. Consequently, it can be postulated that, in addition to Ni^{2+}, interactions involving positively charged species such as $Ni(HCO_3)^+$ and $Ni(OH)^+$ contribute to the elevated uptake of nickel in the SGW2 environment.

In regard to the differences observed in sorption experiments specifically for nickel, the variations in distribution coefficients were relatively lower compared to cesium. This can be attributed to the fact that the sorption extent for Ni was already above 95%, indicating a high degree of sorption saturation. As a result, even minor heterogeneities or changes in the experimental system could have practical implications on the resulting distribution coefficient. These observed variations should be acknowledged as they may not be solely attributable to deliberate experimental adjustments but could also be influenced by statistical deviations and the inherent intricacies of nickel sorption. Factors such as ionic exchange and surface complexation, which contribute to substantial sorption levels, further contribute to the complexity of the phenomenon.

Sorption experiments with synthetic calcite

Based on an extensive review of the literature, the decision to utilize synthetic calcite in the sorption experiments with nickel (Ni) and cesium (Cs) was driven by multiple factors. Firstly, the investigation considered the limited sorption capacity of natural calcite at neutral to alkaline pH conditions. Secondly, the structural characteristics and sorption mechanisms of calcite were taken into account. To ensure reliable and controlled experiments, a deliberate choice was made to conduct the sorption studies without the addition of a carrier, thus eliminating the presence of competing ions. In addition, the mass-to-volume ratio was systematically varied within the range of 1:20 to 1:3 (corresponding to sample weights of 0.25-1.67 g). Three liquid phase solutions were employed, including simulated groundwater SGW2, 0.00166 mol/l $CaCl_2$, and 0.0033 mol/l $CaCl_2$. Figure 2-16 presents the distribution of nickel between synthetic calcite and the investigated solutions. The decision to use synthetic calcite was primarily driven by the limited availability of Bukov Calcite Infill after its distribution to other institutions, necessitating judicious usage of the available resources.

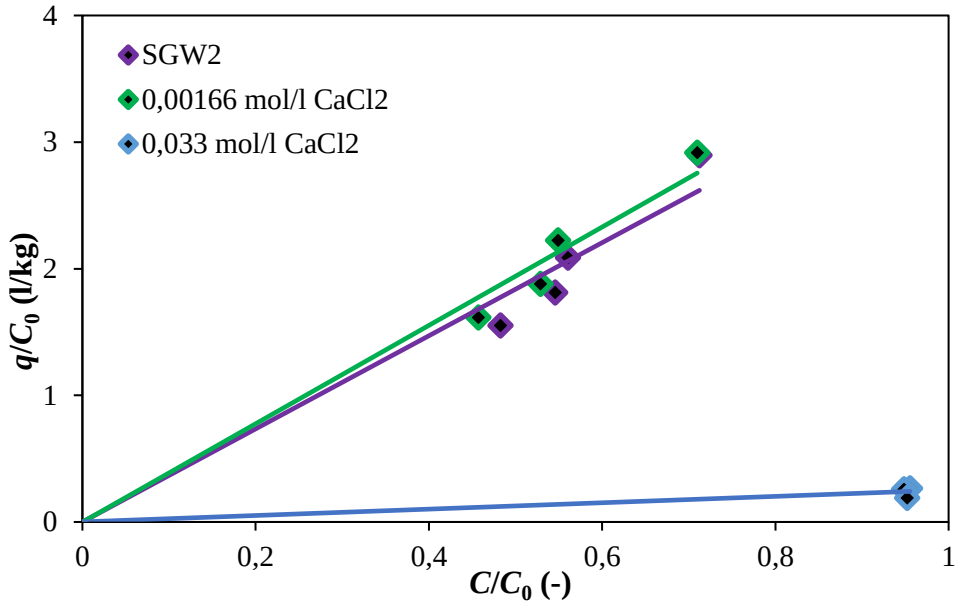

Figure 2-16 The nickel distribution between synthetic calcite and synthetic groundwater (SGW2) was quantified after a 7-day interaction period under controlled aerobic atmospheric conditions

The sorption of Ni in the liquid phase exhibited consistent behavior under equivalent ionic strength conditions. However, when the ionic strength was increased by a factor of twenty, the sorption of Ni decreased significantly, reaching a very low level. This behavior indicates a sorption mechanism involving the cation exchange of Ni^{2+} for calcium ions on the surface of calcite. The obtained K_d values (refer to Table 2-10) are of the same order of magnitude as those reported in studies conducted by Alvarez et al. (2019), Bradbury and Baeyens (2010), and Zachara et al. (1991). The low K_d values observed for synthetic calcite can be attributed, as discussed by Zachara et al. (1991), to the disparate ionic radii of Ni^{2+} in comparison to calcium ions.

Table 2-10 The obtained values of the linear distribution coefficient (K_d) for cesium and nickel on synthetic calcite were measured in the presence of SGW2 (synthetic groundwater) and CaCl2 solutions at two distinct concentrations

Liquid phase		K_d, m³/kg
$CaCl_2$	0.033 mol/l	$(2.5 \pm 0.3)\times10^{-4}$
	0.00166 mol/l	$(38.8 \pm 1.5)\times10^{-4}$
SGW2		$(36.8 \pm 2.0)\times10^{-4}$

Comparing the K_d(Ni) values of synthetic calcite with the rock sample PVP-2, it is evident that the K_d(Ni) values for synthetic calcite are significantly lower. Both materials had similar specific surface areas. This indicates that specific surface area values do not always reflect the sorption capacity of a given material. In the sorption experiment of cesium (Cs) with synthetic calcite, no significant decrease in the activity of ^{134}Cs in the liquid phase was observed under any conditions or for any of the solutions. This suggests that the sorption of Cs on synthetic calcite was lower than the detectability limit (K_d (m/V) < 0.29 ml/g). Torstenfelt et al. (1982) also reported very low Cs sorption on calcite with impurities from other minerals, with R_d(Cs) = 1 ml/g. The result of Cs sorption being undetectable under the experimental conditions supports the theory of minimal sorption of monovalent cations on calcite with a larger ionic radius compared to calcium ions (Curti, 1997).

In the case of further experiments involving samples of Bukov Calcite Infill with a substantial amount of calcite, it is anticipated that calcite will not exert a significant influence on the sorption of nickel and cesium. To effectively capture the sorption of cesium in Bukov Calcite Infill samples characterized by a high calcite content, higher sample masses will need to be employed to ensure the reliable quantification of the tracer concentration variation in the solution resulting from the solid-phase interaction.

2.3.2 Sorption of Cs

Evaluating the Sorption Characteristics of Cesium on Bukov URF Materials under Diverse Experimental Conditions

In a manner analogous to the experimental investigations conducted for the sorption of nickel (Ni), similar protocols were applied to evaluate the sorption dynamics of cesium (Cs). Cs sorption mechanisms exhibit distinct attributes, as specific sorption sites are traditionally associated with the presence of mica minerals. However, under the concentration ranges deployed in the sorption experiments (10^{-5} mol/L) conducted herein, it is conceivable that only Type II sorption sites or planar sites may be pragmatically available for Cs sorption. Frayed edge sites (FES), a subclass of sorption sites often linked with Cs sorption, are presumed to be fully saturated by the non-active carrier (Fuller et al., 2016). The quantification of FES was undertaken via RIP measurements, as delineated in the previous chapter 1.3.3.3. An elevated concentration of the non-active carrier was employed to facilitate a more comprehensive understanding of sorption dynamics at increased Cs concentrations. This approach was designed to reveal the sorption capacities of a variety of Bukov host rocks under elevated Cs conditions. This comprehensive view allows for an appreciation of the roles that not only micas but also other mineral constituents may play in the sorption of Cs. Experimental data, encompassing the quantity of adsorbed Cs as a function of its concentration in the liquid phase (*C*), were modeled employing linear isotherms and are graphically represented in Figure 2-17. Moreover, distribution coefficients derived from the sorption isotherms, the coefficient of determination (R^2), and the sorption percentage are compiled separately in Table 2-11. Moreover, it is important to note that the choice of employing a higher concentration of non-active carrier was deliberate. This approach provided us with valuable insights into the potential competitive adsorption mechanisms that may occur under scenarios where multiple species compete for sorption sites. This exploration is of high relevance in understanding and predicting the behavior of Cs in more complex, real-world geochemical environments where various minerals and ion species co-exist. Thus, the results of these investigations are expected to not only enhance our theoretical understanding of sorption processes but also provide practical inputs for geochemical modeling.

Table 2-11 The distribution coefficients for Bukov Calcite Infills, enriched host rocks and for Bukov Chlorite Infills under specific sorption experimental conditions. Additionally, the provided information includes the standard deviations of the distribution coefficients, the R2 values that indicate the adequacy of fit for the linear isotherm model, and the average percentage of sorption derived from a range of m/V ratios.

Materials	K_d (m^3/kg)	R^2	Sorption (%)	Sorption % highest-lowest from the *m*/*V* ratio range
Bukov Host rock with high plagioclase contents	0.0168 ± 0.0006	0.994	71.55 ± 8.76	62.43-84.87
Bukov Host rock with high amphibole contents	0.0127 ± 0.0003	0.994	70.04 ± 9.78	56.38-82.82
Bukov Host rock with high biotite contents	0.041 ± 0.003	0.974	87.30 ± 4.39	85.07-90.34

Host rock of Bukov Calcite Infill	0.100 ± 0.002	0.998	94.15 ± 2.29	90.68-97.35
Bukov Calcite Infill with adrock mixture	0.0034 ± 0.0001	0.995	37.06 ± 8.37	24.65-46.59
Bukov Calcite Infill	< 0.00022	-	-	-
Bukov Chlorite Infill extracted from 1.site	0.215 ± 0.032	0.865	98.58 ± 1.60	95.01-99.38
Bukov Chlorite Infill extracted from 2.site	0.346 ± 0.027	0.958	98.95 ± 0.96	96.96-99.41

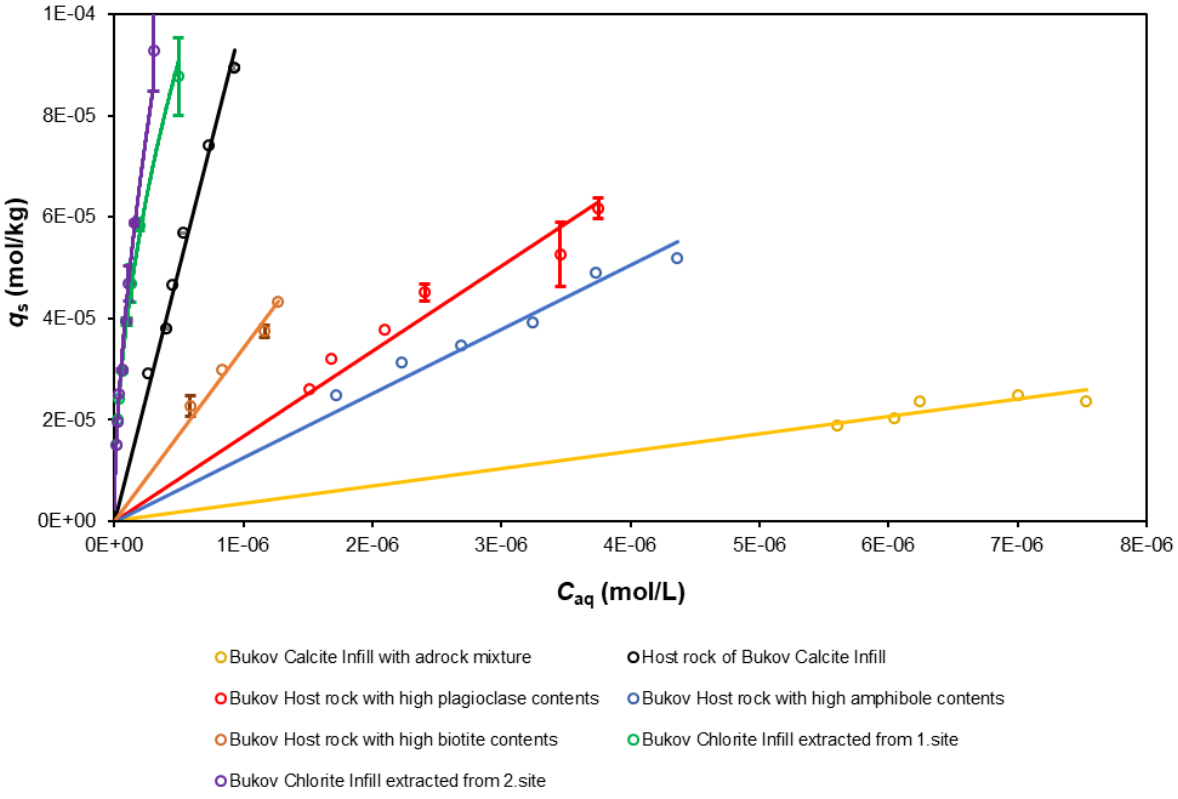

Figure 2-17 Distribution of cesium between Bukov materials and SGW2 after 14-day interaction: linear sorption isotherm-based determination of distribution coefficients under aerobic conditions

As per the findings detailed in Chapter 2.3.1, there was no significant reduction observed in the liquid-phase activity of ^{134}Cs for Cs. This observation aligns with previous studies conducted on synthetic calcite (Smith et al., 2010) and is consistent with the works of Torstenfelt et al. (1982) and Curti (1997). Conversely, Cs sorption on quartz, a constituent of the Bukov Calcite Infill, exhibited relatively low sorption capacity (Cornell, 1993; Muuri et al., 2016). However, a minor degree of sorption was discernible when the Bukov Calcite Infill was mixed with rock, likely attributed to the presence of chlorite, plagioclase, and dolomite. Among the analyzed host rock materials, the host rock of Bukov Calcite Infills demonstrated the highest sorption capacity. This enhanced sorption behavior can be attributed to its elevated specific surface area and cation exchange capacities, resulting in an increased number of planar sorption sites available for Cs sorption. The results obtained from the enriched host rocks reveal a positive correlation between Cs sorption and the abundance of biotite in the host rock, followed by the content of plagioclase and amphibole. This

underscores the significant role played by plagioclase and biotite in Cs sorption (Muuri et al., 2016). Furthermore, it was evident that the sorption capacity was highest in the biotite host rock, underscoring the pronounced influence of these minerals. Additionally, the number of available sorption sites, after accounting for non-active carrier occupation, was substantially greater in the Bukov Calcite Infills owing to the presence of plagioclase and biotite in this intricate system, as observed by Söderlund et al. (2015).

The Bukov Chlorite Infills exhibited the highest sorption levels, which can be attributed to their composition rich in chlorite and kaolinite, as well as their high specific surface area and cation exchange capacities. These samples demonstrated the highest number of planar and II type sorption sites among the studied materials. In scenarios with high concentrations of non-active Cs, samples with the highest specific surface area and cation exchange capacities, leading to an increased number of planar sorption sites, exhibited the greatest sorption capability for Cs. In cases where the specific surface area was comparable, the composition and amount of plagioclase and biotite present in the samples played a crucial role in determining the sorption behavior.

Differentiation and Nonlinear Sorption Behavior of Bukov Chlorite Infills: Insights from a Selected Concentration and m/V Ratio Range

In the Bukov Chlorite Infills study, we observe a non-linear relationship between q_s and C_{aq} across a spectrum of mass/volume (m/V) ratios, underscoring the inherent non-linearity in sorption processes. It is apparent that as m/V ratios increase, indicating lesser quantities of solid phase, there is a consequent decrease in sorption, a prediction that is consistent with the linear isotherm method. This correlation is predominantly attributed to significant alterations in specific surface area (SSA) across diverse m/V ratios. Moreover, an increased presence of certain trace minerals, such as chlorite and kaolinite, known for their high sorption capabilities, could potentially amplify the heightened sorption observed at lower m/V ratios. Due to the non-linear sorption phenomena observed at the predetermined concentration of $1x10^{-5}$ mol/L, we expanded the scope of our investigation by implementing sorption experiments at a lower concentration of $1x10^{-7}$ mol/L and a higher concentration of $1x10^{-3}$ mol/L. Detailed results, including numerical and graphical representations, can be located in Table 2-12 and Figure 2-18 respectively. These offer a comprehensive view of the sorption behavior under varying conditions, thereby enhancing the robustness of the studied chlorite infills sorption characterization.

Table 2-12 The distribution coefficients for Bukov Chlorite Infills for different concentration 1x10-5 mol/l, 1x10-7 mol/l and 1x10-3 mol/l with the R2 values that indicate the adequacy of fit for the linear isotherm model, and the average percentage of sorption derived from a range of m/V ratios

Material	10^{-5} mol/l			10^{-7} mol/l			10^{-3} mol/l		
	K_d (m^3/kg)	R^2	Sorption (%)	K_d (m^3/kg)	R^2	Sorption (%)	K_d (m^3/kg)	R^2	Sorption (%)
Bukov Chlorite Infill extracted from the 1.site	0.215 ± 0.032	0.865	98.58 ± 1.60	3.694 ± 0.203	0.988	99.88 ± 0.06	0.057 ± 0.002	0.996	92.98 ± 4.63
Bukov Chlorite Infill extracted from 2.site	0.346 ± 0.027	0.958	98.95 ± 0.96	9.891 ± 0.621	0.985	99.95 ± 0.03	0.056 ± 0.002	0.996	92.93 ± 5.22

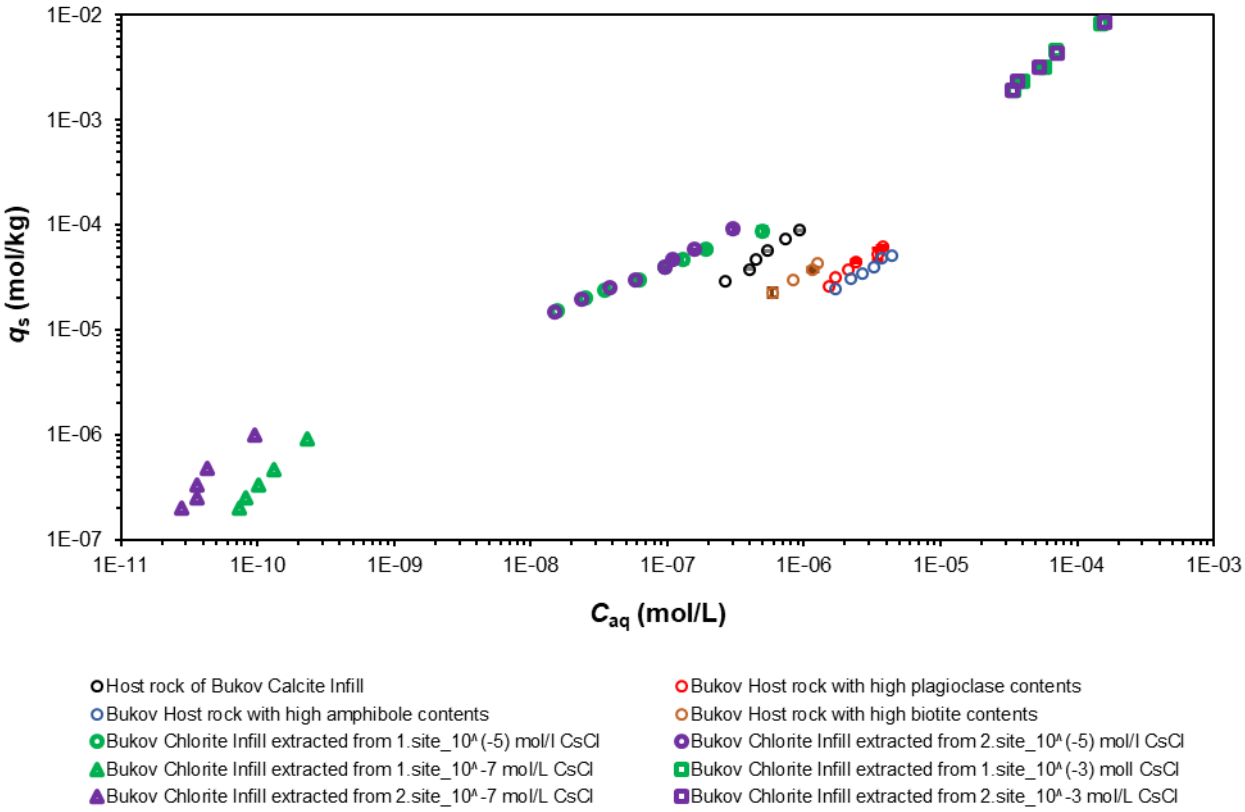

Figure 2-18 Distribution of cesium between Bukov materials and SGW2 after 14-day interaction: linear sorption isotherm-based determination of distribution coefficients under aerobic conditions and different cesium concentrations for Bukov Chlorite Infills

Closer analysis of the data reveals that the sorption capacity (q) is congruous with the linear isotherm model at the specified concentration of $1x10^{-7}$ mol/L and at the heightened concentration of $1x10^{-3}$ mol/L. Pertinently, the Bukov Chlorite infills, under conditions of increased concentration, demonstrate analogous distribution coefficients and sorption patterns. This suggests that the availability of sorption sites remains relatively uniform across both infill structures at these particular concentrations.

At lower concentrations, the sorption data retain a suitable degree of linearity. However, there is a slight increase in the accessibility of specific Cs sites, particularly at site 2, notwithstanding the fact that sorption exceeds 99% at both sites materials. An anomaly in the pattern emerges at a concentration of 10^{-5} mol/L, where sorption exhibits a non-linear trend. This deviation could be attributable to the sensitive variations in mineral quantities that occur in response to changes in the *m*/*V* ratios.

Considering the intrinsic properties of the Bukov Chlorite Infills, which do not conform to a well-defined granitic structure but rather serve as a porous intermediary within contiguous geological formations, it is a credible supposition that these infills sustain remarkable sorption capacities in both fragmented states and densified forms under authentic in situ conditions. When contrasted with other components derived from the Bukov region, which predominantly originate from hard rock formations with limited porosity, the sorption capacity of Bukov Chlorite Infills is notably substantial. These characteristics underscore the geochemically advantageous features of Bukov Chlorite Infills and their potential role as a sorption buffer within the infill region.

2.3.3 Sorption of Ni

2.3.3.1 Calcite (Nickel Sorption Studies on Bukov Calcite Infill: Unified Effort of Multiple Institutes Employing their Distinct Methodologies)

As mentioned in Chapter 1.3.3.1 and in previous agreements between institutions, the extracted material, Bukov Calcite Infill, underwent additional processing and was distributed from UJV among the participating institutions. Its purpose was to be prepared and used in experiments investigating the sorption of nickel. The specific steps taken to prepare the material before conducting characterization and sorption experiments are described in Figure 2-19, and a detailed explanation of the material preparation procedures prior to the experiments can be found in Chapter 1.3.3.2.

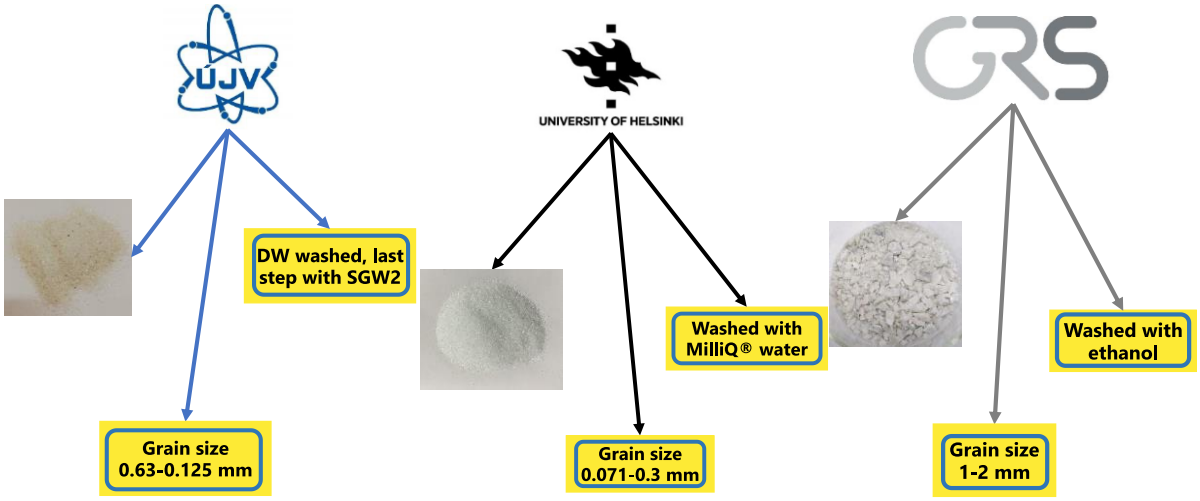

Figure 2-19 Preparation of Bukov Calcite Infill for sorption experiments conducted by collaborating institutes

It is observable that the preparation of the Bukov Calcite Infill material varied among the different institutions involved. While the same material was employed for the experiments, each institution utilized distinct granular sizes and employed different rinsing processes. Further details regarding the material preparation protocols can be found in Chapter 2.2.1.1 for GRS, Chapter 2.2.1.2 for the University of Helsinki, and Chapter 2.2.1.3 for UJV. Additionally, each institution conducted a certain level of characterization on the prepared Bukov Calcite Infill. A diagram, depicted in Figure 2-20, provides a comprehensive description of the analyses conducted on the material prior to the nickel sorption experiments. For a comprehensive understanding of these methods, individual descriptions provided by each institution can be found in Chapter 2.2.1.1 for GRS, Chapter 2.2.1.2 for the University of Helsinki, and Chapter 2.2.1.3 for UJV.

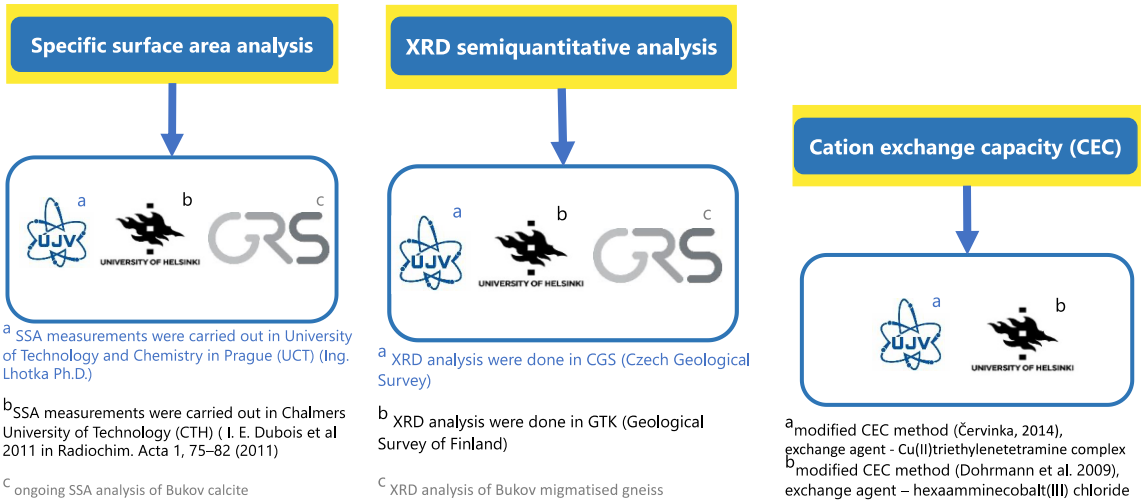

Figure 2-20 Diagram representing the characterization of Bukov Calcite Infill conducted by collaborating institutes

The analysis of the specific surface area and mineralogical composition of the prepared materials by UJV and the University of Helsinki reveals distinct characteristics. Variations in the treatment process account for a significantly higher surface area of Bukov Calcite Infill prepared by the University of Helsinki. Despite this difference, both UJV and the University of Helsinki observed a remarkably similar mineralogical composition for the prepared materials. Furthermore, considering the disparities in the measured surface area, a sample exchange was conducted, and the specific surface areas of the respective materials were measured by both institutions for cross-laboratory comparison, as depicted in Figure 2-21. It is noteworthy that comparable surface areas were observed between Bukov Calcite Infill prepared by UJV and pure calcite prepared by the University of Helsinki. However, a considerable variation in the measured specific surface area was observed for Bukov Calcite Infill prepared by the University of Helsinki, likely stemming from the distinct preparation process and the utilization of the BET method.

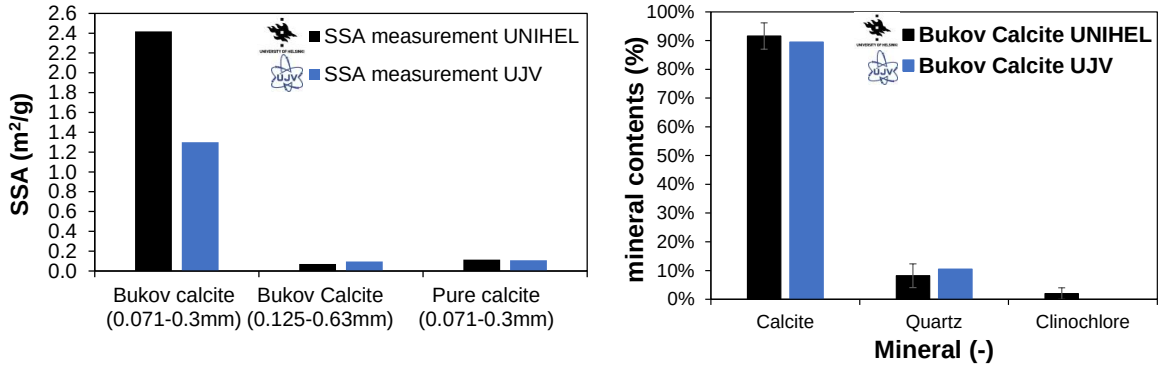

Figure 2-21 Determination of the specific surface area of Bukov Calcite Infill as measured by UH and UJV (left), accompanied by an analysis of the sample's mineralogical composition (right)

As previously mentioned, the characterization of Bukov Calcite Infill was performed in anticipation of its subsequent utilization in nickel sorption experiments conducted by GRS, UH, and UJV institutions. Given that each institution employed distinct conditions for the sorption experiments, followed by variations in their execution, a diagram illustrating the specific sorption experiment conditions for each institution is displayed in Figure 2-22. It is important to note that a comprehensive description of the experimental conditions and execution of the sorption experiments can be found in Chapter 2.2.1.1 for GRS, Chapter 2.2.1.2 for UH, and

Chapter 2.2.1.3 for UJV. Furthermore, apart from the different sorption experiment conditions, variations were observed in the execution of the experiments and the resultant distribution coefficients among the institutions. These differences are elucidated in Figure 2-22, with detailed descriptions provided in Chapter 2.2.1.1 for GRS, Chapter 2.2.1.2 for UH, and Chapter 2.2.1.3 for UJV.

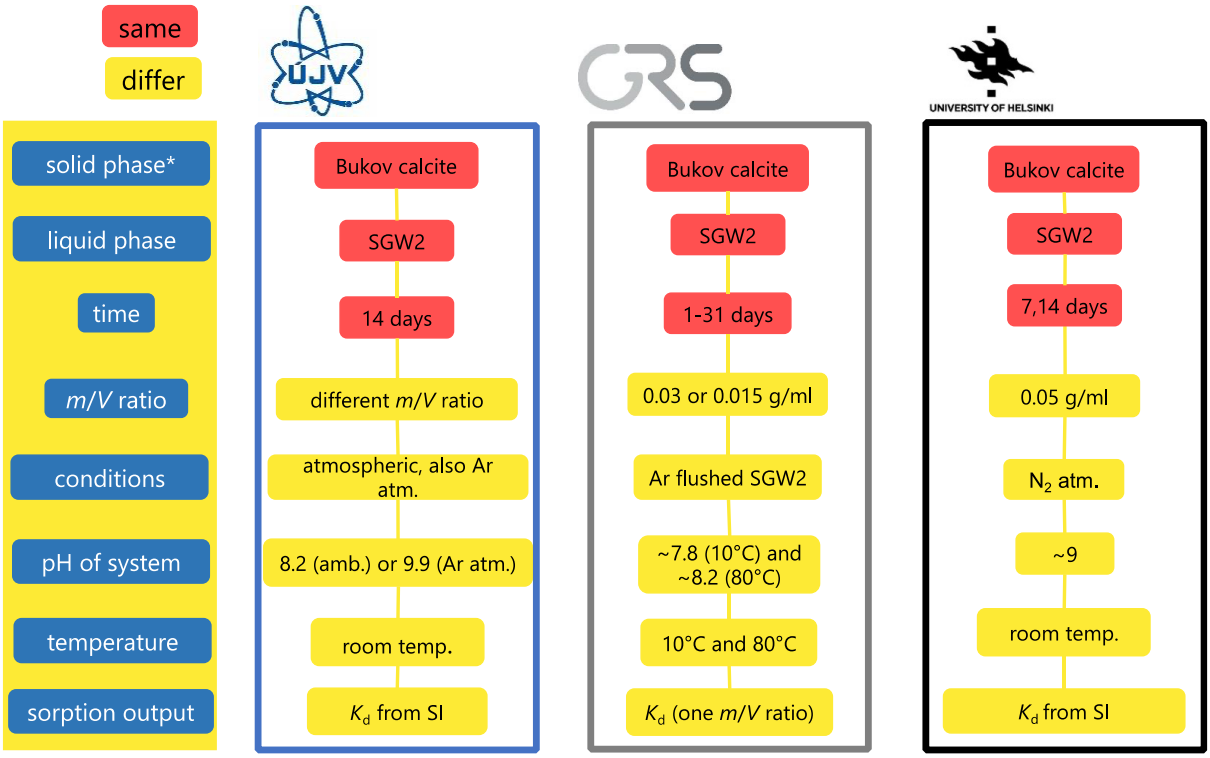

*Sorption exp. also done with migmatised gneiss (GRS,UJV) and Brazilian pure calcite (UniHel)

Figure 2-22 Schematic representation of batch sorption experiments conditions conducted by collaborating institutes

The provided diagram in Figure 2-22 demonstrates the consistent use of the SGW2 liquid phase in all instances. The interaction time for the sorption experiments was approximately uniform across the participating institutions, either through periodic sampling at predetermined time intervals (e.g., UJV at 14-day intervals) or by examining the kinetic profile of the Ni sorption process (e.g., GRS from day 1 to day 31). The choice of sorption experiment methodology led to variations in the mass-to-volume (*m*/*V*) ratio. UJV implemented a method involving changes in the m/v ratio for subsequent determination of the linear isotherm and resulting distribution coefficient, in contrast to GRS and UH, where a single or two m/v ratios were employed.

As mentioned before, each institution employed different methodologies for conducting the sorption experiments. These methods ranged from omitting the addition of any active Ni carrier (as done by GRS) to using only active ^{63}Ni without incorporating inactive carriers (UH), or employing both active and inactive carriers at a concentration of $1x10^{-5}$ mol/L (as performed by UJV). Furthermore, the distribution coefficients were obtained through a singular m/V ratio (GRS), sorption isotherms with varying concentration ratios (UH), and from the slope of the linear isotherm with changing *m*/*V* ratio (UJV). A comprehensive description of the quantitative analysis of Ni in the sorption experiments is provided in Chapter 2.2.1.1 for GRS, Chapter 2.2.1.2 for UH, and Chapter 2.2.1.3 for UJV.

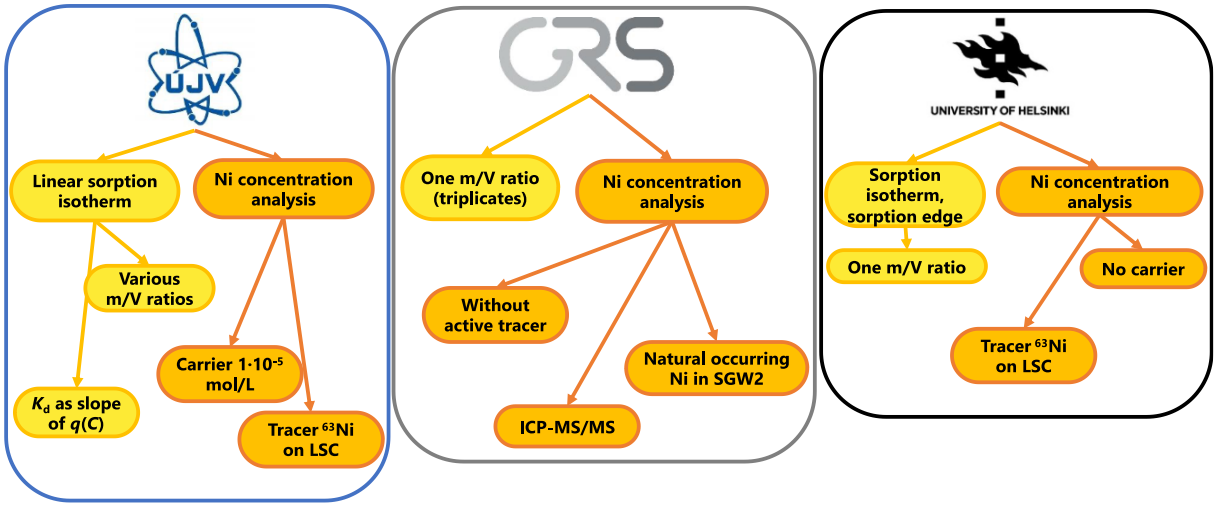

Figure 2-23 Comprehensive Methodologies employed in the execution of batch sorption experiments by collaborative institutes

The resulting distribution coefficients for Ni sorption on Bukov Calcite Infill by each institution were subsequently compared under varying pH and initial concentrations, as illustrated in Figure 2-24. It can be observed that the sorption of Ni on Bukov Calcite Infill prepared by UH becomes essentially constant from pH 8 onwards, reaching a certain plateau value for the distribution coefficient, with no significant increase in sorption with higher pH levels. In comparison, when comparing the values at comparable initial concentrations, the results obtained by GRS and UH exhibit similarities, while UJV shows lower values due to the utilization of a higher concentration of inactive Ni carrier. Regarding UJV, considering the preparation method and the measured specific surface area derived from the grain size, it becomes evident that the distribution coefficients are slightly lower than those obtained by GRS and UH. Above all, the study demonstrates the pronounced sorption capacity of Ni on calcite within the SGW2 water environment. Furthermore, all institutions have substantiated that the naturally acquired calcite infill, following appropriate modifications, exhibits a significant sorption capability for Ni, akin to other examined rock samples.

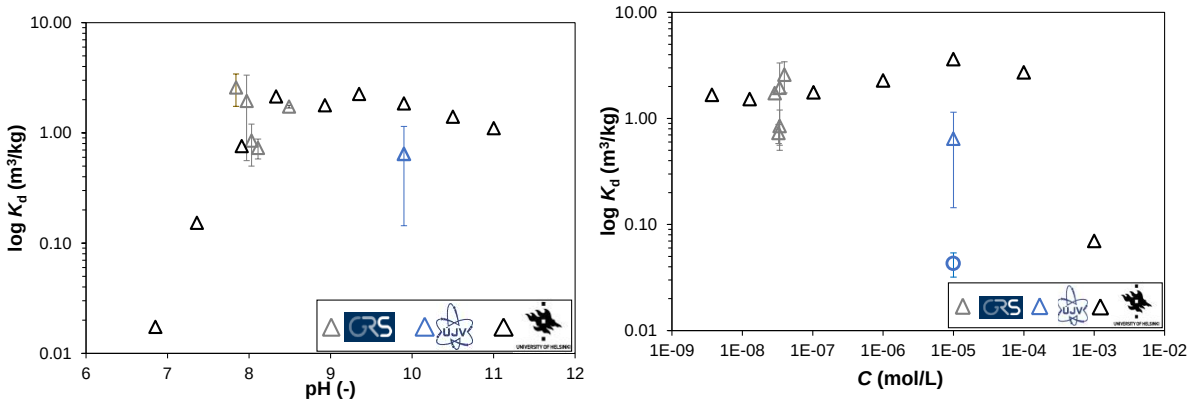

Figure 2-24 Distribution coefficients of nickel on Bukov Calcite Infill: findings by GRS (represented by grey triangles), University of Helsinki (black triangles), and UJV (blue triangles), analyzed across a pH range (left) and various initial nickel concentrations (right)

2.3.3.2 Host rocks from Bukov URF

Evaluating the Sorption Characteristics of Nickel on Bukov URF Materials under Diverse Experimental Conditions (UJV)

After conducting preliminary experiments with Bukov migmatized gneiss PVP-2 and synthetic calcite, we selected the most appropriate methods for sorption experiments to determine distribution coefficients of the calcite infill and other utilized materials. The detailed extraction and preparation procedures of the calcite infill and other materials from Bukov URF are described in Chapter 1.3.3. The distribution of the Bukov Calcite Infill extended beyond UJV, as it was also provided to GRS and UH for conducting batch sorption experiments using their respective methodologies. In Chapter 2.3.3.1, we aimed to integrate and compare our sorption results for nickel on the calcite material. Moreover, for a comprehensive characterization of the complex system and an exploration of the sorption affinity of cesium and nickel on various minerals in complex rock samples, host rocks bearing biotite, plagioclase, and amphibole minerals were carefully extracted and prepared. Additionally, sorption experiments were conducted on chlorite infills with high chlorite and kaolinite contents (see Chapter 1.3.3). Overall, our investigation focused on assessing the sorption capabilities of calcite infills in comparison to rocks with different compositions within the Bukov URF rock formation, aiming to simulate the realistic in situ conditions of a hypothetical deep geological repository for radioactive waste. The distribution coefficients, which quantify the partitioning of substances under specific conditions, are documented in Table 2-13. Additionally, Figure 2-25 visually represents the data on the quantity *q* associated with the linear isotherm observed in relation to *concentartions*.

Table 2-13 The distribution coefficients for Bukov Calcite Infills, enriched host rocks and for Bukov Chlorite Infills under specific sorption experimental conditions. Additionally, the provided information includes the standard deviations of the distribution coefficients, the R2 values that indicate the adequacy of fit for the linear isotherm model, and the average percentage of sorption derived from a range of m/V ratios

Conditions	**Material**	**K_d (m^3/kg)**	**R^2**	**Sorption (%)**	**Sorption % highest-lowest from the *m/V* ratio range**
Ambient atmosphere, SGW2	Bukov Host rock with high plagioclase contents	1.238 ± 0.117	0.957	99.50 ± 0.16	99.31-99.55
Ambient atmosphere, SGW2	Bukov Host rock with high amphibole contents	0.401 ± 0.018	0.994	98.49 ± 0.60	98.14-98.73
Ambient atmosphere, SGW2	Bukov Host rock with high biotite contents	2.756 ± 0.306	0.942	99.78 ± 0.06	99.73-99.81
Ambient atmosphere, SGW2	Host rock of Bukov Calcite Infill	0.978 ± 0.039	0.994	99.39 ± 0.18	99.05-99.57
Ar atmosphere, SGW2		2.648 ± 0.212	0.975	99.78 ± 0.07	99.68-99.85
Ambient atmosphere, SGW2	Bukov Calcite Infill with adrock mixture	0.351 ± 0.059	0.922	98.62 ± 0.47	97.95-98.85
Ambient atmosphere, SGW2	Bukov Calcite Infill	0.043 ± 0.004	0.953	89.07 ± 7.92	80.59-95.24
Ar atmosphere, SGW2		0.515 ± 0.092	0.887	98.81 ± 0.17	98.80-98.98

Ambient atmosphere, SGW2	Bukov Chlorite Infill extracted from 1.site	0.837 ± 0.008	0.999	99.33 ± 0.28	98.84-99.63
Ar atmosphere, SGW2		1.932 ± 0.124	0.984	99.72 ± 0.17	99.56-99.81
Ambient atmosphere, SGW2	Bukov Chlorite Infill extracted from 2.site	1.187 ± 0.018	0.999	99.40 ± 0.28	99.21-99.59
Ar atmosphere, SGW2		2.947 ± 0.175	0.986	99.78 ± 0.11	99.70-99.82

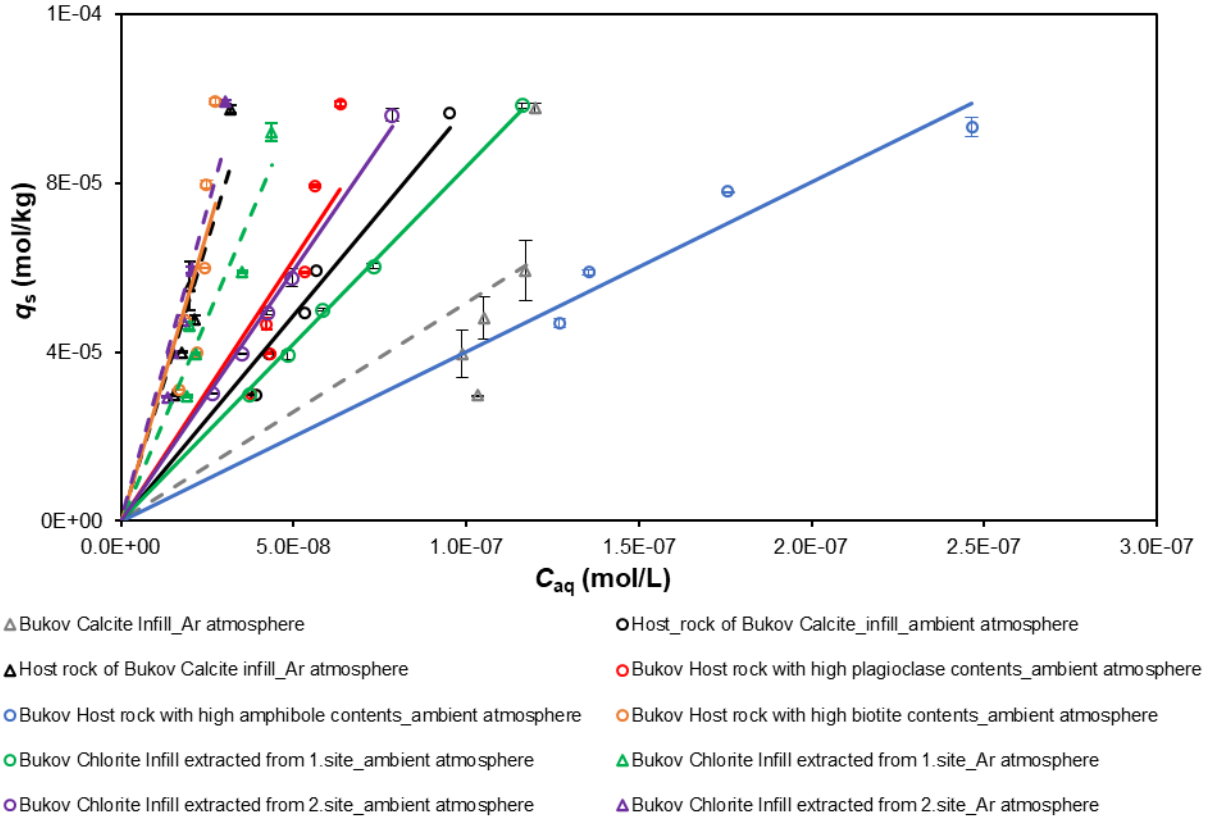

Figure 2-25 Distribution of nickel between Bukov materials and SGW2 after 14-day interaction: linear sorption isotherm-based determination of distribution coefficients under aerobic and anaerobic conditions

The Bukov Calcite Infill, shows the lowest extent of nickel (Ni) sorption under aerobic conditions, when compared with other materials. Other Bukov materials, however, demonstrate higher sorption parameters, with distribution coefficients for Ni surpassing the threshold of 0.3, indicating a sorption rate exceeding 99%. Interestingly, upon further examination, the sorption of Ni across different Bukov host rocks has negligible variance, as indicated by the slight differences in the detection counts of the measured ^{63}Ni. Such observations suggest that the sample heterogeneity, primarily driven by the mass-to-volume (*m*/*V*) ratios, is potentially a contributing factor to these phenomena. Further Ni sorption, evaluated at a concentration of 10^{-5} mol/L, shows no correlation with the derived Cation Exchange Capacity (CEC) measurements. This anomaly alludes to the potential presence of sorption sites for Ni that are uncorrelated, operating under the specific pH conditions represented by SGW2. In spite of their diverse mineralogical compositions, Bukov

host rocks uniformly manifest significant Ni sorption potential. The sorption sites in these host rocks are observed to be readily accessible to Ni, with no individual mineralogical compositions substantially impeding the sorption process. Among these, a host rock characterized by an enrichment of biotite exhibits the highest distribution coefficient. However, when viewed from a relative standpoint, this deviation is fairly minor - 0.5% when compared to Bukov host rock with a high plagioclase content, and a 1.7% variance when contrasted with a Bukov sample featuring an elevated amphibole content. Across a range of materials, the discrepancies in sorption remain insignificant, with a generalized sorption rate of approximately 99%. This rate, observed under specific particle size and SGW2 compositional conditions, supersedes that of Cs. This comparative analysis of Ni and Cs sorption rates could be used to further understand the role of ion size and valence in the sorption behavior. Bukov Calcite Infill, due to its superior sorption properties, holds its own against other host rocks and chlorite infills. Notably, despite the high Ni sorption, only minor alterations are observed under argon (Ar) atmospheric conditions, which could potentially modify the composition and inherent properties of SGW2 or the rock samples themselves.

Overall, all analyzed samples consistently exhibit high Ni sorption, thus indicating a potential for significant Ni sorption during the course of geochemical migration processes. This outcome further highlights the critical need for additional investigations focused on the temporal and spatial evolution of sorption sites under various geochemical conditions. Each sample exhibits a robust capacity for Ni sorption site accommodation, underscoring the importance of detailed characterization studies for a more comprehensive understanding of sorption dynamics in natural systems.

2.3.4 Sorption of Ra

2.3.4.1 Radium sorption on biotite

In the study, the experimental batch sorption results were interpreted with the geochemical modeling software PHREEQC, a commonly used modeling tool for aqueous, mineral, and gas condition applications (Parkhurst and Appelo, 2013). In PHREEQC modeling, the thermodynamic calculations of modeled reactions are based on thermodynamic database values for a given element. In the case of Ra, especially when compared to the more easily analyzable Ba, the reaction properties tend to be less well defined in available databases. As such, in this study, Ba was used as an analog for Ra in the modeling endeavor. The thermodynamic database of the Lawrence Livermore National Laboratory (LLNL) was used in the PHREEQC modeling part of this study.

Based on the DFT molecular modeling results obtained previously (Fabritius et al., 2022), it was determined that for surface complexation reactions on phlogopite there are 5.6 strong sites nm-2 on the frayed edge sites (FES) available for sorption reactions, and 5.6 weak sites nm-2 on the plane surface. For ion exchange reactions, there are 4.2 sites nm-2 available on the K+ layer edge of the phlogopite mineral. The sorption site densities limit the physical amount of sorption sites that are available for the sorption reactions of the solutions' cations. In the present study, the PHREEQC model uses the sorption site densities of phlogopite as analog for the whole rocks, as well. However, in an effort to upscale the model to better take into account the properties of the different tested rock types, in the modeling of sorption on each rock type the sample specific SSA and CEC was used. The SSA and CEC values provide limiting parameters for the magnitude of possible Ba sorption on the rock in the conditions of the Ra batch sorption experiments simulated in the model.

In the PHREEQC model, the sorption of Ba was represented by a combination of ion exchange and surface complexation on the sorbing surface. Cation exchange reactions were expressed as binary ion exchange following the Gaines-Thomas convention (Appelo and Postma, 2005):

$$M - K + \frac{1}{2}Ba^{2+} \leftrightarrow \frac{1}{2}Ba - M_2 + K^+$$

where the cation exchange sites (M-) are initially occupied by the phlogopite cation layer K+. The surface complexation part of the sorption model was characterized using the diffuse double layer model approach based on Dzombak and Morel (1990) (Li et al., 2018). The approach entails the use of two types of surface complexation sorption sites on the surface of phlogopite: strong sites on the mineral sheet edges (S_sOH) and weak sites on the lesser affinity plane surface (S_wOH), with following reactions were considered:

$S\_sOH + Ba^{2+} \rightleftharpoons S\_sOHBa^{2+}$

$S\_wOH + Ba^{2+} \rightleftharpoons S\_wOBa^{+} + H^{+}$

To further improve the fit of the modeled data on the experimental results, the employed PHREEQC model was combined with its Microsoft COM version Iphreeqc and the Python programming language to create a model optimization tool (Charlton and Parkhurst, 2011; Wissmeier and Barry, 2011; Parkhurst and Appelo, 2013; Li et al., 2018; Fabritius et al., 2022). In the employed optimization process, the optimal balance between the three considered sorption reactions (sorption as surface complexation on strong sites and weak sites, and ion exchange) as their respective log K parameters is calculated iteratively. The best possible fit of the experimental and modeled data is established by continuously recalculating previously set reaction parameters after each consecutive calculation step. If the fit is unsatisfactory, the fitting process is reinitiated with slightly different sorption reaction log K parameter values. With enough iterations, the most suitable fit is then selected based on the least-squares difference between the experimental and sorption reaction log K based modeled distribution coefficient data. In the modeling part of the present study, all tested rock/water combinations are modeled as separate exercises to ensure the best possible correspondence between the experimentally obtained K_d trends and modeled K_d.

In the batch sorption experiments, it was observed that Ra sorbed very well on biotite and the whole rocks with the magnitude of sorption correlating closely to the overall salinity of the reference groundwaters. The comparison of experimental and PHREEQC modeled distribution coefficient results of Ra sorption on biotite for ALLMR, OLGA, and OLSR are shown in Figure 2-26. In the three tested reference groundwater series, namely the fresh mildly reducing granitic ALLMR, fresh glacial meltwater OLGA, and saline reducing OLSR, the distribution coefficients of Ra were observed to decrease with the increasing Ba concentration and inherent salinity of the reference groundwater. In the lowest tested isotherm conditions of 2.6×10^{-9} M, where no $BaCl_2$ was added due to the desired concentration achieved solely with the spiked 200 Bq of ^{226}Ra, the distribution coefficients of Ra on biotite were 0.25 ± 0.09 $m^3\ kg^{-1}$, 0.17 ± 0.02 $m^3\ kg^{-1}$, and 0.014 ± 0.002 $m^3\ kg^{-1}$ for the experimented reference groundwaters ALLMR, OLGA, and OLSR, respectively. For the ALLMR, OLGA, and OLSR reference groundwaters, the expected decrease of distribution coefficients in the higher Ba isotherm concentration conditions is observed in the experimental results at the Ba concentration of 1×10^{-3} M: 0.048 ± 0.020 $m^3\ kg^{-1}$, 0.010 ± 0.002 $m^3\ kg^{-1}$, and 0.006 ± 0.003 $m^3\ kg^{-1}$, respectively. The pH values of the sorption samples tended to stabilize in the mildly acidic to neutral conditions: pH varied from 6.3 to 7.3 for selected ALLMR samples, 6.3 to 6.6 for OLGA, and 6.4 to 6.8 for OLSR.

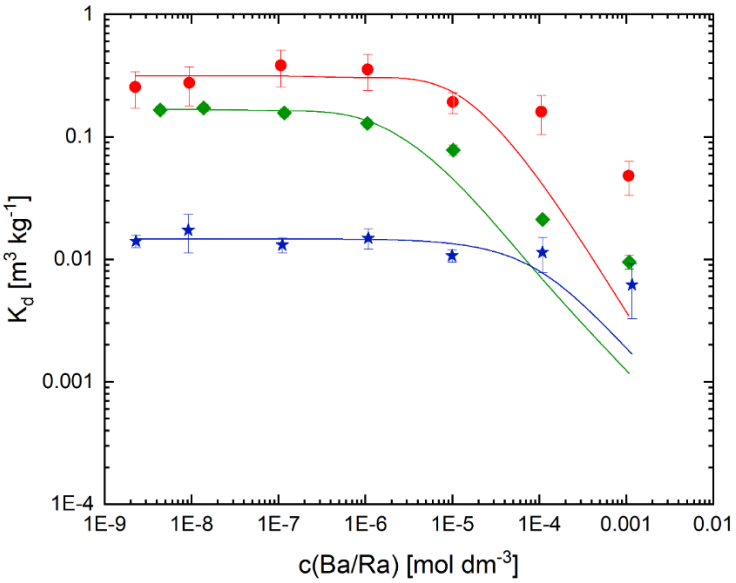

Figure 2-26 Sorption distribution coefficient of Ra on biotite as function of Ba/Ra concentration in pore water obtained in the fresh mildly reducing granitic pore water ALLMR (● red), fresh glacial meltwater OLGA (◆ green), and saline reducing reference groundwater OLSR (★ blue). Data points in the graph represent the averages of duplicate or triplicate samples. The curves (——) represent PHREEQC modeled data of the three experimental setups, color-coded respectively.

2.3.4.2 Radium sorption on gneisses and pegmatite granite by thin section autoradiography

Sorption experiments with ^{226}Ra were done on geological thin section samples of Olkiluoto mica gneiss in Allard reference water set to 10^{-7} M with $BaCl_2$. Barium concentration of 10^{-7} M was chosen for the experiments to simulate the natural levels of Ba at the disposal depth of the Olkiluoto region of the Baltic Sea (c. 10^{-7} to 10^{-5} M) (Vaaramaa et al., 2003; Hellä et al., 2014). After the sorption experiment, the thin section surface was scanned with a regular tabletop scanner, and analyzed with storage phosphor plate autoradiography and micro pattern gas detector BeaQuantTM autoradiography. Finally, the sample was analyzed with SEM/EDX to create elemental maps of the sample surfaces, which were used to determine the available minerals for sorption. A wide scale of elements was measured but for simplicity, the surface minerals were roughly identified thus: Si-dominating and other-elements-lacking areas as quartz; Na and Si strong areas as plagioclase; Na, Si, and K strong areas as K-feldspar; and Si, K, and Fe strong areas as micas. Employing this classification, for mica gneiss (Figure 2-27), a tripartite division was observed: the surface was found to be divided nigh equally between quartz, plagioclase and K-feldspar, and micas. Trace components of Ti and S-bearing minerals were observed. Due to the small size of individual mineral grains, satisfactory separation between plagioclase and K-feldspar, and between the different mica minerals, was unobtainable. In the analysis, mica minerals were not differentiated.

Comparing the thin section mineral maps and surface scans with the autoradiographs confirms the assessment that mica minerals primarily act as high affinity sorbents for Ra in mica-bearing rocks. On the mica gneiss, the ^{226}Ra activity hotspots and spread visible in the autoradiographs correspond well with the red mica spots of the SEM/EDX images and the dark micas of the surface scans. In the phosphor plate autoradiography, the activity hotspots are seen as dark spots in the image, whereas on the BeaQuantTM autoradiograph, the activity concentration is represented as a color scale. On mica gneiss, where the micas

are very evenly divided along the thin section surface, ^{226}Ra is also more widely spread, though contained mainly on the mica grains. The even spread of micas makes it challenging to estimate sorption on other minerals species, such as on K-feldspar or plagioclase. Clearly observable from the rock sample is the lack of meaningful Ra sorption on quartz. Activity analyzing the BeaQuantTM autoradiographs, the larger quartz grains were found to be devoid of ^{226}Ra activity, or only had very small amounts of activity just above the detection limit. Based on the results, the four rock minerals in focus can be roughly ordered based on their affinity to sorb Ra, from highest to lowest: micas (biotite and muscovite), plagioclase, K-feldspar, and quartz. The results are in very good agreement with the previous study by Muuri et al., (2018), where Ba (as analog to Ra) sorption on quartz, plagioclase, K-feldspar, and biotite was studied with batch sorption experiments.

Using the residual ^{226}Ra activity in the used sorption solutions and wash solutions (measured in gamma detection), and the retained ^{226}Ra on the thin section surface (measured in alpha spectrometry), distribution coefficients K_d were first calculated for the whole thin section sample surface:$(5.6 \pm 1.1) \times 10^{-3}$ m^3 kg^{-1} for mica gneiss. Even though the solid-to-solution ratios between the batch sorption and thin section sorption experiments were similar, 50 g l^{-1} and 40 g l^{-1}, respectively, due to the differences of the sample types, the K_d results between the two methods in question are not directly comparable. The ALLMR reference water is a modification of the more common Allard reference water, and thus the two have very similar chemical compositions. Ergo, at least in this limited sense, the K_d results of the mica gneiss rock in thin section sorption experiments agree well with the batch sorption experiments. The sample series can be further compared with the area distribution coefficient (K_a) results. For the thin section sample, using the rough area of the active surfaces of the thin section sample (surface area that was under the ^{226}Ra sorption solution), following K_a value was obtained: $(6 \pm 2) \times 10^{-3}$ m^3 m^{-2} for mica gneiss. As can be seen in the mass distribution coefficients of the thin section and the batch sorption results, the results of the two samples types in K_a are highly similar with each other. For mica gneiss, the batch sorption Ka, $(1.5 \pm 0.3) \times 10^{-3}$ m^3 m^{-2}, is within the same order of magnitude but somewhat lower than the thin section value would suggest. The reason for this discrepancy might be that the simple geometrical area of the thin section active surface does not perfectly represent the actual available surface for sorption reactions for different rock types. Even if the thin section sample is very thin (25 µm), the thickness should be considered non-negligible.

With the quantitative ^{226}Ra activity results of the BeaQuantTM autoradiography and the corresponding mineral map of the surface, mineral specific distribution coefficients of Ra sorption were calculated. For mica gneiss, five different spots on the BeaQuantTM autoradiograph (Figure 2-27) were sufficiently well identified mineral-wise for heterogeneous K_d calculations: a and b represent micas; c and d combined phases of plagioclase and K-feldspar; and e quartz. Mineral-specific K_d was estimated thus: 0.033 ± 0.008 m^3 kg^{-1} for micas; $(3.3 \pm 0.5) \times 10^{-3}$ m^3 kg^{-1} for the combined phase of plagioclase and K-feldspar; and $(7 \pm 2) \times 10^{-4}$ m^3 kg^{-1} for quartz. The obtained K_d results agree well with the previously established qualitative order of minerals for the sorption affinity of Ra. As the mineral specific K_d of Ra was challenging to determine due to the small size of the mineral grains, and the subsequent roughness of the region of interest (ROI) selection, one must consider each of the selected BeaQuantTM areas to have at least some 'contamination' of the competing minerals in them, affecting the accuracy of the calculated K_d. This effect was factored in the uncertainties of the mineral specific K_d.

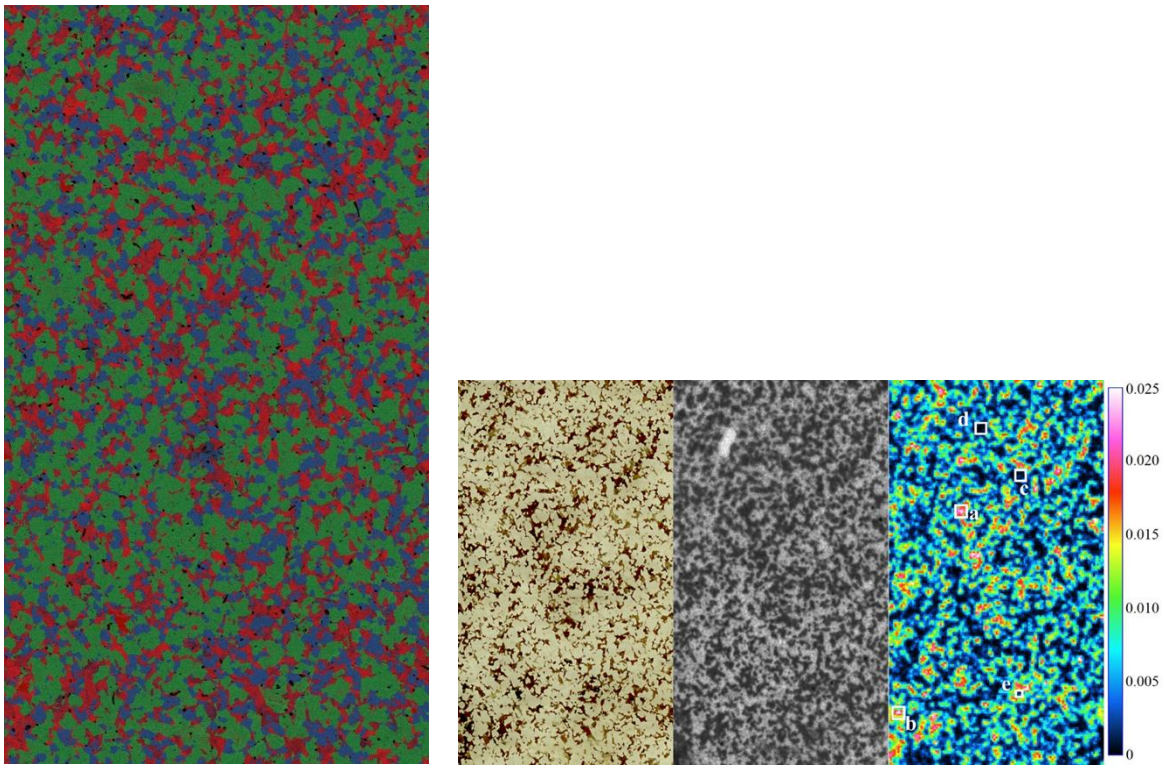

a. SEM/EDX for mineralogy b. Surface scan – phosphor plate AG – BeaQuant™ AG

Figure 2-27 Comparison of thin section sorption study results for mica gneiss. Images have been arranged thus: a) SEM/EDX elemental analysis; and b) corresponding surface scan (left), the corresponding phosphor plate autoradiograph (center), and the corresponding BeaQuant™ autoradiograph (right). Scale on the right indicates sorbed ^{226}Ra activity concentration in units of Bq/pxl (pixel size 100 × 100 µm). All images are aligned and scaled to show the same region of the sample surface. Region dimensions are 11.4 × 20.3 mm. SEM/EDX elemental analysis legend and identified mineral species: blue Si (quartz), green Na, and Si (K-feldspar and plagioclase), and red Mg, Fe, and Si (micas). Notations **a-e** denote locations of mineral specific K_d analysis.

2.3.5 Sorption of Se

Selenium(IV) sorption was conducted on various materials, including Grimsel granodiorite and the main minerals of Grimsel granodiorite (plagioclase, biotite, quartz and K-feldspar). Former researchers found that the Se(IV) sorption on biotite can be representative of the total Se(IV) sorption in complex mineral assemblages such as Grimsel granodiorite. Thus, to quantitatively predict the Se(IV) sorption in groundwater conditions of a deep geological repository, a surface complexation model of Se(IV) sorption on biotite with one type of strong sorption sites and two types of weak sorption sites was developed based on experimental data obtained from titration, sorption edge and sorption isotherm experiments.

2.3.5.1 Se(IV) sorption on Grimsel granodiorite and its main minerals

The K_d of Se(IV) sorbed on crushed Grimsel granodiorite and its main minerals are shown in Figure 2-28. The whole rock and mineral samples (except for quartz) have a trend that the K_d values increase with the decrease of selenite concentration. In the high concentration area (10^{-6} M to 10^{-3} M), the K_d values of all the rock samples remained almost the same, which is caused by insufficiency of free sorption sites.

The K_d of Se(IV) sorption on biotite increased dramatically in the low concentration area (10^{-10} M to 10^{-7} M), showing that biotite is the most favored mineral for Se(IV) sorption among all the main minerals of Grimsel granodiorite. The K_d values stabilized between 0.0595±0.0097 m^3/Kg and 0.0713±0.0164 m^3/Kg when the concentrations were lower than 10^{-7} M. The large amount of sorption on biotite was caused by its sheet structure which results in the distinctively largest SSA among all of the rock samples. It has been observed by E. Muuri et al. that there is a linear trend of the distribution coefficient magnitudes according to the magnitudes of specific surface area (Muuri et al., 2017).

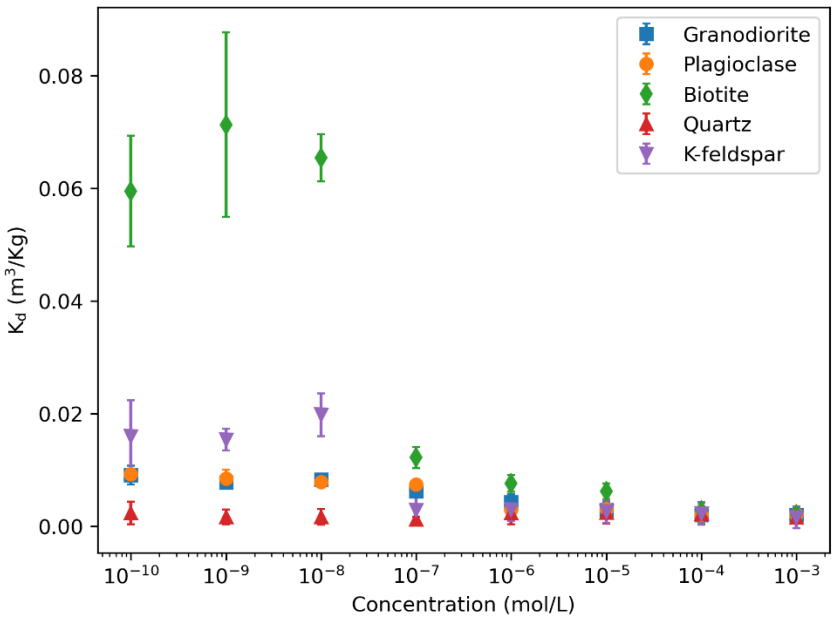

Figure 2-28. Sorption of Se(IV) on Grimsel granodiorite (GG) and its main minerals (■,Grimsel granodiorite; ●, plagioclase; ♦ , biotite; ▲, quartz; ▼, K-feldspar) depending on Se(IV) concentrations from 10^{-10} M to 10^{-3} M in a background solution of Grimsel groundwater simulant. (a): Kd values as a function of Se(IV) concentration; (b): the SSA corrected Kd values as a function of Se(IV) concentrations.

Se(IV) has the second largest K_d values on K-feldspar in the low concentration area, though the K_d values are about 4 times lower than those on biotite. The relatively high K_d values of Se on K-feldspar than on plagioclase and Grimsel granodiorite, which have similar mineral structures as K-feldspar, might

be due to the inhomogeneity of the samples as the K-feldspar was only 90 % pure and some impurities which have high selenium sorption abilities might exist. The K_d values of Se(IV) on quartz were found to be negligible in the whole concentration areas. This is due to the very small SSA of quartz resulting in the scarce of sorption sites.

The K_d values of Se(IV) on Grimsel granodiorite and plagioclase are almost the same through the whole concentration range whereas the one on K-feldspar is about twice as high. If we compare the compositions of Grimsel granodiorite and plagioclase, one can find the similarities of these two samples. 65% of Grimsel granodiorite is composed of feldspar group minerals (40% plagioclase and 25% K-feldspar) together with 20% of quartz,10% of biotite and 5% of chlorite. In the plagioclase mineral sample, 80% are feldspar group minerals (75% plagioclase and 5% K-feldspar) with 5% biotite and other minerals like quartz and amphibole in low concentrations. The main compositions of these two samples are feldspars (plagioclase and K-feldspar) while the difference is that Grimsel granodiorite has 20% of quartz and 5% of biotite. The quite similar sorption behaviours of Se(IV) on Grimsel granodiorite and plagioclase indicates that the influence of 20% of quartz in Grimsel granodiorite was compensated by the surplus of biotite. This also results in the very similar specific surface area values of them. The K_d values for both Grimsel granodiorite and plagioclase didn't change much in low concentrations range and they varied between 0.0062±0.0003 m^3/Kg to 0.0093±0.0003 m^3/kg.

There is a linear relation between specific surface area and the K_d values among all the rock samples, as can be seen in Figure 2-29. Though biotite has the largest sorption capacity compared with the other rock samples, the specific surface area corrected K_d values of Se(IV) on biotite are quite similar with the ones for Grimsel granodiorite and plagioclase. This proves that the high sorption ability of biotite comes mainly from its high specific surface area which provides more sorption sites for Se on biotite. The sorption ability of quartz is still the smallest even corrected with specific surface area. The reason of this can be found in the crystalline structure of it. The relative stabilities of primary silicates have an increasing relation with the increasing Si to O ratio which continues through the amphiboles (0.364), the micas (0.4) and to the tectosilicates (0.5) (Essington, 2015). Quartz is one member of the tectosilicate family and it is composed of a three-dimensional network of Si tetrahedron in which each oxygen atom is shared by neighbouring tetrahedron. In the structure of quartz, all the tetrahedrons share their four O^{2-} with the neighbouring tetrahedrons. The maximum sharing of oxygen atoms imparts greater structural stability as a result of the high percentage of covalent character in the Si—O bond. This means that the surface of quartz is quite inactive and not easy to react with other ions, imparting the high stability of quartz.

According to the theory mentioned above, the sorption of Se(IV) ions can be roughly described in the following sequence: tectosilicates < phyllosilicates < inosilicates (Essington, 2015; Söderlund et al., 2015). This sequence can be shown clearly in Figure 2-29 as the distinctive larger K_d value of selenium on biotite than the other four samples, because biotite is a member of phyllosilicate while plagioclase, K-feldspar and quartz are the members of tectosilicate. 85% of Grimsel granodiorite are composed of tectosilicate minerals (40% plagioclase, 25% feldspar, 20% quartz, see Table 5), so Grimsel granodiorite can be roughly grouped to the tectosilicate family when we discuss about the results of this experiment.

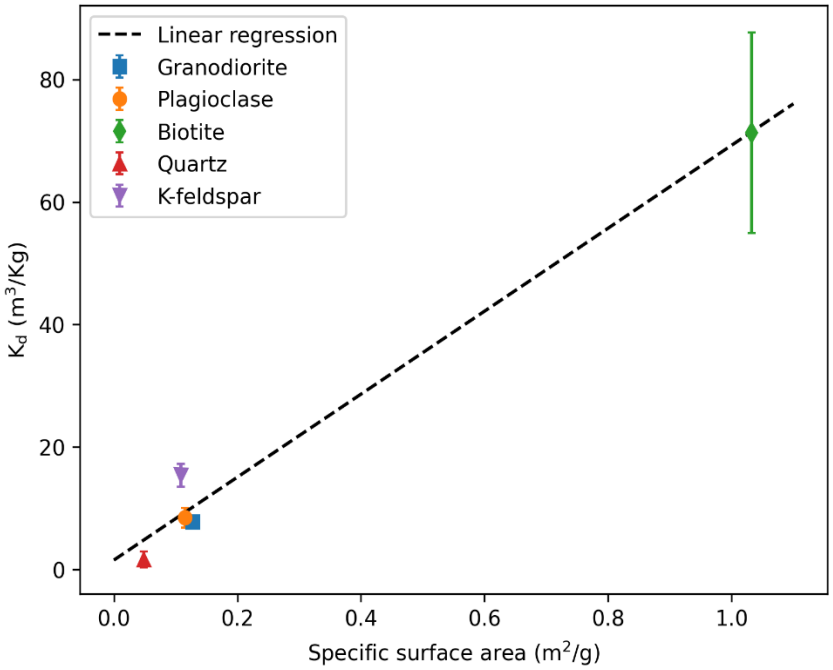

Figure 2-29. Distribution coefficients of Se(IV) on Grimsel granodiorite and its main minerals as a function of their specific surface area in 10^{-9} M Se(IV) concentration.

2.3.5.2 Surface complexation modelling of Se(IV) sorption on biotite

The experimental studies in the above Section 2.3.5.1 have shown that biotite has much larger specific surface area than the other main minerals of granite and granodiorite and the Se sorption on biotite can, basically, represent its sorption on the whole bedrock. The result was also proved by other researches (Yang et al., 2018). Thus, this aim of this section is to develop a multi-site surface complexation model for Se(IV) sorption onto biotite based on experimental data to assess the sorption behavior of Se(IV) onto biotite and granite rock samples. A batch forward titration combined with backtitration method was used to overcome the problem of mineral dissolution in order to measure the pKs of protonation and deprotonation reactions of sorption sites on surfaces of biotite. Molecular modelling was used to obtain some basic modelling parameters, such as site densities and site types. The technique of PHREEQC coupling with Python was used to calculate and optimize the fitting processes.

Titration

In the studies of mineral surface site capacities and intrinsic surface protonation and deprotonation constants for amphoteric $\equiv SOH$ type surface sites, batch forward titration combined with the backtitration of the supernatants is more favored instead of continuous titration. The main problem of continuous titration is that it ignores the H^+/OH^- consumption arising from the dissolution of minerals, which is quite significant at extreme pH values (pH >10 and pH < 5). The ignorance of mineral dissolutions, together with other proton consuming or releasing mechanisms (such as proton and cation exchange reactions that we will show later) will cause two high H^+/OH^- consumption in extreme pH areas.

To overcome the problem of mineral dissolution during titration, researchers pointed out a batch backtitration method which could compensate the amount of mineral dissolved (Baeyens and Bradbury, 1995b, 1995a; Bradbury and Baeyens, 1995; Schulthess and Sparks, 1986). In this method, the supernatants from forward titration samples are back-titrated to a common end point. The quantities of acid or base consumed in the backtitration are subtracted from the quantities of the base or acid consumed in the forward titration. The theory can be explained by the following. In our case, biotite, in

the minerals composition of $(KMg_{1.76}Fe_{0.7}Ti_{0.54})(Al_{1.08}Si_{2.92}O_{10})(OH_{0.44}F_{0.56}O)$, will dissolve in forward titration process and the dissolution reaction can be described by

$$(KMg_{1.76}Fe_{0.7}Ti_{0.54})(Al_{1.08}Si_{2.92}O_{10})(OH_{0.44}F_{0.56}O) + 1.32H_2O + 8.6H^+ \Leftrightarrow$$

$$K^+ + 1.76Mg^{2+} + 0.7Fe^{2+} + 0.54TiO_2 + 1.08Al^{3+} + 2.92H_4SiO_4 + 0.56F^-$$

8.6 mol H^+ are consumed by the dissolution of 1 mol biotite. In the backtitration, OH^- is consumed by the reaction products to reach a neutral pH and the following species are formed:

$$K^+ \Longrightarrow K^+$$

$$1.76Mg^{2+} \Longrightarrow 1.76Mg^{2+}$$

$$0.7Fe^{2+} + 1.4OH^- \Longrightarrow 0.7Fe(OH)_2$$

$$0.54TiO_2 \Longrightarrow 0.54TiO_2$$

$$1.08Al^{3+} + 3.24OH^- \Longrightarrow 1.08Al(OH)_3$$

$$2.92H_4SiO_4 \Longrightarrow 2.92H_4SiO_4$$

$$0.56F^- \Longrightarrow 0.56F^-$$

4.64 mol OH^- are consumed by backtitration to neutral pH. This leaves 3.96 mol H^+ per mol of dissolved biotite not accounted for by backtitration. This part of H^+ should be added to the backtitration data.

Similarly, in the basic direction, 2.96 mol OH^- are consumed by the dissolution of 1 mol biotite while 6.92 mol H^+ are consumed by backtitration, indicating 3.96 mol H^+ more are consumed in the backtitration.

The chemical analysis results of Si and Al in the supernatants after titration show that the concentrations of Si and Al rise sharply at pH ≤ 5 and pH ≥ 10 (Figure 2-32), indicating severe dissolution of biotite in the extreme pH conditions. The amounts of Si and Al remain constant at neutral pH (pH 6 ~ 8), which could be regarded as the background concentrations of these two elements. Thus, the difference between the concentrations of Si and Al at pH ≤ 5 and pH ≥ 10 and the background concentrations could be considered as the dissolved amounts of these two elements. Based on these assumptions together with the batch titration theory mentioned above, the correction of the H^+ and OH^- consumed in the backtitration can be calculated.

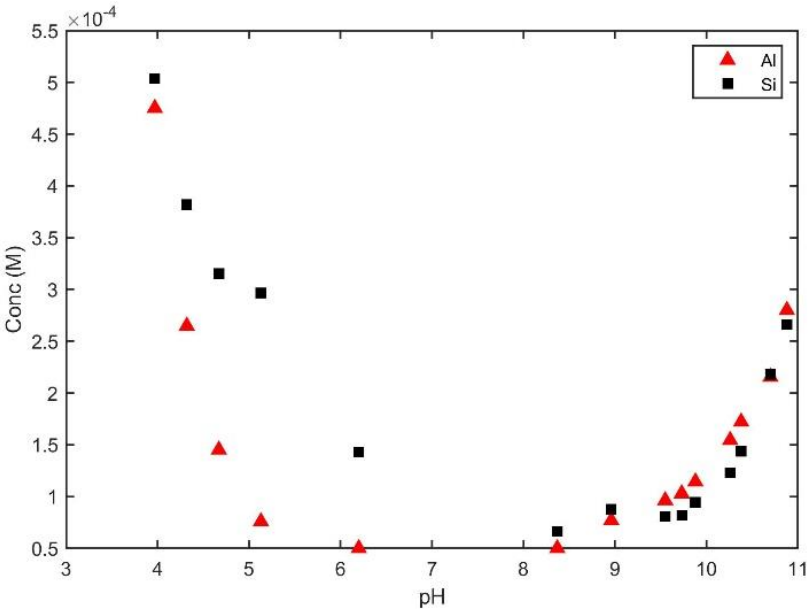

Figure 2-30. Concentration of Al and Si elements in supernatants as a function of pH after forward titration of converted biotite in 0.01 M $KClO_4$.

However, the whole H^+/OH^- consumption in the batch forward titration can not be compensated by just backtitration, especially in the extreme pH regions. Other factors, mainly proton exchange and cation exchange reactions between the dissolved cations and the biotite surface K^+, have effects on the titration process as well. If we simplify the biotite mineral as $M(OH)_3$, the process of cation exchange can be described by the following:

In the forward titration, $M(OH)_3$ dissolves and consumes H^+:

$$M(OH)_3+3H^+ \Leftrightarrow M^{3+}+3H_2O$$

In the backtitration, dissolved M^{3+} ions are titrated to the neutral pH:

$$M^{3+}+3OH^- \Leftrightarrow M(OH)_3$$

In the ideal situation, the amount of OH^- consumed could indicate all the amount of H^+ consumed by mineral dissolution. However, the fact is that, part of the M^{3+} will exchange with the surface K^+ and will be removed from the solution. The reaction can be written as:

$$3K\_biotite+M^{3+} \Leftrightarrow M\_biotite+3K^+$$

For example, Puhakka and Olin studied the cation exchange reactions of Ni^{2+} with the K^+ on the iron-rich biotite (annite) surfaces. The results show that K^+ will be replaced by Ni^{2+} on the basal surfaces of biotite (Puhakka and Olin, 2014).

The exchanged cations will not be accounted for by the backtitration. Following Gaines & Thomas convection (Gaines and Thomas, 1953), the ion exchange selectivity coefficient is defined by:

$$K_{N/M}^{G-T}=\frac{[M_{biotite}][K^+]^3}{[K_{biotite}]^3[M^{3+}]}$$

where $[M_{biotite}]$ and $[K_{biotite}]$ represent the equivalent fraction of the corresponding sites. $[K^+]$ and $[M^{3+}]$ are the concentrations of different cations.

Similarly, the proton exchange reaction can be described by:

$$K\_biotite+H^+=H\_biotite+K^+$$

and the selectivity coefficient can be defined by Gaines & Thomas convection as shown above.

By recording the cation exchange abilities of different cations with K^+ on biotite surface, the corresponding selectivity coefficients of the cation exchange reactions could be measured (Table 2-14). The selectivity coefficient of the proton exchange reaction is assumed to be one, since the study of the exchange reactions of hydrogen ions is greatly complicated because of the instability of the mineral. This assumption was also adopted by other researches (Bradbury and Baeyens, 2009a, 2009b; Gilbert and Laudelout, 1965).

Table 2-14. Cation exchange reactions of the dissolved cations with biotite surface K^+ and the calculated selectivity coefficients according to the Gaines and Thomas convection.

Cation exchange reaction	Selectivity coefficients (K)
K-biotite + H^+ = H-biotite + K^+	1 (logK=0)
K-biotite + Na^+ = Na-biotite + K^+	3.4
2K-biotite + Mg^{2+} = Mg-biotite + $2K^+$	0.16
2K-biotite + Ca^{2+} = Ca-biotite + $2K^+$	0.17

3K-biotite + Al^{3+} = Al-biotite + $3K^{+}$	0.59

The CEC of converted biotite was determined by checking the end point of the cation exchange curve of Al^{3+} which has the largest cation exchange ability. There is a clear trend that the quantity of cation exchange ions is going to be saturated at the end point region (Figure 2-31). A CEC value of 19.5 meq/kg was estimated and used in the selectivity coefficients calculations. The CEC value measured by ammonium acetate for non-converted biotite in our previous work with the same particle size from 0.075 mm to 0.3 mm was 12.64 meq/kg (Li et al., 2018).

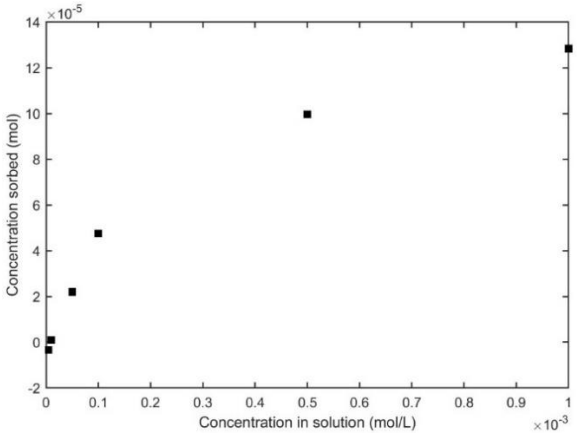

Figure 2-31. The amount of Al^{3+} sorbed on the surface of concerted biotite as a function of aqueous Al^{3+} concentration from 5×10^{-6} M to 1×10^{-3} M.

The titration results show that backtitration is the main calibration for the forward titration data. This proves that mineral dissolution occurred during the titration processes and introduced errors into the titration data and continuous titration is not suitable for titrating minerals like biotite. Comparing with backtitration, the contributions of the calibrations of cation exchange and proton exchange to the titration curve are insignificant.

The experimental titration data were modelled in terms of protonation reactions. The sorption of Se on biotite happens through surface complexation mechanism, i.e. on the hydroxyl surface functional groups (≡SOH) which are amphoteric and exist at broken bonds and edge sites on mineral surfaces (Li et al., 2018; Rovira et al., 2008; Söderlund et al., 2016b). In essence, a titration plot is a proton adsorption and desorption isotherm for the ≡SOH sites. A quantitative understanding about the acid/base behaviour of surface binding sites is critical for any model description. The proton sorption and desorption behaviours of the sorption sites (≡SOH) could be modelled in terms of protonation reactions:

$$\equiv SOH + H^{+} \Leftrightarrow \equiv SOH_2^{+}$$

and deprotonation reactions:

$$\equiv SOH \Leftrightarrow \equiv SO^{-} + H^{+}$$

The reaction constants can be described without an electrostatic term like,

$$K_{protonation} = \frac{[\equiv SOH_2^{+}]}{[\equiv SOH] \cdot \{H^{+}\}}$$

and

$$K_{deprotonation} = \frac{[\equiv SO^-]\cdot\{H^+\}}{[\equiv SOH]}$$

respectively, where [] represents concentrations in M and {} represents activities.

As described earlier, the sorption site densities of two types of weak sorption sites were calculated by molecular modelling, while the sorption site density of the strong sorption sites was estimated by the fitting of sorption isotherm data, which will be discussed later. The general parameters that were used for the titration modelling as well as the sorption edge and sorption isotherm modelling later are shown in Table 2-15. These basic parameters were fixed for the whole modelling procedures.

Table 2-15. General parameters used in titration and sorption data modelling. SSA, Mass and CEC data are measured from experiments. The sorption site densities of two weak sorption sites ($\equiv S^{W1}OH$ and $\equiv S^{W2}OH$) are from molecular modelling results while the sorption site density of the strong sorption site ($\equiv S^{S}OH$) is the optimized modelling parameter

Parameter	Biotite
SSA(m^2/g)	1.0323
Mass (g)	0.5
Sorption site densities (sites/nm^2)	0.00068 ($\equiv S^{S}OH$)
	3.2 ($\equiv S^{W1}OH$)
	1.4 ($\equiv S^{W2}OH$)
CEC (meq/Kg)	12.64

The modelled protonation and deprotonation reaction constants for the strong sorption sites and two types of weak sorption sites are shown in Table 2-16 and the results are shown in Figure 2-32 with experimental data for comparison. One thing should be mentioned for the calculated results is that it is assumed that the protonation/deprotonation reaction constants for strong sorption sites ($\equiv S^{S}OH$) is the same as those for the first type of weak sorption sites ($\equiv S^{W1}OH$) (Ervanne et al., 2013; Missana et al., 2009; Wang et al., 2001). The reason for assuming this is that the unknown parameters are too many without this assumption, which creates too much uncertainty and unpredictability to the modelling results.

The site types and site densities as well as the corresponding protonation and deprotonation constants play a central role in the sorption data modelling. The set of parameters describing the amphoteric behaviours of ≡SOH type sites will become non-adjustable parameters in all the following modelling approaches.

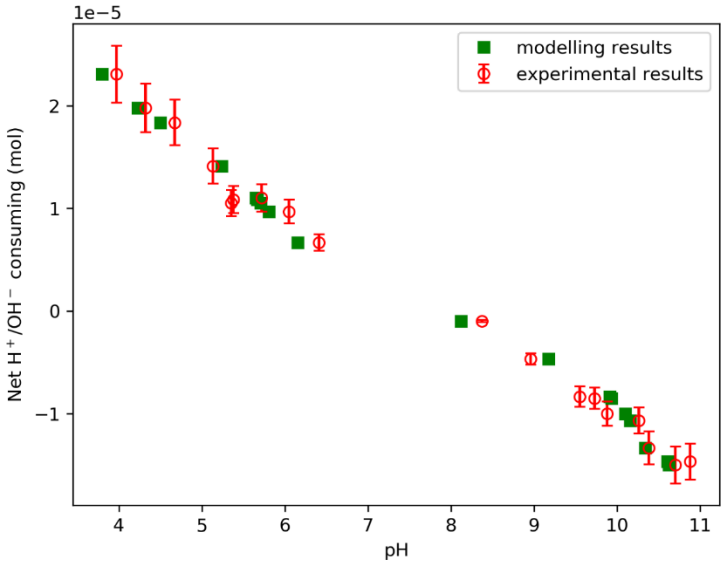

Figure 2-32. Titration experimental data for Se(IV) sorption on converted biotite in 0.01 M $KClO_4$ solution from pH 3 to pH 11 (●) and the modelling results (■).

Table 2-16. Protonation and deprotonation reaction of hydroxyl surface functional groups (≡SOH) and the corresponding reaction constants of biotite in 0.01 M $KClO_4$.

Reactions	logK
$\equiv S^{S}OH+H^{+} \Leftrightarrow \equiv S^{S}OH_2^{+}$	5.05
$\equiv S^{S}OH \Leftrightarrow \equiv S^{S}O^{-}+H^{+}$	-8.78
$\equiv S^{W1}OH+H^{+} \Leftrightarrow \equiv S^{W1}OH_2^{+}$	5.05
$\equiv S^{W1}OH \Leftrightarrow \equiv S^{W1}O^{-}+H^{+}$	-8.78
$\equiv S^{W2}OH+H^{+} \Leftrightarrow \equiv S^{W2}OH_2^{+}$	6.10
$\equiv S^{W2}OH \Leftrightarrow \equiv S^{W2}O^{-}+H^{+}$	-11.22

Sorption edge

The sorption edge measurements were carried out by measuring the sorption of 10^{-9} M total Se with a radioactive Se-75 tracer on biotite in 0.01 M $KClO_4$ solution. The tested Se is in +IV oxidation state (Se(IV)). According to the previous work (Li et al., 2018), Se(IV) will not be oxidized to +VI state or reduced to elementary selenium during the experiments. The sorption edge experimental results (Figure 2-33) show that the sorption of Se on biotite surfaces decreases as pH increases from 3 to 8, while in the basic region, the K_d values decrease to near 0 and the sorption was considered negligible in comparison with the sorption in the acidic region. In the deep groundwater conditions of granitic rock, the water is usually in a slightly basic state (7-10), which makes Se a highly mobile element.

Two main sorption mechanisms, ion exchange and surface complexation, are considered influencing the sorption of radioelements on mineral surfaces. Ion exchange sites originate from the isomorphous substitution of lattice elements, causing permanent negative or positive charge regions on the surface of mineral platelets. Charge neutrality is maintained by the presence of an excess of counter-charge ions in solution held electrostatically in close proximity. The electrostatically bound ions can undergo exchange with the ions in solution. This kind of sorption mechanism has a weak dependency on pH

except at low pH (Bradbury and Baeyens, 2009a, 2002). However, Figure 2-33 shows a strong pH dependency of Se sorption, which indicates the fitting of the second sorption mechanism, i.e. surface complexation. Surface complexation happens to nuclide bounding on sorption sites which are perceived as being surface hydroxyl groups (≡SOH). The ≡SOH groups can undergo protonation ($\equiv SOH_2^+$) and deprotonation ($\equiv SO^-$) reactions, depending on the pH conditions of background solutions. The protonation and deprotonation properties of the sorption sites have been analysed by titration experiments in the above section.

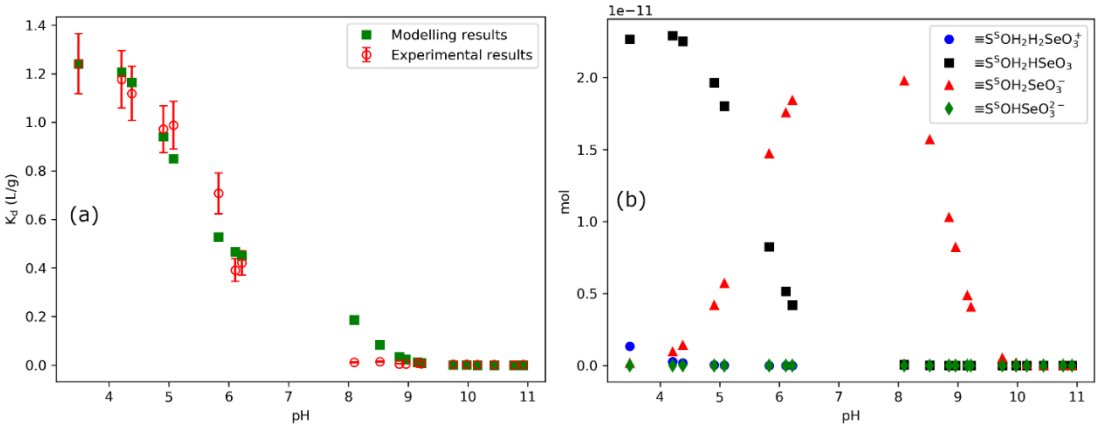

Figure 2-33. a) Sorption edge data (●) of 10^{-9} M Se(IV) on 0.5 g converted biotite in 25 mL 0.01 M $KClO_4$ solution from pH 3 to 11 and the modelling results (■) with strong sorption sites. b) The calculated moles of different sorption species on the surface of biotite as a function of pH from 3 to 11

In the modelling of Se sorption edge process, only the uptake on strong sorption sites was considered because of the very low concentration of tracer ions used in the experiments (10^{-9} M). The two model parameters required to calculate sorption edge are the $\equiv S^SOH$ site density and the surface complexation reaction constant K. The aqueous speciation of Se will play an import role in the sorption edge modelling because different Se species with three different valences (SeO_3^{2-}, $HSeO_3^-$, H_2SeO_3) exist in the experimental pH range from 3 to 11. The aqueous speciation and sites distribution provides a guide for choosing reasonable surface complexation reactions. For most of the pH range, $HSeO_3^-$ and SeO_3^{2-} are the two dominant species in the background solution. The surface complexation reactions representing the sorption of the two species on $\equiv S^SOH$ will be identified first:

$$SeO_3^{2-} + \equiv S^SOH \Leftrightarrow \equiv S^SOHSeO_3^{2-}$$

$$HSeO_3^- + \equiv S^SOH \Leftrightarrow \equiv S^SOH_2SeO_3^-$$

In the acidic area, the protonated sorption hydroxyl groups $\equiv SOH_2^+$ will become popular and the complexation reaction with $HSeO_3^-$ happens (The amount of SeO_3^{2-} is insignificant in the acid environments and the complexation of SeO_3^{2-} with $\equiv SOH_2^+$ will be omitted). The complexation will be expressed as:

$$H^+ + HSeO_3^- + \equiv SOH \Leftrightarrow \equiv S^SOH_2HSeO_3$$

Also, in strong acidic pH region (pH<4), the amount of H_2SeO_3 species could not be neglected. The complexation between $\equiv S^SOH_2^+$ and H_2SeO_3 should also be considered:

$$H^+ + H_2SeO_3 + \equiv S^SOH \Leftrightarrow \equiv S^SOH_2H_2SeO_3^+$$

The selectivity coefficients of the strong sorption sites, K^S, for the surface complexation reactions could be expressed like:

$$K^{S}_{SeO_3^{2-}} = \frac{[\equiv S^{S}OHSeO_3^{2-}]}{\{SeO_3^{2-}\}\cdot[\equiv S^{S}OH]}$$

where $K^{S}_{SeO_3^{2-}}$ is the complexation selectivity coefficient, and [] the concentration of sorption sites and {} the activity of aqueous species. The selectivity coefficients $K^{S}_{HSeO_3^-}$, $K^{S}_{H_2SeO_3}$ and $K^{S}_{H_3SeO_3^+}$ have similar expressions.

The modelled sorption edge data shown in Figure 2-33 a are based on the selectivity coefficients listed in Table 2-17 which have been optimized by the least squares method (best fit). Comparing the selectivity coefficients calculated, which indicate the abilities/possibilities of surface reactions, the reaction between SeO_3^{2-} and $\equiv S^{S}OH$ is highly unlikely (logK = -2.23), while the reaction between $HSeO_3^-$ and $\equiv S^{S}OH$ happens more easily (logK = 7.89). The calculated moles of different sorption species on the surface of converted biotite are illustrated in Figure 2-33b. It shows that the production of $\equiv S^{S}OHSeO_3^{2-}$ which results from the reaction between $\equiv S^{S}OH$ and SeO_3^{2-} is quite low and it will not cause obvious influence for K_d values if pH is below 10. At pH conditions between 6 and 10, the main sorption species on biotite surface is $\equiv S^{S}OH_2SeO_3^-$ which results from the reaction between $\equiv S^{S}OH$ and $HSeO_3^-$. This is the most important reaction that occurs under the conditions of deep geological repository. If pH is below 5, the main sorption species on biotite surface becomes $\equiv S^{S}OH_2HSeO_3$ which is the production of H^+, HSeO3$^-$ and $\equiv S^{S}OH$. This might be important process in surface water conditions. The $\equiv S^{S}OH_2H_2SeO_3^+$ species will appear only under pH 5 and may become important under acidic conditions. The inconsistence between the modelled and experimental results was found between pH 8 and 9 due to reactions between $\equiv S^{S}OH$ and $HSeO_3^-$. However, the modelled and calculated results are in good agreement under other pH conditions.

Table 2-17. Surface complexation reactions of different Se species on strong sorption sites and the related reaction selectivity coefficients used in the modelling of sorption edge results

Reactions	log K
$SeO_3^{2-} + \equiv S^{S}OH \Leftrightarrow \equiv S^{S}OHSeO_3^{2-}$	-2.23
$HSeO_3^- + \equiv S^{S}OH \Leftrightarrow \equiv S^{S}OH_2SeO_3^-$	7.89
$H^+ + HSeO_3^- + \equiv S^{S}OH \Leftrightarrow \equiv S^{S}OH_2HSeO_3$	13.46
$H^+ + H_2SeO_3 + \equiv S^{S}OH \Leftrightarrow \equiv S^{S}OH_2H_2SeO_3^+$	13.02

Sorption isotherm

The sorption isotherm experimental results (Figure 2-34) show that a clear increasing trend exists for K_d values with the decrease of Se concentration; however, a drastic increase happens when the Se concentration decreases from 10^{-7} M to 10^{-8} M. Two platforms could be observed in the low concentration area (10^{-10} M to 10^{-8} M) and high concentration area (10^{-7} M to 10^{-3} M). This may indicate different sorption mechanisms when the concentration changed. The K_d values stabilized at 0.01 ~ 0.02 m^3/kg in the high concentration area and at 0.06 ~ 0.07 m^3/kg in the low concentration area.

Sorption isotherms for Se on biotite were measured at slightly basic environments (pH ~ 7.7) over concentration ranges from 10^{-10} M to 10^{-3} M. All the strong sorption site parameters, including surface site density and surface reactions derived from the sorption edge modelling were fixed. The surface reactions of Se species between the two types of weak sorption sites are the remaining unknown parameters at this stage.

According to the Se speciation distribution calculations, $HSeO_3^-$ is the dominant Se species at the experimental conditions. Furthermore, as shown by the sorption edge modelling results (Figure 2-33), the reactions between $\equiv S^SOH$ and $HSeO_3^-$ and the reaction between $\equiv S^SOH$, H^+ and $HSeO3^-$ are the main reactions from pH 7 to 10. Thus, $HSeO_3^-$ will be considered as the main reactant with the two weak sorption sites which determines the main shape of the isotherm curve in high concentration area. Table 2-18 shows the surface complexation reactions between $HSeO_3^-$ and $\equiv S^{W1}OH$/ $\equiv S^{W2}OH$ together with the optimized logK values.

The modelling results of site occupations indicate that the strong sorption sites with a low site density of 0.00068 sites/nm^2, dominate the Se(IV) sorption in the low concentration area (< 10^{-8} M). However, with the increase of Se(IV) concentration, the contribution of the weak sorption sites becomes more important due to the low site density of the strong sorption sites. The mechanisms of the strong sorption sites are still under discussion. Dähn et al. (2011) illustrates that strong sorption happens onto the mineral surface as a mixture of surface complexes bound to the edge sites of the *cis*-vacant (cv) and *trans*-vacant (tv) of Al octahedrons. However, more evidence is needed to understand the true nature of the so-called "strong" sorption site in the case of Se(IV) sorption on biotite.

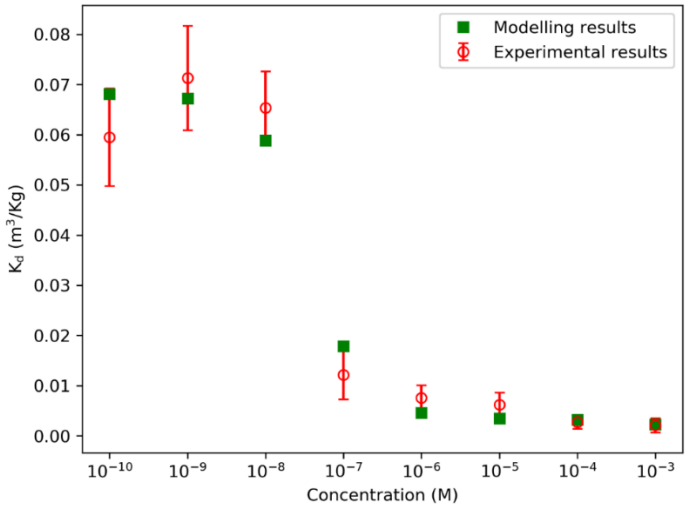

Figure 2-34. Se(IV) sorption isotherm data (●) on converted biotite in 0.01 M $KClO_4$ solution covering Se(IV) concentration from 10^{-10} M to 10^{-3} M. The modelling results (■) were based on the sorption of Se(IV) species on the strong sorption sites ($\equiv S^SOH$) and two types of weak sorption sites ($\equiv S^{W1}OH$ and $\equiv S^{W2}OH$)

Table 2-18. Expected surface complexation reactions between Se(IV) species and weak sorption sites on converted biotite surface at pH around 7.7. The selectivity coefficients were optimised from the modelling of sorption isotherms.

Surface complexation reaction	log K
$HSeO_3^- + \equiv S^{w1}OH \Leftrightarrow \equiv S^{w1}OH_2SeO_3^-$	2.78
$H^+ + HSeO_3^- + \equiv S^{w1}OH \Leftrightarrow \equiv S^{w1}OH_2HSeO_3$	3.78
$HSeO_3^- + \equiv S^{w2}OH \Leftrightarrow \equiv S^{w2}OH_2SeO_3^-$	2.48
$H^+ + HSeO_3^- + \equiv S^{w2}OH \Leftrightarrow \equiv S^{w2}OH_2HSeO_3$	2.62

Model validations

To validate the surface complexation model, especially to test the feasibility of the model at pH 9.5 which is the pH of the Grimsel groundwater (Hoehn et al., 1998; Muuri et al., 2018; Tachi et al., 2015), another batch sorption experiment was done with the same experimental conditions except for pH. In the validation experiments, the pH was adjusted to 9.5 by adding NaOH standard solution into the sample vials. The pH was checked and adjusted during the whole experimental period.

The modelling of the experimental results was done by optimizing the pH parameter while keeping the other parameters the same as the sorption isotherm modelling we presented in the last parts. The best fit was achieved at pH 9.34 which is in fare agreement with the experimental conditions. The experimental and modelling results are shown in Figure 2-35.

The model predicted the K_d values well at both high and low concentration regions. At the concentration of 10^{-7} M, the sorption of Se(IV) on biotite is believed to be dominated by both strong and weak sorption sites. Our model showed a higher K_d value than the real experimental result. Except for the point at 10^{-7} M, the modelled results are all within the experimental errors. This means that the multi-site surface complexation model we developed here could be used to describe the Se(IV) sorption on biotite over a large pH ranges at least from pH 7.5 to 9.5 which covers most of the pHs of groundwaters in the bedrocks of a nuclear waste repository.

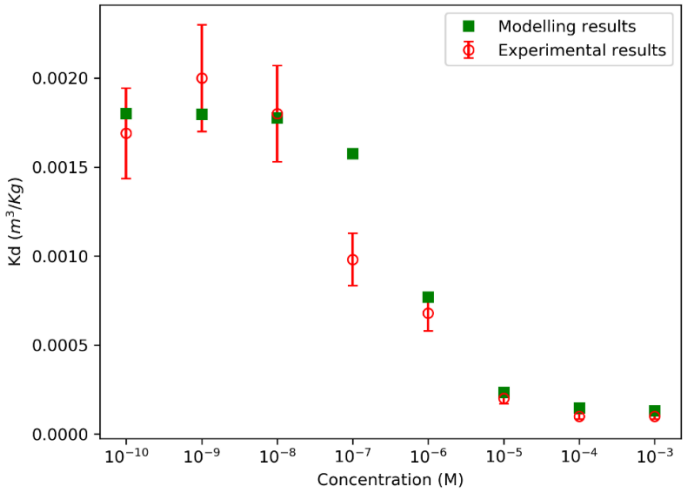

Figure 2-35. Se(IV) sorption isotherm data (●) on converted biotite in 0.01 M KClO4 solution covering Se(IV) concentration from 10^{-10} M to 10^{-3} M at pH ~9.5. The modelling results (■) were based on the sorption of Se(IV) species on the strong sorption sites (≡S^SOH) and two types of weak sorption sites (≡S^{W1}OH and ≡S^{W2}OH) at pH 9.34

2.3.6 Sorption of Ba

2.3.6.1 Calcite dissolution and precipitation in NaCl and Na_2CO_3 aqueous solutions

Figure 2-36 shows the changes in the calcite content in the NaCl solution versus time, indicating clearly the capability of 0.1 mol/L NaCl solution to extract calcium cations from calcite. The equilibrium concentration of calcium in the solution approaches 70 mg/L, therefore, the extraction efficiency of 0.1 mol/L NaCl must be higher than 0.35%. The equilibrium concentration of calcium in the solution was further diminished when the 0.1 mol/L Na_2CO_3 aqueous solution was introduced into the calcite suspension. This highlights the importance of co-occurring extraction and precipitation of calcium and carbonate ions for the availability of free cations in the extraction solution.

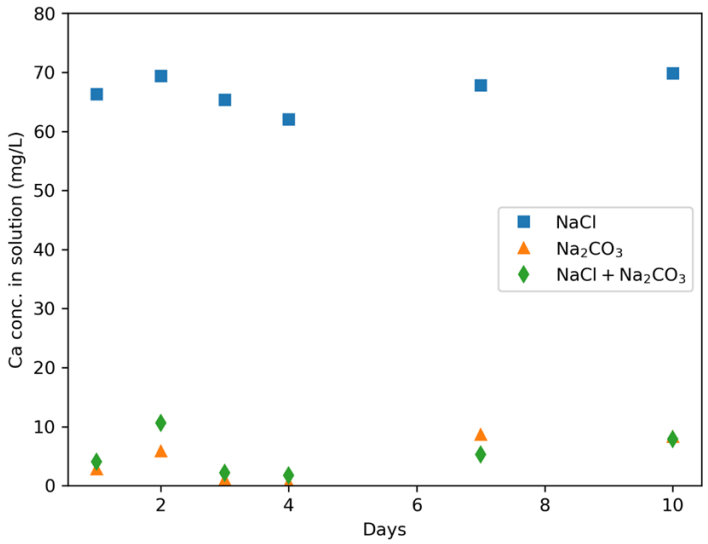

Figure 2-36 Time-dependent changes of Ca^{2+} concentration in three different studied solutions with initial pH of 8.

The pure phase-calcite dissolution in various background solutions (0.1 M NaCl, 0.1 M Na_2CO_3, 0.1 M NaCl and 0.1 M Na_2CO_3) were modelled by PHREEQC. The amount of calcite that can react reversibly with the aqueous phase was calculated. Considering that experimental data clearly indicated that calcite dissolution reached equilibrium within a two-days period, kinetic effects were not considered in the modelling process. The calcite dissolution was modelled according to the total average amount of Ca species in the aqueous phase and the pH values measured at the end of the experiments. The modelled equilibrium constants (log K_{Ca}) of the calcite dissolution reactions and the amount of dissolved calcite in various background solutions are summarized in Table 2-19.

Table 2-19 Summary of the modelling results of the dissolution of pure-phase calcite in three different background solutions. The model was done based on the experimental measured Ca concentrations and the measured pH values.

Solutions	Final pH (exp.)	Modelled Ca concentration in solution (mM)	Modelled dissolved calcite (10^{-6} moles)	Modelled log K_{Ca}
0.1 M NaCl	8.11	1.670	83.50	-8.33
0.1 M Na_2CO_3	8.67	0.113	5.65	-7.61
0.1 M NaCl + 0.1 M Na_2CO_3	8.50	0.132	6.62	-7.69

The modelling results of calcite dissolution shows that calcite is more easily to be dissolved in 0.1 M NaCl than in 0.1 M Na_2CO_3 or in 0.1 M NaCl + 0.1 M Na_2CO_3. This is caused by the existence of CO_3^{2-} in the solution which can hinder the calcite dissolution reaction. The distribution of the modelled Ca species is shown in Figure 2-37. The figure shows that in 0.1 M NaCl solution, Ca^{2+} is the dominant Ca species, while the concentration of the other species are negligible compared with the Ca^{2+} concentration. In the solutions of 0.1 M Na_2CO_3 and 0.1 M Na_2CO_3 + 0.1 M NaCl, the Ca speciations are quite similar, and the Ca species of Ca^{2+}, $CaHCO_3^+$ and $CaCO_3$(aq) are all exist as the main Ca species.

As shown in Figure 2-37, the concentrations of different Ca species in 0.1 M Na_2CO_3 and 0.1 M NaCl + 0.1 M Na_2CO_3 solutions are almost the same. This indicates that the effect of Na^+ and Cl^- ions on calcite dissolution is minor. The figure also shows that in the 0.1 M NaCl solution, the dominant Ca species is Ca^{2+}, while the concentration of the other species are negligible compared with the concentration of Ca^{2+}.

The modelled results also show that the equilibrium constants K_{Ca} in 0.1 M NaCl is smaller than in 0.1 M Na_2CO_3 and 0.1 M NaCl + 0.1 M Na_2CO_3. This is more likely to be related to the formation of spherulitic microstructures coprecipitated from the sodium cations.

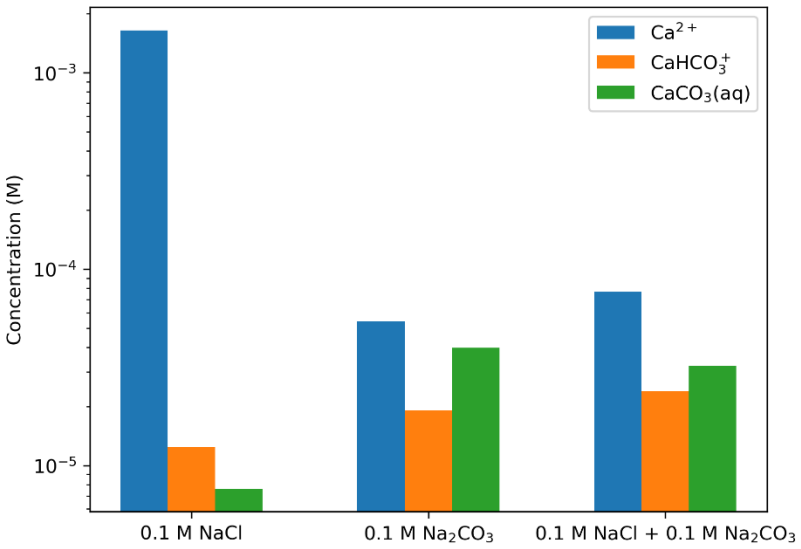

Figure 2-37 Ca species distribution in three different background solutions modelled by PHREEQC.

2.3.6.2 Immobilization of barium cation in calcite suspension saturated with NaCl and Na2CO3

The implication of barium precipitation with carbonate ions for its immobilization in the calcite suspension is highlighted in Figure 2-38. Since the decrease of the barium equilibrium concentration in the solution correlates well with the increase in Na_2CO_3 content, we can assume that besides the electrostatic interaction of barium with negatively charged ions on the calcite surfaces, the other prevalent mechanism of barium immobilization is a precipitation of $BaCO_3$ or $Ba(HCO_3)_2$. Therefore, the mixture of 0.1 mol/L NaCl and Na_2CO_3 solutions increases the barium immobilization efficiency at least by three times in comparison to NaCl treated calcite.

The interactions between 0.01 M Ba or 0.1 M Ba with solutions including different concentrations of CO_3^{2-} were modelled based on the equilibrium reactions between witherite ($BaCO_3$) and background solutions. The equilibrium constant (K_{wi}) were calculated by the model. The modelled percentage of Ba species remaining in the supernatant after the experiments are shown in Figure 2-38, together with the experimental measured data. Different K_{wi} values were obtained from the modelling of experimental data with 0.01 M total Ba species or 0.1 M total Ba species. When Ba species concentration was 0.01 M in the solution with CO_3^{2-} from 0.1 M to 3 M, the modelled K_{wi} values was -7.00; when Ba species concentration was 0.1 M, the modelled K_{wi} values was -7.90. This observed trend indicates that an increase in the concentration of Ba species within the solution leads to reduction in the dissolution percentage of witherite. This outcome aligns with expectations, as both mineral dissolution and precipitation processes are governed by surface reactions. A greater quantity of precipitated witherite leads to a decreased proportion of surface reactions, providing a rational explanation for the observed phenomenon.

The modelled concentration of Ba species in four different background solutions are shown in Figure 2-39. The Ba species are similar for both Ba concentration conditions (0.01 M and 0.1 M). Ba^{2+} is dominant Ba species when CO_3^{2-} concentration is low in the background solution. With the increase of CO_3^{2-} concentration, $BaHCO_3^-$ becomes to be relatively more abundant and its concentration will be larger than Ba^{2+} concentration when CO_3^{2-} concentration reaches 3 M. Figure 2-39 also shows that the total concentration of Ba species becomes smaller with the increase of CO_3^{2-} concentration, which indicates that more witherite ($BaCO_3$) precipitates in higher CO_3^{2-} concentration solutions.

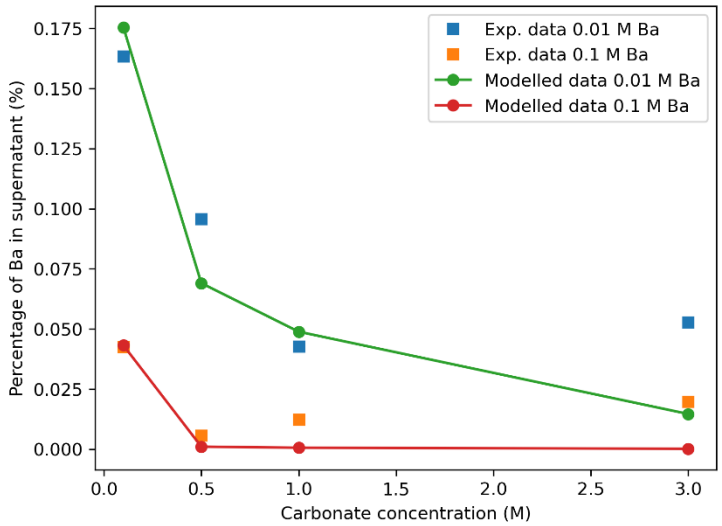

Figure 2-38 Experimental and modelled data of Ba (0.01 M and 0.1 M) interactions with background solutions including carbonate concentrations 0.1 M, 0.5 M, 1.0 M and 3.0 M.

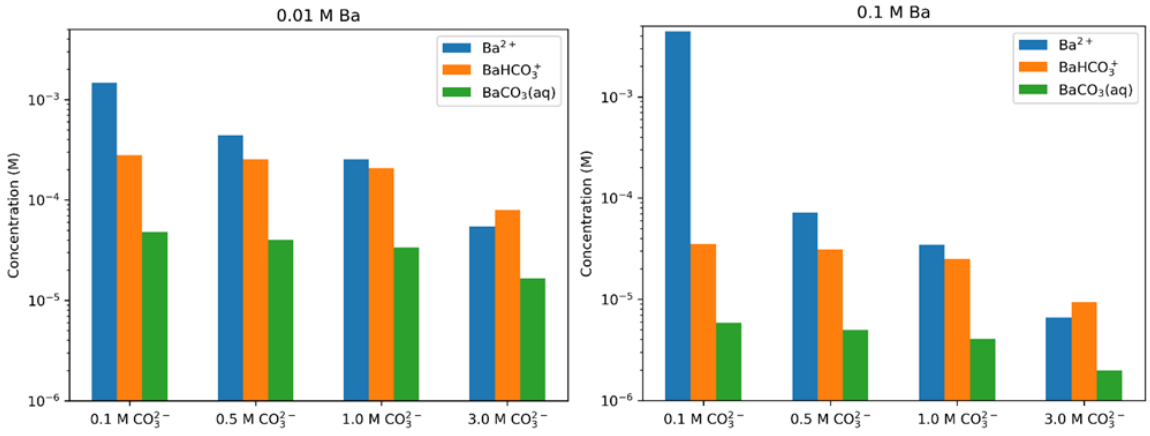

Figure 2-39 Ba species distributions in different background solutions with various CO_3^{2-} concentration. (Left: initial total Ba species concentration is 0.01 M; Right: initial total Ba species concentration is 0.1 M.

2.3.6.3 Barium and calcite interactions *in various barium concentrations*

The Ba sorption coefficient, Figure 2-40, which is constant from concentrations 10^{-10} M to 10^{-5} M indicates that sorption or pure phase precipitation are not the main mechanisms to define the Ba concentrations in the solution, otherwise a change of sorption coefficient should be observed. The precipitation process can be defined by the following distribution equation:

$$\frac{[CaCO_3]}{[BaCO_3]} = K_d \frac{[Ca^{2+}]}{[Ba^{2+}]}$$

where K_d is the concentration-based effective distribution coefficient, $[CaCO_3]$ and $[BaCO_3]$ are relative fractions in the solid phase, and $[Ca^{2+}]$ and $[Ba^{2+}]$ are equilibrium activities/concentrations in the aqueous phase. In our work, the much larger amount of calcite in the system defines that $[CaCO_3]$ and $[Ca^{2+}]$ are constant. With constant K_d, sorption coefficient of Ba, defined as $[BaCO_3]/([BaCO_3]+[Ba^{2+}])$, is also constant. Thus, the experimental results indicate that co-precipitation is the main mechanism to define the Ba species concentration in the aqueous phase and the sorption efficiency in the experimental process.

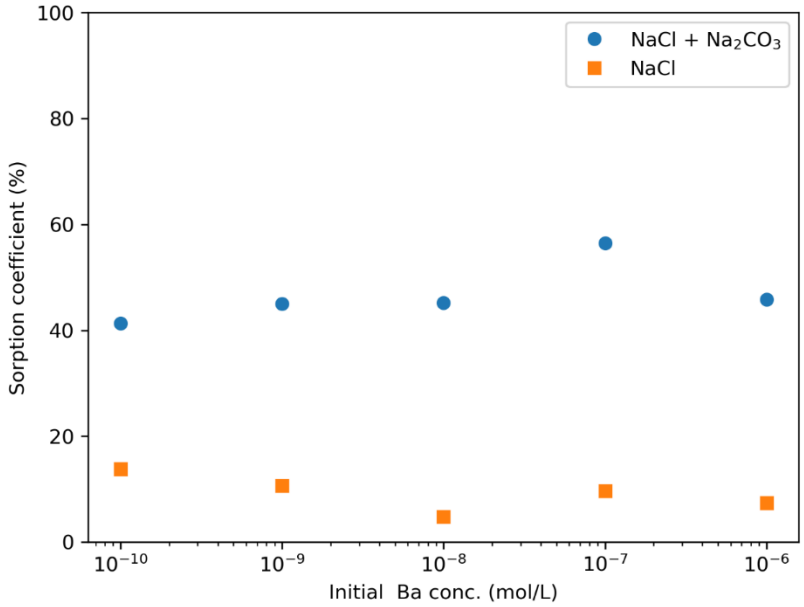

Figure 2-40 ^{133}Ba removal by calcite at pH 8 in 0.1 mol L^{-1} NaCl and mixture of 0.1 M NaCl and 0.1 mol L^{-1} Na_2CO_3 (Initial ^{133}Ba activity was 31.91 Bq ml^{-1}).

To model the experimental sorption efficiencies, we defined the formation of a solid phase ($Ca_xBa_{(1-x)}CO_3$) to simulate the co-precipitation process. The model assumes that $Ca_xBa_{(1-x)}CO_3$ will be in equilibrium with the background solution and the equilibration of $Ca_xBa_{(1-x)}CO_3$ is defined by both the K_{Ca} and K_{wi} that we obtained from the model in the upper sections. The fraction factor (defined as the mole fraction ratio Ca/Ba in the co-precipitation) was calculated based on the best fit of the modelled sorption efficiencies and the experimental ones. The modelled fraction factors in both solutions are shown in Figure 2-41. An almost linear relation between the fraction factors and the Ba initial concentrations indicates the formation of co-precipitations. Figure 2-41 shows that in the 0.1 M NaCl, the fraction factors are almost one magnitude higher than the fraction factors in 0.1 M Na_2CO_3 + 0.1 M NaCl solution. This indicates that CO_3^{2-} in the solution caused more Ba^{2+} to be co-precipitated with $CaCO_3$. This conclusion is also supported by the modelled effective distribution coefficients of the co-precipitation processes in this two solutions as shown below.

The effective distribution coefficient, K_d, of the co-precipitation process shown above can be calculated by

$$K_d = \frac{[CaCO_3]/[BaCO_3]}{[Ca^{2+}]/[Ba^{2+}]}$$

The modelled concentrations of [Ca^{2+}] and [Ba^{2+}] in the two background solutions are shown in Table 2-20. The constant [Ca^{2+}] concentrations are controlled by the equilibrium between calcite and the background solutions. The [Ba^{2+}] concentrations, which is in linear relation with the initial Ba concentrations, are controlled by the co-precipitation of $Ca_xBa_{(1-x)}CO_3$. The modelled effective distribution coefficients of the co-precipitation process are shown in Table 2-20. In the 0.1 M NaCl solution, the K_d value is calculated to be 8.15 L/g, while in the 0.1 M NaCl + 0.1 M Na_2CO_3 solution, the K_d value is calculated to be 1.72 L/g. The difference of the K_d values are in the same trend as the fraction factors shown in Figure 2-41, which shows that CO_3^{2-} in the solution will facilitate the co-precipitation process of Ba^{2+} with $CaCO_3$ to form $Ca_xBa_{(1-x)}CO_3$.

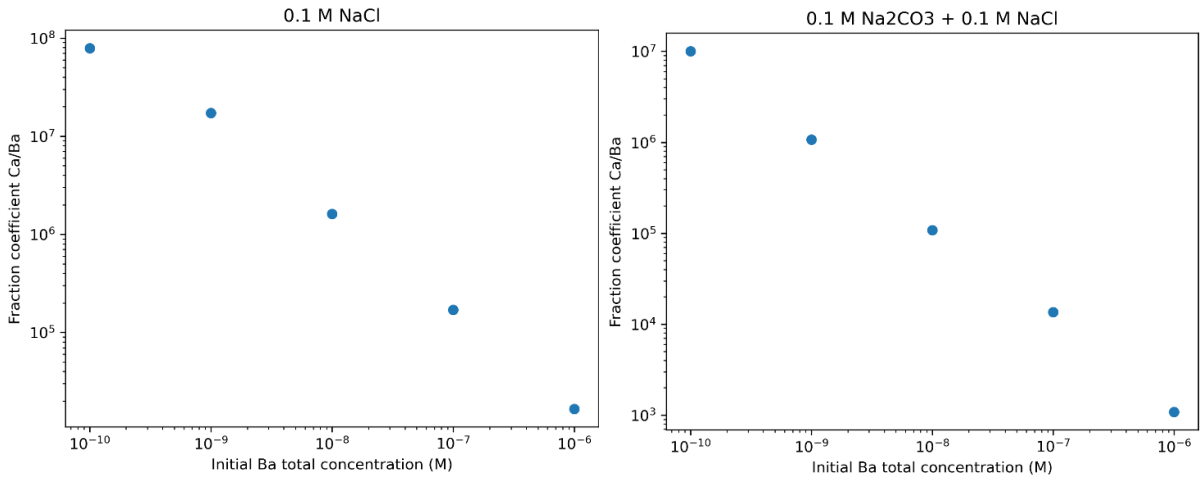

Figure 2-41 *The modelled fraction coefficient of Ca/Ba in co-precipitation of $Ca_xBa_{(1-x)}CO_3$. (Left) In the 0.1 M NaCl background solution; (Right) In the 0.1 M Na_2CO_3 + 0.1 M NaCl background solution.*

Table 2-20 *The modelled concentrations of $Ca^{2+}$and Ba^{2+} in the aqueous phase after reaching equilibrium between $Ca_xBa_{(1-x)}CO_3$ and different background solutions.*

Initial Ba concentration (mol·L^{-1})	0.1 M NaCl		Modelled K_d (L/g)	0.1 M NaCl + 0.1 M Na_2CO_3		Modelled K_d (L/g)
	[Ca^{2+}] (mol·L^{-1})	[Ba^{2+}] (mol·L^{-1})		[Ca^{2+}] (mol·L^{-1})	[Ba^{2+}] (mol·L^{-1})	
1E-6	1.89E-03	9.26E-07	8.15	3.43E-04	5.42E-07	1.72
1E-7	1.89E-03	9.03E-08	8.15	3.44E-04	4.36E-08	1.72
1E-8	1.89E-03	9.52E-09	8.15	3.44E-04	5.48E-09	1.72
1E-9	1.89E-03	8.94E-10	8.15	3.44E-04	5.50E-10	1.72
1E-10	1.89E-03	6.88E-11	8.15	3.44E-04	5.87E-11	1.72

2.3.6.4 Barium and calcite interactions *in various pH conditions*

The sorption edge modelling was performed with all the parameters obtained from the previous sections, including the equilibrium constants of calcite (K_{ca}), equilibrium constants of witherite (K_{wi}) and the fraction factors of $Ca_xBa_{(1-x)}CO_3$. The sorption edge modelling can be regarded as the validation process of the developed co-precipitation model in this work. The modelled sorption efficiencies and the experimental

data are shown in Figure 2-42. As can be seen, the modelled data can re-produce all the experimental sorption coefficients in a good way, which proves that our assumptions of the formation of co-precipitation, $Ca_xBa_{(1-x)}CO_3$, can reflect the realities happened in the experimental process. Figure 2-42 shows that Ba sorption efficiency increases with the increase of pH. This is caused by the increase of the CO_3^{2-} concentration in the solution, attributed to the increasing pH. This conclusion is in agreement with conclusion drawn in the above sorption isotherm modelling section.

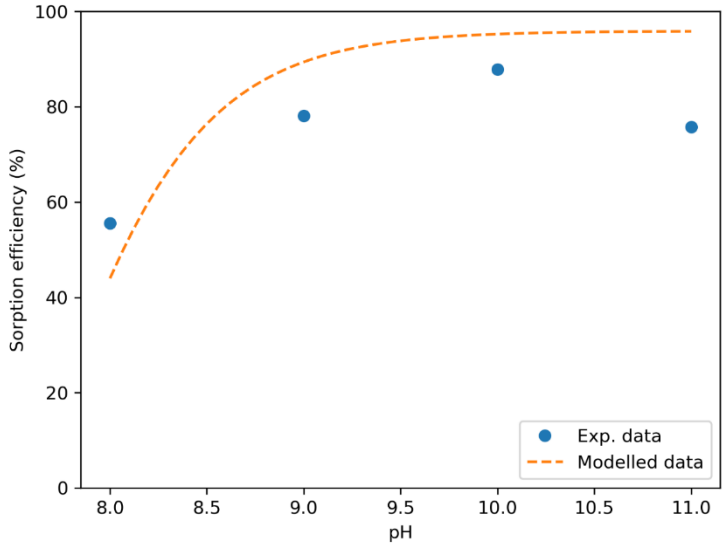

Figure 2-42 The removal of Ba by calcite from pH 8 to 11 in 0.1 M NaCl and 0.1 M Na_2CO_3 solution.

2.3.7 Results from desorption

2.3.7.1 Post-Active ^{63}Ni Sorption Experiments: Leaching Investigations and Analysis of Leached Ions in Liquid Phases in Context of Non-Active Sorption Experiments

In addition to the sorption experiments, comprehensive investigations of the aqueous phase chemistry are of great importance during the course of sorption processes. Analyzing the dynamic changes in the concentrations of the monitored cations provides valuable insights into their behavior and interactions, thus elucidating their influence on the sorption kinetics and mechanisms of the target elements, Ni and Cs. Furthermore, studying the leaching phenomena involving competitive cations allows for a deeper understanding of the intricate binding mechanisms that govern the sorption of the studied element onto the studied materials. These supplementary experiments play a crucial role in complementing the findings and conclusions derived from the sorption experiments. Ultimately contributing to the comprehensive understanding of the complex sorption processes that transpire at the interface between Bukov materials and SGW2 water.

^{63}Ni leaching after sorption experiments

Following the sorption experiment involving the radioactive isotope nickel ^{63}Ni with the majority of the Bukov materials, separation of the liquid and solid phases of the rock samples was conducted using analytical techniques to minimize material loss from the vials and to ensure the retention of any residual liquid phase within the vial containing the solid phase. Subsequently, precise weighing of the vial, including the solid phase and residual liquid phase after the sorption experiment, was performed. This was followed by the introduction of the chosen leaching agent, which could either be 0.1 mol/L hydrochloric acid (HCl) or 1 mol/L magnesium chloride ($MgCl_2$). The quantification of the leached ^{63}Ni after a sufficient time period (typically around 14 days, consistent with the interaction time used in the sorption experiment) was carried out following the same methodology as described in Chapter 2.2.1.3.

The quantity of leached nickel was assessed using the leaching factor f_L, reported as a percentage (see equation below), following a similar methodology as described for the desorption ratio in Tachi et al. (2001). However, modifications were made to account for the presence of ^{63}Ni in the remaining liquid phase after decantation and its dilution through the addition of a leaching solution.

$$f_L = \frac{\left(\frac{V_{\text{leaching solution}} \cdot A_{\text{leached } ^{63}Ni}}{f_p} - V_{\text{after sorption exp.}} \cdot A_{\text{after sorption experiment } ^{63}Ni}\right)}{A_{^{63}Ni \text{ in solid phase}}} \cdot 100$$

Here, V_{leaching} solution (ml) denotes the volume of the leaching agent employed, $V_{\text{after sorption experiment}}$ (ml) refers to the volume of the residual liquid phase following decantation subsequent to the sorption experiments, $A_{\text{leached } ^{63}Ni}$ (cpm/ml) indicates the volumetric activity of ^{63}Ni in the leaching agent, $A_{\text{after sorption experiment } ^{63}Ni}$ (cpm/ml) signifies the volumetric activity of ^{63}Ni in the liquid phase measured during the sorption experiments, $A^{^{63}Ni \text{ solid phase}}$ (cpm/g) represents the activity of ^{63}Ni in the solid phase, equivalent to the sorption quantity q, and f_p (-) represents the conversion factor accounting for the measurement efficiency of activity in various solutions.

This conversion factor, f_p, holds significant importance in accounting for the desorption agent behavior within the scintillation cocktail environment, which exhibits variations compared to the liquid phase of SGW2 utilized in the sorption experiments. The conversion factor for activity measurement efficiency in diverse solutions reflects the ratio between the measured activity of ^{63}Ni in a specific solution and the activity of ^{63}Ni in distilled water, which serves as the reference solution with minimal influence on measurement efficiency employing liquid scintillation counting techniques (Thomson and Temple, 2020). For the 0.1 mol/L HCl solution, the determined conversion factor was 1.067, while for the 1 mol/L $MgCl_2$ solution, the conversion factor was 1. The leaching factors for individual leaching solutions, expressed as the average values of the leaching factors for each m/V ratio along with their corresponding standard deviations, are presented in Table 2-21 and Figure 2-43.

Table 2-21 The leaching factors corresponding to distinct leaching solutions, the experimental conditions employed in the sorption experiments, and Bukov materials utilized for the sorption experiment with ^{63}Ni

Conditions	Materials	f_L (H^+)	f_L (Mg^{2+})
Ambient atmosphere	Bukov Host rock with high plagioclase contents	89.8 ± 0.3	1.81 ± 0.29
Ambient atmosphere	Bukov Host rock with high amphibole contents	91.5 ± 1.3	3.91 ± 0.16
Ambient atmosphere	Bukov Host rock with high biotite contents	89.5 ± 0.3	0.95 ± 0.21
Ambient atmosphere	Host rock of Bukov Calcite Infill	79.4 ± 11.4	0.71 ± 0.12
Ar atmosphere	Host rock of Bukov Calcite Infill	89.4 ± 2.3	-
Ambient atmosphere	Bukov Calcite Infill	45.9 ± 4.2	2.52 ± 0.97
Ar atmosphere	Bukov Calcite Infill	37.9 ± 11.0	-

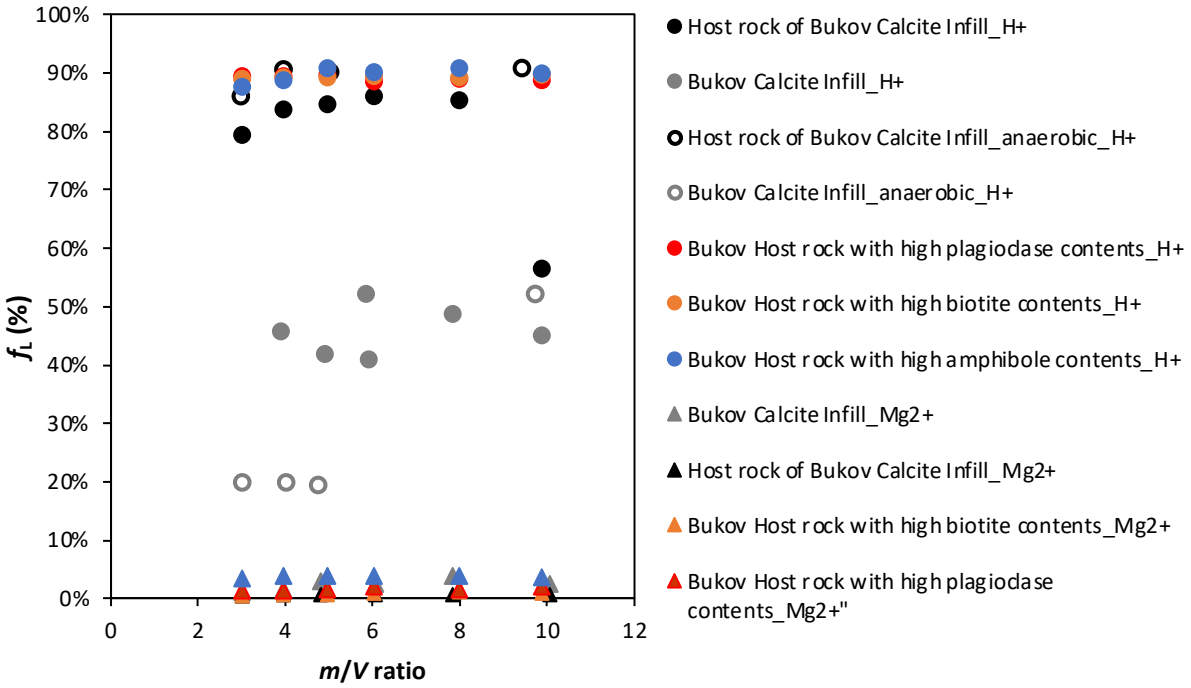

Figure 2-43 The leaching factors corresponding to distinct leaching solutions, the experimental conditions employed in the sorption experiments, and Bukov materials utilized for the sorption experiment with ^{63}Ni

From the obtained f_L values in Table 2-19 and Figure 2-36, it is evident that the use of the leaching agent $MgCl_2$, which is commonly employed for extracting easily exchangeable cations in sequential leaching of metallic elements (Tessier et al., 1979; Bacon and Davidson, 2008), reveals minimal binding of nickel at sites where its exchange with Mg^{2+} could potentially occur. This implies that in the specific system of SGW2 with elevated pH, the sorption of Ni is predominantly governed by surface complexation, as evidenced by various studies (Bradbury and Baeyens, 1995; Zhao et al., 2017). Throughout the designated leaching period, the majority of the nickel remains firmly bound in the solid phase. As for the choice of 0.1 mol/l HCl, it was selected due to its compatibility without significant alterations in the measured activities upon contact with the scintillation cocktail, as indicated by the conversion factor f_p. Clearly, the solid-to-liquid ratio does not exert influence, and the use of hydrochloric acid at the specified concentration effectively leaches nickel from the surrounding rocks. Substantial pH reduction induces adequate system changes that lead to the efficient leaching of nickel. In the case of Bukov Calcite Infill, the leaching factor is lower compared to the surrounding rocks, suggesting that changes in pH and increased hydrogen cation concentration fail to effectively leach nickel. This could be attributed to factors such as the calcite structure, the distinctive binding mechanisms between nickel and calcite (Pokrovsky et al., 2002), which may contribute to a lower desorption ratio, as observed in previous studies (Lamana 2010; Lakshtanov and Stipp, 2007), or the limited dissolution of calcite particles, resulting in minimal surface modification of calcite accompanied by the visible formation of a calcium chloride coating. The Bukov Calcite Infill sample, predominantly composed of calcite, exhibits a diminished impact of hydrogen ions and low pH on nickel leaching compared to the Bukov host rocks.

Development of the liquid phase chemistry during the contact of the rock and the SGW2 and the sorption experiments with Cs and Ni

Regarding the experiments focused on simulating equilibration and studying the evolution of SGW2 chemistry, a specific rock sample migmatized gneiss (PVP-2), used in the preliminary sorption experiments, see chapter was used also for these investigations. The equilibration process followed the same approach as the sorption experiments detailed in chapter and 2.2.1.3. The solid phase, which underwent liquid phase washing, was subjected to the liquid phase at a ratio of 1:10 (with a sample weight of 4 g). The concentration of selected cations was monitored in the collected supernatants using

the AAS (atomic absorption spectroscopy) method (measurements detailly described in chapter 2.2.1.3), while the concentration of anions was determined using the capillary electrophoresis method using Agilent 7100, Agilent Technologies, DEU. The alkalimetric determination of HCO_3^- concentration followed the ČSN-ISO 9963-1 standard method.

The concentrations of ions resulting from the equilibration of SGW2 with the rock sample are summarized inFigure 2-44. Since maintaining an exact 1:10 phase ratio (corresponding to *V/m* = 10 ml/g) was not consistently feasible in these experiments, the evolution of the liquid phase chemistry is presented as a function of the phase ratio *V/m*. The obtained data revealed the release of nearly all monitored ions, with the exception of Ca^{2+}, see Figure 2-44. The observed increase in ion concentration can be attributed to the mechanical grinding of rock grains during agitation and the dissolution of mineral components present in the rock sample. The decrease in calcium concentration within the rock-SGW2 system, compared to SGW2 water alone, may result from the capture of Ca^{2+} or the formation of solid carbonate phases (calcium carbonate). The confirmation of solid carbonate phase formation was achieved through speciation calculations, as discussed previously.

To elucidate the disparate sorption behaviors exhibited by Cs and Ni, additional sorption experiments were conducted without the inclusion of radioisotopes. The solid phase, migmatized gneiss PVP-2, underwent meticulous washing in SGW2 and was subsequently exposed to the liquid phase at a ratio of 1:10 (with a sample weight of 4 g). The liquid phase, derived from SGW2 water, was supplemented with $NiCl_2$ or CsCl at a concentration of 1x10-5 mol/l. The concentrations of selected ions were monitored employing a methodology akin to that expounded in chapter 1.3.3.3. Figure 2-44 portrays the time-dependent evolution of the chemical conditions upon the phase ratio *V/m*. The solid lines represent ion concentrations in the liquid phase in the absence of the rock sample.

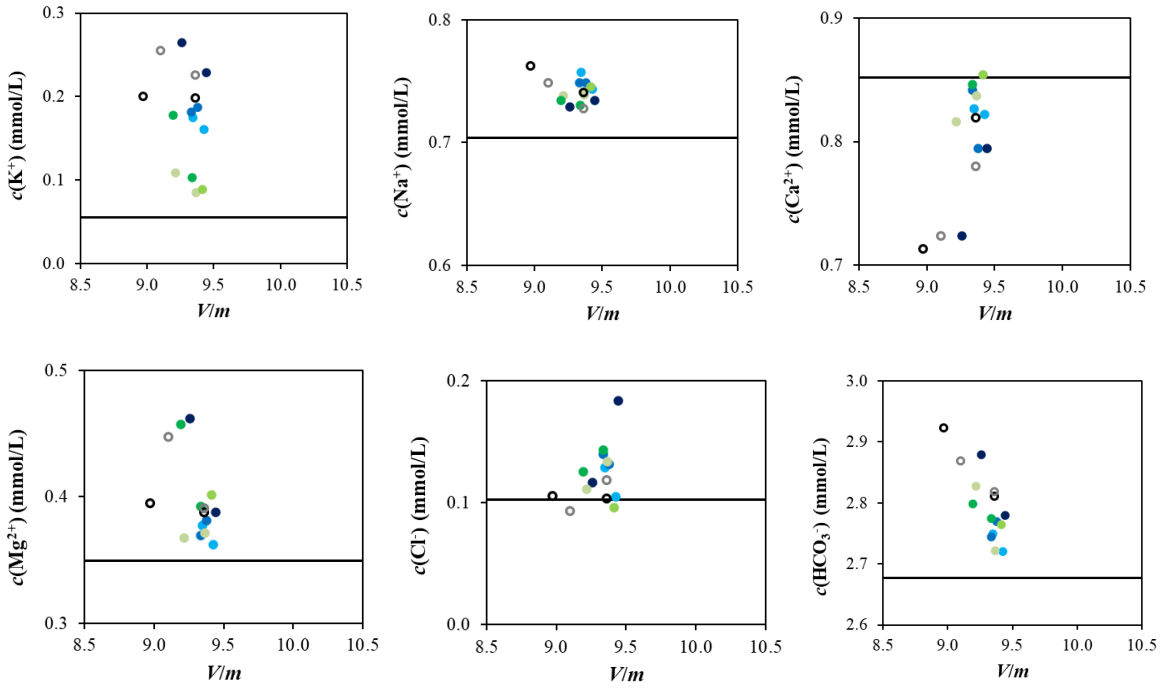

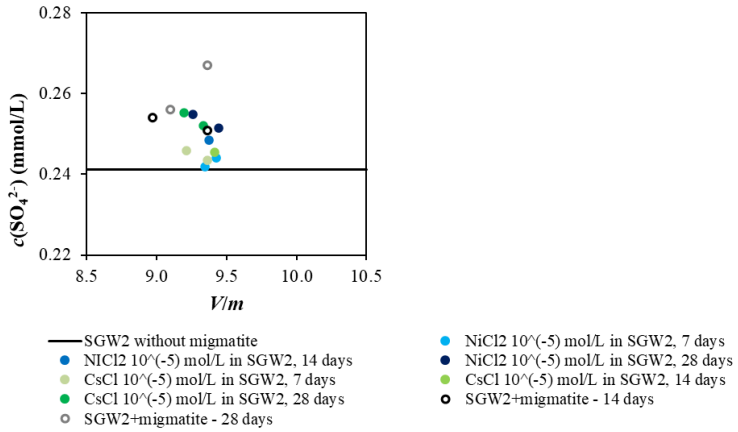

Figure 2-44 Measured ion concentrations during non-active sorption experiment with Ni and Cs on migmatized gneiss PVP-2, and the interaction experiment of PVP-2 with synthetic SGW2 water

The chemistry of the ions involved in the sorption experiments exhibited a high degree of similarity to that of the liquid phase when the rock was in contact with SGW2. With the exception of calcium, all ions, in presence of non active cesium and nickel carriers, were released into the liquid phase. Notably, potassium displayed a distinct behaviour during the sorption of cesium, as its release into the liquid phase did not occur to the same extent as observed during its interaction with SGW2 or during the sorption of nickel. Since potassium has a similar charge as cesium, it was expected that potassium would be the main exchangeable cation. In order to investigate the behaviour of potassium in the liquid phase of SGW2 water following its interaction with other host rocks and determine if similar trends are observed as in the case of PVP-2, additional non-active sorption experiments were conducted with the other host rocks. The leached potassium concentrations resulting from the non-active sorption experiments are presented on a concentration scale relative to the potassium concentration in SGW2 water, as depicted in Figure 2-45.

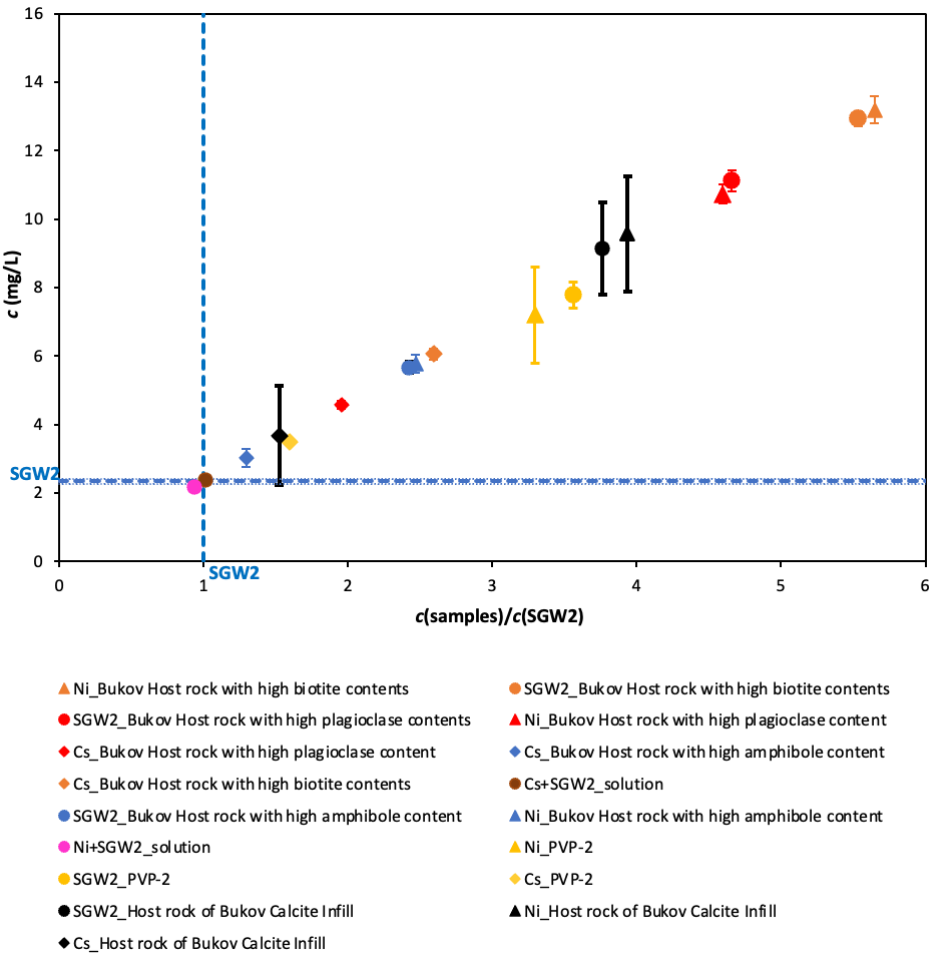

Figure 2-45 The potassium concentration in each sample after non-active sorption experiments was analyzed as a function of the ratio between the potassium concentration in the samples and the potassium concentration in pure SGW2

The analysis of leached potassium concentrations in non-active sorption experiments reveals that the sorption of Cs results in a lower release of potassium in all samples compared to the non-active nickel sorption experiments or experiments using SGW2 alone. One possible explanation is the Cs exchange sites, which induce the collapse of biotite interlayers (Park et al., 2019), leading to a reduced leaching of potassium in non-active sorption experiments involving all Bukov materials. Among the samples, the highest released amount of potassium is observed in the sample with the highest biotite content, specifically in Bukov samples with high biotite contents. For the Host rock of Bukov Calcite Infill and Bukov host rock with high plagioclase contents, as well as for PVP-2, the released amount of potassium is quite similar. However, the lowest amount of released potassium, consistent with the Cs sorption experiment, is observed in the Bukov host rock with high amphibole contents. Furthermore, the sorption of nickel occurs with minimal cation exchange, which aligns with findings from other studies where surface complexation is the predominant sorption mechanism at the given pH (Bradbury and Baeyens, 1995).

2.3.7.2 Leaching experiments with calcite and migmatite and determination of desorption distribution ratios for stable elements

Inventories of REEY: Total digestions of reference granites

A comparison of chondrite-normalized contents of REEY in these standards (Figure 2-46a) confirms their quantitative leaching by microwave total digestion using HBF_4, as the reference values agree with

the values measured in this study within the measurement uncertainties. For other analyzed elements (Figure 2-46b) this digestion method, which was developed for quantitative analysis of REEY (Zimmermann et al., 2020), provides reasonable estimates of contents of Cs, Rb, Th, U, Mn, and Ti for both reference materials, whereas contents of Ba, Sr, Zr, Ni, and V agreed with reference values only for one of the reference materials and deviations of contents of Fe, Al, P from reference values were larger than measurement uncertainties for both reference granites. Since the total digestions results in this study should solely facilitate putting into context the concentrations A_0 estimated by the extraction with 0.1 M HCl, their use is considered justified.

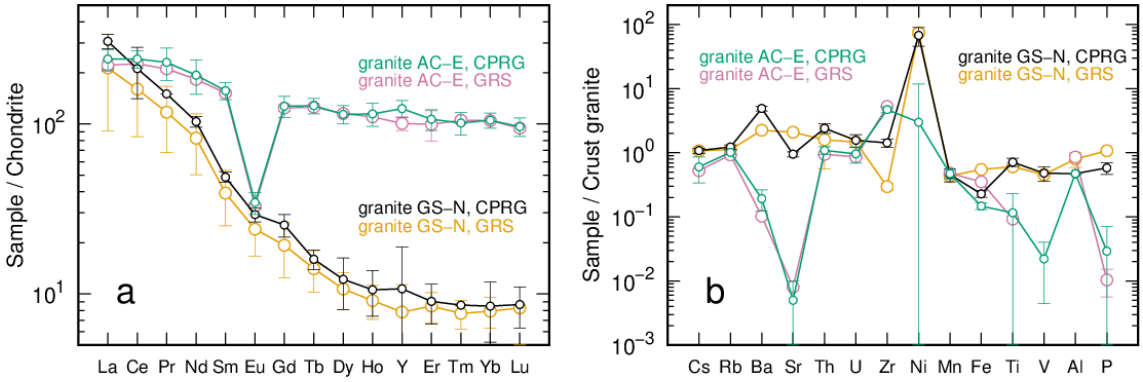

Figure 2-46 Comparison of reference values (CPRG) and values from total digestions of granites AC-E and GS-N (GRS) for REEY (a) and other elements (b) normalized by chondrite abundances (Evensen et al., 1978)

Inventories of REEY: REEY fractionation

Disregarding the positive lanthanum anomaly, which was expectedly observed for fracture filling and migmatite in the aqueous (SGW2) leaching and is usually explained by anomalously low hydrolysis constants of La as compared to its REEY neighbours (Bau, 1999), the patterns of aquatic leaching and extraction with 0.1 M HCl for fracture filling are similar and show an enrichment of middle (Sm to Dy) and heavy REEY (Figure 2-47). The overall upwards convex pattern of total digestion leaching is similar, e. g., to the pattern of calcite gangue minerals from base metal mineralization at Dikulushi, DR Congo, which originated from medium temperature (< 100–200°C) fluid (Debruyne et al., 2016).

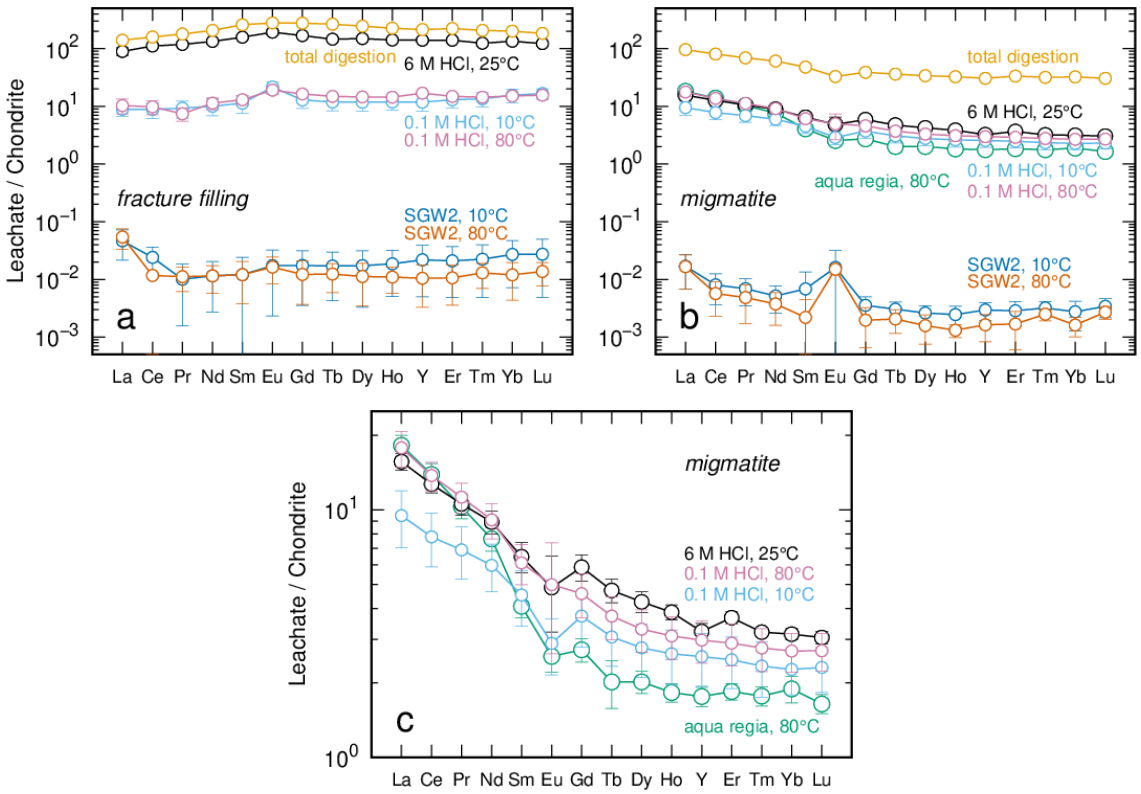

Figure 2-47 Concentrations of REEY released by fracture filling (a) and migmatite (b) upon total digestion, extractions with aqua regia, 6 M HCl, 0.1 M HCl, and leaching with SGW2. (c) shows a y-axis close-up of (b). Data for total digestion and extractions represent averages from triplicate batches, and for SGW2 averages from six triplicate batches (except 5 single batches for fracture filling and 2 for migmatite to be discussed in the following). Released inventories were related to the total sample mass and normalized by chondrite abundances (Evensen et al., 1978; abundance of Y was downscaled from Anders & Ebihara, 1982, by the factor of 1.0366 used in the latter paper to upscale the data from the former one).

Notably, aqueous leaching of REEY shows (i) a fractionation of middle and heavy REEY (MREE and HREE) vs. light REEY (LREE) with respect to desorption from fracture filling at 10°C and (ii) its clear dependence on the temperature (Figure 2-47a). These observations agree with similar observations by Quinn et al. (2007) for amorphous ferric hydroxide with free $REEY^{3+}$ ions as adsorbing species. Similarly, controlled calcite precipitation experiments reviewed by Debruyne et al. (2016) show a preferred retention of LREE over MREE and HREE with a trend break at Eu, as also observed here at 10 °C. Based on previous work, Debruyne et al. (2016) tentatively attributed the onset of fractionation above Sm or Eu to a difference in local coordination geometry of REEY with a transition from sevenfold to sixfold coordination. The absence of reliable thermodynamic data on temperature dependence of carbonate complexation of REEY (Migdisov et al., 2016) precludes a meaningful consideration of its possible effect on REEY desorption from calcitic fracture filling. However, in 0.1 M HCl and otherwise identical conditions no difference between 10 and 80 °C were observed (Figure 2-47a), which points out a probable effect of carbonate complexation. Moreover, for migmatite in 0.1 M HCl, a fractionation of LREE, Sm, and Eu vs. the other MREE and HREE with respect to desorption becomes obvious when comparing patterns observed at 10 and 80 °C (Figure 2-47b). This agrees with higher stability and mobility of LREE in chloride-bearing aqueous solutions and with their increase with increasing temperature (Migdisov et al., 2016).

For migmatite, the release of LREE, Sm, and Eu in 6 M HCl at 25 °C as compared to 0.1 M HCl at 80 °C remained nearly unchanged (an average ratio of 0.96 within a range of 0.88–1.06) but increased for the other MREE and HREE (an average ratio of 1.21 within a range of 1.08–1.29) (Figure 2-47c). This underlines the importance of the temperature effect (80 °C vs. 25 °C) for the fractionation of LREE vs. MREE and HREE and indicates its prevalence over the effect of chloride concentration (6 M vs. 0.1 M).

Even higher chloride concentration of 9.45 M applied at 80 °C in the aqua regia extraction to migmatite samples already treated by 6 M HCl confirms this tendency and shows a clear fractionation of LREE vs. MREE and HREE (Figure 2-47b,c), presumably as a result of chloride complexation, with the ratio between releases from aqua regia and 6 M HCl varying in the range of 0.86–1.16 for La to Nd as compared to 0.43–0.63 for Sm to Lu.

The aqueous leaching data for migmatite reveal a temperature effect, which has a magnitude similar to that for fracture filling but shows no clear fractionation tendency and may be attributed to the presence of c. 5.9 mass% of carbonates in migmatite and dominating carbonate complexation in SGW2 (Figure 2-47b). BET analyses (Figure 2-48) reveal that during aqueous leaching the specific surface areas of migmatite at 80 °C increase by a factor of 1.4–1.8 as compared to the value for unreacted material (0.25 ± 0.01 m²/g), whereas at 10 °C they vary in the range of 0.75–1.14 of the latter. This higher sorption capacity, which may be attributed to a transformation or neoformation of secondary minerals on the surface of migmatite grains, can explain the higher retention of REEY at 80 °C as compared to 10 °C. Indeed, the often-observed minor to negligible mobility of REEY during alteration of rocks was argued to be almost entirely due to the formation of REEY-bearing secondary minerals (Bau et al., 1998). The supernatants from batches at 80 °C as compared to those at 10 °C show a depletion of Mn and Ca, which might have participated in this formation (Figure 2-49b).

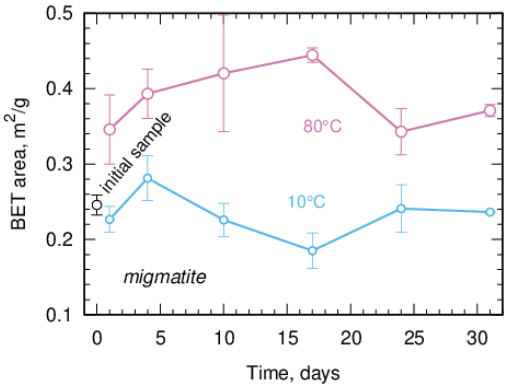

Figure 2-48 BET area for migmatite samples before and after reaction at 10 and 80 °C (grain fraction 1–2 mm, triplicate averages).

Inventories of REEY: Sources of REEY

A comparison of data for fracture filling and migmatite in Figure 2-47 provides furthermore important clues concerning possible source(s) of REEY in these materials. Firstly, aqueous leaching at 10°C shows a LREE enrichment accompanied by a positive Eu anomaly for migmatite and a HREE enrichment for fracture filling, which agrees with the origin of water soluble REEY in migmatite from high-temperature hydrothermal fluids and those in fracture filling from low-temperature hydrothermal fluids or pore waters (e. g., meteoric waters) (Perry & Gysi, 2020; Zhao et al., 2021). A strong positive Eu anomaly in aqueous leaching of migmatite agrees also with observations for natural water samples from migmatites from the Black Forest (Göb et al., 2013). The water accessible REEY inventory in fracture filling is on average 5.1 times higher than in migmatite, which underlines that fracture filling's inventory does not originate from migmatite's one.

Secondly, the water accessible patterns differ strongly from the patterns of the total digestion, which proves there are at least two retention pools of REEY in fracture filling and migmatite, a water accessible one with a much lower capacity and a less accessible one. The REEY concentrations in the less accessible pool exceed those in the water accessible one by about 4 and 5 orders of magnitude for fracture filling and migmatite, respectively. It can be suggested that these pools originate, e. g., from different episodes of contact with meteoric waters for fracture filling and metamorphic vs. hydrothermal deposition for migmatite. Although plagioclase is a major constituent of the studied migmatite (Table

2-1) and can be expected to be Eu-enriched during partial melting in lower crust (Krämer et al., 2015), amphibole's (migmatite's second major constituent) representative hornblende was observed to have an order of magnitude higher REEY content and to be characterized, like another major constituent biotite, by a negative Eu anomaly (Tillberg et al., 2019), which can explain the negative Eu anomaly in total digestion pattern of migmatite (Figure 2-47b). This pattern corresponds also to a pattern observed previously for a sample of biotitic migmatite from the URF Bukov, which showed however a higher La/Lu ratio (Bukovská et al., 2018). The strong difference between the total digestion patterns of fracture filling, with an upwards convex pattern, and migmatite, with a LREE-enriched, negative-Eu-anomaly pattern, confirms that fracture filling's REEY inventory stems from another source than migmatite, as fracture filling would otherwise inherit the pattern of migmatite (Möller, 2000). Besides, the total REEY inventory in fracture filling is on average 5.6 times higher than in migmatite, which supports origination of the less accessible fracture filling's inventory from another source than migmatite.

The reason for the occurrence of the high positive Eu anomaly of 3.26 or 7.25 at 10 or 80 °C, respectively (calculated from chondrite-normalised data as $Eu_{CN}/(Sm_{CN}\times Gd_{CN})^{0.5}$ according to, e. g., Göb et al. (2013)), in water accessible REEY inventory of migmatite despite the negative Eu anomaly of 0.77 of its total REEY inventory (Figure 2-47b) can be attributed according to Möller et al. (1997) to a decoupling of Eu from its neighbouring REEY during the high T-P metamorphosis, during which it is in oxidation state of 2+ and has a larger ionic radius than at temperatures below about 200–250 °C, at which it oxidizes to Eu^{3+}. Eu remained thus preferentially in the intergranular space of newly formed minerals and was incorporated either in their surface layers or in accessory minerals, being as a result more accessible than neighbouring REEY to aqueous leaching. This mechanism was invoked by Möller et al. (1997) to explain a common observation of positive Eu anomaly in aqueous leaching of gneisses, although their total REEY inventory shows a small negative Eu anomaly.

Inventories of REEY: Phases responsible for REEY retention in fracture filling

For fracture filling, the REEY pattern of extraction with 0.1 M HCl appears to represent rather an intermediate stage between the patterns of aqueous leaching and extraction with 6 M HCl or total digestion both showing very similar patterns (Figure 2-47a). The extraction with 6 M HCl dissolved 98.0 ± 3.1 mass% of fracture filling and released 64 ± 4 % of the total REEY inventory (Table 2-22, Table 2-23), and the remaining 2 mass% of fracture filling represent obviously a refractory contaminating phase contributing about 36 % of the total REEY inventory. Concentrated HCl is known to dissolve carbonates, phosphates, borates, sulphates (except barite), and metal oxides such as iron and manganese oxides (Müller et al., 2014). Indeed, along with the host calcite phase (356535 ± 13090 mg/kg Ca), 6 M HCl dissolved also 4988 ± 460 mg/kg Fe, 3858 ± 462 mg/kg Mn, 2131 ± 5 mg/kg Mg or 90, 64, 72, and 77 % of their total inventories, respectively (Figure 2-49a), whereas the releases of trace elements Na, K, Ti, P, and S were considerably lower than that of 549 ± 40 mg/kg REEY and their role in incorporation of REEY in fracture filling can be hence neglected. For comparison, extraction with 0.1 M HCl at 10 or 80 °C released 18–19, 11, 15–17, and 12–13 % of the total inventories of Ca, Fe, Mn, and Mg, respectively. The loss of 18–19 % of Ca correlates with the loss of 16–18 % of mass in this extraction (Table 2-22). Furthermore, Ca/Fe, Ca/Mn, and Ca/Mg ratios vary only moderately from 76–77, 72–77, and 182–184 for extraction with 0.1 M HCl at 10 or 80 °C to 65, 83, and 151 with 6 M HCl, respectively. This indicates that Fe and Mn, either as structural ions or as contaminating particulates (Cao et al., 2020), as well as Mg, most probably as a structural ion, are relatively homogeneously distributed withing the calcite phase of fracture filling. In contrast to this, REEY inventory accessible with 6 M HCl is a factor of 11.8 or 9.6 higher than that accessible with 0.1 M HCl at 10 or 80 °C with Ca/REEY ratio increasing from 586 to 1361 or 1173, respectively.

These observations indicate that (i) REEY withing the surface layer (with a thickness of 64 µm based on data in Table 2-22 and assuming a homogeneous dissolution of a 1-mm grain with a cubic habit in contact with 0.1 M HCl at 80°C), which hosts 18–19 % of Ca, are depleted with respect to the grain core covered by this layer, and (ii) Fe, Mn, and Mg do not govern the REEY incorporation in the calcite phase of fracture filling. The close similarity of REEY patterns of the extraction with 6 M HCl and the total digestion indicates that the REEY-enriched grain core and the refractory contaminating phase formed

co-genetically. The major and minor element abundancies of this refractory phase can be estimated from the difference between the releases of the extraction with 6 M HCl and total digestion to consist of about 59.1 % Ca, 26.9 % Si, 4.8 % Fe, 4.3 % Al, 2.5 % Mn, 1.1 % Mg, 0.5 % REEY, and 0.5 % mg/kg K.

Table 2-22 Masses (%) dissolved in extractions

	0.1 M HCl 10 °C	0.1 M HCl 80 °C	6 M HCl	aqua regia
fracture filling	15.7 ± 0.5	18.1 ± 0.6	98.0 ± 3.1	–
migmatite	2.7 ± 0.3	5.9 ± 0.5	4.6 ± 1.3	8.1 ± 6.6

Table 2-23 Released REEY inventories (mg/kg)

	SGW2 10 °C	SGW2 80 °C	0.1 M HCl 10 °C	0.1 M HCl 80 °C	6 M HCl 25 °C	aqua regia	total digestion
fracture filling	0.07 ± 0.06	0.05 ± 0.02	46 ± 14	57 ± 3	549 ± 40	–	849 ± 15
migmatite	0.02 ± 0.01	0.02 ± 0.01	18 ± 4	27 ± 4	27 ± 2	23 ± 2	198 ± 14

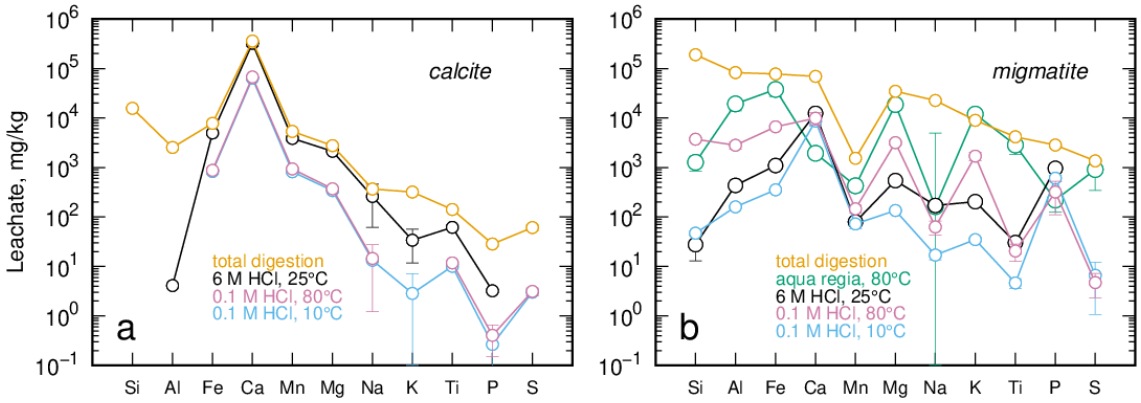

Figure 2-49 Concentrations of major and minor stable elements released by calcite (a) and migmatite (b) upon total digestion, extractions with aqua regia, 6 M HCl, and 0.1 M HCl. Data for total digestion and extractions represent averages from triplicate batches. Released inventories were related to the total sample mass. Abundances of Na, K, Ti, P, and S in calcite are below 0.1 %, which qualifies them as trace elements, and shown for comparison with migmatite.

Inventories of REEY: Release of REEY from the surface of fracture-filling grains

Leaching with SGW2 can be expected to access only the outermost surface layer of fracture-filling grains. Its REEY inventory contributes only 0.1–0.15 % of the REEY inventory accessible with 0.1 M HCl (Table 2-23) but is characterized by a similar Ca/REEY ratio of 1204 at 10 °C. Based on the Ca inventory released to SGW2 at 10 °C and assuming a homogeneous dissolution of a 1-mm grain with a cubic habit, this water-accessible surface layer can be estimated to have a thickness of 70 nm. Releases of 13 water-accessible REEY (Pr–Lu) at 10 °C show a strong positive correlation with releases of Mn (correlation coefficients in the range 0.88–1.00 with an average of 0.96 ± 0.04), Fe (0.86–0.96, 0.92 ± 0.03), and Al (0.63–0.91, 0.84 ± 0.07), as shown in Figure 2-50 for Eu, Dy, and the total REEY release, and the releases of Mn, Fe, and Al correlate with each other (correlation coefficients of 0.93, 0.92, and 0.79 for the pairs Mn-Fe, Fe-Al, and Al-Mn, respectively). Notably, Ca/Fe and Ca/Mn ratios of 59 and 45 for this layer differ only moderately from those of extractions with 0.1 M and 6 M HCl discussed in the previous sub-section, whereas Ca/Al ratio of 61 is much lower than that of 78181 for 6 M HCl with

one third of Al accessible with 6 M HCl residing in the water-accessible layer. According to the aqueous leaching data obtained at 80°C, this layer contains about 4 % and 1 % of the total inventory of Si and Al in fracture filling and their releases at a Si/Al ratio of 31 correlate with a correlation coefficient of 0.93 (the missing detection of Si for 0.1 M HCl and 6 M HCl extractions can be probably attributed to its re-precipitation following high releases of Ca, whereas the missing detection of Si for aqueous leaching at 10 °C is probably related to the solubility of Si, which for amorphous silica or quartz at 10 °C is lower by a factor of 3.4 or 6, respectively, than at 80 °C (Gunnarsson & Arnórsson, 2000)).

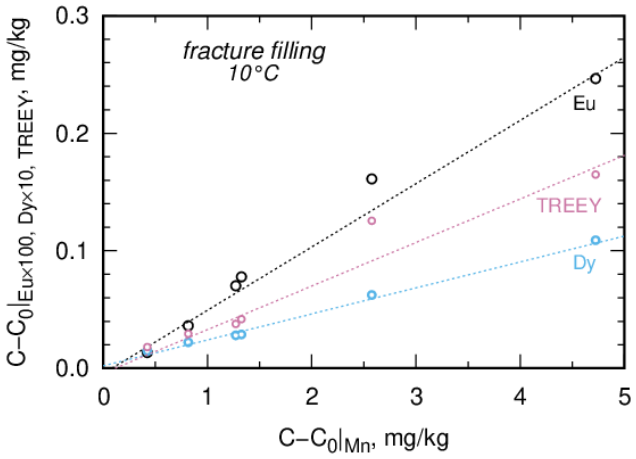

Figure 2-50 Concentrations of Eu (×100), Dy (×10), and the total REEY concentration (TREEY) released by fracture filling upon leaching with SGW2 at 10 °C in dependence on Mn releases. Data represent averages from triplicate batches (except 4 single batches to be discussed in the following). Released inventories were related to the total sample mass.

The water-accessible Ca/Mg ratio of 3.3 reveals a Mg enrichment by a factor 45–55 with respect to fracture-filling phases accessible with 0.1 M HCl and 6 M HCl extractions (Figure 2-49a). This ratio is much closer to Ca/Mg ratios of 6.9 and 3.1 for aqueous leaching and total digestion of migmatite (Figure 2-49b), which may indicate some contamination of the outermost surface layer of fracture-filling grains with nanoscale migmatite particles. E. g., grain surfaces of calcite in chalk were found to be partially covered by 1–4 nm thick clay particles (Skovbjerg et al. 2012). Unfortunately, the data set of water-accessible major and minor elements obtained here is to small to substantiate or reject this indication. Yet, the trace element data obatined for fracture filling reveal Rb/Cs ratios of 11.8 ± 1.6 and 12.9 ± 2.7 for aqueous leaching at 10 °C and 80 °C, respectively, which differ strongly from the ratios of 3.1 and 5.6 for 0.1 M HCl and 6 M HCl extractions. At the same time, these Rb/Cs ratios are close to the ratios of 11.8 ± 1.5 and 8.2 ± 2.2 obtained for aqueous leaching of migmatite at 10 °C and 80 °C, respectively, and of 12.0 for total digestion of migmatite. According to Göb et al. (2013), Rb/Cs ratios for less altered migmatites and gneisses vary in the range of 5–20 with a median of about 8, which agrees with the obtained values and may provide some support to the inference on possible contamination of calcite grains with nanoscale migmatite particles.

Inventories of REEY: Release of REEY-enriched colloids in aqueous leaching

In 5 out of 36 aqueous leaching batches with fracture filling an anomalously high release of REEY was observed (Figure 2-51a). The REEY inventory released in these batches was a factor of 39–846 higher than the average REEY inventory released in the other leaching batches. Moreover, for three batches, these releases correspond to 47–127 % of REEY inventory released by 0.1 M HCl at 10 °C (cf. Figure 2-47a). Based on measured supernatant Ca concentrations, the anomalously high releases of REEY in these five batches were accompanied by a release of 0.3–6.2 % of Ca, with Ca and REEY releases characterized by a correlation coefficient of 0.99 and a Ca/REEY ratio of 350 ± 62, whereas in the other batches a release of up to 0.05 % or a precipitation of up to 0.4 % of the initial Ca in fracture filling and no correlation between Ca and REEY releases were observed. This Ca/REEY ratio is lower than that of

586 obtained from the extraction with 6 M HCl, which indicates that the released REEY are hosted by some contaminating mineral phase characterized by a higher REEY inventory than the calcite phase of the fracture filling and buried within it.

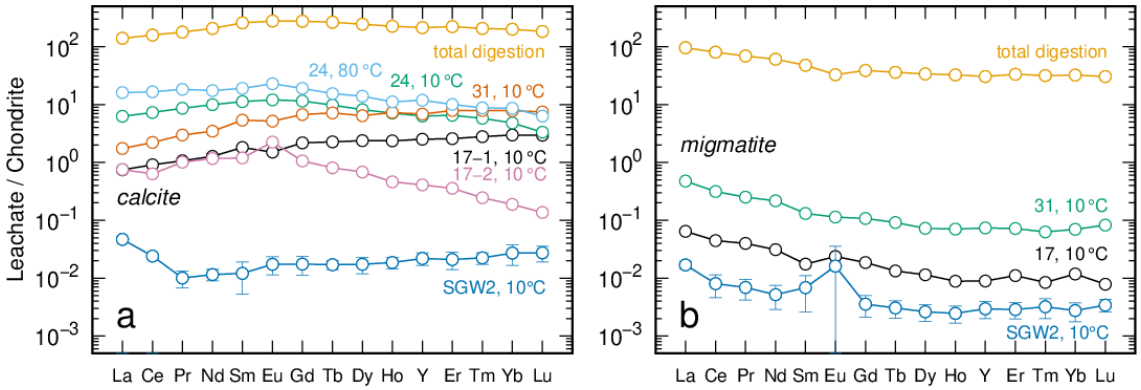

Figure 2-51 Concentrations of REEY released as REEY-enriched particles by fracture filling (a) and migmatite (b) after leaching with SGW2 for 17, 24, and 31 days at 10 °C and 24 days at 80°C. Data for total digestion and leaching with SGW2 at 10 °C from Figure 2-47 are shown for comparison. Released inventories were related to the total sample mass and normalized by chondrite abundances (Evensen et al., 1978).

A consideration of the releases in the REEY-enriched, 24-day batch at 80 °C, at which Si could be detected in aqueous leaching batches (Figure 2-49a), subtracted by the releases from the other two batches of the common triplicate batch, which measure the contribution from the outermost surface layer of calcite grains, provides additional details on this putative contaminating mineral phase. The resulting Ca/Fe, Ca/Mn, and Ca/Mg ratios of 63, 53, and 176 are comparable to those of 65, 83, and 151, respectively, obtained from the extraction with 6 M HCl (Figure 2-49a) and manifest a moderate (by 57 %) enrichment of Mn, possibly related to the contribution of the contaminating phase, and a depletion of Mg of the REEY-enriched releases, whereas the Ca/Si ratio of 245 can be attributed to the contribution of the contaminating phase. Assuming that the Ca/REEY ratio of 376 for this batch and the Mn enrichment by 57 % is completely due to the contaminating phase, the composition of the contaminating phase corresponds to a formula $Mn_{2.5}Si_{1.5}REEY$.

The ratio between Si and REEY in this formula would increase for the case that the enveloping calcite phase incorporates non-negligible amounts of REEY as structural ions. E. g., it can be alternatively assumed that REEY-depleted layer of fracture filling accessible with 0.1 M HCl does not contain contaminating mineral phases and its Ca/REEY ratio of 1267 ± 94 is completely due to REEY incorporated as structural ions in the calcite phase, which is representative of the calcite phase accessible with 6 M HCl and enveloping the contaminating mineral phase buried within it. Subtracting this contribution from the Ca/REEY ratio of 376 of the discussed REEY-enriched batch results in a Ca/REEY ratio of 539 for the contaminating phase, which is much closer to the Ca/REEY 586 obtained from the extraction with 6 M HCl. The composition of the contaminating phase would then correspond to a formula $Mn_{3.6}Si_{2.2}REEY$.

Overall, Fe and Mn releases in the REEY-enriched batches strongly correlated with REEY and Ca releases (correlations coefficients of 0.98–1.0) at Fe/REEY and Mn/REEY ratios of 7.7 ± 1.9 and 6.5 ± 1.6, and Ca/Fe and Ca/Mn ratios of 47 ± 9 and 55 ± 4, respectively, which manifests a moderate (by 40–50 %) enrichment of Fe and Mn in releases with respect to the calcite phase of fracture filling characterized by respective Ca/Fe and Ca/Mn ratios of 65 and 83 obtained from extraction with 6 M HCl.

These observations indicate that some REEY-enriched fracture-filling particulates with a characteristic Fe-Mn signature of the calcite phase are released into supernatant solution, pass through the filter with a pore size of 0.45 µm during the filtration step and are dissolved upon subsequent acid treatment. Based on the simplifying assumption that in a batch a single particulate of a pure $CaCO_3$ with a density

of 2.71 g/cm³ and a cubic habit is released, their Ca inventory of 0.3–6.2 % of the initial Ca in fracture filling corresponds to a mass range of 1–17 mg and a size range of 1–20 µm. Obviously, such particulates could only pass through a filter with a pore size of 0.45 µm, if at least one of their dimensions is below that value. It seems however more probable that multiple colloidal particulates with a size <0.45 µm were released in the aqueous leaching batches.

In two further batches, 17–1 and 31, REEY-enriched colloids with a Ca/REEY ratio of 330 ± 2 show a HREE enrichment, a LREE depletion, and a negative Eu anomaly of 0.76 and 0.85, respectively (Figure 2-51a), which are not characteristic of the studied fracture filling and should obviously have a different origin. Such pattern was also observed for a fracture filling sample from URF Bukov (Bukovská et al., 2018; according to a discussion there, that sample have originated from the same tunnel BZ-XII-J-219.4m as the fracture filling sample studied here), a hydrothermal carbonate from Nkana–Mindola (Debruyne et al., 2016), and a hydrothermal type A dolomite from the George Fisher massive sulphide deposit (Rieger et al., 2021).

The combination of a LREE depletion and a negative Eu anomaly in these two batches represents a special feature. A negative Eu anomaly in fracture calcites can be inherited from parent gneisses and granites during fluid-rock interactions along the flow pathway (Möller et al., 1997; Munemoto et al., 2015), however, the LREE enrichment characteristic of these rocks and migmatite (Figure 2-51b) would usually also be inherited unless calcite precipitates from a Cl^--rich saline hydrothermal fluid, which is able to retain LREE (Rieger et al., 2021). An alternative source for a negative Eu anomaly in carbonates can be their deposition at a temperature above 200–250 °C, at which, as discussed above, Eu is in oxidation state of 2+ and has an ionic radius of 1.17 Å (Shannon, 1976), which is much larger than that of 0.99 Å for Ca^{2+} and prevents its incorporation in carbonates. A hydrothermal origin of colloids in these two batches would also agree with their chondritic Y/Ho values of 28.0–28.1, which are typical of hydrothermal fluids, whereas the sub-chondritic Y/Ho values of the fracture-filling sample (24.9) and colloids in the other fracture-filling batches (23.4–24.6) would agree with the observed previously stronger Ho partition into calcite (Tanaka and Kawabe, 2006; Rieger et al., 2021) because of the anomalously weak surface complexation of Y relative to Ho and its REE neighbours (Bau & Koschinsky, 2009).

One possible explanation for the presence of the REEY-enriched colloids 17–1 and 31 would be that they were deposited at a different location and different hydrochemical and thermal conditions than the enveloping calcite phase as a result of high-temperature fluid-rock interaction and were transported by hydrothermal fluids to the studied site. An alternative scenario assumes that in the first step. a contaminating mineral phase formed in-situ at temperatures above 200–250 °C, producing thus a Eu^{2+} enrichment in the solution, from which in the second step, after a cooling down below these temperatures and oxidation of Eu^{2+} to Eu^{3+}, enveloping calcite phase or another contaminating phase incorporating Eu^{3+} was formed. Both scenarios presuppose a presence of hydrothermal fluids, which agrees with the observation of atypical presence of secondary inclusions of aqueous solution and of higher hydrocarbons in the calcite sample, which have originated from the same tunnel BZ-XII-J-219.4m as the fracture filling sample studied here, due to, presumably, its heat overprint (Bukovská et al., 2018). Considering that major elements Fe and Mn, which are relatively homogeneously distributed in the calcite phase as discussed in the previous section, are characterised by very similar Ca/Fe and Ca/Mn ratios for these REEY-enriched colloids and fracture filling (45 ± 3 vs. 46 and 60 ± 1 vs. 67, respectively), it can be supposed that these colloids were formed in Ca-, Fe-, and Mn-reach fluids during the transport to or upon reaching the deposition site, where they were co-precipitated and incorporated into the studied fracture filling.

Colloids in the other three batches show MREE enrichment similar to the patterns of extraction with 6 M HCl and total digestion albeit with a factor 2.5–7.5 higher Ln/Lu ratio. The colloids in batch 17-2 show additionally a positive Eu anomaly of 1.99, which is more pronounced than in the other fracture-filling batches and a negative Ce anomaly of 0.72 (calculated from chondrite-normalised data as $Ce_{CN}/(La_{CN}\times Pr_{CN})^{0.5}$ according to, e. g., Göb et al. (2013)), which indicates their possible origin from fluids with a high oxygen fugacity (Göb et al., 2011). Hydrothermal calcites of REEY mineral deposits

with a strong metasomatic overprint are characterized by MREE and HREE enrichments, whereas in magmatic settings LREE enrichment is expected (Debruyne et al., 2016; Perry & Gysi, 2020). Numerical modelling predicts that low temperatures and high salinities (100–250 °C; 20 wt.%) facilitate incorporation of HREE into calcite, whereas above 350 °C the LREE are more compatible in its structure (Perry & Gysi, 2018).

The presence of both, MREE and HREE enriched mineral phases in the studied fracture filling may evidence that its REEY incorporation occurred following at least two infiltration episodes, as these enrichments are usually ascribed to different mechanisms (Zhao et al., 2021). Taking into account the discussion on REEY patterns in the previous section, it can be suggested that the MREE-enriched phase postdates the more deeply buried MREE-enriched phase, as it is readily available for aqueous leaching. It can be further speculated that the buried MREE-enriched phase may have been partially uncovered, e.g., during the preparation of the grain fraction 1–2 mm of fracture filling, in some sub-samples and became thus accessible to aqueous leaching.

Inventories of REEY: Phases responsible for REEY retention in migmatite

The REEY inventory accessible with 6 M HCl (27 ± 2 mg/kg, 13 ± 2 % of the total REEY inventory in migmatite, Table 2-23) is only a factor of 1.5 higher or equal to that accessible with 0.1 M HCl at 10 or 80 °C, respectively. Considering the much lower or comparable inventories of Al, Na, Ti, and S accessible with 0.1 M HCl at 10 °C (Figure 2-49b), the role of Al-, Na-, Ti-, and S-containing mineral phases accessible with HCl in incorporation of REEY in migmatite can be most probably neglected. Furthermore, despite a factor of 6–134 higher release of Si, Fe, and Mg with 0.1 M HCl at 80 °C as compared to 6 M HCl, the REEY inventory does not increased, which suggests that only a portion of HCl-accessible Si-, Fe-, and Mg-containing mineral phases, if any, can be responsible for the retention of REEY.

In addition to minerals dissolved by HCl, aqua regia can dissolve further metal oxides (e.g., uranium oxides), sulphides and organic matter as well as leach elements from certain silicates such as biotite and feldspar (Xu et al. 2012). Aqua regia released additionally about the same REEY inventory of 23 ± 2 mg/kg (Table 2-23), but a factor of 5–93 higher inventories of Si, Al, Fe, Mn, Mg, K, and Ti (Figure 2-49b). The missing correlation between these releases indicates that mineral phases hosting these element inventories are characterized by much lower REEY concentrations than the HCl-accessible ones. Elemental abundances in the mineral residue after the consecutive extractions with 6 M HCl and aqua regia show a significant (by more than 0.1 %) increase from those obtained by total digestion for Si (from 38.3 % to 49.2 %), Ca (13.9 % to 14.3 %), and Na (4.5 % to 5.8 %) as well as decrease for Al (from 16.6 % to 16.3 %), Fe (15.6 % to 10.1 %), Mg (7.0 % to 4.1 %), K (1.8 % to 0 %), Ti (0.8 % to 0.3 %), and P (0.6 % to 0.4 %).

Notably, the mass digested in migmatite by the extraction with 0.1 M HCl at 80 °C (5.9 ± 0.5 mass%, Table 2-22) corresponds to its carbonate content assessed through decomposition of solid carbonates with 6 M HCl by the carbonate bomb method (5.9 ± 0.2 mass%) and to the mass digested by the extraction with 6 M HCl at 25 °C (4.6 ± 1.3 mass%). This indicates that for migmatite, a preferential dissolution of carbonates, perhaps accompanied with a minor dissolution of some other non-refractory secondary accessory phases, as discussed above for fracture filling, is a more probable source of REEY in the extractions with 0.1 M or 6 M HCl than primary major or accessory phases of migmatite, as during the genesis of migmatite, REE concentrations in partial melts are controlled by accessory minerals, which may be refractory or remain as inclusions in residual major minerals (Nabelek, 1999). A partial dissolution of other, non-carbonate phases in extractions of migmatite with HCl is evidenced by considerable releases of Si and Al (Figure 2-49b) and may be additionally indicated by a strong temperature dependence of Ca/Fe, Ca/Mn, and Ca/Mg ratios, which do not depend on temperature for fracture filling but decrease for migmatite from 25, 120, and 64 at 10 °C to 1.5, 68, and 3 at 80 °C, respectively. Taking into account that REEY patterns of these extractions and of the total digestion for migmatite are very similar with characteristic LREE enrichment and negative Eu anomaly, it can be further inferred that the carbonate phase in migmatite does not represent a contamination originating

from the fracture filling and inherits its REEY inventory from migmatite as a result of water-rock interactions in the pore space of the migmatite.

For the putative carbonate phase in migmatite, Ca/REEY ratio equals to 422 ± 59 and 454 for the extractions with 0.1 M and 6 M HCl, respectively, whereas for fracture filling the values of 1267 ± 94 and 586 were observed as discussed above. This suggests that calcite phase in both materials incorporated REEY at similar concentrations, however, in migmatite the REEY are much more homogeneously distributed across the grains of the calcite phase than in fracture filling. Notably, whereas Mg/REEY and Fe/REEY ratios for extractions of fracture filling and migmatite with HCl vary in the ranges of 4–116 and 9–243, respectively, Mn/REEY ratio varies in a much narrower range of 3–18. Moreover, whereas the former ranges extend to 176 and 392 for total digestion of both materials or even to 800 and 1620 for extraction of migmatite with aqua regia, the range for Mn/REEY ratio remains unchanged. Again, for REEY-enriched colloids released during aqueous leaching, discussed above for fracture filling and to be discussed below for migmatite, Mg/REEY and Fe/REEY ratios vary broadly in the ranges of 0.5–355 and 3–629, respectively, whereas Mn/REEY ratio varies in the ranges of 5–12. The both residues, a Ca-silicate phase after 6 M HCl extraction of fracture filling and a Ca-aluminosilicate phase after aqua regia extraction from migmatite, show a Mn/REEY ratio of 5 and 7, respectively, whereas Mg/REEY and Fe/REEY vary in the ranges of 2–110 and 9–262. This, along with the correlation between REEY and Mn aqueous releases as discussed to Figure 2-50, points out a possible co-genetic or co-deposition relation between Mn and REEY in the studied system.

Inventories of REEY: Release of REEY from the surface of migmatite grains

As discussed above on sources of REEY in migmatite, the occurrence of the high positive Eu anomaly of its water accessible REEY pattern despite the negative Eu anomaly of the patterns from total digestion as well as extractions with HCl and aqua regia can be attributed to a preferential Eu incorporation in the surface layers of grains of migmatite's major or minor minerals or in its accessory minerals. In a further difference to the patterns from extractions with HCl, aqua regia, and total digestion, water-accessible fraction of migmatite shows a negative Ce anomaly of 0.74 at 10 °C and 0.63 at 80 °C (Figure 2-47b), which indicates their possible origin from fluids with a high oxygen fugacity (Göb et al., 2011). In the latter paper, oxidation of Ce^{3+} to less soluble Ce^{4+} is argued to lead either to coupled positive and negative Ce anomalies occurring in adjacent coprecipitating minerals or to decoupled ones developing during transport. In the latter case, the migrating fluid carries a negative Ce anomaly which is inherited upon REEY adsorption or precipitation from the fluid at another location. Since HCl and aqua regia extractions do not indicate a presence of minerals with a positive Ce anomaly, it can be assumed that REEY deposited on the surface of migmatite grains were transported to the studied site after having been leached from a rock with a similar REEY pattern to the studied migmatite by oxic fluids. Considering further that carbonate-rich waters were found to stabilize Ce^{4+} in polycarbonate complexes and hence preserve positive Ce anomalies (Möller & Bau, 1993), this transport occurred most probably before arrival of carbonate-rich waters and formation of carbonate phases in the studied fracture. From the aforementioned, it can be inferred that the REEY pattern observed for the surface of migmatite grains possibly documents an occurrence of inflow of fluids, which might have preserved or not their oxygen fugacity along the migration pathway, prior to infilling the fracture with the studied carbonate phase.

Although the extractions with HCl were argued in the preceding sub-section to dissolve primarily a carbonate phase in migmatite, evidence was also presented for a dissolution of non-carbonate phases. Their effect in aqueous leaching, in which SGW2 contacts the prevailing surface area of non-carbonate migmatite minerals, can be assumed. However, the limited data set on non-REEY elements released in aqueous leaching of migmatite (Figure 2-49b) does not allow a differentiation of the contribution of its carbonate and non-carbonate phases. Yet, in a similarly to fracture filling, releases of 8 REEY at 10 °C, 12 REEY at 80 °C, and of total REEY show a strong positive correlation with releases of Mn (correlation coefficients in the range 0.77–0.99).

Inventories of REEY: Release of REEY-enriched colloids in aqueous leaching

In 2 out of 36 aqueous leaching batches with migmatite a factor of 4.4–31 increased release of REEY was observed, which was however a factor 4–30 lower than the lowest colloidal REEY release for fracture filling (Figure 2-51). No considerable Ca release is observed for these colloids either. Colloids in the batch 17 show a strong difference from the other batches for Fe/REEY and Ti/REEY ratios of 629 and 52, respectively, which lie between the respective values of 392 and 21 for total digestion (with even lower values for extractions with HCl) as well as 1620 and 122 for aqua regia extraction. It can be inferred hence that these colloids represent a mineral phase not accessible with HCl. In contrast, these ratios for colloids in the batch 31 are close to the values obtained for extraction with 0.1 M HCl at 10 °C, which suggests that they belong to a mineral phase readily accessible with HCl.

Similarly to the water-accessible REEY pattern, colloids in the batch 17 carry a positive Eu anomaly of 1.31 and a negative Ce anomaly of 0.88. However, the deviation from the unity is in this case considerably smaller than in the former case. Considering its a factor of only 4.4 higher REEY inventory than the water-accessible one, a dilution of REEY transported by oxic fluids, as discussed in the preceding sub-section, by REEY incorporated in migmatite grains during metamorphic fractionation can be suggested to explain this observation. The same probably applies also to colloids in the batch 31, which possess a higher REEY inventory and show accordingly a lower deviation of Eu and Ce anomalies from the unity.

Inventories of other trace elements

This sub-section will be added later.

The trace element data obatined for fracture filling (Figure 2-52a) reveal that water-accessible inventories of Cs, Rb, Ba, V, U, and I, which reside in the outermost layer of fracture-filling grains, are responsible for the release of these elements in extractions with 0.1 M HCl. This lends support to the assumption made above that REEY-depleted layer of fracture filling accessible with 0.1 M HCl does not contain contaminating mineral phases. If so, 16–18 % of total Sr and 5–6 % of total Ni residing in this pure calcite phase are probably incorporated as structural ions at Ca/Sr and Ca/Ni ratios of about 2630 and 30000, respectively. The remaining calcite phase, which contains contaminating phases and is accessible with 6 M HCl, hosts further up to 65 % of total Sr (Ca/Sr ratio of 2700) and 10 % of total Ni (Ca/Ni ratio of 49300). The refractory residue of fracture filling hosts 19 % of total Sr (Ca/Sr ratio of 1260) and 85 % of total Ni (Ca/Ni ratio of 970). Notably, water-accessible Ca/Sr and Ca/Ni ratios of 544 and 1471, respectively, measured at 10 °C do not match the values from HCl extractions, characteristic of calcite phase, and are much closer to the values for refractory residue and values of 253 and 884 for migmatite (Figure 2-52b), which points out a possible contamination of the outermost surface layer of fracture-filling grains.

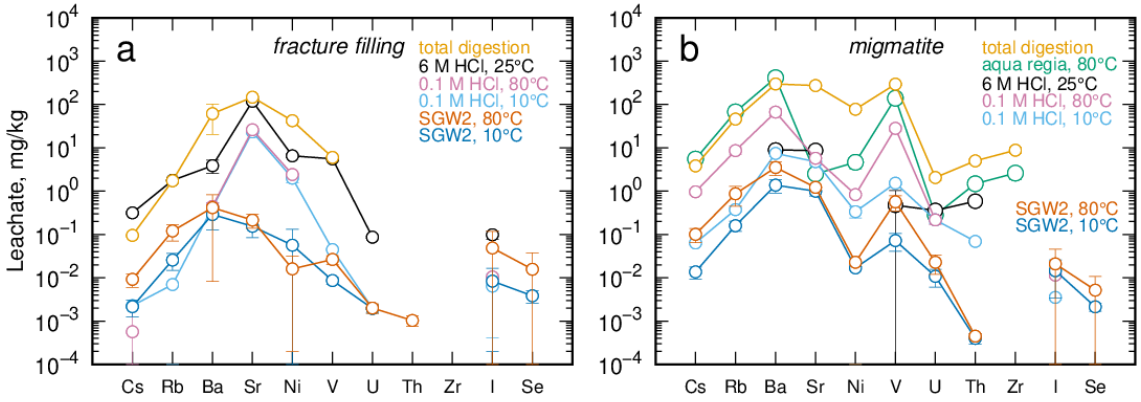

Figure 2-52 *Concentrations of trace elements released by fracture filling (a) and migmatite (b) upon total digestion, extractions with aqua regia, 6 M HCl, 0.1 M HCl, and leaching with SGW2. Data for total digestion and extractions represent averages from triplicate batches, and for SGW2 averages from six triplicate batches (except 5 single batches for fracture filling and 2 for migmatite with colloids as discussed above). Released inventories were related to the total sample mass.*

A comparison of element trends in **Erreur ! Source du renvoi introuvable.** suggests the Ba-Sr couple as a proxy for establishing possible genetic relationship of this contamination with migmatite. Indeed, this couple shows the same trend for aqueous leaching of fracture filling (Ba/Sr ratio of 1.9), aqueous leaching of migmatite (Ba/Sr ratio in the range of 1.4–2.9), and extractions/digestion of migmatite (Ba/Sr ratio in the range of 1.02–166) and an opposite trend to extractions/digestion of fracture filling (Ba/Sr ratio in the range of 0.02–0.42). Furthermore, water-accesible Rb/Cs ratios of 11.8 ± 1.6 and 12.9 ± 2.7 for fracture filling at 10 °C and 80 °C, respectively, differ strongly from the ratios of 3.1 and 5.6 for 0.1 M HCl and 6 M HCl extractions (**Erreur ! Source du renvoi introuvable.**). At the same time, these Rb/Cs ratios are close to the ratios of 11.8 ± 1.5 and 8.2 ± 2.2 obtained for aqueous leaching of migmatite at 10 °C and 80 °C, respectively, and of 12.0 for total digestion of migmatite. According to Göb et al. (2013), Rb/Cs ratios for less altered migmatites and gneisses vary in the range of 5–20 with a median of about 8, which agrees with the obtained values and provides support to the inference on possible contamination of the surfaces of calcite grains originating from migmatite.

Considering that a contamination of grain surfaces of calcite in chalk by 1–4 nm thick clay particles were observed by Skovbjerg et al. (2012), a possibility exists that grain surfaces of the studied fracture filling are contaminated by migmatite particulates. This possibility can be assessed based on trace element inventories released with colloids (Figure 2-53), which as discussed in preceding sections bear contaminating phases in fracture filling or represent phases buried below the outermost surface layer in migmatite grains. The striking feature of the observed migmatite colloids is that they bear no Ni, whereas the outermost surface layer of fracture-filling and of migmatite grains bear comparable Ni inventories (Figure 2-52). Though this evidence is by no means extensive, it prioritizes the alternative explanation that at least some contaminating ions, such as Ni, are incorporated as structural ions in the outermost surface layer of fracture filling. An absence of Ni in 4 of 5 colloids from fracture filling suggests further that Ni extracted with HCl is most probably incorporated as structural ion in its calcite phase (at a ratio of at least 30000). Ca/Sr ratio for colloids in fracture filling adjusted for the water-accessible contribution from the grain surface lies in the range of 1780–2725 overlapping with the values observed for extractions with HCl, which supports the inference that the colloids comprise of a contaminating phase enveloped by a calcite phase.

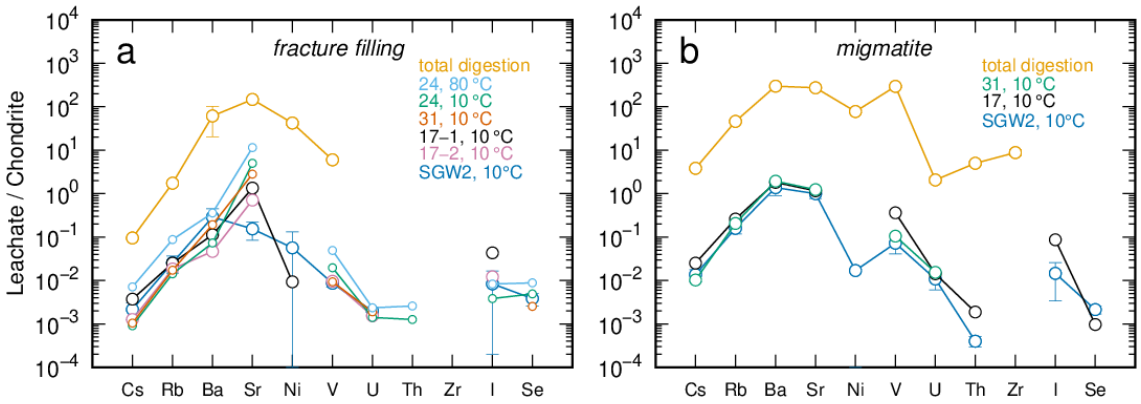

Figure 2-53 Concentrations of trace elements released as REEY-enriched colloids by fracture filling (a) and migmatite (b) upon leaching with SGW2 for 17, 24, and 31 days at 10 °C and 24 days at 80 °C. Data for total digestion and leaching with SGW2 at 10 °C from Erreur ! Source du renvoi introuvable. are shown for comparison.

Another view on the possibility of contamination of fracture-filling grain surfaces by migmatite particulates presents an analysis of correlations between leaching-time dependent element releases. This analysis reveals for fracture filling reacted at 80 °C that releases of Cs, Rb, Sr, Ba, U, Al, and Si (phase I) as well as Rb, Sr, U, and V (phase II) mutually correlate with correlation coefficients in the range of 0.71–0.98 and average value of 0.86 ± 0.07 for 21 element pairs in a putative phase I and of 0.84–0.98 (0.90 ± 0.05) for 6 element pairs in a putative phase II. Notably, for migmatite reacted at 80°C, mutually correlations (0.68–0.98, 0.89 ± 0.08) are observed between releases of Cs, Rb, Sr, Ba, U, V, and Si in a putative phase III, which features V instead of Al in the phase I. Though these correlations

do not necessarily imply presence of the corresponding mineral phases in the outermost layer of fracture-filling and migmatite grains, they still indicate such a possibility. The similarity of the phases I and III indicates also that they formed co-genetically as secondary phases upon interaction between the underlying grain surfaces and migrating fluids with the inherited REEY – and other trace element – signature of a rock similar to the studied migmatite, as discussed above for REEY released from the surface of migmatite grains. The mutual correlations (0.75–0.97, 0.90 ± 0.08) between Se, U, V, and Si indicate additionally an existence of a phase IV in migmatite representing a possible counterpart of water-accessible Se in fracture filling (Figure 2-52a).

The discussed contamination of grain surfaces poses a question on how it could have happened for a continuous carbonate phase precipitated possibly within a short period of time. Taking into account the observed increased mechanical stability of grain fraction 1–2 mm as compared to smaller fractions, as discussed to the sample preparation, and based on the thermal expansion coefficients measured by Markgraf & Reeder (1985), a cooling down of 1-mm calcite grains precipitated at 250 °C, which is within the range of homogenization temperatures observed for studied calcite as discussed in the preceding sections, to the in-situ temperature of 15 °C would produce fractures with an aperture of 7.6 µm. Though this value applies to a pure calcite phase and can be smaller for the studied fracture filling because of contaminating phases, it exemplifies that the surface layer of calcite grains strongly disturbed due to post-formational water-grain interactions may be a factor 10–100 thicker than the outermost layer of about 70 nm accessible at the experimental conditions of the present study. This value represents admittedly a maximum aperture, since upon a cooling down of 1-mm calcite grains to, e. g., 200 °C, produces fractures with an aperture of 1.6 µm, which can be infiltrated by migrating colder fluids and can be at least partially closed through precipitation of secondary phases.

2.4 References

Alvarez, M. C. C. C. (2019). Nickel isotope fractionation during adsorption on the calcite surface and coprecipitation with calcite (Doctoral dissertation, Université Paul Sabatier-Toulouse III).

Anders, E., & Ebihara, M. (1982). Solar-system abundances of the elements. *Geochimica et Cosmochimica Acta*, *46*(11), 2363-2380.

Appelo, C.A.J., Postma, D. (2005) Geochemistry, Groundwater and Pollution, second ed. A.A. Balkema Publishers, Amsterdam. https://doi.org/10.1201/9781439833544.

Bau, M. (1999). Scavenging of dissolved yttrium and rare earths by precipitating iron oxyhydroxide: experimental evidence for Ce oxidation, Y-Ho fractionation, and lanthanide tetrad effect. *Geochimica et Cosmochimica Acta*, *63*(1), 67-77.

Bau, M., & Koschinsky, A. (2009). Oxidative scavenging of cerium on hydrous Fe oxide: evidence from the distribution of rare earth elements and yttrium between Fe oxides and Mn oxides in hydrogenetic ferromanganese crusts. *Geochemical Journal*, *43*(1), 37-47.

Bau, M., Usui, A., Pracejus, B., Mita, N., Kanai, Y., Irber, W., & Dulski, P. (1998). Geochemistry of low-temperature water–rock interaction: evidence from natural waters, andesite, and iron-oxyhydroxide precipitates at Nishiki-numa iron-spring, Hokkaido, Japan. *Chemical Geology*, *151*(1-4), 293-307.

Bacon, J. R., & Davidson, C. M. (2008). Is there a future for sequential chemical extraction?. *Analyst*, *133*(1), 25-46.

Baeyens B., Bradbury M.H. (1995). A quantitative mechanistic description of Ni, Zn and Ca sorption on Na-montmorillonite. Part II: Sorption measurements. *Technical Report NTB 95-05*, Nagra, Wettingen, Switzerland.

Benedicto, A., Missana, T., & Fernández, A. M. (2014). Interlayer collapse affects on cesium adsorption onto illite. *Environmental science & technology*, *48*(9), 4909-4915.

Bradbury, M. H., & Baeyens, B. (1995). A Quantitative Mechanistic Description of Ni, Zn and Ca Sorption on Na-Montmorillonite Part III: Modelling. Nagra Technical Report 95-06.

Bradbury, M. H., & Baeyens, B. (1997). A mechanistic description of Ni and Zn sorption on Na-montmorillonite Part II: Modelling. *Journal of Contaminant Hydrology*, *27*(3), 223–248.

Bradbury, M.H., Bayens, B. (2000) A generalized sorption model for the concentration dependent uptake of cesium by argillaceous rocks. J. Contam. Hydrol. 42, 141–163.

Bradbury, M. H., & Baeyens, B. (2002). Sorption of Eu on Na- and Ca-montmorillonites: Experimental investigations and modelling with cation exchange and surface complexation. *Geochimica et Cosmochimica Acta*, *66*(13), 2325–2334.

Bradbury, M. H., & Baeyens, B. (2009a). Sorption modelling on illite Part I: Titration measurements and the sorption of Ni, Co, Eu and Sn. *Geochimica et Cosmochimica Acta*, *73*(4), 990–1003.

Bradbury, M. H., & Baeyens, B. (2009b). Sorption modelling on illite. Part II: Actinide sorption and linear free energy relationships. *Geochimica et Cosmochimica Acta*, *73*(4), 1004–1013.

Bradbury, M. H., Baeyens, B., & Thoenen, T. (2010). Sorption data bases for generic Swiss argillaceous rock systems. Switzerland.

Bukovská, Z., Verner, K. et al. (2018). *Comprehensive geological characterization of URF Bukov. Final report*. SÚRAO TZ 247/2018, Radioactive Waste Repository Authority, Prague, Czech Republic.

Cao, C., Liu, X. M., Bataille, C. P., & Liu, C. (2020). What do Ce anomalies in marine carbonates really mean? A perspective from leaching experiments. *Chemical Geology*, *532*, 119413.

Charlton, S.R., Parkhurst, D.L. (2011) Modules based on the geochemical model PHREEQC for use in scripting and programming languages. Comput. Geosci. 37–10, 1653–1663.

Chen, W., Fan, X. W., Guo, C. N., Song, X. D., Liu, Y. Q., & Xu, N. (2019). Determination of iron content in high purity rare earth by inductively coupled plasma-tandem mass spectrometry. *Chinese Journal of Analytical Chemistry*, *47*(3), 403-409.

Cornell, R. M. (1993). Adsorption of cesium on minerals: a review. *Journal of radioanalytical and nuclear chemistry*, *171*, 483-500.

Curti, E. (1997). Coprecipitation of radionuclides: basic concepts, literature review and first applications.

Červinka, R., Gondolli, J., Havlová, V., & Rukavičková, L. (2016). Selection of representative groundwater samples and preparation of their synthetic equivalents. *Technical Report 41/2016*, SURAO, Prague, Czech Republic, in Czech.

Dähn, R., Baeyens, B., & Bradbury, M. H. (2011). Investigation of the different binding edge sites for Zn on montmorillonite using P-EXAFS – The strong/weak site concept in the 2SPNE SC/CE sorption model. *Geochimica et Cosmochimica Acta*, *75*(18), 5154–5168.

Debruyne, D., Hulsbosch, N., & Muchez, P. (2016). Unraveling rare earth element signatures in hydrothermal carbonate minerals using a source–sink system. *Ore Geology Reviews*, *72*, 232-252.

Dohrmann, R., & Kaufhold, S. (2009). Three New, Quick CEC Methods for Determining the Amounts of Exchangeable Calcium Cations in Calcareous Clays. *Clays and Clay Minerals*, *57*(3), 338–352.

Dzombak, D., Morel, F. (1990) Surface Complexation Modeling: Hydrous Ferric Oxide. John Wiley & Sons, New York.

Ervanne, H., Puukko, E., & Hakanen, M. (2013). Modeling of Sorption of Eu, Mo, Nb, Ni, Pa, Se, Sn, Th and U on Kaolinite and Illite in Olkiluoto Groundwater Simulants. Working Report 2013-31, Posiva, Finland.

Essington, M. E. (2003). *Soil and Water Chemistry: An Integrative Approach*. CRC Press.

Evensen N. M., Hamilton P. J., and O'Nions R. K. (1978). Rare-earth abundances in chondritic meteorites. *Geochimica et Cosmochimica Acta, 42*, 1199-1212

Fletcher, N. D., Manard, B. T., Metzger, S. C., Ticknor, B. W., Bostick, D. A., & Hexel, C. R. (2020). Determining P, S, Br, and I content in uranium by triple quadrupole inductively coupled plasma mass spectrometry. *Journal of Radioanalytical and Nuclear Chemistry*, *324*, 395-402.

Gaines, G. L., & Thomas, H. C. (1953). Adsorption Studies on Clay Minerals. II. A Formulation of the Thermodynamics of Exchange Adsorption. *The Journal of Chemical Physics*, *21*(4), 714–718.

Gilbert, M., & Laudelout, H. (1965). Exchage properties of hydrogen ions in clays. *Soil Sci.*, *100*, 157–162.

Govindaraju, K. (1984). Report (1973–1984) on two ANRT geochemical reference samples: Granite GS-N and Potash Feldspar FK-N. *Geostandards Newsletter*, *8*(2), 173-206.

Govindaraju, K. (1987). 1987 compilation report on Ailsa Craig granite AC-E with the participation of 128 GIT-IWG laboratories. *Geostandards Newsletter*, *11*(2), 203-240.

Govindaraju, K., & Roelandts, I. (1989). 1988 compilation report on trace elements in six ANRT rock reference samples: diorite DR-N, serpentine UB-N, bauxite BX-N, disthene DT-N, granite GS-N and potash feldspar FK-N. *Geostandards Newsletter*, *13*(1), 5-67.

Göb, S., Loges, A., Nolde, N., Bau, M., Jacob, D. E., & Markl, G. (2013). Major and trace element compositions (including REE) of mineral, thermal, mine and surface waters in SW Germany and implications for water–rock interaction. *Applied Geochemistry*, *33*, 127-152.

Havlová, V., Zuna, M., Brázda, L., Kolomá, K., Galeková, E., Rosendorf, T., & Jankovský, F. (2020). *Radionuclide migration processes in a crystalline rock environment and the migration parameters of Bohemian massif rocks* . *Technical Report* 333/2018, SURAO, Prague, Czech Republic.

Hoehn, E., Eikenberg, J., Fierz, T., Drost, W., & Reichlmayr, E. (1998). The Grimsel Migration Experiment: Field injection–withdrawal experiments in fractured rock with sorbing tracers. *Journal of Contaminant Hydrology*, *34*, 85–106.

Holgersson, S. (2012). Studies on batch sorption methodologies: Eu sorption onto Kivetty granite. *Procedia Chemistry*, *7*, 629-640.

Huitti, T., Hakanen, M., & Lindberg, A. (1998). Sorption of cesium on Olkiluoto mica gneiss, granodiorite and granite.

Igarashi, T., Mahara, Y., Ashikawa, N., & Okamura, M. (1998). Evaluation of radioactive strontium distribution coefficient by analyzing background stable strontium. *Journal of nuclear science and technology*, *35*(3), 190-197.

Ikonen, J., Sardini, P., Jokelainen, L., Siitari-Kauppi, M., Martin, A., & Eikenberg, J. (2016). The tritiated water and iodine migration in situ in Grimsel granodiorite. Part I: determination of the diffusion profiles. *Journal of Radioanalytical and Nuclear Chemistry*, *310*(3), 1041–1048.

Klosa, D. (1994). Eine rechnergestützte Methode zur Bestimmung des Gesamtkarbonatgehaltes in Sedimenten und Böden. *Z. Angew. Geol.*, *40*, 18-21.

Kočan, K. (2022). *Nickel migration in barrier materials.* (Master's thesis, Czech Technical university in Prague).

Kraemer, D., Kopf, S., & Bau, M. (2015). Oxidative mobilization of cerium and uranium and enhanced release of “immobile” high field strength elements from igneous rocks in the presence of the biogenic siderophore desferrioxamine B. *Geochimica et Cosmochimica Acta*, *165*, 263-279.

Lakshtanov, L. Z., & Stipp, S. L. S. (2007). Experimental study of nickel (II) interaction with calcite: Adsorption and coprecipitation. *Geochimica et Cosmochimica Acta*, *71*(15), 3686-3697.

Lamana, R. T. *Nickel sorption on calcite surface: a macroscopic experimental study, 2010* (Doctoral dissertation, Master Thesis, McGill University, Montréal, Canada).

Lee, C. P., Lan, P. L., Jan, Y. L., Wei, Y. Y., Teng, S. P., & Hsu, C. N. (2006). Sorption of cesium on granite under aerobic and anaerobic conditions. *Radiochimica Acta*, *94*(9-11), 679-682.

Li, T. P., & Li, A. Y. (2021). Determination of Trace Elements in Attapulgite Clay by Inductively Coupled Plasma-Tandem Mass Spectrometry. *Rock and Mineral Analysis*, *40*(2), 196-205.

Li, X., Puhakka, E., Ikonen, J., Söderlund, M., Lindberg, A., Holgersson, S., Martin, A., & Siitari-Kauppi, M. (2018). Sorption of Se species on mineral surfaces, part I: Batch sorption and multi-site modelling. *Applied Geochemistry*, *95*, 147–157.

Liu, S., Jacques, D., Govaerts, J., & Wang, L. (2014). Conceptual model analysis of interaction at a concrete–Boom Clay interface. *Physics and Chemistry of the Earth, Parts A/B/C*, *70–71*, 150–159.

Liu, X., Dong, S., Yue, Y., Guan, Q., Sun, Y., Chen, S., ... & Yang, Y. (2020). 87Sr/86Sr isotope ratios in rocks determined using inductively coupled plasma tandem mass spectrometry in O2 mode without prior Sr purification. *Rapid Communications in Mass Spectrometry*, *34*(8), e8690.

Manard, B. T., Metzger, S. C., Rogers, K. T., Ticknor, B. W., Bostick, D. A., Zirakparvar, N. A., & Hexel, C. R. (2020). Exploration of ICP platforms for measuring elemental impurities in uranium ore concentrates. *International Journal of Mass Spectrometry*, *455*, 116378.

Matyskin, A.V. (2018) Solubility and Crystal Structure of Radium Sulfate and Carbonate. PhD thesis. Chalmers University of Technology.

McCurdy, E. (2020). Avoidance of Spectral Overlaps on Reaction Product Ions with O2 Cell Gas: Comparison of Quadrupole ICP-MS and ICP-QQQ. *Agil. Handbook of ICP-QQQ Applications using the Agilent 8800 and 8900*, 5991-2802EN, 229-231.

Migdisov, A., Williams-Jones, A. E., Brugger, J., & Caporuscio, F. A. (2016). Hydrothermal transport, deposition, and fractionation of the REE: Experimental data and thermodynamic calculations. *Chemical Geology*, *439*, 13-42.

Missana, T., Alonso, U., & Garcia-Gutierrez, M. (2009). Experimental study and modelling of selenite sorption onto illite and smectite clays. *J Colloid Interface Sci*, *334*(2), 132–138.

Muuri, E., Matara-aho, M., Puhakka, E., Ikonen, J., Martin, A., Koskinen, L., & Siitari-Kauppi, M. (2018). The sorption and diffusion of 133Ba in crushed and intact granitic rocks from the Olkiluoto and Grimsel in-situ test sites. *Applied Geochemistry*, *89*, 138–149.

Muuri, E., Siitari-Kauppi, M., Matara-aho, M., Ikonen, J., Lindberg, A., Qian, L., & Koskinen, L. (2017). Cesium sorption and diffusion on crystalline rock: Olkiluoto case study. *Journal of Radioanalytical and Nuclear Chemistry*, *311*(1), 439–446.

Möller, P., & Bau, M. (1993). Rare-earth patterns with positive cerium anomaly in alkaline waters from Lake Van, Turkey. *Earth and Planetary Science Letters*, *117*(3-4), 671-676.

Möller, P., Stober, I., & Dulski, P. (1997). Seltenerdelement-, Yttrium-Gehalte und Bleiisotope in Thermal- und Mineralwässern des Schwarzwaldes. *Grundwasser*, *2*(3), 118-132.

Möller, P. (2000). Rare earth elements and yttrium as geochemical indicators of the source of mineral and thermal waters. In *Hydrogeology of crystalline rocks* (pp. 227-246). Springer, Dordrecht.

Müller, G., & Gastner, M. (1971). The 'Karbonat-Bombe', a simple device for the determination of carbonate content in sediment, soils, and other materials. *Neues Jahrbuch für Mineralogie-Monatshefte*, *10*, 466-469.

Müller, E. I., Mesko, M. F., Moraes, D. P., Maria das Graças, A. K., & Flores, É. M. (2014). Wet digestion using microwave heating. In *Microwave-assisted sample preparation for trace element analysis* (pp. 99-142). Elsevier.

Munemoto, T., Ohmori, K., & Iwatsuki, T. (2015). Rare earth elements (REE) in deep groundwater from granite and fracture-filling calcite in the Tono area, central Japan: Prediction of REE fractionation in paleo-to present-day groundwater. *Chemical Geology*, *417*, 58-67.

Muuri, E., Siitari-Kauppi, M., Matara-Aho, M., Ikonen, J., Lindberg, A., Qian, L., Koskinen, L. (2017) Cesium sorption and diffusion on crystalline rock: Olkiluoto case study. J. Radioanal. Nucl. Chem. 311, 439–446. https://doi.org/10.1016/j.heliyon.2019.e02296.

Nabelek, P. I. (1999). Trace element distribution among rock-forming minerals in Black Hills migmatites, South Dakota: A case for solid-state equilibrium. *American Mineralogist*, *84*(9), 1256-1269.

Nakano, K. (2018). Ultra-low-level determination of phosphorus, sulfur, silicon and chlorine using the Agilent 8900 ICP-QQQ. *Agil. Technol. Appl. Note*, 5991-6852EN, 1-6.

Perry, E. P., & Gysi, A. P. (2018). Rare earth elements in mineral deposits: speciation in hydrothermal fluids and partitioning in calcite. *Geofluids*, *2018*.

Perry, E., & Gysi, A. P. (2020). Hydrothermal calcite-fluid REE partitioning experiments at 200 C and saturated water vapor pressure. *Geochimica et Cosmochimica Acta*, *286*, 177-197.

Park, S. M., Alessi, D. S., & Baek, K. (2019). Selective adsorption and irreversible fixation behavior of cesium onto 2: 1 layered clay mineral: A mini review. *Journal of hazardous materials*, *369*, 569-576.

Parkhurst, D.L., Appelo, C.A.J. (2013) Description of Input and Examples for PHREEQC Version 3: a Computer Program for Speciation, Batch-Reaction, One-Dimensional Transport, and Inverse Geochemical Calculations (U.S. Geological Survey Techniques and Methods Report 6-A43). Reston, Virginia.

Pokrovsky, O. S., & Schott, J. (2002). Surface chemistry and dissolution kinetics of divalent metal carbonates. *Environmental science & technology*, *36*(3), 426-432.

Puhakka, E., Li, X., Ikonen, J., & Siitari-Kauppi, M. (2019). Sorption of selenium species onto phlogopite and calcite surfaces: DFT studies. *Journal of Contaminant Hydrology*, *227*, 103553.

Puhakka, E., & Olin, M. (2014). Ab Initio Studies on Cation Exchange and Surface Complexation Reactions on Biotite Surface. *Final Workshop Proceedings of the Collaborative Project "Crystalline ROCK Retention Processes" (7th EC FP CP CROCK), KIT Scientific Report 7656, KIT Scientific Publishing, Karlsruhe*, 125–131.

Quinn, K. A., Byrne, R. H., & Schijf, J. (2007). Sorption of yttrium and rare earth elements by amorphous ferric hydroxide: influence of temperature. *Environmental science & technology*, *41*(2), 541-546.

Rieger, P., Magnall, J. M., Gleeson, S. A., Oelze, M., Wilke, F. D., & Lilly, R. (2021). Differentiating between hydrothermal and diagenetic carbonate using rare earth element and yttrium (REE+ Y)

geochemistry: a case study from the Paleoproterozoic George Fisher massive sulfide Zn deposit, Mount Isa, Australia. *Mineralium Deposita*, 1-20.

Rovira, M., Gimenez, J., Martinez, M., Martinez-Llado, X., de Pablo, J., Marti, V., & Duro, L. (2008). Sorption of selenium(IV) and selenium(VI) onto natural iron oxides: Goethite and hematite. *J Hazard Mater*, *150*(2), 279–284.

Schulthess, C. P., & Sparks, D. L. (1986). Backtitration Technique for Proton Isotherm Modeling of Oxide Surfaces. *Soil Science Society of America Journal*, *50*(6), 1406.

Shannon, R. D. (1976). Revised effective ionic radii and systematic studies of interatomic distances in halides and chalcogenides. *Acta crystallographica section A: crystal physics, diffraction, theoretical and general crystallography*, *32*(5), 751-767.

Simonin, J. P., & Bouté, J. (2016). Intraparticle diffusion-adsorption model to describe liquid/solid adsorption kinetics. *Revista mexicana de ingeniería química*, *15*(1), 161-173.

Skovbjerg, L. L., Hassenkam, T., Makovicky, E., Hem, C. P., Yang, M., Bovet, N., & Stipp, S. L. S. (2012). Nano sized clay detected on chalk particle surfaces. *Geochimica et Cosmochimica Acta*, *99*, 57-70.

Smith, K. S. (1999). Metal sorption on mineral surfaces: an overview with examples relating to mineral deposits. *Reviews in economic geology*, *6*, 161-182.

Söderlund, M., Hakanen, M., & Lehto, J. (2015). Sorption of niobium on boreal forest soil. *Radiochimica Acta*, *103*(12), 859–869.

Söderlund, M., Hakanen, M., & Lehto, J. (2016). Sorption of cesium on boreal forest soil I: the effect of grain size, organic matter and mineralogy. *Journal of Radioanalytical and Nuclear Chemistry*, *309*, 637-645.

Stage, E., Huber, F., Heck, S., & Schäfer, T. (2012). Sorption/desorption of 137Cs (I), 152Eu (III) and 233U (VI) onto new CROCK derived Äspö diorite–A batch type study. In *1st Workshop Proceedings of the Collaborative Project "Crystalline Rock Retention Processes"(7th EC FP CP CROCK), KIT Scientific Reports* (Vol. 7629, pp. 51-62).

Sugiyama, N., & Nakano, K. (2014). Reaction data for 70 elements using O2, NH3 and H2 gases with the Agilent 8800 Triple Quadrupole ICP-MS. *Agil. Technol. Appl. Note*, 5991-4585EN, 1-14.

Tachi, Y., Shibutani, T., Sato, H., & Yui, M. (2001). Experimental and modeling studies on sorption and diffusion of radium in bentonite. *Journal of contaminant hydrology*, *47*(2-4), 171-186.

Tachi, Y., Ebina, T., Takeda, C., Saito, T., Takahashi, H., Ohuchi, Y., & Martin, A. J. (2015). Matrix diffusion and sorption of Cs+, Na+, I– and HTO in granodiorite: Laboratory-scale results and their extrapolation to the in situ condition. *Journal of Contaminant Hydrology*, *179*, 10–24.

Tagami, K., & Uchida, S. (2005). Sample Storage Conditions and Holding Times for the Determination of Total Iodine in Natural Water Samples. *Atomic Spectroscopy*, *26*(6).

Tanaka, K., & Kawabe, I. (2006). REE abundances in ancient seawater inferred from marine limestone and experimental REE partition coefficients between calcite and aqueous solution. *Geochemical Journal*, *40*(5), 425-435.

Tessier, A. P. G. C., Campbell, P. G., & Bisson, M. J. A. C. (1979). Sequential extraction procedure for the speciation of particulate trace metals. *Analytical chemistry*, *51*(7), 844-851.

Thomson, J., & Temple, S. (2020). Sample preparation techniques for liquid scintillation analysis. In *Handbook of radioactivity analysis* (pp. 803-860). Academic Press.

Tillberg, M., Maskenskaya, O. M., Drake, H., Hogmalm, J. K., Broman, C., Fallick, A. E., & Åström, M. E. (2019). Fractionation of rare earth elements in greisen and hydrothermal veins related to a-type magmatism. Geofluids, 2019.

Torstenfelt, B., Andersson, K., & Allard, B. (1982). Sorption of strontium and cesium on rocks and minerals. *Chemical Geology*, *36*(1-2), 123-137.

Tsukamoto, M., & Ohe, T. (1991). Intraparticle diffusion of cesium and strontium cations into rock materials. *Chemical geology*, *90*(1-2), 31-44.

Wang, P., Anderko, A., & Turner, D. R. (2001). Thermodynamic Modeling of the Adsorption of Radionuclides on Selected Minerals. II: Anions. *Industrial & Engineering Chemistry Research*, *40*(20), 4444–4455.

Wang, Y., Yuan, X., Liu, L., Ma, J., Fan, S., Zhang, Y., & Li, Q. (2021). Multielement principal component analysis and origin traceability of rice based on ICP-ms/MS. *Journal of Food Quality*, *2021*, 1-12.

Wauters, J., Sweeck, L., Valcke, E., Elsen, A., & Cremers, A. (1994). Availability of radiocaesium in soils: a new methodology. *Science of the Total Environment*, *157*, 239-248.

Wissmeier, L., Barry, D.A. (2011) Simulating tool for variably saturated flow with comprehensive geochemical reactions in two- and three-dimensional domains. Environ. Model. Software 26–2, 210–218. https://doi.org/10.1016/j.envsoft.2010.07.005.

Yang, X., Ge, X., He, J., Wang, C., Qi, L., Wang, X., & Liu, C. (2018). Effects of Mineral Compositions on Matrix Diffusion and Sorption of ^{75} Se(IV) in Granite. *Environmental Science & Technology*, *52*(3), 1320–1329.

Yoshida, Y., Nakazawa, T., Yoshikawa, H. (2015) Partition coefficient of Ra in witherite. Journal of Radioanalytical and Nuclear Chemistry. 303, 147-152. https://doi.org/10.1007/s10967-014-3357-x.

Zachara, J. M., Cowan, C. E., & Resch, C. T. (1991). Sorption of divalent metals on calcite. *Geochimica et cosmochimica acta*, *55*(6), 1549-1562.

Zhao, Y., Wei, W., Li, S., Yang, T., Zhang, R., Somerville, I., Santosh, M., We, H., Wu, J., Yang, J., Chen, W. & Tang, Z. (2021). Rare earth element geochemistry of carbonates as a proxy for deep-time environmental reconstruction. *Palaeogeography, Palaeoclimatology, Palaeoecology*, *574*, 110443.

Zhao, X., Qiang, S., Wu, H., Yang, Y., Shao, D., Fang, L., ... & Fan, Q. (2017). Exploring the sorption mechanism of Ni (II) on illite: batch sorption, modelling, EXAFS and extraction investigations. *Scientific Reports*, *7*(1), 8495.

Zheng, Z., Tokunaga, T. K., & Wan, J. (2003). Influence of Calcium Carbonate on U(VI) Sorption to Soils. *Environmental Science & Technology*, *37*(24), 5603–5608.

Zhu, Y., Nakano, K., Shikamori, Y., & Itoh, A. (2021). Direct determination of rare earth elements in natural water samples by inductively coupled plasma tandem quadrupole mass spectrometry with oxygen as the reaction gas for separating spectral interferences. *Spectrochimica Acta Part B: Atomic Spectroscopy*, *179*, 106100.

Zimmermann, T., von der Au, M., Reese, A., Klein, O., Hildebrandt, L., & Pröfrock, D. (2020). Substituting HF by HBF 4–an optimized digestion method for multi-elemental sediment analysis via ICP-MS/MS. *Analytical Methods*, *12*(30), 3778-3787.

3 Calcite surface charge measurements

To consider the influence of calcite on radionuclide (RN) retardation and transport processes surface charge (this chapter) and sorption (Chapter 2) experiments were carried out with Bukov (Chapter 1.3.2.1, Figure 1-3 - Figure 1-8) and commercially bought samples (Chapter 3.2.1.1). In the following, the complexity and challenges related to sound surface charge measurements are briefly illustrated (Chapter 3.1) followed by an in-depth material characterization (Chapter 3.2.1). Due to the difficulties arising from calcite-inherent properties, different experimental boundary conditions were applied in this study to examine the development of surface potential development (Chapter 3.2.2). Collected data and approaches of interpretation are provided in Chapter 3.3.

Initially, our work aimed to describe the surface charge of different calcite samples to develop a model capable of predicting the surface charge development under different geochemical conditions. Finally, this model was supposed to be the basis for further development to describe surface complexation and precipitation processes as well as the formation of solid-solutions.

Different experiments were carried out to reveal the importance of geochemical boundary conditions upon surface charge development, such as e.g. equilibrium vs. non-equilibrium conditions, concentration of potential determining ions (PDI), CO_2 partial pressure (pCO_2) and e.g. sample preparation and composition. Despite the effort taken, we think that none of our experiments reached full equilibration within the chosen experimental time frame. Nevertheless, the study offers valuable insight into the complexity of calcite surfaces, equilibrium processes, and promising experimental approaches.

3.1 Brief theoretical background on calcite surface charge

It should be noted in advance that it is way beyond the scope of this study to give a comprehensive overview of calcite surface chemistry here. The following, very brief overview rather points out relevant aspects for this study. Moreover, general information such as dissolution kinetics of calcite are fairly well known, can be obtained from various publications such as (Eriksson et al., 2007; Heberling et al., 2014), and will not be discussed in detail in this report.

Calcite is one of the main fracture filling materials in crystalline rock and a major constituent of clay formations which are both internationally accepted potential host rock formations. However, despite its ubiquitous presence and hence importance there is still a great variety and inconsistency of data and model approaches in past and current literature in terms of calcite surface charge behavior. The difficulty to find comparable data sets lies in our opinion in a) different calcite compositions but also and especially in b) ill-defined experimental boundary conditions.

The surface charge can be derived via different techniques such as potentiometric titration, streaming potential measurements or zeta potential measurements. While potentiometric titrations are specifically challenging in terms of calcite due to its fast dissolution kinetics and buffer capacity, zeta potential measurements are reported to deliver trustworthy data (e.g. Al Mahrouqi et al., 2017; Heberling et al., 2011; Lützenkirchen et al., 2011; Eriksson et al., 2007). The zeta potential describes the electrical potential at the mineral surface and determines the electrostatic interaction between the mineral surface and any charged species in solution or, e.g., other charged surfaces. The surface functional groups react with the surrounding fluid, counterions accumulate at the surface and form together with co-ions a so called electric double layer. The sign and magnitude of the zeta potential define the ability of, e.g., RNs or other compounds in solution to sorb or desorb from the surface and hence, characterizes the retardation capacity of a mineral surface (Al Mahrouqi et al., 2017).

While the surface charge often depends on the pH, in terms of calcite a different picture establishes. Here, the pH is of minor relevance in terms of protonation and deprotonation of surface sites (Stipp, 1999; Heberling et al., 2011; Heberling et al., 2016) and so-called potential determining ions (PDIs), such as Ca2+, Mg2+, carbonate species and possibly sulfate, take over (e.g. Cicerone et al., 1992; Song et al., 2017; Stipp, 1999; Heberling et al., 2016; Tertre and Beaucaire, 2012). It is assumed that

PDIs sorb in an outer-sphere manner controlling the development of surface charge while protonation and deprotonation take place only to a minor extent directly at mineral surface (0-plane). However, the pH nevertheless determines solution speciation which in turn may affect the development of calcite surface charge (Heberling et al., 2014).

There is no general value or rule of thump to assess the isoelectric point of a calcite surface since it strongly depends amongst others on the concentration of PDIs and on the pCO_2 as described above. However, due to its dissolution kinetics calcite tends to be positively charged below pH 7, but not below 5 (calcite is dissolving) in equilibrated solutions under fixed pCO_2 conditions. Increasing or decreasing the concentration of PDIs, using non-equilibrated solutions and/or changing the pCO_2 yields completely different results and complicate subsequent data evaluation immensely (e.g. Heberling et al., 2011).

Besides solution composition and pressure conditions it has been reported that sample preparation may also have influence on the surface charge behavior. It is assumed that sample topography directly resulting from sample preparation affects the surface reactivity of calcite (e.g. Wolters et al., 2012; Li et al., 2016; Heberling et al., 2011). However, research is still ongoing an no overall consensus has been reached jet.

3.2 Materials and Methods

3.2.1 Material preparation and characterization

In the experimental investigations, two types of calcites were employed: Bukov calcite sourced from the Underground Research Facility situated in the Czech Republic, and commercially acquired pure calcite bought from the United Kingdom. Figure 3-1 shows the visual representations of the Bukov calcite and pure calcite. X-ray diffraction (XRD) analysis confirmed that pure calcite is 100% pure while Bukov calcite was found to comprise 91.6% magnesian calcite, 8.2% quartz, and 0.2% clinochlore. The observed distinctions in coloration and appearance are attributed to the presence of impurities within the calcite samples.

While specific surface area was not a focus of this work, a small grain size was required to conduct zeta potential measurements as the maximum recommended particle diameter for the Zetasizer device was between 3.8 nm to 100 µm (Malvern Instruments Ltd., 2013). To ensure the suitability of samples for analysis, the calcite samples were crushed and sieved before experiments. The particle size of the crushed calcite samples was determined using a Microtrac SYNC analyzer to make sure that the size of the calcite samples were fall within acceptable range (3.8 nm to 100 µm). The measured size distribution of crushed pure calcite and Bukov calcite are presented in Figure 3-2.

Figure 3-1 Exemplification of the appearance of Bukov calcite (left) and pure (right) calcite.

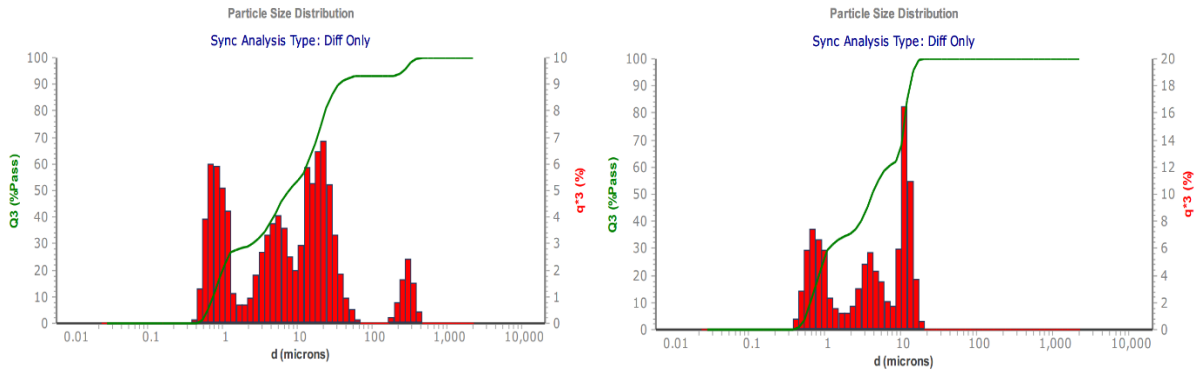

Figure 3-2 Particle size distributions of crushed Bukov calcite (left) and pure calcite (right) measured by Microtrac SYNC analyzer.

3.2.2 Instrumentation and experimental methods

Each sample in this work consisted of 0.75 g of prepared calcite weighed into 50 ml centrifuge tubes, which were filled with 50 ml of an equilibration solution. Samples were then be placed in batches of 7 into an unpressurized glove box where they were equilibrated using a CO_2/N_2 gas mixture (1% CO_2 + 99% N_2). This gas was bubbled directly into each individual sample tube to facilitate the interaction of CO_2 with the solution and reduce the time required for each experiment. No dedicated gas delivery system was available, and a simple custom one was created using a series of flexible plastic tubing that would decrease in diameter in a series of steps. A 5x8 mm tube was connected to the gas bottle, from where it would extend inside the glove box towards a Y-shaped splitter connected to two 3x5 mm tubes on the other end. These tubes would in turn connect to smaller Y splitters with two 2x4 mm tubes on each end leading to T-shaped junctions. These junctions would transfer the gas into 1.3 mm tubes that extended into the sample solution and delivered the gas to the samples. A schematic of this setup and the final built tubing system are illustrated in Figure 33.

For the first series of samples, emphasis was placed on validating the equilibration procedure. Samples were bubbled for 1 h daily using the CO_2/N_2 mixture, with 0.5 ml aliquots being taken each day before and after bubbling. Three days time was estimated to be sufficient to establish equilibrium, but for samples following the pure calcite/SGW2 batch the length was increased to 5 days to produce more reliable results, dedicating a week of daily 1-h bubbling to each. The pH was not controlled at this stage and merely measured and recorded to observe trends.

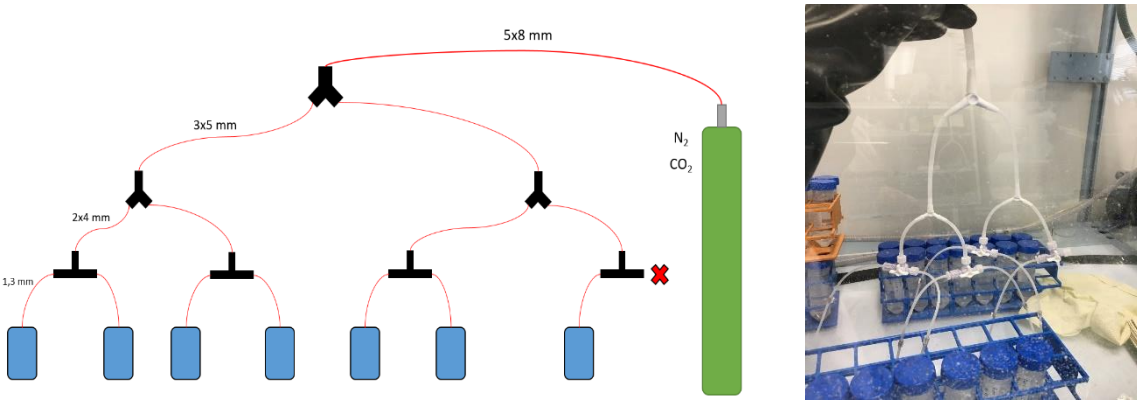

Figure 3-3 Schematic illustration of the equilibration setup used in the experiments of surface charge measurements (left); and a real illustration of the tubing system built in glovebox (right).

Table 3-1 The summary of experimental conditions of Series 1. The concentration of CaCl2 in the experiments was 0.001 M. The concentration of NaCl in the experiments was 0.01 M. The composition of SGW2 is shown in Table 3-2.

Calcite	Solution	# of samples	Experiment length	pH control	pH range	Bubbling
Pure (0.75 g)	SGW2 (50 ml)	7	3 days	no	≈ 8 - 9	1 h daily
Pure (0.75 g)	$CaCl_2$ (50 ml)	7	5 days	no	≈ 8	1 h daily
Pure (0.75 g)	NaCl (50 ml)	7	5 days	no	≈ 7 - 8.5	1 h daily
Bukov (0.75 g)	SGW2 (50 ml)	7	5 days	no	≈ 9.5	1 h daily
Bukov (0.75 g)	$CaCl_2$ (50 ml)	7	5 days	no	≈ 8 - 8.5	1 h daily
Bukov (0.75 g)	NaCl (50 ml)	7	5 days	no	≈ 8 - 8.5	1 h daily
Bukov (0.75 g)	NaCl (50 ml)	7	3 days (continued)	yes	7.8 - 9	1 h daily

Table 3-2 The chemical composition that was used to prepare the simulant of SGW2. The same composition was used for the whole experiments.

Chemical	Amount
$MgSO_4 \bullet 7\ H_2O$	0.2808 g
MgO	0.0139 g
$MgCl_2 \bullet 6\ H_2O$	0.0501 g
$Ca(OH)_2$	0.3464 g
$KHCO_3$	0.0275 g
$NaHCO_3$	0.3026 g

In the second series, samples were bubbled for 1 h at a time using the same CO_2/N_2 mixture, and 0.5 ml aliquots were taken before and after. However, bubbling was now performed only during the first 3 days, allowing the samples to sit and stabilize undisturbed for the remaining 2 days. The pH of the samples was systematically maintained within the range of 6.5 to 11 by periodically adding HCl and NaOH. Each sample had a unique pH value, increasing incrementally: 6.5, 7.5, 8.5, 9, 9.5, 10.5, and

11. In addition, pH adjustments were now made after bubbling as the process was noted to significantly disturb the solution's pH. For the last 2 days where no bubbling occurred, only the pH was monitored and adjusted if necessary, with aliquots being taken before and after measurement/adjustment. On the final day, after the final pH adjustment, 3 hours were allowed to pass to let the solution stabilize before samples for zeta potential measurements were taken.

Table 3-3 The summary of experimental conditions of Series 2. The concentration of CaCl2 in the experiments was 0.001 M. The concentration of NaCl in the experiments was 0.01 M. The composition of SGW2 is shown in Table 3-2.

Calcite	Solution	# of samples	Experiment length	pH control	pH range	Bubbling
Pure (0.75 g)	SGW2 (50 ml)	7	5 days	yes	6.5 – 11	1 h / 3 days
Pure (0.75 g)	NaCl (50 ml)	7	5 days	yes	6.5 – 11	1 h / 3 days
Pure (0.75 g)	$MgCl_2$ + NaCl 2.5 mM + 5 mM (50 ml)	7	5 days	yes	6.5 – 11	1 h / 3 days
Pure (0.75 g)	$MgCl_2$ + NaCl 3.75 mM + 2.5 mM (50 ml)	7	5 days	yes	6.5 – 11	1 h / 3 days

In the third series, the equilibrium achieved using the bubbling method was investigated on a longer timescale. NaCl and SGW2 batches from the second series were selected to undergo further studies to determine if equilibrium had actually been reached or if the samples had not yet fully stabilized in the previous experiments. These batches were bubbled twice every week for 1 h at a time over the course of 1 month, with 0.5 ml aliquots taken before and after each bubbling session. pH control was performed using HCl/NaOH to keep samples in the range of pH 6.5 – 11. The same pH increments as in Series 2 were used, and adjustments were still made after bubbling. On the final week, no bubbling was done on the last 2 consecutive days of the experiment, and samples for zeta potential measurements were taken on the final day after a 3-hour wait following pH adjustment.

3.2.3 Analysis methods

3.2.3.1 Surface charge measurements

The zeta potential measurements were performed using the Zetasizer Nano-ZS instrument, manufactured by Malvern Instruments. Approximately 0.9 mL of each solution was accurately dispensed into cuvettes. Subsequently, the zeta potential of samples were evaluated through the Electrophoretic Mobility measured and by Henry equation. Electrophoretic Mobility is determined using the Laser Doppler Velocimetry (LDV) technique. In the Zetasizer Nano-ZS instrument system, the M3-PALS technique was combined with LDV and Phase Analysis Light Scattering (PALS) techniques to enhance accuracy, especially for low-mobility particles. The PALS technique measures phase shifts in scattered light, which improves measurement precision.

3.2.3.2 MP-OES analysis

MP-AES (microwave plasma-atomic emission spectrometer), which is a new analytical technique commercialized around 2012, consists of a microwave-induced plasma interfaced to an atomic emission spectrophotometer (AES). It is used for simultaneous multi-analyte determination of major and minor elements. MP-AES employs microwave energy to produce a plasma discharge using nitrogen supplied from a gas cylinder or extracted from ambient air, which eliminates the need for sourcing gases in remote locations. The technique has shown much promise for routine analytical application with several advantages such as smaller footprint, multi-element capability, relatively inexpensive, low maintenance cost, good detection power and speed (Balaram, 2020; Hammer, 2008; Li et al., 2013; Niedzielski et al., 2015). Thus, MP-AES was utilized in this work for the determination of elements of interest (Na, Mg, Al, Mn, Fe, K, Ca).

For MP-AES measurements, all 0.5 ml sample aliquots were diluted to 10 ml using the appropriate equilibration solution (0.001 M $CaCl_2$ or 0.01 M NaCl or SGW2 solution as shown in Table 3-1 and Table 3-2). Then, 360 µl concentrated HNO_3 as well as 100 µl of a Cs buffer solution were added to each sample. A series of 10 ml standard solutions was prepared for each equilibration solution. Standard concentrations were 0 ppm, 0.5 ppm, 1 ppm, 5 ppm, 20 ppm and 50 ppm.

3.3 Results and discussion

3.3.1 Equilibrium test

For pure calcite samples, the bubbling of CO_2 initially increased noticeably the Ca concentration in the background solution in the first two days, after which Ca concentration stays relatively stable with minor fluctuations around a certain value, as shown in Figure 3-4 (a & b). Over time, most samples appear to gradually plateau around a certain concentration, with increases and decreases becoming steadily smaller in magnitude.

For Bukov calcite samples, no trend can be observed during the equilibrium test. The Ca concentrations from the Bukov calcite appear to fluctuate randomly over a wide range of concentrations.

Overall, pure calcite appears to equilibrate well using the bubbling method in all solutions that were tested (SGW2, CaCl2, NaCl). By comparison, equilibration of Bukov calcite using the bubbling method appears to be less effective than pure calcite. As could be inferred from CEC results, the magnitude of the fluctuations in Ca concentration and the unpredictable shapes of the curves suggest that the issue does not lie with simple adjustable variables like time, but rather originates from the inherent properties of Bukov calcite. As such, the equilibration method used in this work was deemed unsuitable for it, and the use of Bukov calcite in all subsequent experiments was discontinued.

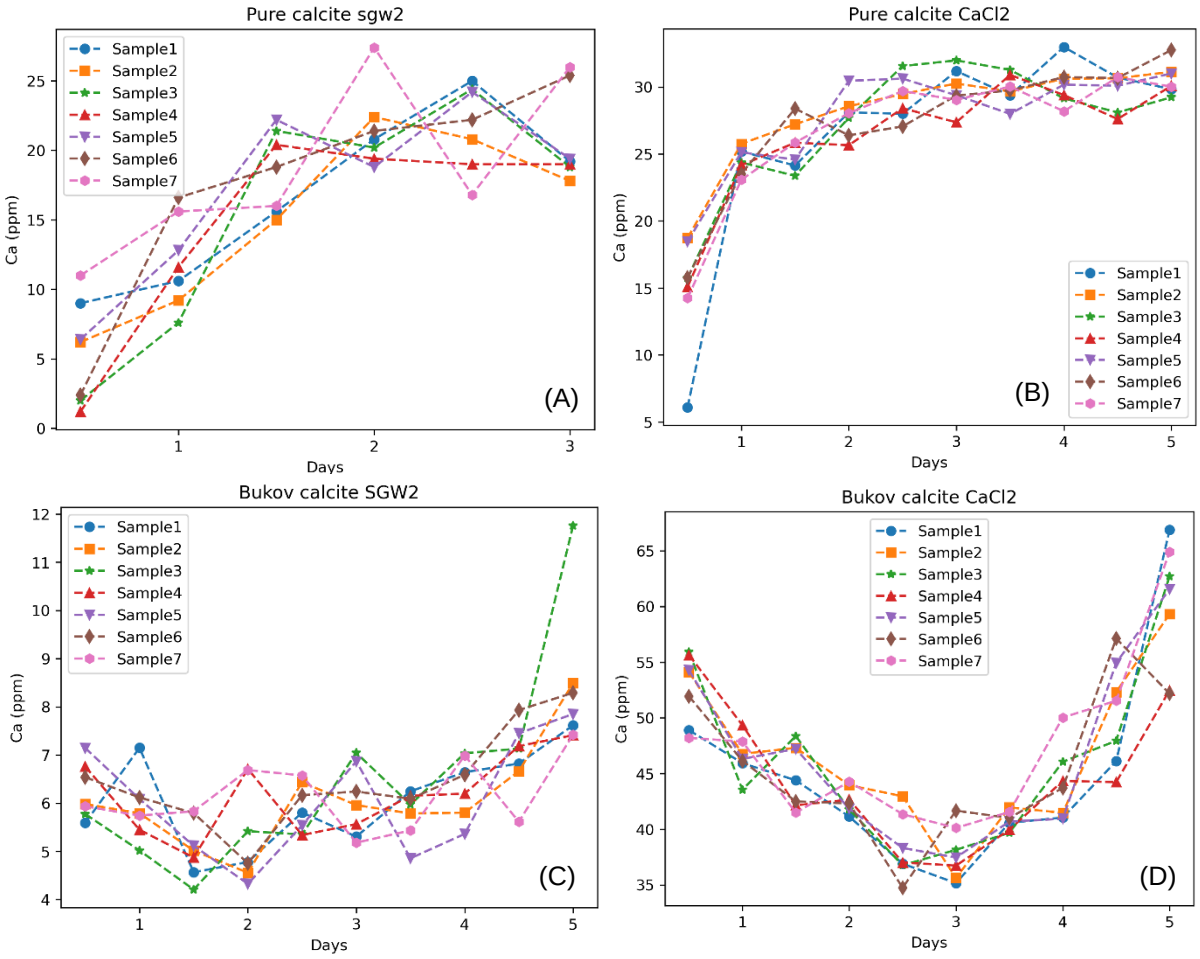

Figure 3-4 The evolution of Ca concentrations in SGW2 and $CaCl_2$ background solutions contacted with Pure calcite (A & B) and Bukov calcite (C & D) as a function of time to test the equilibration between calcite surfaces and aqueous phases.

3.3.2 Experimental measurements of surface charge

3.3.2.1 Zeta potential measurements as a function of pH

Pure calcite in SGW2 solutions appears particularly stable with pH control. In almost all samples there was no significant fluctuation in Ca concentration over time (Figure 3-5, left).

At pH 6.5, it is evident that equilibrium was not achieved, as shown by the continuous increase in Ca concentrations over the observation period. This can be attributed to the dissolution of calcite under the specified pH conditions, as indicated by the greater quantity of Ca released compared to the samples with higher pH conditions. By contrast, at pH 8.5 – 11 all samples appear highly stable with much less calcite dissolution. Ca concentration starts and remains low, barely fluctuating throughout the whole experiment.

Greater sample stability appears to be reflected in zeta potential results as well (Figure 3-5, right). A clear downward trend can be observed between the samples, with the zeta potential becoming more negative as the pH increases. This is in line with the theoretical assumption that the calcite surface would become more negatively charged at higher pH values due to the prevalence of anionic species in solution.

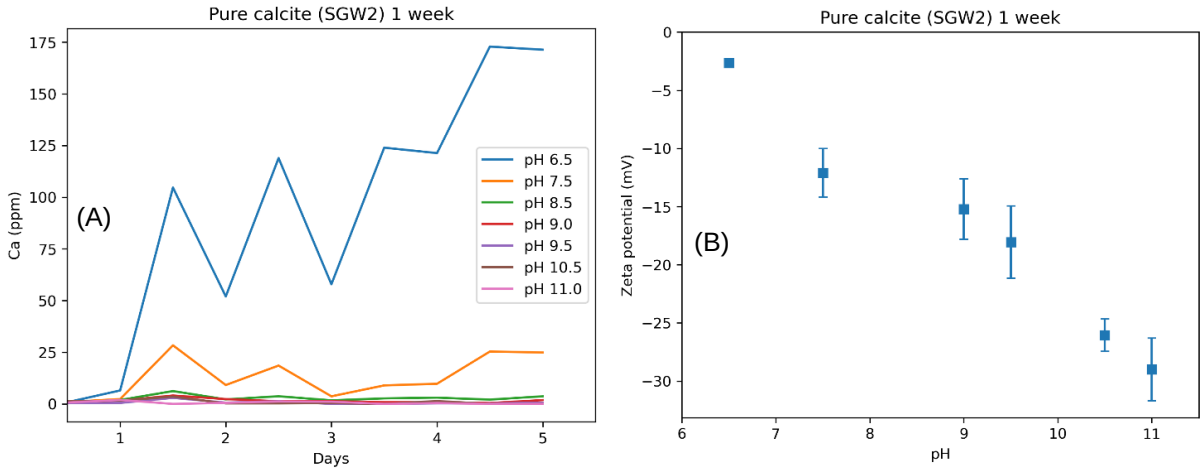

Figure 3-5 The time evolution of Ca concentration (left) and the measured zeta potential as a function of pH (right) for pure calcite in SGW2 background solutions.

Pure calcite in 0.01 M NaCl seems to behave very similar as in SGW2 solutions, as shown in Figure 3-6. For the samples at pH 6.5 and 7.5, calcite was observed to be unstable and high concentration of Ca was detected. Similar as concluded in SGW2 solutions, this was caused by the dissolution of calcite under these pH conditions. At pH 8.5 – 11, the dissolution of calcite became much less compared to the dissolution conditions in pH 6.5 – 7.5, which is the same as in SGW2 solutions. The difference is that the Ca content of all sample was higher than those observed in SGW2 solutions. A decreasing trend of zeta potentials with the increase of pH was also observed as shown in Figure 3-6.

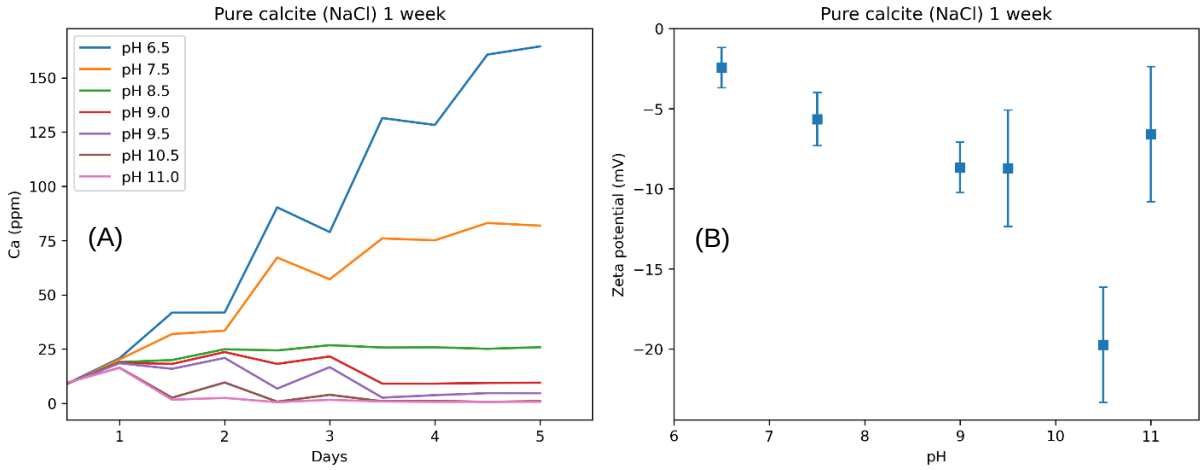

Figure 3-6 The time evolution of Ca concentration (left) and the measured zeta potential as a function of pH (right) for pure calcite in 0.01 M NaCl background solutions.

3.3.2.2 The Effects of Mg cations on zeta potential

As describe in Section 3.1, PDIs (such as Ca^{2+}, Mg^{2+} and CO_3^{2-} species) play a significant role in determining the zeta potential of calcite. To study the effects of PDIs, different concentrations of Mg^{2+} were mixed with NaCl, and the measured calcite dissolution and zeta potentials are shown in Figure 3-7.

The measured Ca concentrations in both mixtures show very similar results as in SGW2 and pure NaCl solutions. The dissolved Ca content decreases as pH is increased, and the calcite samples become stable and at high pH solutions.

However, the measured zeta potential results are drastically different than those in SGW2 and pure NaCl solutions, which shows the significant effects of Mg^{2+} on calcite zeta potentials. As can be seen, in both mixtures of NaCl and $MgCl_2$ solutions, the decreasing trend of zeta potential with increasing pH disappeared. The measured zeta potentials seem to remain in a constant level in both mixtures. A possible explanation is the specific adsorption of metal ions (Mg^{2+}) to the calcite surface. As established previously, calcite readily sorbs divalent metal ions, and their complexation with charged surface groups can alter the overall surface charge to the point of switching its sign from negative to positive (Lakshtanov and Stipp, 2007; Zachara et al., 1991). Mg^{2+} is a divalent cation that is highly similar to Ca^{2+} in terms of its chemical properties, which is why it is often found incorporated into the calcite crystal structure where it can influence its growth and precipitation (Song et al., 2017; Astilleros et al., 2010; Abdollahpour et al., 2022). However, Mg^{2+} has a smaller ionic radius than Ca^{2+} and may bind to surface groups more strongly and selectively due to reduced steric hindrance (Zachara et al., 1991, Shannon, 1976). As such, even though the total ionic strength of the solution in this work was kept constant, it can be observed that increasing Mg^{2+} in the solution resulted in more positive calcite zeta potentials.

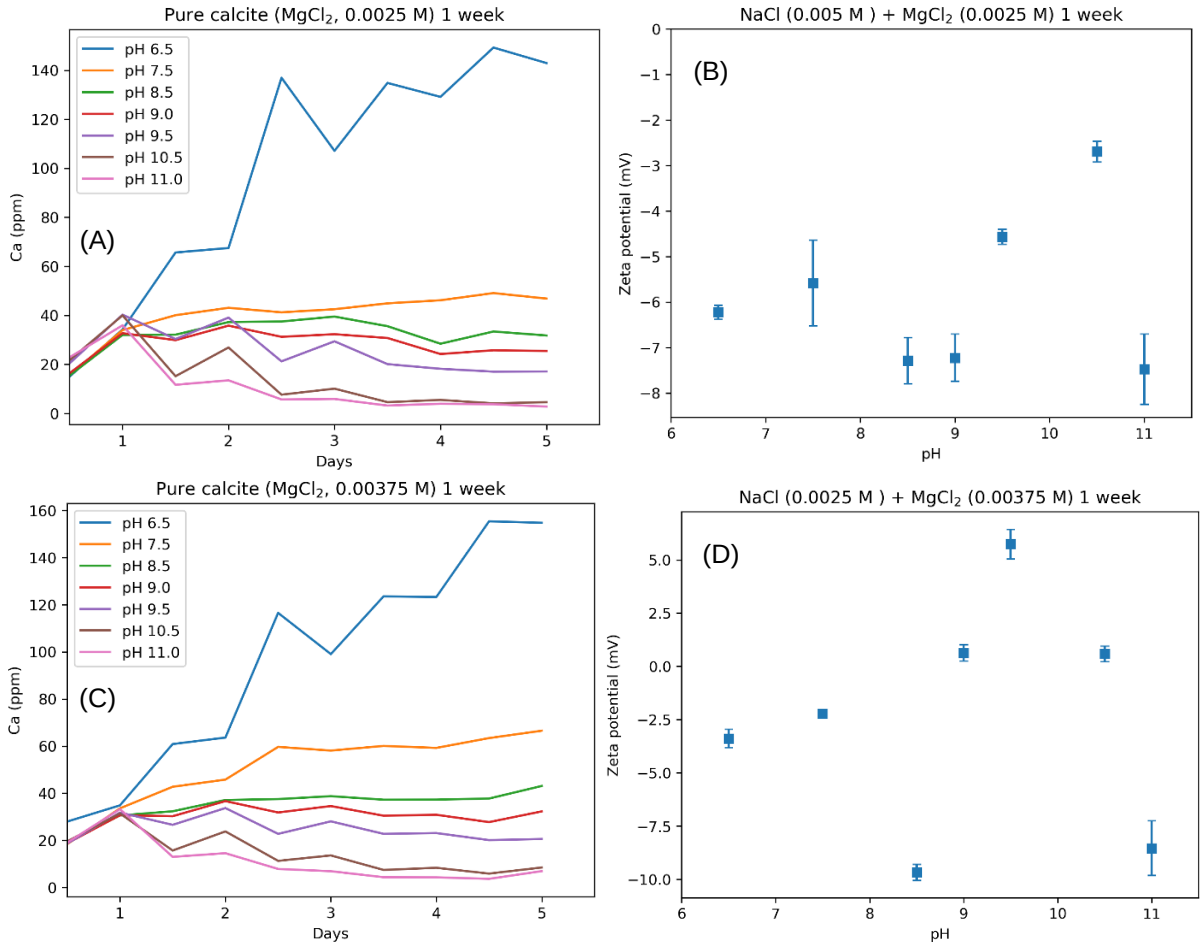

Figure 3-7 The time evolution of Ca concentration and the measured zeta potential as a function of pH for pure calcite in 0.0025 M $MgCl_2$ + 0.005 M NaCl solution (up) and 0.00375 M $MgCl_2$ + 0.0025 M NaCl solution (down).

3.3.2.3 The Effects of equilibrium time

In this part of the work, the experimental time was extended from one week to one month for the exact samples as shown above. The observed calcite dissolution and zeta potential results are shown in Figure 3-8.

Pure calcite in SGW2 maintained a steady equilibrium during the additional one month experiments. At pH 6.5, the calcite sample was much more stable compared to the first week results as shown in Figure 3-5. At pH 7.5, the curve is trending towards a straight line, although noticeable fluctuations in concentration remain. At pH 8.5 and above, the samples appear to be at an effectively constant Ca concentration, with the most significant fluctuations being approximately 1-3 ppm in magnitude. In addition, beyond pH 9 Ca concentration remains very low and rarely exceeds 1 ppm. When approaching pH 11, most of the results were under the MP-AES' detection limit. As such, high pH again appears to have significantly reduced the dissolution of calcite and contributed to sample stability. It is also unlikely that the results would change to any notable extent if the experiment were conducted for even longer. Over the course of one month most of the samples appear to have settled around a certain Ca concentration and show no signs of significant variation or any new developing trends. The more unstable samples seem to have been influenced most by pH and would not benefit from longer equilibration times. Zeta potential results are also very similar to the results of one week equilibration time (Figure 3-5). A little more negative zeta potential values than before were reached at pH around 11, which was possibly due to a longer equilibration time. However, the difference was not significant and within the variation of experimental and measurement errors.

Pure calcite in 0.01 M NaCl solution also appears to maintain its equilibrium over the course of one additional month. For the most part, Figure 3-8 simply continues the trends established during the first week as shown in Figure 3-6, and no improvements to sample stability can be observed. At pH 6.5 the sample still fails to equilibrate after one month, and a rising trend in Ca concentration is seen at the end of the experiments. When the pH is larger than 6.5, all samples can reach a finally plateau after one month equilibration time. As such, while pH clearly has the most influence on equilibration, in this case a longer equilibration time seems to offer a small benefit by allowing lower-pH samples to stabilize better. Zeta potential results after one month were improved compared with the one-week results. A clearer trend of more negative zeta potentials versus pH increases were observed. Slightly more negative zeta potentials were reached at the pH around 11 after one month, the same as in the SGW2 background solutions.

Overall, extending the equilibration time from one week to one month does not seem to have had significant effect on calcite equilibrium and zeta potential measurements in both SGW2 solution and 0.01 M NaCl solution. All samples seem to equilibrate well during the first one week of the experiment and maintain the same equilibration during the following month. However, long equilibration time can help with the equilibration at low pH conditions.

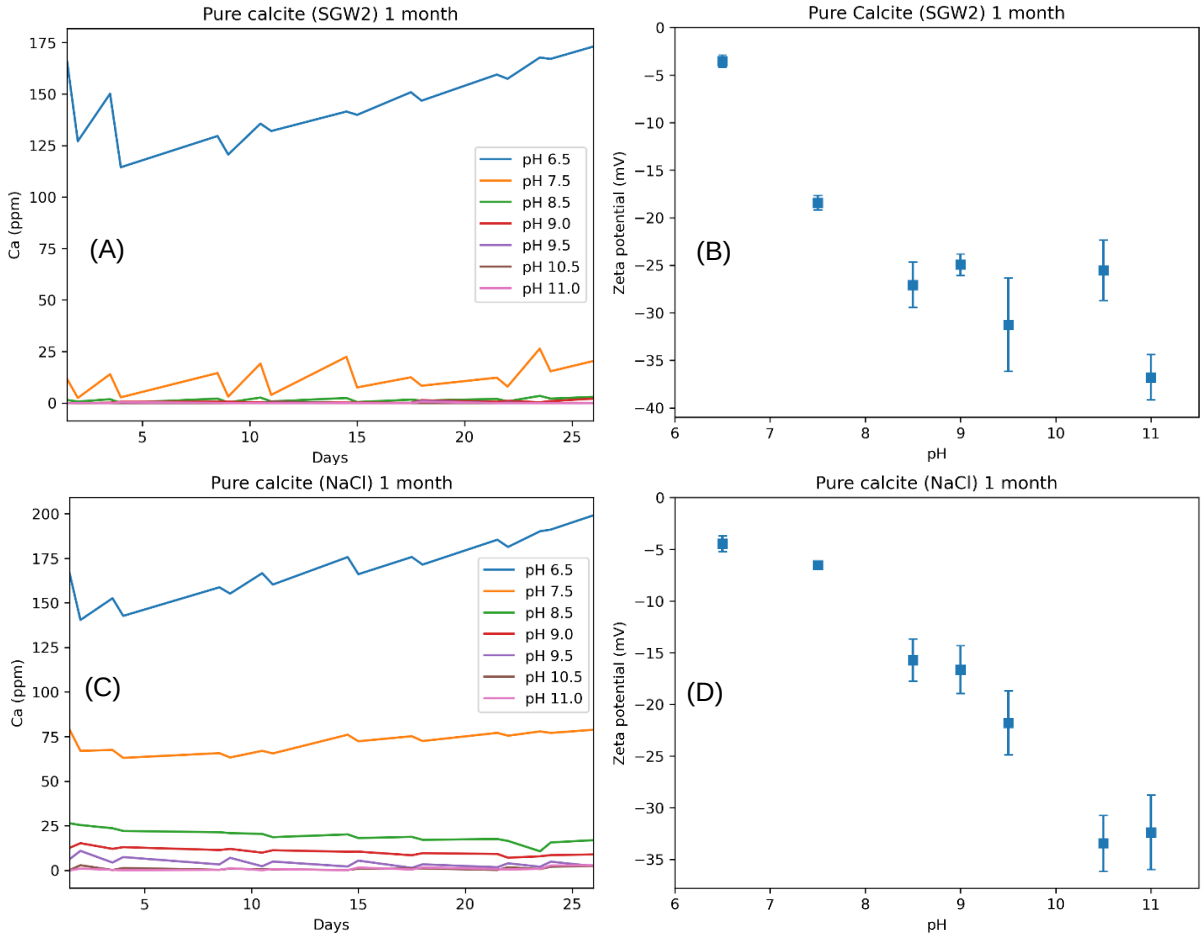

Figure 3-8 The time evolution of Ca concentration and the measured zeta potential as a function of pH for pure calcite in SGW2 solution (up) and 0.01 M NaCl solution(down) during one-month experimental time.

3.4 References

Abdollahpour, M., Heberling, F., Schild, D., & Rahnemaie, R. (2022). Magnesium Coprecipitation with Calcite at Low Supersaturation: Implications for Mg-Enriched Water in Calcareous Soils. Minerals, 12(2), Article 2.

Al Mahrouqi, D., Vinogradov, J., & Jackson, M. D. (2017). Zeta potential of artificial and natural calcite in aqueous solution. *Advances in colloid and interface science*, *240*, 60-76.

Astilleros, J. M., Fernández-Díaz, L., & Putnis, A. (2010). The role of magnesium in the growth of calcite: An AFM study. Chemical Geology, 271(1), 52–58.

Balaram, V. (2020). Microwave plasma atomic emission spectrometry (MP-AES) and its applications – A critical review. Microchemical Journal, 159, 105483.

Cicerone, D. S., Regazzoni, A. E., & Blesa, M. A. (1992). Electrokinetic properties of the calcite/water interface in the presence of magnesium and organic matter. *Journal of Colloid and Interface Science*, *154*(2), 423-433.

Eriksson, R., Merta, J., & Rosenholm, J. B. (2007). The calcite/water interface: I. Surface charge in indifferent electrolyte media and the influence of low-molecular-weight polyelectrolyte. *Journal of colloid and interface science*, *313*(1), 184-193.

Hammer, M. R. (2008). A magnetically excited microwave plasma source for atomic emission spectroscopy with performance approaching that of the inductively coupled plasma. Spectrochimica Acta Part B: Atomic Spectroscopy, 63(4), 456-464.

Heberling, F., Bosbach, D., Eckhardt, J. D., Fischer, U., Glowacky, J., Haist, M., ... & Winkler, B. (2014). Reactivity of the calcite–water-interface, from molecular scale processes to geochemical engineering. *Applied geochemistry*, *45*, 158-190.

Heberling, F., Trainor, T. P., Lützenkirchen, J., Eng, P., Denecke, M. A., & Bosbach, D. (2011). Structure and reactivity of the calcite–water interface. *Journal of colloid and interface science*, *354*(2), 843-857.

Heberling, F., Paulig, L., Nie, Z., Schild, D., & Finck, N. (2016). Morphology controls on calcite recrystallization. *Environmental Science & Technology*, *50*(21), 11735-11741.

Lakshtanov, L. Z., & Stipp, S. L. S. (2007). Experimental study of nickel(II) interaction with calcite: Adsorption and coprecipitation. Geochimica et Cosmochimica Acta, 71(15), 3686–3697.

Li, S., Leroy, P., Heberling, F., Devau, N., Jougnot, D., & Chiaberge, C. (2016). Influence of surface conductivity on the apparent zeta potential of calcite. *Journal of colloid and interface science*, *468*, 262-275.

Li, W., Simmons, P., Shrader, D., Herrman, T. J., & Dai, S. Y. (2013). Microwave plasma-atomic emission spectroscopy as a tool for the determination of copper, iron, manganese and zinc in animal feed and fertilizer. Talanta, 112, 43-48.

Malvern Instruments Ltd. (2013). Zetasizer Nano User Manual mano0485.

Niedzielski, P., Kozak, L., Wachelka, M., Jakubowski, K., & Wybieralska, J. (2015). The microwave induced plasma with optical emission spectrometry (MIP–OES) in 23 elements determination in geological samples. Talanta, 132, 591-599.

Shannon, R. D. (1976). Revised effective ionic radii and systematic studies of interatomic distances in halides and chalcogenides. Acta Crystallographica Section A: Crystal Physics, Diffraction, Theoretical and General Crystallography, 32(5), Article 5.

Song, J., Zeng, Y., Wang, L., Duan, X., Puerto, M., Chapman, W. G., ... & Hirasaki, G. J. (2017). Surface complexation modeling of calcite zeta potential measurements in brines with mixed potential determining ions (Ca2+, CO32−, Mg2+, SO42−) for characterizing carbonate wettability. *Journal of colloid and interface science*, *506*, 169-179.

Stipp, S. L. S. (1999). Toward a conceptual model of the calcite surface: hydration, hydrolysis, and surface potential. *Geochimica et Cosmochimica Acta*, *63*(19-20), 3121-3131.

Tertre, E., Page, J., & Beaucaire, C. (2012). Ion exchange model for reversible sorption of divalent metals on calcite: implications for natural environments. *Environmental science & technology*, *46*(18), 10055-10062.

Wolthers, M., Di Tommaso, D., Du, Z., & de Leeuw, N. H. (2012). Calcite surface structure and reactivity: molecular dynamics simulations and macroscopic surface modelling of the calcite–water interface. *Physical Chemistry Chemical Physics*, *14*(43), 15145-15157.

Zachara, J. M., Cowan, C. E., & Resch, C. T. (1991). Sorption of divalent metals on calcite. Geochimica et Cosmochimica Acta, 55(6), 1549–1562.

4 Matrix diffusion

4.1 Background

A simplified description of fluid transport in fractured crystalline rock is based on the dual porosity model (e.g., Smith et al., 1991). In the dual porosity model, diffusion into the rock material adjacent to the fractures is included via matrix diffusion. The matrix-controlled transport is determined by the sorption on solid surfaces as well as parameters controlling the diffusion process, particularly the diffusion coefficient and the matrix porosity.

The term matrix diffusion is applied to the processes by which solute, flowing in distinct flow paths, penetrates the surrounding rock. Diffusion into the rock occurs in a connected system of pores and micro fractures – diffusion through the solid phase is insignificant by comparison. The importance of matrix diffusion in the context of a radioactive waste repository is that it provides a mechanism for greatly enlarging the area of rock surface in contact with advecting radionuclides, from that of the flow path surfaces (and infills) to a much larger portion of the bulk rock.

Radioelement migration within a rock matrix under natural long-term conditions (in relation to groundwater flow path: outward migration = release; inward migration = retardation) is a complex process controlled by various parameters. Pure physical matrix parameters such as porosity, hydraulic conductivity and diffusivity are usually sufficient to describe transport in well-defined laboratory systems. In natural rock matrices transport in a complex way by physical pore properties such as pore size distribution, connectivity, tortuosity, constrictivity and the petrographical and chemical nature and charge of the pore surfaces. The latter is including the surface area. Due to the structural and compositional heterogeneity of natural rock matrices the various minerals/phases present have different influence on radionuclide transport. The transport properties of a certain rock not only reflect features of its geological history (crystallization, alteration, weathering, tectonics etc.) but are also prone to possible changes of conditions in the future and to sampling and other experimental influences.

The objective of the overall experiments within the Repro cluster is to investigate rock matrix retention properties under in situ conditions and to demonstrate that assumptions applied in the safety case are in line with the site evidence. Repro-lab is focused on rock matrix characterisation and matrix diffusion to compare the conditions between in situ and laboratory; for example stress relaxation which might open the pore space and increase the conductive diffusivity of the rock.

Three different experiments are applied to investigate rock matrix retention **in situ**: tracer experiments in water phase, diffusive gas transport in rock matrix and electrical method for logging of the rock matrix pore structure. In addition investigation of the rock matrix pore structure, in situ will be carried out after migration experiments with different probe molecules are done. Experiments will be executed along an artificial flow channel along a drill holes sections. The drilled cores from these sections are objects for laboratory experiments.

Six different experimental methods are applied to investigate the rock matrix retention properties **at the laboratory**: PMMA impregnation technique for porosity, CT tomography for 3D structure characterisation, tracer diffusion experiments in water phase (stagnant conditions and from flow), pycnometer measurements for porosity and He gas diffusion experiments and electrical conductivity measurements for formation factors.

In order to understand the microstructural, petrological-chemical and rock-phase-specific features the in situ transport properties are crucial. Therefore, with the help of related modelling from the planned in situ experiments, a qualitative and quantitative assessment is needed of:

1. Pore space parameters (bulk porosity, spatial porosity distribution, connectivity, anisotropy, heterogeneity, porosity profile, pore size distribution)
2. Hydraulic conductivity parameters
3. Diffusion properties (apparent/effective diffusivity, diffusion pathways, dependence on the probe molecules used)

4. Retardation properties (size, accessibility, distribution of rock-phase specific internal surfaces).

In this work, the electromigration technique was used for matrix diffusion studies of both anionic and cationic ions. The purpose was to test the use of this new technique to obtain transport parameters diffusivity (D_e) as well as distribution coefficients (K_d). Compared with the traditional through diffusion methods for transport studies, the electromigration technique can decrease the experimental time from months to days due to the acceleration of the migration of studied ions by an electric field. The technique also has the advantage of providing Kd values for intact rock samples to avoid the crushing effects of them as used in batch sorption studies. Therefore, the electromigration technique has received increasing attention for directly providing sorption and diffusion data under intact rock conditions. The results shown in this work will be used to justify the electromigration technique as an appropriate technique for studying diffusion of radionuclides under nuclear waste repository conditions.

4.2 Materials and methods

4.2.1 Grimsel samples

4.2.1.1 Rock sample processing

Grimsel granodiorite was chosen as the studied intact rock sample for electromigration technique because of the extensive characterization of the parameters (e.g., porosity, permeability, mineralogy and pore structure distributions) and wide studies with batch sorption experiments and through diffusion experiments. (Ikonen et al., 2016; Kuva et al., 2018; Sammaljärvi et al., 2012)

The mineral composition of Grimsel granodiorite was measured by X-ray Diffraction (XRD, D8 Discover (A25) powder diffractometer equipped with LYNXEYE detector) and thin section analysis with polarizing microscopy in the Geological Survey of Finland (Table 4-1). The XRD spectra were recorded for 3 h at an angle interval of 4-100° 2θ (CuKα) with a step size of 0.0092° 2θ. Grimsel granodiorite is a mixture of several minerals with around 40 wt.% of plagioclase, 20–25 wt.% of K-feldspar, 20–30 wt.% of quartz, 6–10 wt.% of biotite and 5 wt.% of chlorite. Biotite and chlorite content is up to 15 wt.% of the material and these minerals have a relatively large specific surface area compared to the other minerals existing in Grimsel granodiorite.

Table 4-1 Mineralogy analysis of Grimsel granodiorite by using the XRD (wt.%) and polarizing microscopy (point-counting by 500 points, vol.%) performed in the Geological Survey of Finland

Minerals	XRD (wt.%)	Polarizing microscopy analysis (vol.%)
Plagioclase	40	36.5
K-feldspar	25	17.2
Quartz	20	32.8
biotite	10	6.4
Muscovite + sericite	---	2.1
Epidote	---	1.1
Amphibole	---	3.2
chlorite	5	0.3

The diameter and length of the rock sample were measured to be 49.5 mm and 26.5 mm, respectively. After cutting and polishing, the rock sample was immersed in background electrolyte (0.2 M NaCl + 0.002 M NaHCO3) for at least two weeks for the purpose of background saturation. The 0.2 M NaCl in the background water simulates the salinity of the common groundwater, while 0.002 M NaHCO3 was added as a pH buffer to resist the pH change caused by hydrolysis reactions occurring on electrodes during the operation of electromigration experiments. After saturation, the rock sample was sealed tightly with epoxy in a plastic cylindrical shell, which has the same inner diameter as the diameter of the rock sample (Figure 4-1). The tightness of the holder was also checked, and the results show that the tracer ions can only migrate through the rock sample by its micropores.

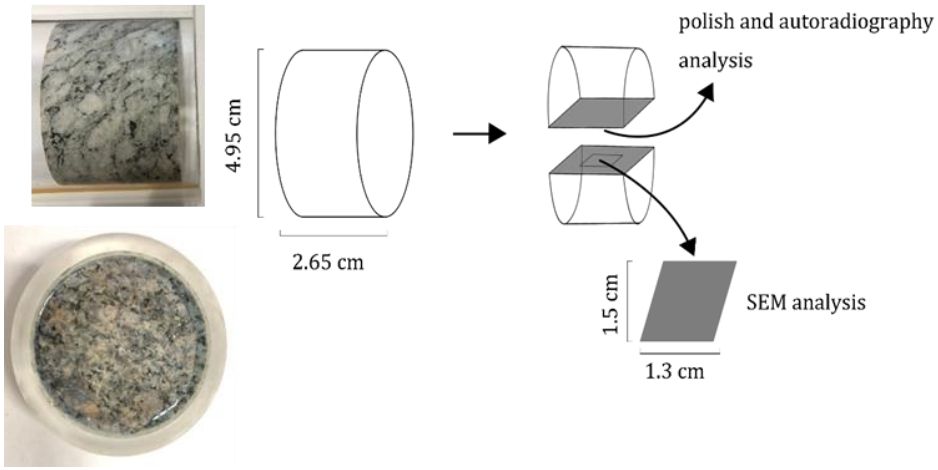

Figure 4-1 Left: Grimsel granodiorite rock core that was sealed in a cylinder for the electromigration device. The same sample was impregnated with C-14-PMMA for autoradiography. Right: The sample sawing procedures and the surfaces for autoradiography and SEM/EDS analysis.

4.2.2 C-14-PMMA autoradiography

C-14-PMMA autoradiography was applied to the Grimsel granodiorite studied for porosity measurement (Hellmuth et al., 1995; Sardini et al., 2006; Sammaljärvi et al., 2017; Voutilainen et al., 2019). The sample is first dried and then impregnated with a tracer solution of C-14-labeled methyl methacrylate (C-14-MMA). This tracer intrudes into the sample's connected porosity. Once the tracer has intruded into all accessible pore spaces, the tracer is fixed in place by polymerizing it. When the tracer has been polymerized, the sample can be sawed, polished and placed on an autoradiographic film for film autoradiography or an imaging plate for digital autoradiography.

The XCT was used to obtain the three dimensional structure of a Bukov sample. C-14-PMMA autoradiography was used to obtain the spatial porosity and scanning-micro X-ray fluorescence (µXRF) was used to obtain elemental maps from the same sample, which were then converted into mineral maps using the Bruker AMICS automated mineralogy software. The mineral maps and XCT data were then combined using an in-house modified version of the deep learning method to obtain 3D mineral maps. When the porosity map and mineral map are combined to calculate mineral-specific porosities a 3D porosity map suitable for diffusion simulations and modeling was obtained.

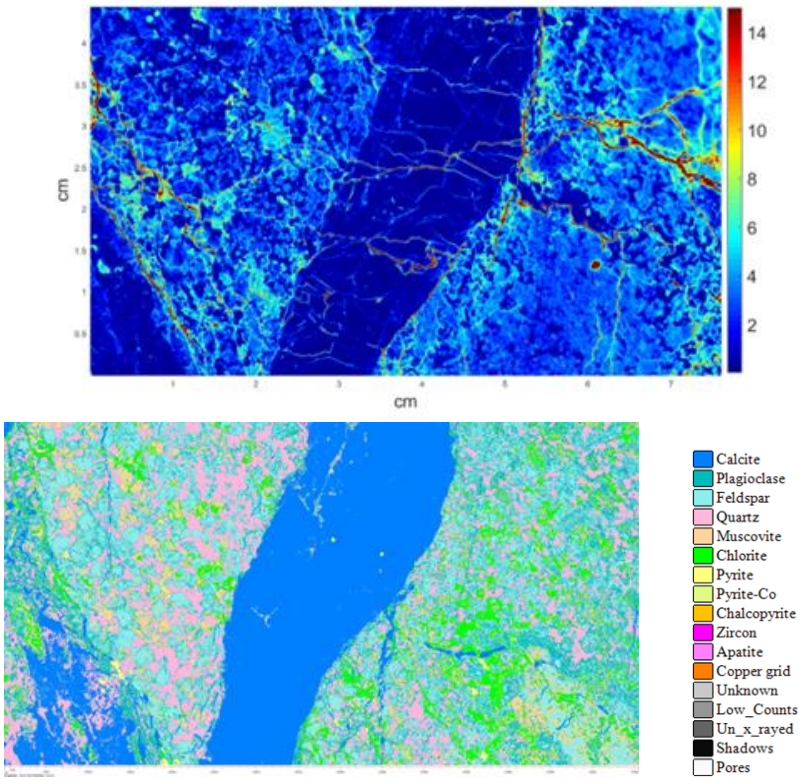

Figure 44-2 *Porosity map of a Bukov core sample obtained by C-14-PMMA autoradiography (up) Mineral map from a Bukov core sample obtained by µXRF.*

4.2.3 Electromigration

4.2.3.1 Electromigration device development

The electromigration device used in this study was modified based on the former design of Löfgren and Neretnieks (2006) and André et al. (2009) by introducing a potentiostat that can maintain a constant voltage across the rock sample and by adding $NaHCO_3$ buffer to stabilize the pH conditions of the background electrolyte. The modified electromigration device has the functions of voltage-self-controlling, continuous-current-recording and solution-pH-stabilization (Li et al., 2020). A schematic figure of the electromigration device is shown in Figure 4-3. The volume of the source and recipient chambers is 152 mL, while the volume of the two electrode chambers at both ends is 250 mL. The four-electrode plates with a dimension of 1 cm × 2 cm are made of titanium. A platinum wire was used to connect the titanium electrodes. A voltage meter and an ampere meter were utilized to record the instant voltage over the rock sample and the current going through the whole device, respectively. The filters (Äspö underground rock, 0.7% porosity) with a length of 1 cm were used to separate the electrolyte in the two electrode chambers from the electrolyte in the source/recipient chambers. A constant potential of 2 V, 3 V and 4 V was applied over the rock sample, while the whole voltage applied to the electromigration device changes with time according to the resistance change of the rock sample. This process was controlled by the four-electrode system and the Amperometric i-t curve technique of the potentiostat. The current going through the electromigration device was also recorded continuously as a function of experimental time by the potentiostat.

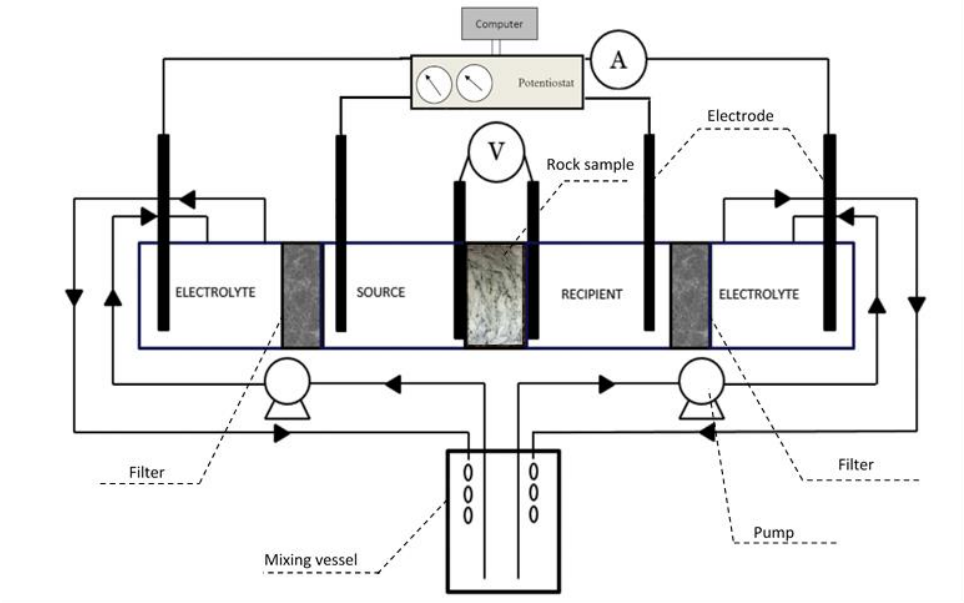

Figure 4-3 Schematic figure of the electromigration device run with Grimsel granodiorite. A potentiostat was introduced in the modified device to improve the stability of the whole system.

4.2.3.2 Electromigration measurements with Cs, Sr, Co

The diffusion experiment was performed with three tracers, CsCl, $SrCl_2$ and $CoCl_2$. The concentrations of the tracers in the source chamber as well as other running conditions are shown in Table 4-2. Before running the electromigration experiments, the speciation of the tracers in the background electrolyte (pH 8) was checked by Phreeqc with the database of Thermoddem V1.10 (15/12/2020) which is a database that gathers the thermodynamic properties of mineral phases from wastes and natural environments. The percentages of the tracers that exist in the sample dissolved ionic form are Cs^+ (91%), Sr^{2+} (96%) and Co^{2+} (76%). The remaining tracers exist in Cl-complexing formats, such as CsCl, $SrCl^+$ and $CoCl^+$. To simplify the system, we assumed that all the tracers were in the speciation format of Cs^+, Sr^{2+} and Co^{2+}. Three voltages 2V, 3V and 4V, were applied in the experiments to study the effect of different voltages on the retardation processes. The ionic strength of the tracer ions was designed to be the same to avoid the influence of the electric double layer. Thus, the initial concentration of Cs^+ (0.1 M) was 3 times higher than the concentration of Sr^{2+} and Co^{2+} (0.033 M). The background electrolyte was 0.2 M NaCl and buffered by 0.002 M $NaHCO_3$ to simulate the ionic strength and pH value of normal groundwater.

Table 4-2 The initial conditions of the electromigration experiments. "×" means no additions

Tracer	Cs^+ (M)	Sr^{2+} (M)	Co^{2+} (M)	Voltages tested (V)	Background electrolyte
CsCl	0.1	×	×	2, 3, 4	0.2 M NaCl +2 mM $NaHCO_3$
$SrCl_2$	×	0.033	×	2, 3, 4	0.2 M NaCl +2 mM $NaHCO_3$
$CoCl_2$	×	×	0.033	2, 3, 4	0.2 M NaCl +2 mM $NaHCO_3$

Before running the electromigration experiments with tracers, the device was stabilized by running it with background electrolyte under the applied voltage overnight to saturate the rock sample with background electrolyte. After stabilization, tracers were added to the source chamber, resulting in the final concentration of the tracers being listed in Table 4-2. To balance the ionic strength throughout the through-electromigration cell, NaCl with the same ionic strength as the tracer was immediately added into the recipient chamber.

After the addition of the tracers, the source and recipient chambers were both stirred for 5 min by magnetic stirrers for full dissolution. At the same time, 100 µL of sample from the source chamber and 1 mL of sample from the recipient chamber were taken to determine the original concentrations of the tracer ions at the beginning of the experiment. After sampling, the same amount of background electrolyte was added into the chambers to keep the hydraulic pressure and the volume of solutions constant. During the experiments, the electrolytes in the source and recipient chambers were stirred all the time by a magnetic stirrer. The tracer concentrations in the recipient chamber were followed by taking out 2 mL of electrolytes from time to time and then adding the same amount of background electrolytes.

4.2.3.3 Data analysis approach

By following the concentration change of the tracer ions in the recipient chamber, a breakthrough curve was obtained from the experiment. Two models were utilized to analyse the diffusivities (D_e) and distribution coefficients (K_d) of different tracers. The ideal plug-flow model was previously used by André et al. (2009) and Löfgren & Neretnieks (2006) for the analysis of electromigration results. However, it considers only the effect of the electromigration process on the behavior of the tracers. For more accurate and realistic data analysis, the advection-dispersion model was developed (Meng et al., 2020). The advection-dispersion model takes into account electromigration, electro-osmosis and dispersion and thus can provide better parameter identification with smaller uncertainties.

4.3 Results and discussion

4.3.1 Characterization of diffusion path

Autoradiography results obtained are shown in Figure 4-4. The mean porosity was determined to be 0.56%. The surface scan shows that there is observable foliation in the sample. The C-14-PMMA autoradiography results also indicate that this foliation is observed in the spatial distribution of porosity. The pore network appears to be well connected, with small clusters of highly porous areas here and there. While there is notable intergranular porosity, all of the grains themselves also appear porous. The porosity map highlights how some highly porous minerals are found among the sample matrix, although considerable porosity is found in all mineral phases.

Results obtained via SEM/EDS analyses are shown in Figure 4-5. Plagioclase, potassium feldspar and quartz were found as large grains. These minerals were often fractured and had fissures running through them. Biotite was found in lamellae of different sizes ranging from hundreds of micrometers to a few tens of micrometers. The biotite lamellae have interlamellar porosity and some of the lamellae were fractured. Biotite was also sometimes found together with muscovite grains. Biotite had altered in several places to chlorite, with the lamellar structure intact. There were also small grains of titanite found sporadically. The fissure population is dominated by open cleavage cracks in mica and grain boundary cracks and an interconnected network of micro fissures exists in the whole granodiorite matrix.

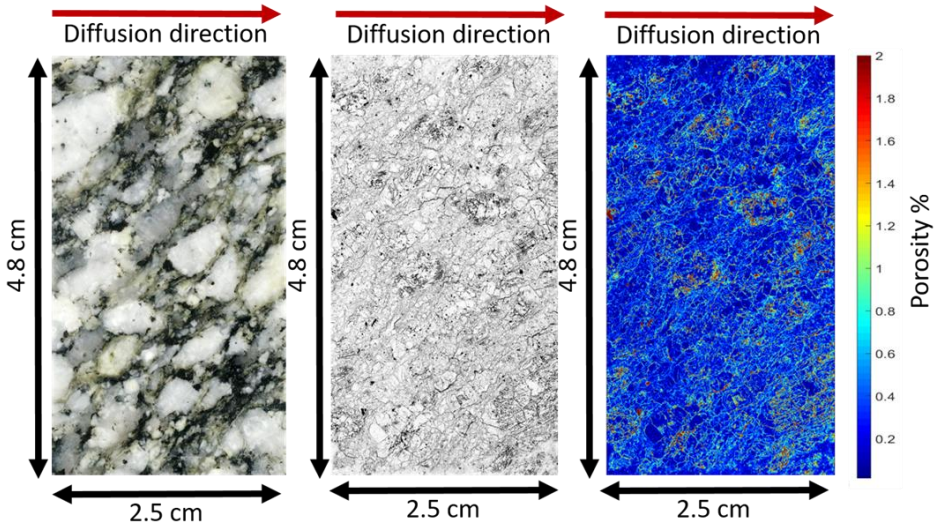

Figure 4-4 Left: Surface scan of the autoradiography sample. Center: Corresponding autoradiograph. Right: Corresponding porosity map. The diffusion direction in the electromigration experiment was from left to right

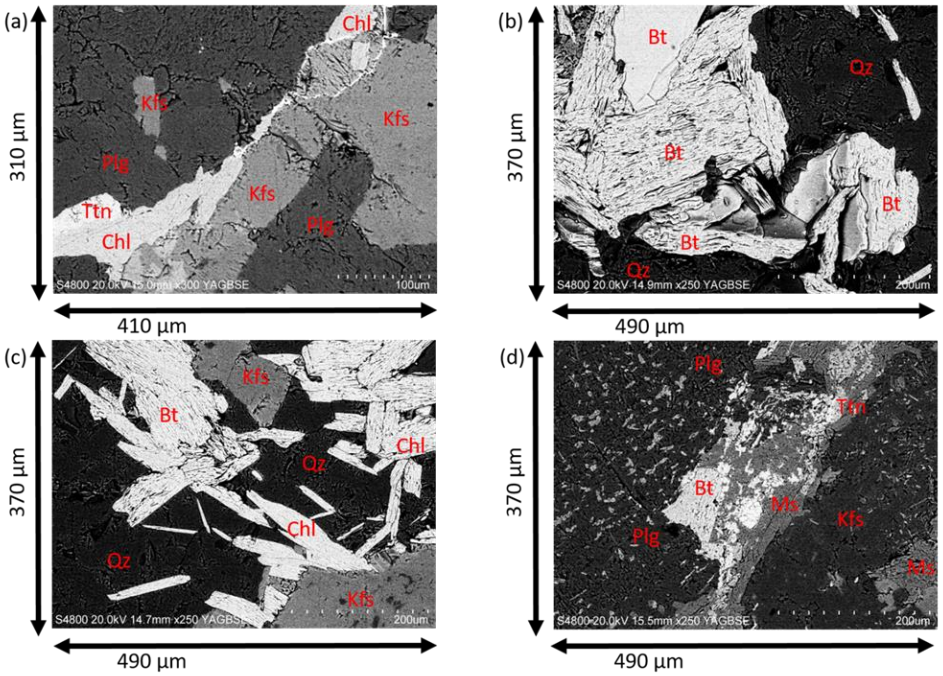

Figure 4-5 SEM results. (a): Plagioclase and feldspar grains, and chlorite grains. (b): Biotite lamellae and quartz grains. (c): Quartz grains, Potassium feldspar grains, Biotite and chlorite lamellae. (d) Plagioclase and feldspar grains. Biotite and muscovite lamellae. Legend: Bt: Biotite, Chl: Chlorite, Kfs: Potassium feldspar, Ms: Muscovite, Plg: Plagioclase, Qz: Quartz, Ttn: Titanite

The pore structure of the sample has some amount of foliation to it, which is at an angle compared to the diffusion direction in the electromigration experiment. This likely influences the pathway the tracers take. This could cause the pathway to be longer than in a sample with no foliation. The sample matrix also contained several highly porous areas interspersed throughout the sample. These highly porous areas are biotite and its alteration product, chlorite. The fissures of micrometer-scale transecting biotite and chlorite grains form a part of the network of main migration pathways in Grimsel granodiorite. Biotite is known to be rather porous, and alteration products such as chlorite are known to be highly porous. They also appeared highly porous on the SEM results. These minerals, biotite and chlorite, also have

high specific surface areas and could act as sites of enhanced sorption for the cationic tracers used in electromigration experiments. As these mineral clusters appear relatively evenly spread throughout the sample, it is likely that their retarding effect on the diffusion applies more or less uniformly on the electromigration experiment, although possible sorption sites are of course spread out and diffusion profiles are affected.

4.3.2 Electromigration experiments

4.3.2.1 Sr

Three voltages (2V, 3V and 4V) over the rock sample were applied in the electromigration experiments with SrCl2 using the modified electromigration device. The potential gradients over the rock sample were 75.47 V/m, 113.21 V/m and 150.94 V/m, respectively. The original concentration of $SrCl_2$ in the source chamber was 0.03 M and the concentration of Sr^{2+} in the recipient chamber was followed for about 3 days. The breakthrough curves as a function of experimental time recorded by potentiostat are shown in Figure 4-6.

First, the traditional ideal plug-flow model was applied to analyze the experimental results by drawing a linear regression line with the last several data points where a pseudo steady state seemed to be established (Figure 4-6). The breakthrough time for Sr^{2+} ions migrating through the rock sample and the concentration change rate of the Sr^{2+} ions in the recipient chamber can be evaluated from the intercept and the slope of the linear regression line, as given in Table 4-3. The results show that the effective diffusion coefficients evaluated from the ideal plug-flow model for Sr^{2+} migrating through the rock sample is around 3.2×10^{-13} m^2/s (the average value under three different voltage gradients). Compared with the reported De values of Sr^{2+} migrating through a crystalline granite rock sample traditionally used through diffusion experiments, the De values obtained by the electromigration method are quite reasonable. For example, Yamaguchi et al. (1993) reported the De values of Sr^{2+} to be $(0.32–1.7)\times10^{-13}$ m^2/s in an Inada granite sample with a similar porosity (0.68±0.03 %) using 0.1 M KCl as the background electrolyte. However, the evaluation of K_d gave nearly zero or negative values, which may indicate that the migration speed for Sr^{2+} ions was too quick and that the sorption process was not completed during the experimental process or that the ideal plug-flow may give results with large errors because of some unrealistic assumptions.

The numerical solution of the advection-dispersion model in the Laplace domain can be easily achieved by the de Hoog algorithm (de Hoog et al., 1982). The D_e and K_d values as well as other parameters, the effective dispersion coefficient, and formation factor, which can be deduced from the advection-dispersion model are listed in Table 4-4. The D_e values calculated by the advection-dispersion model are in agreement with the D_e values calculated by the ideal plug-flow model (average 2.86×10^{-13} m^2/s), especially for the results when 2V voltage was applied. The similarity can also be shown by Figure 4-6, where the comparison of the two models is depicted. However, the advection-dispersion model is believed to be a more accurate modeling method because it avoids the use of many unrealistic assumptions associated with the ideal plug-flow model. In addition, the advection-dispersion model takes into account the effect of dispersion, which plays a non-negligible role in the ionic transport through the rock sample. For example, the breakthrough curve shows a clear curvature at the moment around the breakthrough time and this signifies the effect of the dispersion. The ideal plug-flow model can only use a small portion of the experimental data when a pseudo-steady state is established. However, sometimes it is difficult to define such a pseudo-steady state. The K_d values calculated from the advection-dispersion model vary from the magnitude of 10^{-7} m^3/kg to 10^{-5} m^3/kg. The large distribution of the modeling results may indicate that the sorption process was not completed due to the great acceleration of the migration speed. Taking into account the experimental time (within 80 h), this conclusion is reasonable since the typical equilibration time in batch sorption experiments is one or two weeks.

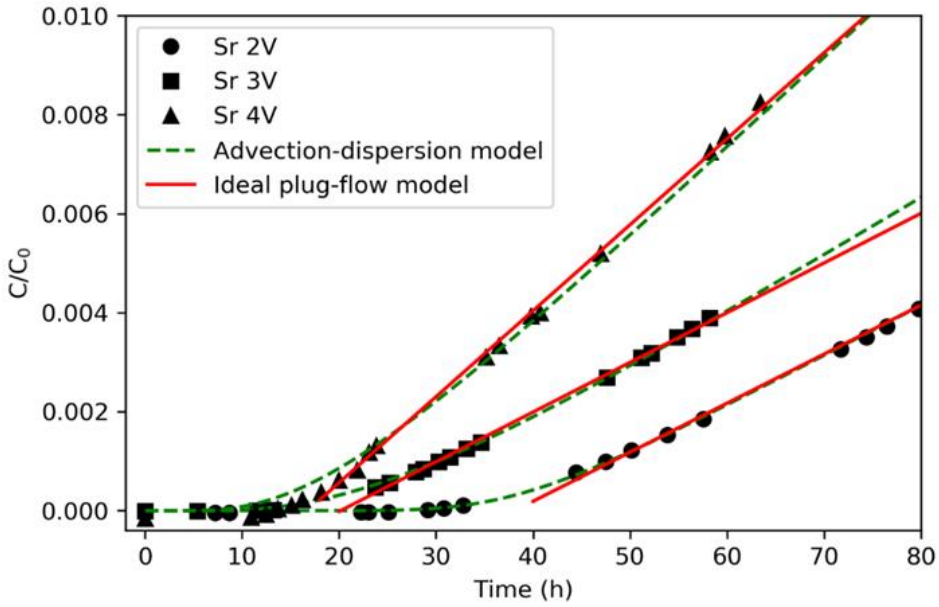

Figure 4-6 The concentrations of Sr followed in the recipient chamber as a function of time with 0.03 M SrCl2 in the source chamber. The voltage over the rock sample were 2V, 3V and 4V, respectively.

Table 4-3. Electromigration modelling results with ideal plug-flow modelling of Sr^{2+} migrating through the rock sample.

Voltage (V)	Voltage gradient (V/m)	Breakthrough time (h)	Slope (mol/L/h)	D_e (m^2/s)
2	75.47	39.59	3.398×10^{-6}	3.84×10^{-13}
3	113.21	21.47	3.459×10^{-6}	2.61×10^{-13}
4	150.94	16.74	5.862×10^{-6}	3.32×10^{-13}

Table 4-4. Parameter evaluation of the breakthrough curves of Sr^{2+} migrating through the rock sample using advection-dispersion model.

Voltage (V)	D_d (m^2/s)	D_e (m^2/s)	F_f	K_d (m^3/Kg)
2	5.57×10^{-9}	3.78×10^{-13}	4.77×10^{-4}	8.90×10^{-7}
3	1.20×10^{-7}	2.43×10^{-13}	3.07×10^{-4}	6.94×10^{-6}
4	2.29×10^{-7}	2.38×10^{-13}	3.01×10^{-4}	1.13×10^{-5}

4.3.2.2 Co

The migration behavior of Co^{2+} ions was tested with the same rock sample under the same experimental conditions as for Sr. The original concentration of $CoCl_2$ in the source chamber was 0.033 M. The breakthrough curves as a function of experimental time recorded by the potentiostat are shown in Figure 4-7. The breakthrough time and the slope data deduced from the linear regression line as well as the D_e values calculated are given in Table 4-5. The modeling results with the advection-dispersion model

are shown in Table 4-6. The average D_e value by the advection-dispersion model is 1.35×10^{-13} m^2/s, which is quite similar to the results from the ideal plug-flow model. The results show that the average effective diffusion coefficient of Co^{2+} ions is 1.23×10^{-13} m^2/s, which is about one-third or half of the diffusion coefficient of Sr^{2+} ($2.8\text{-}3.3 \times 10^{-13}$ m^2/s). In dilute aqueous solutions, the diffusion coefficient for Co^{2+} is 7.32×10^{-10} m^2/s while the diffusion coefficient for Sr^{2+} is 7.91×10^{-10} m^2/s (CRC Press, 2018). The much smaller diffusion coefficient for Co^{2+} was obtained from the electromigration experiments and may indicate that sorption plays an important role when we compare the diffusion coefficients of Co^{2+} and Sr^{2+} ions in the rock samples. Our idea is supported by the former observations that Co^{2+} has a different sorption mechanism than both Sr^{2+} and Cs^{+} ions (Cui & Eriksen, 1997; Park et al., 1992; Muurinen et al., 1985). Previous studies show that, on the same fracture filling materials of granite, the K_d values of Co^{2+} is one and a half orders of magnitude higher than that of Sr^{2+} (Cui et al., 1997). The sorption mechanism of Sr^{2+} on crystalline rock was concluded to be ion exchange (Cui & Eriksen, 1994; Cho & Komarneni, 2009; Liu et al., 2004). The much stronger Co^{2+} sorption indicated that complexation reactions between Co^{2+} and surface sites have formed. Ebner et al. (2001) also compared the sorption behaviors of Cs, Sr and Co ions on magnetite; it shows that the sorption of these three ions on magnetite follows the sequence of $Co^{2+} > Sr^{2+} > Cs^{+}$. Thus, the smaller diffusion coefficient of Co^{2+} than Sr^{2+} observed from the electromigration results can be explained by the different sorption mechanisms of these two ions.

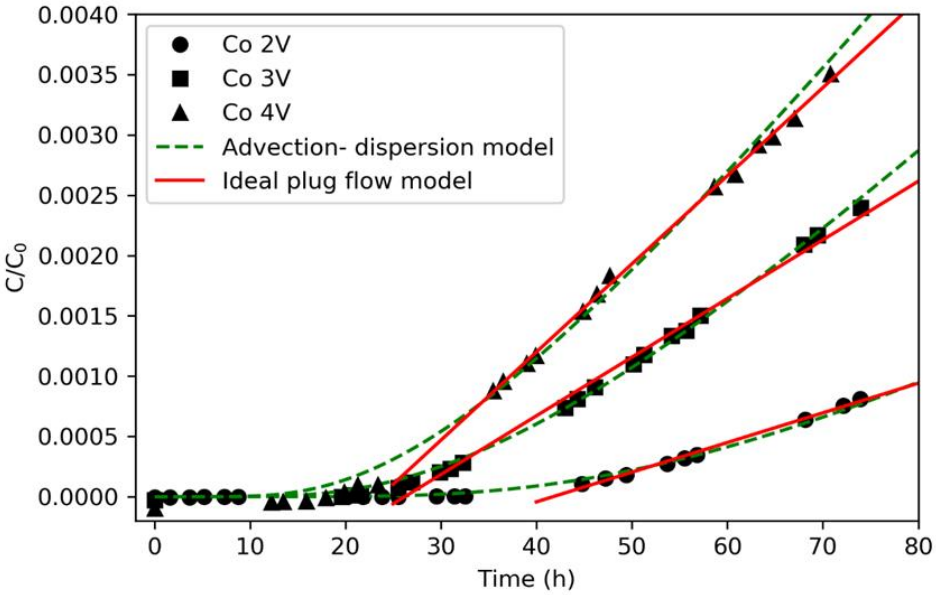

Figure 4-7 The concentration of Co^{2+} ions followed in the recipient chamber as a function of experimental time in the electromigration experiments.

Table 4-5 Electromigration experimental results with ideal plug-flow modelling of Co^{2+} migration through the rock sample.

Voltage (V)	Voltage gradient (V/m)	Breakthrough time (h)	Slope (mol/L/h)	D_e (m^2/s)
2	75.47	43.35	8.648×10^{-7}	9.79×10^{-14}
3	113.21	28.84	1.783×10^{-6}	1.35×10^{-13}
4	150.94	22.01	2.387×10^{-6}	1.35×10^{-13}

Table 4-6. Parameters evaluation of the breakthrough curves of Co^{2+} migrating through the rock sample using advection-dispersion model.

Voltage (V)	D_d (m^2/s)	D_e (m^2/s)	F_f	K_d (m^3/Kg)
2	1.86×10^{-8}	1.59×10^{-13}	4.73×10^{-4}	1.62×10^{-6}
3	1.09×10^{-7}	9.43×10^{-14}	2.62×10^{-4}	1.14×10^{-5}
4	8.41×10^{-8}	1.52×10^{-13}	4.24×10^{-4}	5.71×10^{-6}

4.3.2.3 Cs

The third kind of cation tested was Cs^+ which has +1 oxidation state compared with Sr^{2+} and Co^{2+}, the oxidation state of which is +2. The original concentration in the recipient chamber was 0.1 M in order to maintain the same ionic strength as the tested Sr^{2+} and Co^{2+} experiments. The experimental results as well as the modeling data from the ideal plug-flow model and the advection-dispersion model are shown in Figure 4-8. The modelled D_e and K_d values as well as other parameters from these two models are summarized in Tables 4-7 and 4-8. Both the ideal plug-flow model and the advection-dispersion model give almost the same D_e values. The average D_e value from the ideal plug-flow model is 2.25×10^{-12} m^2/s and the average D_e value calculated by the advection-dispersion model is 2.26×10^{-12} m^2/s. The value is about 8 times larger than the modelled D_e value for Sr^{2+} diffusion and 18 times larger than the modelled D_e value for Co^{2+} diffusion. It is quite reasonable that the diffusion of Cs^+ is much quicker than the diffusion of Sr^{2+} and Co^{2+} ions. The diffusion coefficient of Cs^+ in diluted water is 2.056×10^{-9} m^2/s which is much larger than the diffusion coefficient of both Sr^{2+} and Co^{2+} ions (0.791 m^2/s and 0.732 m^2/s, respectively).

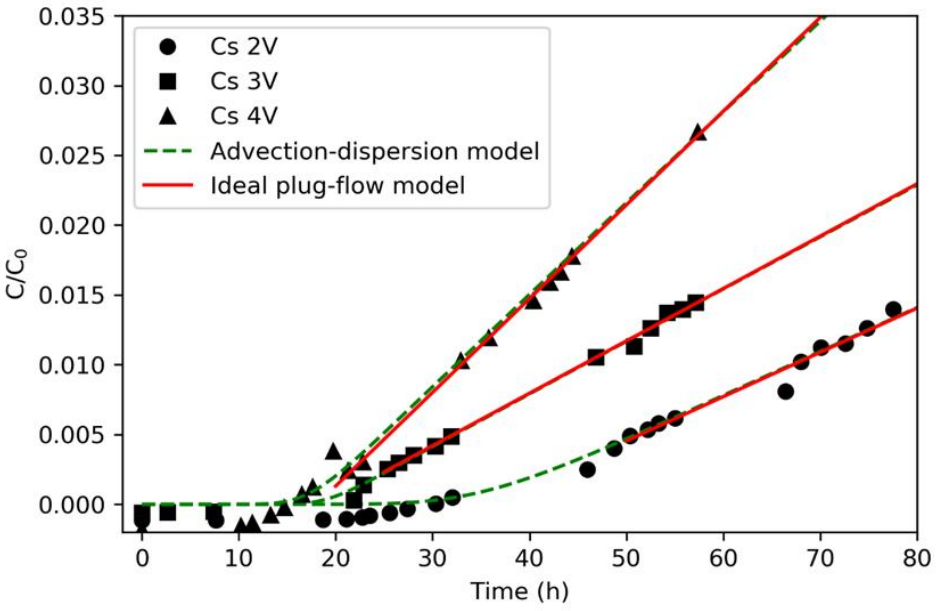

Figure 4-8 The concentration of Cs^+ ions followed in the recipient chamber as a function of experimental time in the electromigration experiments.

Table 4-7 *Electromigration experimental results with ideal plug-flow modelling of Cs^+ migration through the rock sample.*

Voltage (V)	Voltage gradient (V/m)	Breakthrough time (h)	Slope (mol/L/h)	D_e (m^2/s)
2	75.47	43.35	$3.216*10^{-5}$	$2.37*10^{-12}$
3	113.21	28.84	$4.178*10^{-5}$	$1.87*10^{-12}$
4	150.94	22.01	$6.931*10^{-5}$	$2.51*10^{-12}$

Table 4-8. Parameters evaluation of the breakthrough curves of Cs^+ migrating through the rock sample using advection-dispersion model.

Voltage (V)	D_d (m^2/s)	D_e (m^2/s)	F_f	K_d (m^3/Kg)
2	$1.52*10^{-8}$	$2.38*10^{-12}$	$1.16*10^{-3}$	$9.34*10^{-6}$
3	$6.82*10^{-9}$	$1.89*10^{-12}$	$9.21*10^{-3}$	$4.51*10^{-6}$
4	$2.25*10^{-8}$	$2.50*10^{-12}$	$1.22*10^{-3}$	$9.65*10^{-6}$

4.4 References

André, M., Neretnieks, I., & Malmström, M. E. (2009). Measuring sorption coefficients and BET surface areas on intact drillcore and crushed granite samples. *Radiochimica Acta International Journal for Chemical Aspects of Nuclear Science and Technology*, *96*(9–11), 673–677.

Cho, Y. & Komarneni, S. (2009). Cation exchange equilibria of cesium and strontium with K-depleted biotite and muscovite. *Appl. Clay Sci., 44*, 15–20.

Cui, D. & Eriksen, T.E. (1994). Experimental Study of Strontium Sorption on Fissure Filling Material; SKB Report 94-27; SKB: Stockholm, Sweden.

Cui, D., & Eriksen, T. E. (1997). On the Sorption of Co and Cs on Stripa Granite Fracture-Filling Material. *Radiochimica Acta*, *79*(1), 29–36.

CRC Press. CRC Handbook of Chemistry and Physics, 99th ed., CRC Press: Boca Raton, FL, USA, 2018.

de Hoog, F. R., Knight, J. H., & Stokes, A. N. (1982). An Improved Method for Numerical Inversion of Laplace Transforms. *SIAM Journal on Scientific and Statistical Computing, 3*(3), 357–366.

Ebner, A.D., Ritter, J.A., & Navratil, J.D. (2001) Adsorption of Cesium, Strontium, and Cobalt Ions on Magnetite and a Magnetite-Silica Composite. *Ind. Eng. Chem. Res., 40*, 1615–1623.

Hellmuth, K.-H., Klobes, P., Meyer, K., Röhl-Kuhn, B., Siitari-Kauppi, M., Hartikainen, J., Hartikainen, K., & Timonen, J. (1995). Matrix retardation studies: Size and structure of the accessable pore space in fresh and altered crystalline rock. Z. Geol. Wiss., 23, 691–706.

Ikonen, J., Sardini, P., Jokelainen, L., Siitari-Kauppi, M., Martin, A., & Eikenberg, J. (2016). The tritiated water and iodine migration in situ in Grimsel granodiorite. Part I: determination of the diffusion profiles. *Journal of Radioanalytical and Nuclear Chemistry*, *310*(3), 1041–1048.

Kuva, J., Sammaljärvi, J., Parkkonen, J., Siitari-Kauppi, M., Lehtonen, M., Turpeinen, T., Timonen, J., & Voutilainen, M. (2018). Imaging connected porosity of crystalline rock by contrast agent-aided X-ray microtomography and scanning electron microscopy. *Journal of Microscopy*, *270*(1), 98–109.

Li, X., Meng, S., Puhakka, E., Ikonen, J., Liu, L., & Siitari-Kauppi, M. (2020). A modification of the electromigration device and modelling methods for diffusion and sorption studies of radionuclides in intact crystalline rocks. *Journal of Contaminant Hydrology*, *231*, 103585.

Liu, C., Zachara, J.M., & Smith, S.C. (2004) A cation exchange model to describe Cs+ sorption at high ionic strength in subsurface sediments at Hanford site, USA. *Journal of Contaminant Hydrology., 68*, 217–238.

Meng, S., Li, X., Siitari-Kauppi, M., & Liu, L. (2020). Development and application of an advection-dispersion model for data analysis of electromigration experiments with intact rock cores. *Journal of Contaminant Hydrology*, *231*, 103618.

Muurinen, A., Rantanen, J., & Penttilä-Hiltunen, P. (1985). Diffusion Mechanisms of Strontium, Cesium and Cobalt in Compacted Sodium Bentonite. *MRS Online Proceedings Library (OPL)*, *50*, 617.

Löfgren, M., & Neretnieks, I. (2006). Through-electromigration: A new method of investigating pore connectivity and obtaining formation factors. *Journal of Contaminant Hydrology*, *87*(3), 237–252.

Park, C. K., Woo, S. I., Tanaka, T., & Kamiyama, H. (1992). Sorption and Desorption Behavior of 60Co, 85Sr, and 137Cs in a Porous Tuff. *Journal of Nuclear Science and Technology*, *29*(12), 1184–1193.

Sardini, P., Siitari-Kauppi, M., Beaufort, D., & Hellmuth, K.-H. (2006). On the connected porosity of mineral aggregates in crystalline rocks. *American Mineralogist*, *91*(7), 1069–1080.

Sammaljärvi, J., Jokelainen, L., Ikonen, J., & Siitari-Kauppi, M. (2012). Free radical polymerisation of MMA with thermal initiator in brick and Grimsel granodiorite. *Engineering Geology*, *135–136*, 52–59.

Sammaljärvi, J., Lindberg, A., Voutilainen, M., Ikonen, J., Siitari-Kauppi, M., Pitkänen, P., & Koskinen, L. (2017). Multi-scale study of the mineral porosity of veined gneiss and pegmatitic granite from Olkiluoto, Western Finland. Journal of Radioanalytical and Nuclear Chemistry, 314(3), 1557–1575.

Smith, P. A., & Degueldre, C. (1993). Colloid-facilitated transport of radionuclides through fractured media. *Journal of contaminant hydrology, 13*(1-4), 143-166.

Voutilainen, M., Miettinen, A., Sardini, P., Parkkonen, J., Sammaljärvi, J., Gylling, B., Selroos, J.-O., Yli-Kaila, M., Koskinen, L., & Siitari-Kauppi, M. (2019). Characterization of spatial porosity and mineral distribution of crystalline rock using X-ray micro computed tomography, C-14-PMMA autoradiography and scanning electron microscopy. *Applied Geochemistry, 101*, 50–61.

Yamaguchi, T., SAKAMOTO, Y., & SENOO, M. (1993). Consideration on Effective Diffusivity of Strontium in Granite. *Journal of Nuclear Science and Technology*, *30*(8), 796–803.

5 Flow field and fracture aperture analysis [HZDR, UJV]

5.1 Summary

For the FUTURE work package, several overarching goals were formulated in the project proposal. Out of these, the following objectives are specifically addressed in the subchapter regarding transport processes in fractured crystalline host rocks:

- The role of microstructures on radionuclide mobility in crystalline rocks
- The impact of pore size variability and heterogeneity on the mobility of chemical species
- Refined understanding of the relation between fracture/ pore structures and transport as well as the feedback of mineral reactions (dissolution/precipitation, clogging) on pore structure and connectivity

The focus of our investigations reported in this subchapter is on specific characteristics of transport behavior in fractures of crystalline host rocks. This concerns the coupled influence of fracture aperture and wall topography/roughness on fluid residence time and preferred flow paths, e.g., channeling. Furthermore, these questions are related to the influence of fracture mineralization. Different mineralization types, such as calcite and phyllosilicates are dominant in the investigated host rocks from Czech Republic and Finland. Such fracture fillings further alter the advective flow field by a local increase in fluid residence time and a more pronounced heterogeneity of the fluid-rock interface.

According to the proposed work plan, the following steps were conducted:

- The connected pore network and surface topography of fractured crystalline rock samples and mineral infills (provided by SURAO and POSIVA) were analyzed using µCT and confocal/ interferometry microscopy prior to flow, diffusion, and sorption experiments. After the transport experiments, random studies of potential changes in the flow paths were performed. This ensured that no unwanted changes occurred during the long-term flow experiments.
- Batch type and flow-through experiments utilized the reference pore water of the specific host rock to allow comparison with existing studies and direct applicability for subsequent practical use. We analyzed the impact of pore size variability of fracture infills and intact rock.
- Additional objectives included the analysis of the fluid velocity field (diffusive vs. advective transport) in and close to fractures by using PET techniques. We utilized flow-through tracer tests to analyse the mobility of non-sorbing tracers within rock fractures.
- The experimental and analytical results were prepared to provide a basis for rigorous uncertainty and sensitivity studies thus providing an interface to numerical work. Due to the specific situation with laboratory closures during the project period, we used a PET flow field data set as well as CT and surface data for own extensive numerical studies to quantitatively understand the coupling between fracture aperture widths and mineralization affecting surface roughness variability.

Generally, the results contribute to a more realistic view on radionuclide migration in complex systems in order to overcome the current over-conservative consideration of heterogeneities, such as fracture planes, mineral infills, and porosity networks. The activities have been performed under close cooperation of the participating institutions.

5.2 Materials

We used fractured crystalline rocks from the Czech Republic (Bukov URF; Mrakotin quarry) and Finland (Onkalo site) for our transport investigations, cf. overview in Table 5-1. The table provides general information about the material provenance, specific transport-relevant properties and remarks about types of data obtained.

Table 5--1. Overview of sample names, origin, material specifications and comments on the data sets, including information on the different PET nuclides, selected based on differences in transport mechanism. Abbreviations: µCT: microcomputed X-ray tomography, CM: confocal microscopy, BTC: breakthrough curve.

Sample Name	Provenance	Notes on fracture characteristics	Analytical notes
MSVJ2	Mrakotin quarry (CZ)	• open fracture, minor or no infills • complex en-échelon fracture geometry	• aperture (µCT) and surface roughness (CM) analysis • advective flow: PET (F-18)
BZ8_1 (BZ-XII-38.8 -3 -11)	Bukov URF (CZ)	• tight fractures with precipitates • multiple generations of calcite • reduced/ hindered advective flow	• flow/ diffusive flux: PET (Na-22, I-124)
S36_5	Bukov URF (CZ)	• simple fracture geometry • minor or no fracture-filling materials (locally chloritic infill)	• advective flow: PET (F-18) • PET-BTC analysis
OLKR5	Onkalo (FI)	• filled fracture (fine-grained material: sheet silicates and calcite) • advective transport, but unsuccessful second experiment due to clogging	• aperture (µCT) and surface roughness (CM) analysis • advective flow: PET (F-18, I-124)

Samples from Czech Republic for the flow-through experiments were obtained from two sources, (i) from a granite block of the Mrakotin quarry (Fig. 5-1) and (ii) from Bukov, Rožná mine (drill core archive of the SÚRAO Bukov URF or new in-situ drilling) (Fig. 5-2). When selecting suitable samples, special attention was paid to the type of fracture-filling minerals, e.g., calcite or clay minerals. Second concern was potential mechanical damage. This might occur to the core during drilling, often at the interface between fracture filling materials and the surrounding rock. We have carefully examined this because it is of great importance for the integrity of the transport experiments.

Figure 5-1: Drill core sampling in the preparation laboratory of the UJV from a granite block from the Mrakotin quarry.

Figure 5-2: SÚRAO drill core archive (left) and new in-situ drilling campaign (right) to obtain material from Bukov URF.

The procedure for taking and preparing samples with natural fractures for the subsequent flow experiments was thoroughly investigated and optimized within the framework of the project TH02030543 "Development of instruments for the study of contaminant transport in a fractured environment" of the TAČR funding program. The results of this project included utility model No. 34977, i.e., "Equipment for conducting dynamic transport experiments in the form of tracer tests at low flow rates with a rock sample with natural fracture" (TH02030543-V11) and the compilation of a "Certified methodology for migration tests with radionuclides under laboratory conditions" (TH02030543-V9).

5.2.1 Fractured crystalline rocks: complex geometry of open fractures

Mrakotin – Project partner UJV provided sample MSVJ2 from the Mrakotin quarry. A drill core section for PET flow field analysis and a small sample for detailed structural analysis were supplied. First, a structural investigation was performed by µCT analysis of the complete core sample. This dataset (spatial resolution: 46 µm) served as the basis of a finite element method (FEM) model using COMSOL Multiphysics® software and as reference for PET flow field analysis. The µCT analysis of a smaller sample volume (about 20 × 20 × 10 mm^3) was performed to determine the aperture properties and roughness characteristics of the fracture with higher spatial resolution (10 µm). Subsequently, the µCT data were segmented, including extensive manual post-processing, and a geometry for FEM models was created. This geometry, however, is a smoothed and expanded image of the fracture, as meshing was otherwise not possible. The reason for this is a complex *en-échelon* structure of three fracture surfaces with connections that are at or below µCT resolution. The limitation of spatial resolution is again due to the size of the sample. However, an even smaller sample would no longer be representative in terms of tracer transport. The resolution of the small-scale sample is sufficient for a quantitative analysis of the aperture characteristics and provides information about the surface roughness in the range of about 80 µm to 10 mm. Overall, the study of this *en-échelon* geometry goes beyond the usual studies

of simple apertures and allows conclusions to be drawn about transport in realistic geometries. Thus, a very interesting geometry for simulation calculations is available.

5.2.2 Fractured crystalline rocks with fracture-filling mineral

BUKOV URF; BZ8_1 – The core sample (Figs. 5-3, 5-4) was scanned by using µCT techniques with a spatial resolution of 76 µm to get an overview of the structural heterogeneity and to optimize the injection position within the filling material. Scans of smaller sample sections result in a spatial resolution of 30 µm. The higher resolution datasets were used to identify fracture planes and to analyse the material density distribution.

Figure 5-3: Drill core sample BZ8_1 from Bukov URF (BZXII-38,8 m), showing multiple generations of fracture-filling calcite precipitates

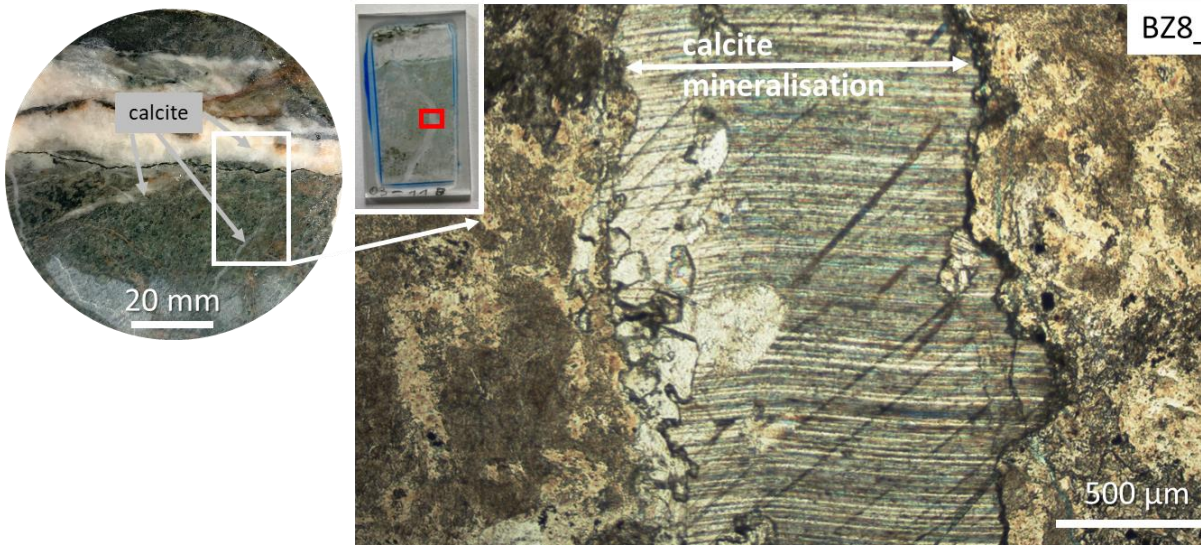

Figure 5-4: Overview of drill core sample BZ8_1 (left) with several calcite generations, the position of a thin section sample and microphotograph of a single fracture-filling generation of calcite precipitates in thin section.

BUKOV URF; S36_5 – This material was sampled in Bukov URF in niche ZK-2, from borehole S36-5 at a depth of 43 m below the bottom (Fig. 5-5).The entire core was scanned in an overview µCT dataset for subsequent PET data reconstruction. The resulting spatial resolution was 52 µm. Two smaller sections with higher spatial resolution (voxel size: 29 µm) were scanned for further quantitative investigations. A thickness distribution (aperture map) of the open fracture was calculated from the data.

Figure 5-5: The drill core from borehole S36 (Bukov URF, ZK-2), on the left before and on the right after the cutting process.

ONKALO SITE; OLKR5 – Structural analysis of the core material: A µCT analysis of the whole core (voxel size 62 µm) was performed. Higher spatial resolution µCT data (voxel size 16 µm) were produced for analysis of fracture geometry and fracture fill. The fracture fill consists mainly of calcite and chlorite, see also optical micrograph (Fig. 5-6). The calcite fill is clearly distinguishable from the host rock in the CT dataset. The data were also used to determine the fracture surface roughness.

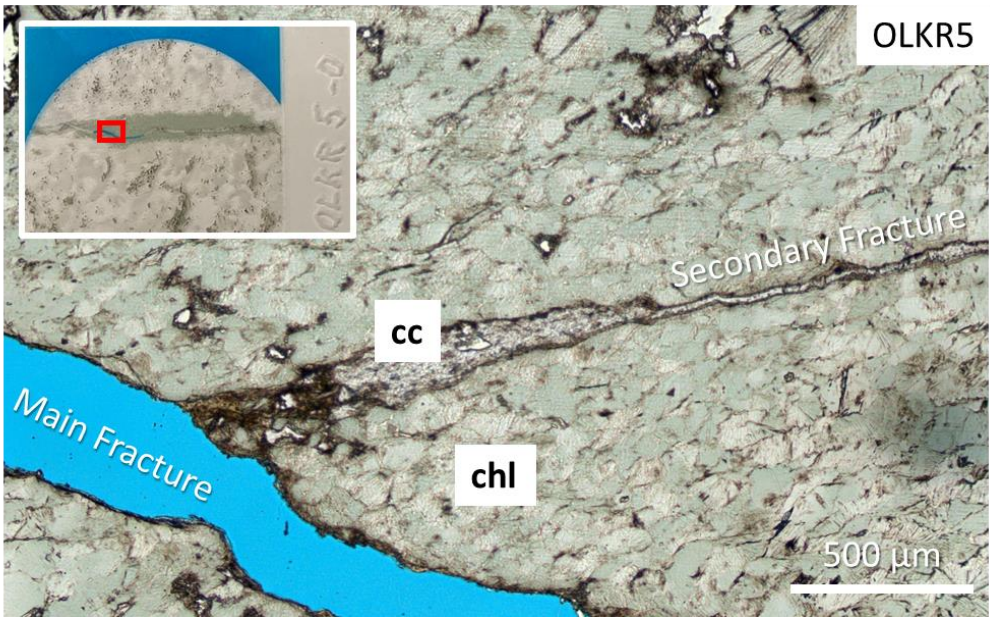

Figure 5-6: Overview of thin section sample OLKR5 (upper left) with filled fracture and the position of the thin section microphotograph. The thin section shows a complex situation of a dominant chlorite-filled fracture, partially open fracture geometry („main fracture“) and a younger („secondary“) calcite-filled fracture generation.

5.3 Methods

5.3.1 Surface topography microscopy

The topography of fracture surfaces with and without precipitates was analysed using an S neox 3D optical profiler (Sensofar Metrology, Spain), operated in the mode of scanning microdisplay confocal microscopy using both a 10× and a 150× confocal objective (Nikon). The z data is determined for every x, y position, based on the light intensities recorded by a CCD camera in a piezo-driven height scan.

The fields of view are 1754 µm × 1321 µm for the 10× objective and 117 µm × 88 µm for the 150× objective, with pixel sizes of 1.3 µm × 1.3 µm and 0.09 µm × 0.09 µm, respectively. Vertical resolution is ~ 10 nm. Visualization and data processing were performed using the software SPIP (version 6.7.4, Image Metrology, Denmark).

5.3.2 Micro-computed tomography (µCT)

A Nikon XT H 225 scanner was used to obtain µ-CT datasets of the complete core samples, including in- and outlets, as well as fiducial markers for PET-data co-registration. In addition, smaller sample sections were analyzed to obtain increased spatial resolution of the CT datasets. Parameters were set to U = 190 kV, I = 175 µA, with a 2.5 mm Cu filter for homogenization of the energy spectrum. The obtained tomograms were reconstructed with the Nikon OEM procedure, including beam-hardening correction.

5.3.3 Positron emission tomography (PET)

A ClearPET™ scanner (Elysia-Raytest) was used for positron emission tomography analysis. The scanner is used in a horizontal position of the gantry, enabling an upright orientation of the drill core samples. Flow-through experiments are thus performed with fluid flow from bottom to top. The scanner provides a voxel length of 1.15 mm, a cylindrical field of view with a diameter of 160 mm, and a length of 110 mm. The sensor assemblage consists of 20 cassettes, with each having 10240 scintillation crystals. The detected γ-events in the energy range of 250-750 keV are stored as single event files for later sorting into coincidence list-mode-files (LMF). The resulting 3D dataset yields the tracer activity (proportional to its concentration). According to the activity and half-life of the radiotracer applied, the sensitivity of a typical PET measurements is in the range of picomol per microliter. The sequential imaging results of the spatiotemporal quantitative datasets of the concentration were used to calculate the flow vectors. Different types of positron emitting tracers were utilized, F-18 for short-term (several minutes) experiments under advective flow conditions and I-124 for long-term (several days) experiments of diffusive tracer flux. For analytical details, the reader is referred to previous studies focusing on transport analysis using PET techniques (Bollermann et al., 2022; Kulenkampff et al., 2016; Pingel et al., 2023).

5.3.4 Migration experiments with radionuclides under laboratory conditions

The rock samples were shaped into the desired form and installed in measurement cells accordingly. Practically, a cylindrical rock sample is placed in a hollow cylinder, and the space between the outside of the rock sample and the inside of the hollow cylinder is filled with a resin of the desired viscosity to fix it in place. The unit's cylinder is fitted with removable, fixed, sealed lids on both sides to seal the inlet and outlet components and isolate the unit from the environment. Both lids are provided with fittings for connecting the inlet or outlet of the tracer substance. To minimize the size of the "dead" volume, the samples can also be completely encased in epoxy resin into which inlet and outlet holes are drilled (see Fig. 5-7). This preparation method has the advantage that it reduces the dead volume between the lid and the specimen to a minimum.

Figure 5-7: Sample MSVJ2 conventionally prepared for migration experiments, sample S36-5 prepared according to the alternative method that minimises the dead volume (right).

5.4 Results and discussion

5.4.1 Large scale tracer experiments [UJV]

The comprehensive procedure from the preparation of samples to the performance of migration experiments with radionuclides is described in the Certified Methodology for Laboratory Migration Tests with Radionuclides (CM TAČR 2402/2021/01). The first step before starting the migration experiments focuses on the measurement of transmissivity (T). Samples S31, S36-1, and S36-5, prepared within the SÚRAO project "Fissure connectivity research at the Bukov URF", were subjected to the experiments within the WP FUTURE within the European EURAD project. The samples MSVJ2 (Mrakotin granite) and S36-5 (migmatized gneiss) were subsequently selected by the project partner HZDR (Leipzig, DE) for characterization by micro-computed tomography and positron emission tomography.

5.4.1.1 Transmissivity measurement

To determine the hydraulic characteristics of the considered samples for migration experiments the measurement of transmissivity were conducted. The overall transmissivity values of measured samples are listed in the Table 5.2. During the experiment, the current volume values in the reservoirs of both laboratory pumps are continuously recorded and simultaneously plotted on a graph by the GDSLAB software. A typical course of the experiment is clearly shown in Figure 5-8. Simultaneously, the input and output pressure values are measured for control. During the experiment, the shape of both the input and output curves is observed. After the linearization of both curves, it is clear from the graph that both curves are parallel, so the experiment is continued for several hours and then stopped. The transmissivity of the fracture is then calculated from this particular section of the graph.

As the most suitable sample for further experiments were selected MSVJ-2 and S36-5. Nevertheless, sample MSVJ-2 was used only for the initial tests with conservative tracer. More complex measurement was conducted on the sample S36-5.

Table 5-2. Transmissivity of the embedded samples

Sample	Transmissivity (T) [m^2/s]

S31	9.02E-13
S36-1	7.31E-12
S36-5	4.30E-13
MSVJ-2	2.69E-12

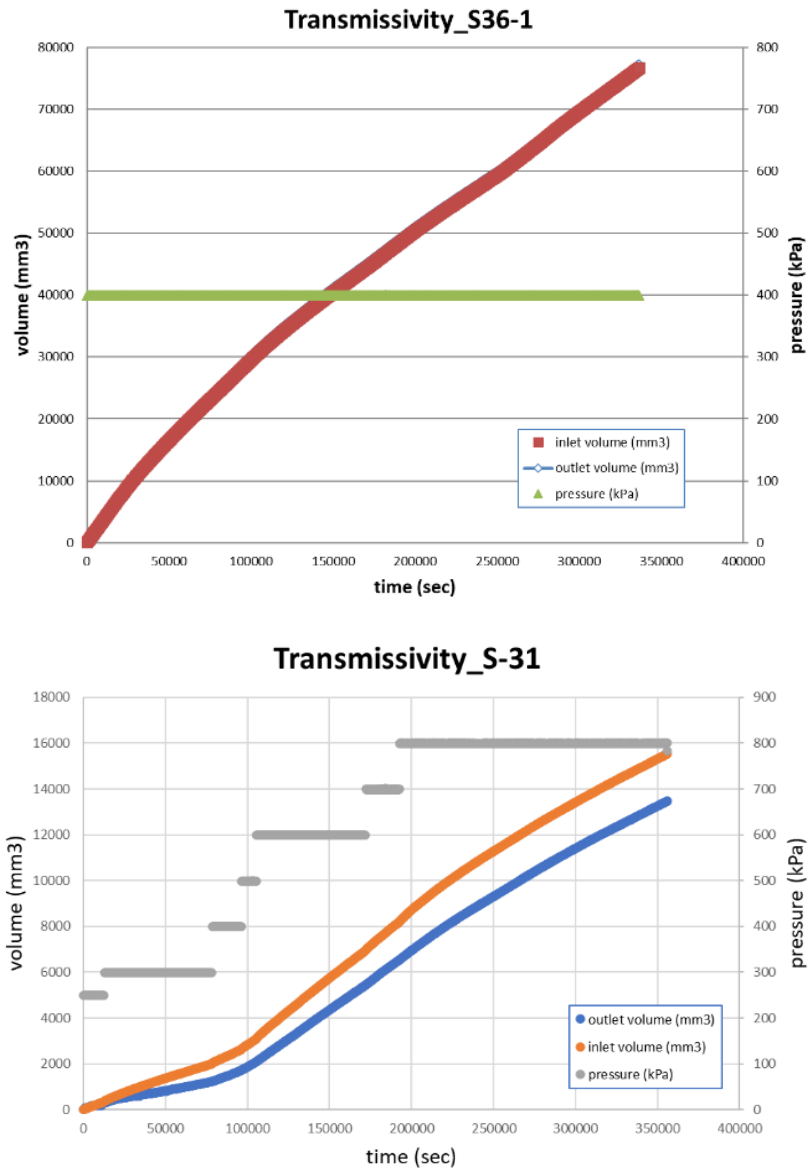

Figure 5-8: Evolution of the volume in the inlet and outlet pumps at a given pressure for samples S36-1, S31

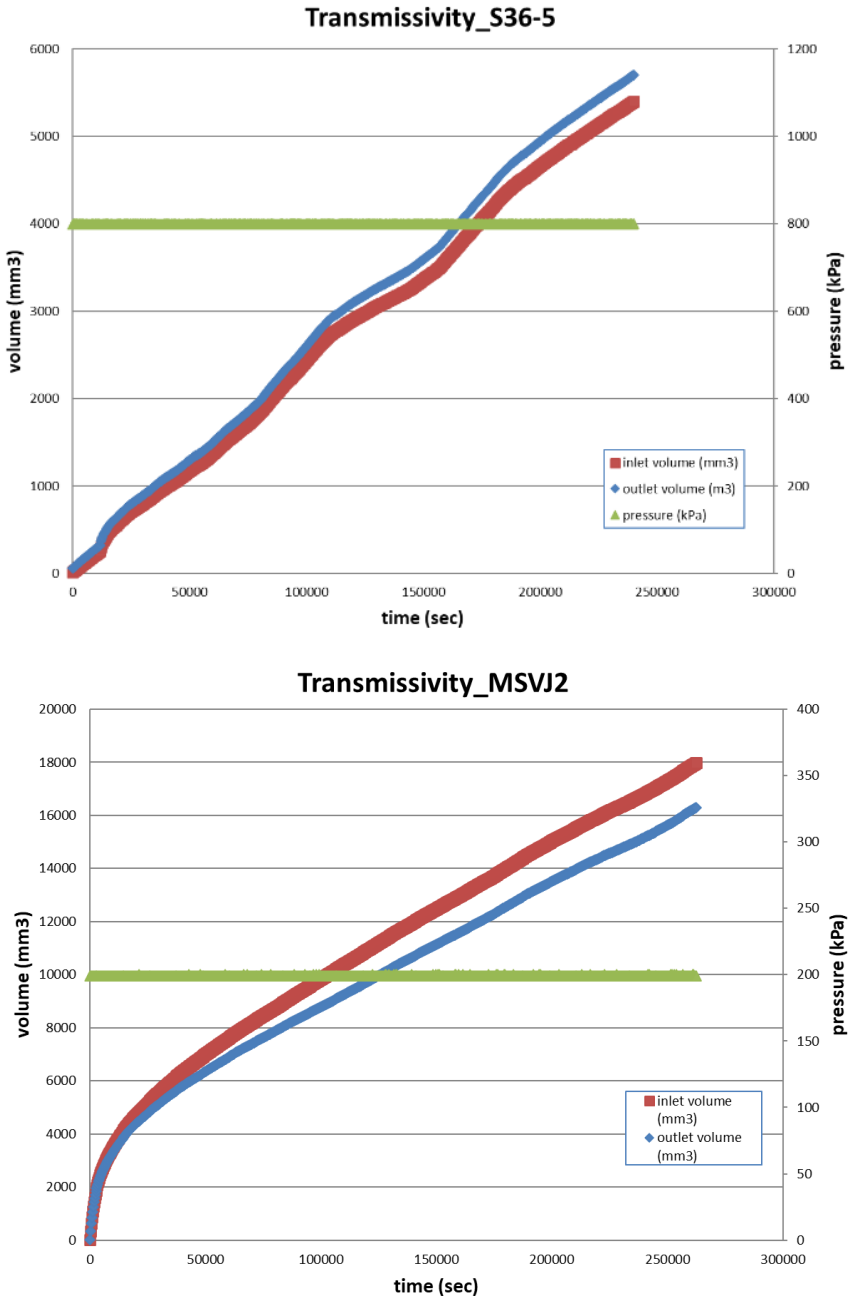

Figure 5-8 (continued): Evolution of the volume in the inlet and outlet pumps at a given pressure for samples S36-5 and MSVJ2

5.4.1.2 Conservative non-active tracer (KI)

Mrakotin – The MSVJ-2 sample was used for initial tests of the experimental setup and flow experiments with conservative tracers. Over time, the seal between the Plexiglas cylinder and the embedded sample deteriorated. The sample has been reassembled in the new design with input/output reservoirs (ports) with defined dead volume (Fig. 5-9).

Figure 5-9: Fixing procedure after the leackage of the sample MSVJ2 was detected

Subsequently, the tracer experiment was performed with 0.01 mol/L KI. The breakthrough curve of iodide was determined online using an ion-selective electrode at a flowrate of 0.017 mL/min (Fig. 5-10). The volume of the injected solution was 1 mL and the rinsing medium was demineralized water. The maximum detected concentration at the outlet compared to the injected solution was 37% at 3h48m post-injection. A slow increase in inlet pressure (4.7 – 6.7 bar) was also observed within 3 days.

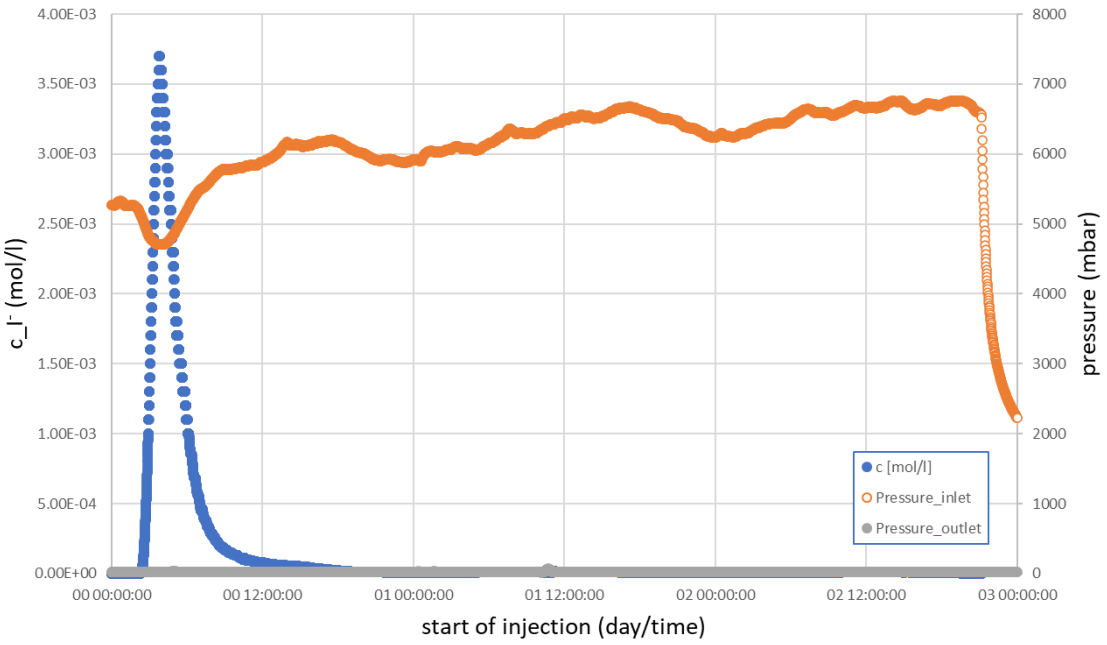

Figure 5-10: BTC of iodide at the flowrate 0.017 mL/min in sample MSVJ2

BUKOV URF; S36_5 – This sample was subjected to several non-active flow experiments with different salt solution injections. Just before the sample was sent to HZDR for µCT/GeoPET measurement, the tracer experiment was performed with 0.01 mol/L KI at a constant flow rate of 0.017 mL/min.

Demineralized water served as the rinse medium and the tracer was injected through the 1ml loop connected to the precise 6-way valve.

After the tests at the HZDR, the breakthrough experiment was repeated in 2023 with identical setup. This time SGW2 (synthetic granite water) was used as the rinsing medium. The iodide concentration was determined both online with an ion-selective electrode and by sampling with a fraction collector for analysis. The Break Through Curves (BTCs) and inlet pressure are shown in Fig. 5-11. From the comparison of the iodide BTC in 2022 and 2023, there is very good agreement. The maximum detected concentration at the outlet compared to the injected concentration was approximately 80% and the recovery was 95% in both cases (Fig. 5-12).

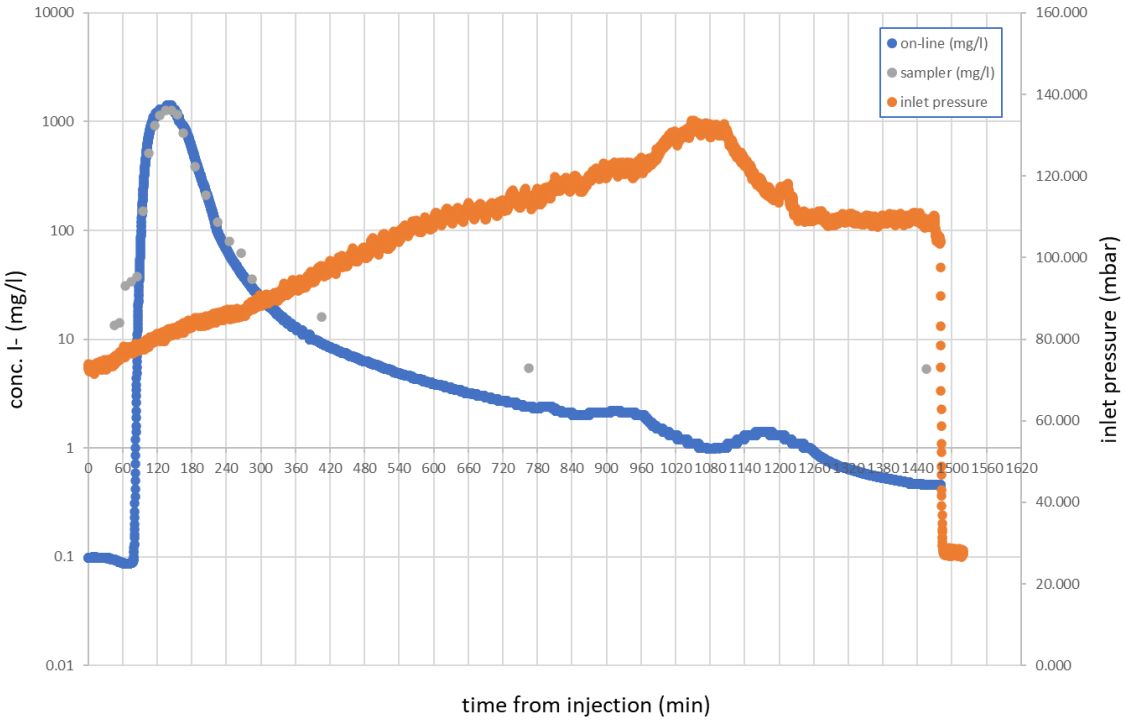

Figure 5-11: BTC of iodide at the flowrate 0.017 mL/min in the sample S36-5

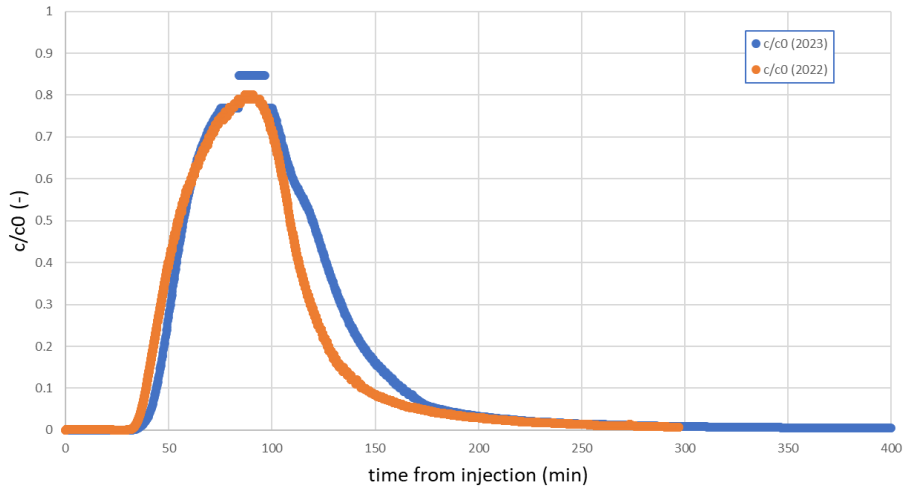

Figure 5-12: Comparison of iodide BTC from tracer test in 2022 and 2023 (sample S36-5)

5.4.1.3 Non-sorbing radioactive tracers (HTO and ^{22}Na)

Additional tracers, specifically non-sorbing tritiated water (HTO) and cationic tracer ^{22}Na+, were used to study the breakthrough of the fracture in the S36-5 sample. HTO emits β^- radiation, while ^{22}Na undergoes combined β^+ and electron capture processes, subsequently transitioning to exited ^{22m}Ne and emits gamma radiation. Both gamma and beta radiation were recorded. As part of routine measurements at UJV, which include the simultaneous detection of gamma and beta radiation, both isotopes were used simultaneously in the flow-through experiment. The experimental parameters, including flow rate and injected tracer volume, were similar to those used for non-radioactive tracers. Quantification of HTO and ^{22}Na included an initial gamma measurement of ^{22}Na, followed by recording spectra for both isotopes with a beta counter.

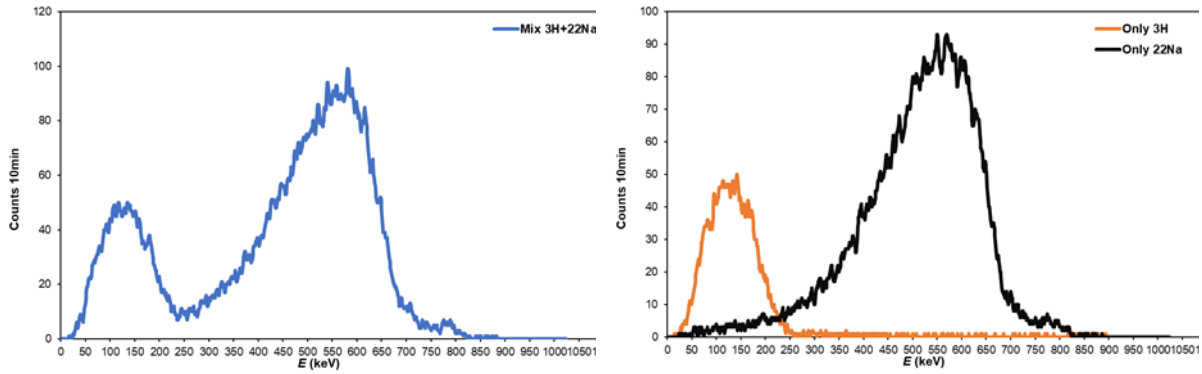

Figure 5-13: The spectra of the beta counter show on the one hand the combination of the isotopes ^{3}H and ^{22}Na (left), while for comparison the spectra of the individual isotopes were analyzed separately (right).

Observations with the beta counter showed that the spectrum of ^{22}Na is well separated fromn the HTO peak (Fig. 5-13). To account for the ^{22}Na contribution within the 0-250 keV energy window designated for HTO, control samples exclusively containing ^{22}Na were prepared to show the measured ^{22}Na activity in the gamma counter. By measuring these control samples with both the gamma and beta counters, the ratio of gamma to beta counts was determined. Using this ratio, the amount of interfering ^{22}Na within the 0-250 keV window specific to HTO could be estimated:

$$\boldsymbol{\beta}_{(0-250keV)}/\gamma = \frac{\beta\,{}^{22}_{(0-250)}\boldsymbol{Na}}{{}^{22}_{\gamma}\boldsymbol{Na}}$$

The equation shows the ratio of the activity measured with the beta counter within the 0-250 keV energy window to the activity measured with the gamma counter for 22Na to identify the amount of 22Na in the 0-250 keV window for mixed HTO+^{22}Na samples. In addition, a more detailed analysis of the breakthrough indicated pronounced gamma peaks in the maximum activity of HTO and ^{22}Na. Therefore, to capture the total HTO activity, the counting window was extended to 350 keV.

Assuming that HTO acts as a non-sorbing tracer, the sampling procedure was configured to collect samples over a 10-minute period, which took a total of 300 minutes (5 hours). Subsequent samples were collected at 10-minute intervals, and during the remaining 50 minutes, a portion of the collected volume was sent to waste. Both the HTO and ^{22}Na tracers were able to flow through the sample without retention. Analysis of the breakthrough curves shown in Figure 5-14 indicates that the breakthrough of HTO was significantly faster and very similar to the breakthrough of the non-reactive iodide, see Fig. 5-15. This observation confirms the non-interacting nature of HTO as a tracer. The recovery of HTO was about 88%. Regarding the ^{22}Na tracer, while there was some delay in breakthrough, sorption was not observed. This delay is likely attributed to the interaction of ^{22}Na with the specific environment of the sample, resulting in significant retardation. It is important to emphasize that the non-occurrence of ^{22}Na sorption is also attributed to the presence of a considerable amount of non-radioactive sodium in the

SGW2 water. The recovery of the initial ^{22}Na activity was about 100 %. Comparison of the BTCs for the conservative tracers (iodide vs. HTO) revealed a very good correlation (Fig. 5-15).

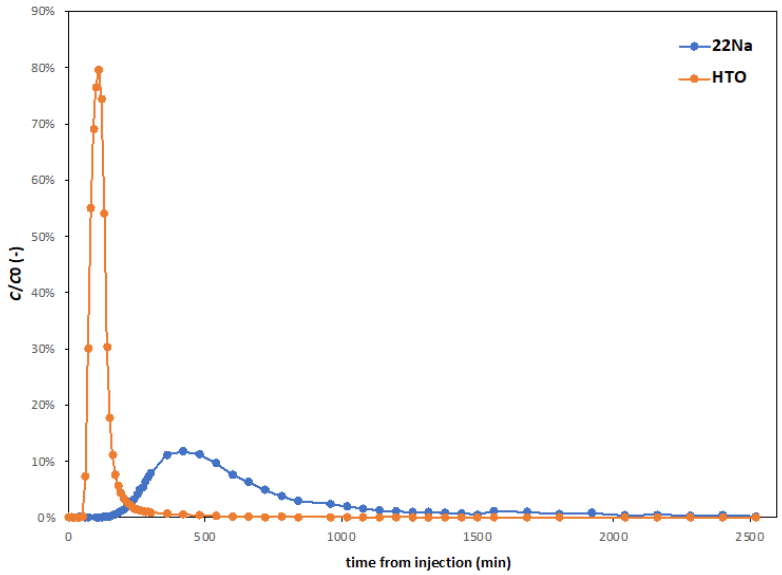

Figure 5-14: Breakthrough curves of HTO and ^{22}Na in sample S36-5

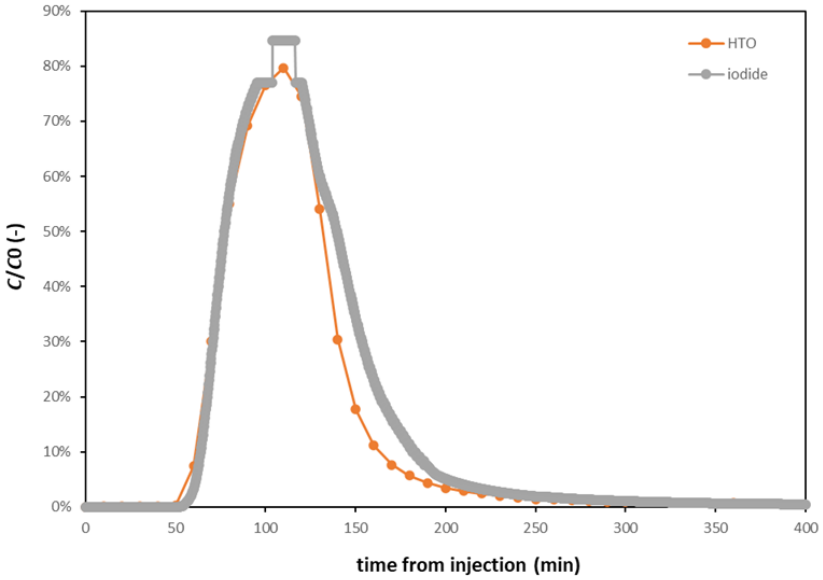

Figure 5-15: Breakthrough curves of iodide and HTO in sample S36-5

5.4.1.4 Sorbing radioactive tracers (^{133}Ba and ^{134}Cs)

Similar to the non-sorbing tracers, the flow-through experiment with the sorbing tracers cesium (^{134}Cs) and barium (^{133}Ba) was performed on sample S36-5 using an analogous methodology. The selected radioisotopes ^{134}Cs and ^{133}Ba exhibited characteristic gamma spectra. By applying a principle likethat used for HTO and ^{22}Na separation, quantitative discrimination between ^{134}Cs and ^{133}Ba in the isotope cocktail was achieved. For the determination of ^{134}Cs, the energy range from 500 to 2046 keV was analyzed. However, as shown in Fig. 5-16, some of the counts overlapped within the energy window of 250-500 keV, where the presence of ^{133}Ba would be indicated (see Fig. 5-16). To quantify the presence of ^{134}Cs within the ^{133}Ba energy window in the combined cocktail, a method similar to the measurement

of ^{3}H and ^{22}Na was used. This was done by evaluating the ratio of counts in the 250-500 keV and 500-2046 keV windows in control samples with comparable activity levels to those in the samples of interest, cf. calculation:

$$\gamma_{250-500keV}/\gamma_{500-2046keV} = \frac{^{134}Cs_{250-500}}{^{134}Cs_{500-2046}}$$

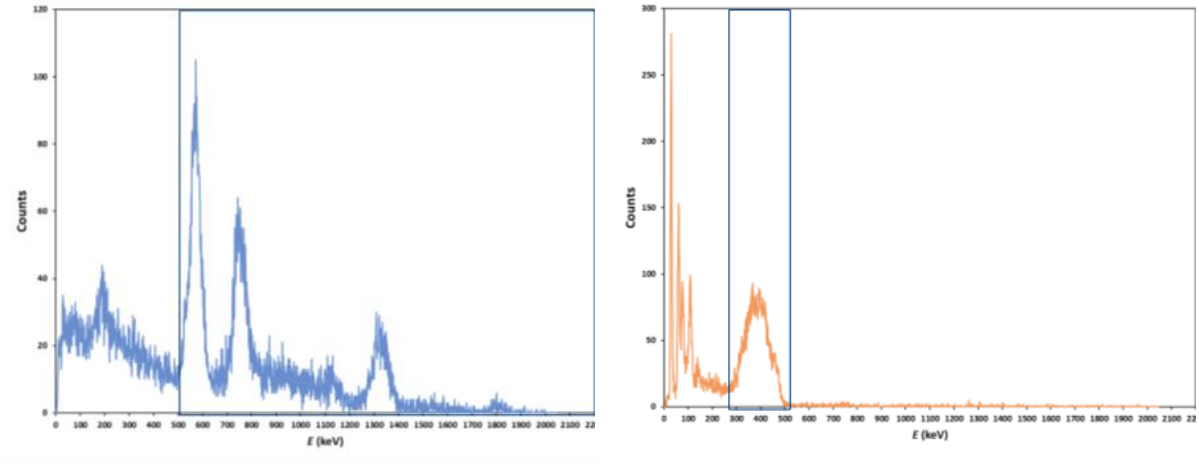

Figure 5-16: The spectrum of ^{134}Cs with the activity determination window of 400-2064 keV (on the left) and the spectrum of ^{133}Ba with the activity determination window of 250-500 keV (on the right).

The activities of ^{134}Cs and ^{133}Ba were approximately 3 kBq and 2.6 kBq, respectively, in the injected volume of 1 mL. In addition to the radioisotopes, the non-radioactive carriers CsCl and $BaCl_2$ were introduced into the SGW2 water to mimic the conditions of the sorption experiments, with concentrations adjusted to 10^{-5} mol/L. Figure 5-17 clearly shows no cesium breakthrough, indicating its distinct sorption properties and the favourable sorption capacity of the specific fracture environment. In contrast, barium showed a 1% recovery of the initially injected activity, likely attributed to the penetration of one of the neutral complexes formed by barium, such as barium sulfate ($BaSO_4$), as indicated by the modelling of barium speciation in SGW2 (Fig. 5-18). This observation is consistent with a similar breakthrough behaviour observed for the non-sorbing tracer HTO. The remaining barium species were adsorbed onto sample S36-5. To confirm the possibility of obtaining breakthrough curves for cesium, a test was repeated with barium and cesium with an increased concentration of the non-radioactive carrier to simulate the background concentration of sodium in the previous experiment, which was approximately $8x10^{-4}$ mol/L. The results confirmed that even at the higher concentration of non-radioactive carriers, barium exhibited a breakthrough with a comparable yield as in the initial case. Notably, there was no cesium breakthrough even at the increased concentration of non-radioactive carriers, and no significant increase in barium breakthrough was observed. These findings indicate the substantial sorption capacity of the tested sample for the investigated radionuclides.

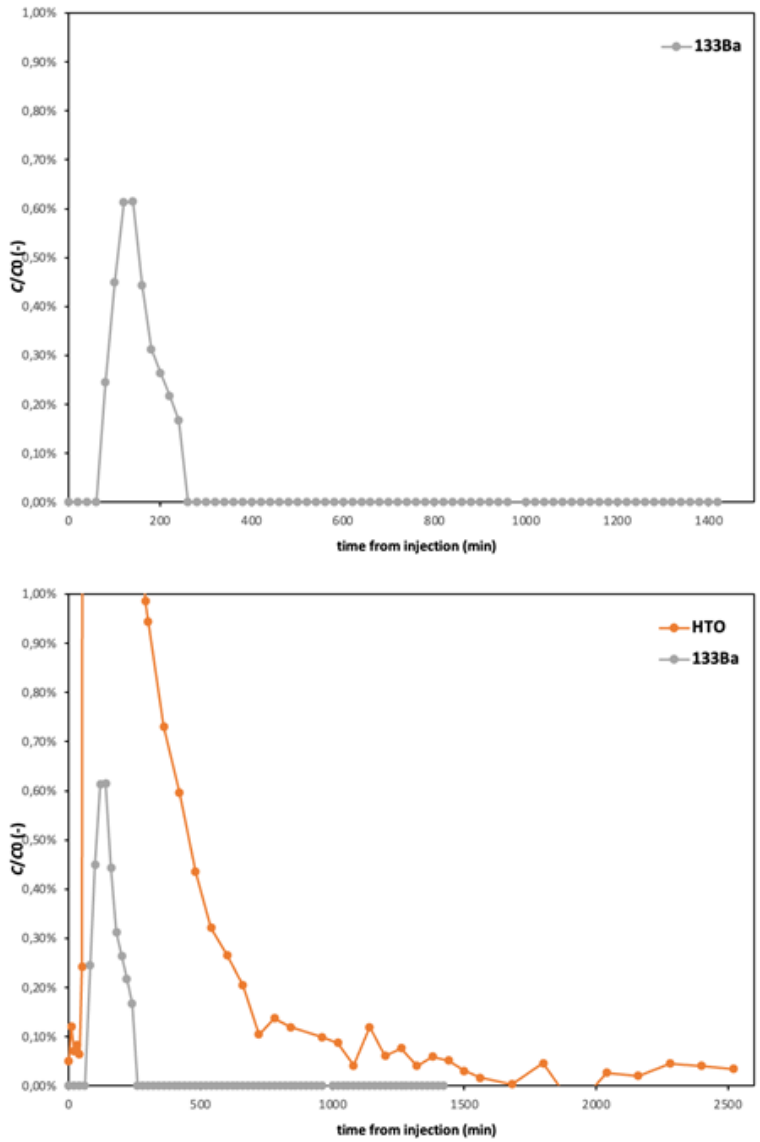

Figure 5-17: Breakthrough curves for ^{133}Ba only (upper) and with HTO comparison (lower) in sample S36-5.

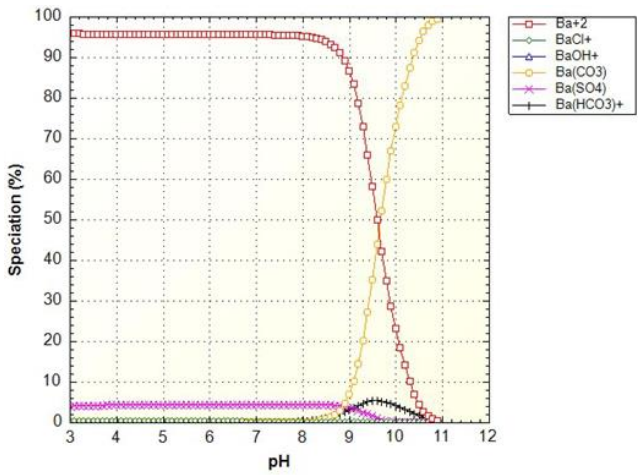

Figure 5-18: Ba speciation in SGW2 water at pH variations in the presence of atmospheric carbon dioxide and oxygen.

5.4.1.5 Sorbing radioactive tracers (^{63}Ni)

After the completion of flow through experiments with sorbing tracers ^{134}Cs and ^{133}Ba, nickel ^{63}Ni was utilized as a sorbing tracer in sorption experiments with Bukov materials. Similarly, the tracer ^{63}Ni was employed in subsequent flow through experiments. Its determination followed the same procedure as described in chapter 2.2.1.3 for sorption experiments. In addition to the ^{63}Ni isotope with an activity of approximately 11 kBq in 1 ml, a non-radioactive carrier of nickel in the form of $NiCl_2$ at a concentration of $8x10^{-4}$ mol/l was introduced, in line with the methodology applied in the second breakthrough experiment with the tracers ^{134}Cs and ^{133}Ba, see chapter 5.4.1.4 The experimental setup was identical to that used for sorbing tracers. However, similarly to cesium, no breakthrough of nickel was observed, indicating complete retention of entire species inventory present in SGW2 within the sample environment. The breakthrough experiments with sorbing tracers revealed that the sample matrix itself exhibited a notable sorption capacity, and at the given flow rate, the sorption kinetics were sufficiently rapid to result in the overall retention of primarily sorbing tracers.

5.4.2 Fracture surfaces and aperture structures [HZDR]

Advective flow through open fractures is controlled by the aperture width and the surface roughness. Roughness analysis depends on the bandwidth of the used technique, i.e., the spatial resolution and the size of the field-of-view. Simple amplitude roughness parameters without specification of bandwidth result in misleading quantitative data. Either converged roughness parameters or power spectral density data provide meaningful insight into surface roughness. **Figure 5.19** shows roughness data as profile PSD values as a function of spatial frequency. We analysed surface topographies of open fractures without fracture filling materials as well as of fracture wall surfaces covered with calcite or sheet silicates (chlorite in sample OLKR5). The PSD curves show a linear behaviour over the entire range of spatial frequencies analysed. This indicates that there are no dominant surface building blocks that would dictate roughness over a range of the spatial frequency spectrum. However, a clear and important piece of information is that mineralization of fracture surfaces in crystalline rocks causes a well-defined spatial frequency-independent reduction in surface roughness, cf. the two bundles of curves and their separation in **Fig. 5.19**. This is an important conclusion for transport modelling applications, since generalizable changes in fracture surface roughness can be derived from these data.

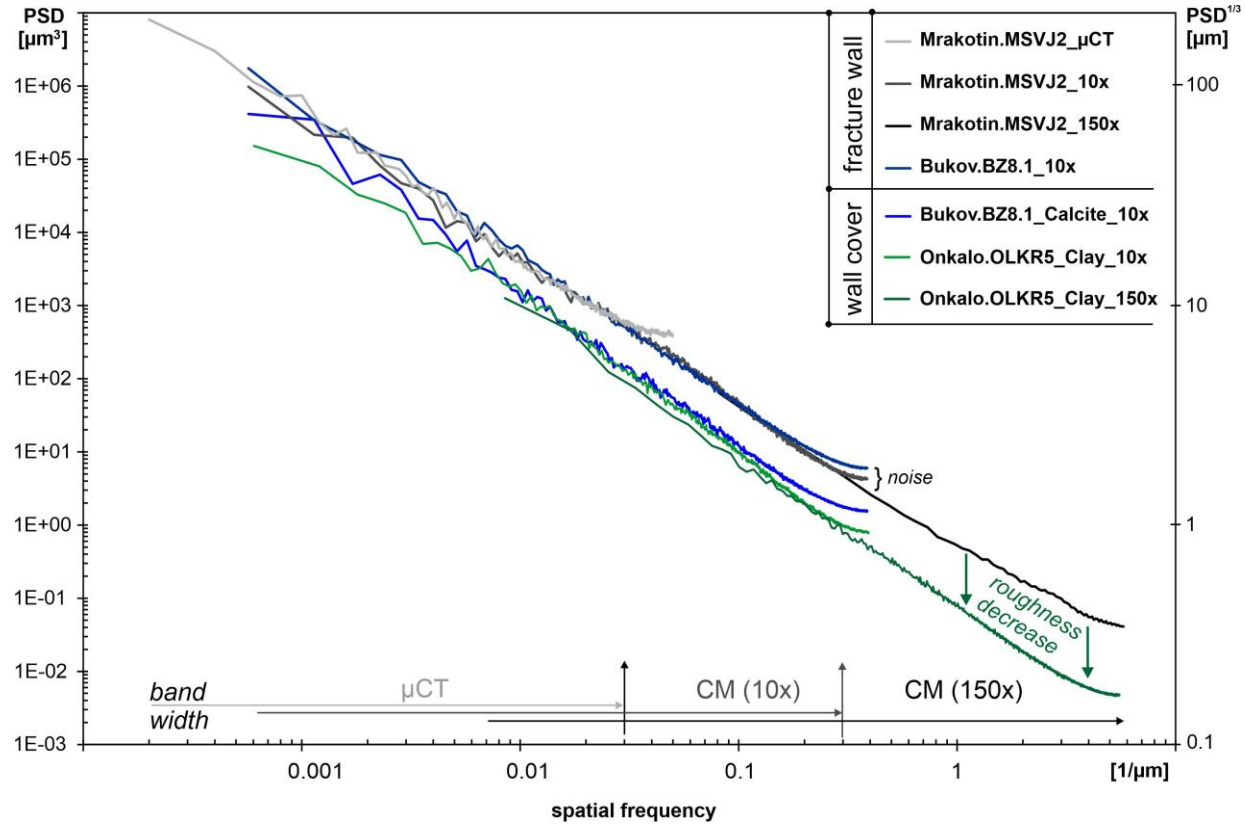

Figure 5-19: Topography analysis of fracture surfaces with and without wall-covering minerals. Investigated samples are from the granite quarry Mrakotin (CZ), the Bukov underground lab (CZ) and from the Onkalo site (FI). The power spectral density of spatial frequencies represents surface building blocks from about 500 nm to 5 mm lateral extent. Note the general reduction in roughness, largely independent of spatial frequency, due to secondary mineralization of the fracture walls.. The absence of plateaus of the PSD distribution indicates the lack of any single dominating surface building blocks.

5.4.3 Structural analysis and core-scale flow field experiments [HZDR]

5.4.3.1 Mrakotin granite (MSVJ2)

The sample was cast in epoxy resin with the injection and discharge points on the fracture plane. Experiments were conducted with 0.01 mol/L [^{18}F]KF solution at a flowrate of 0.017 mL/min resp. 0.008 mL/min, respectively. The driving pressure was ca. 1.5 bar. The breakthrough curve was recorded with a flow-through counter at the outlet. This curve is comparable to the BTC recorded at UJV. Further internal activity-time curves and the input function at the injection cross-section were determined from slices (cross-sections) of the PET dataset. These curves also contain residual or slow-moving portions of tracer, and are therefore not directly comparable to the BTCs, except for the breakthrough time. The overall picture of the transport pattern is a patchy activity distribution with two distinct major flow paths above a more diffuse activity distribution with lower activity.

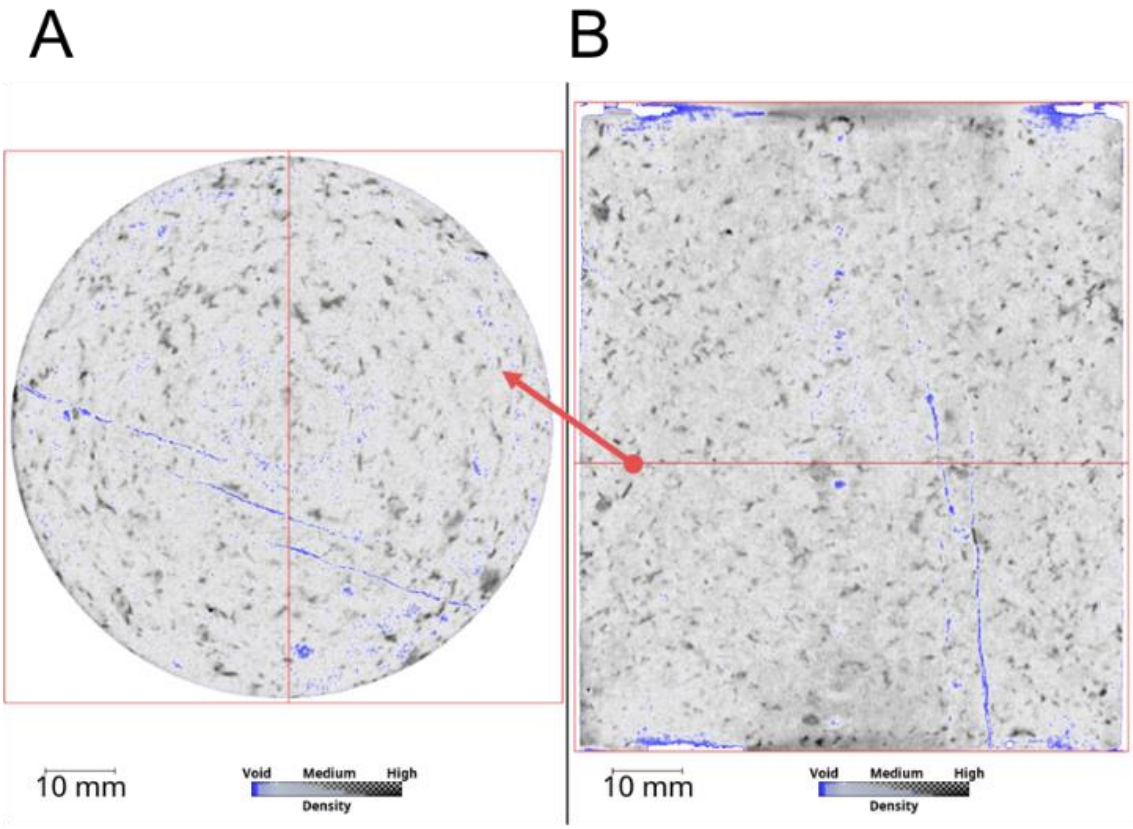

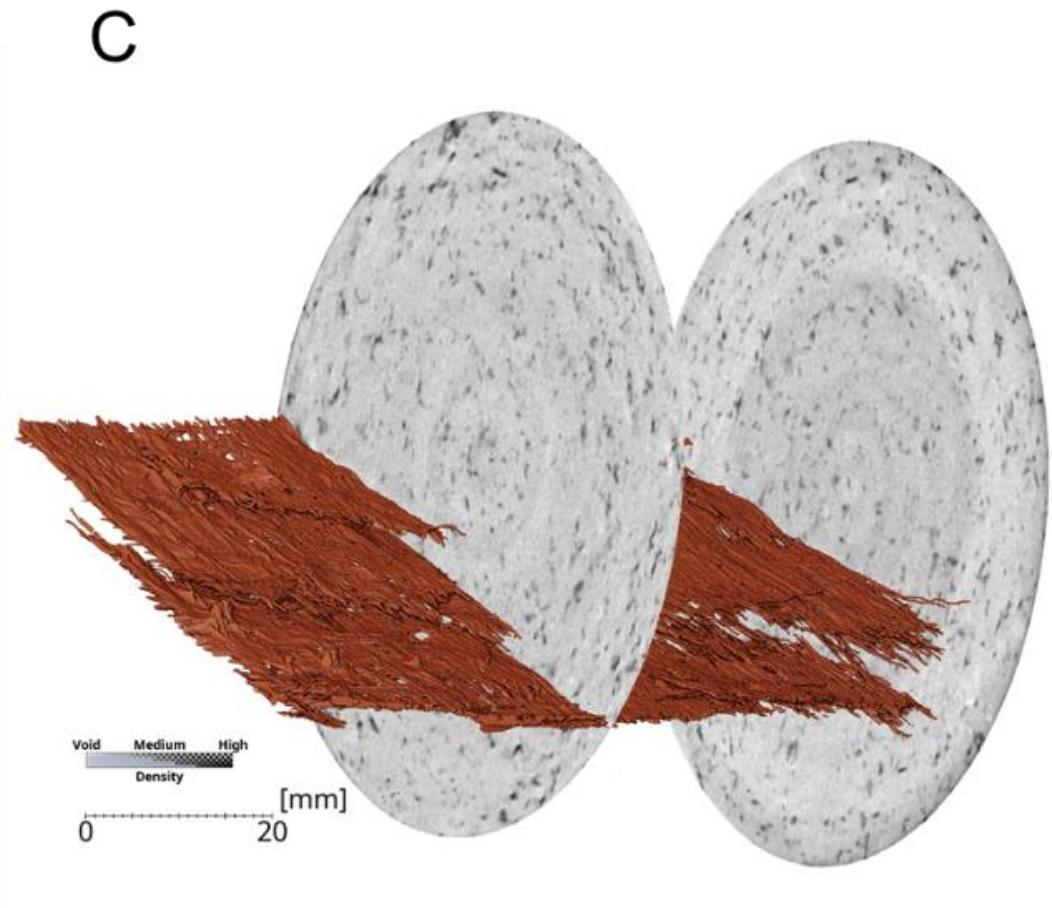

Figure 5-20: Horizontal (A) and vertical (B) slices of Mrakotin (MSVJ2) core sample µCT dataset. (C) shows the segmented en echelon fracture geometry. The width of the fracture opening is partially in the range of the µCT voxel size.

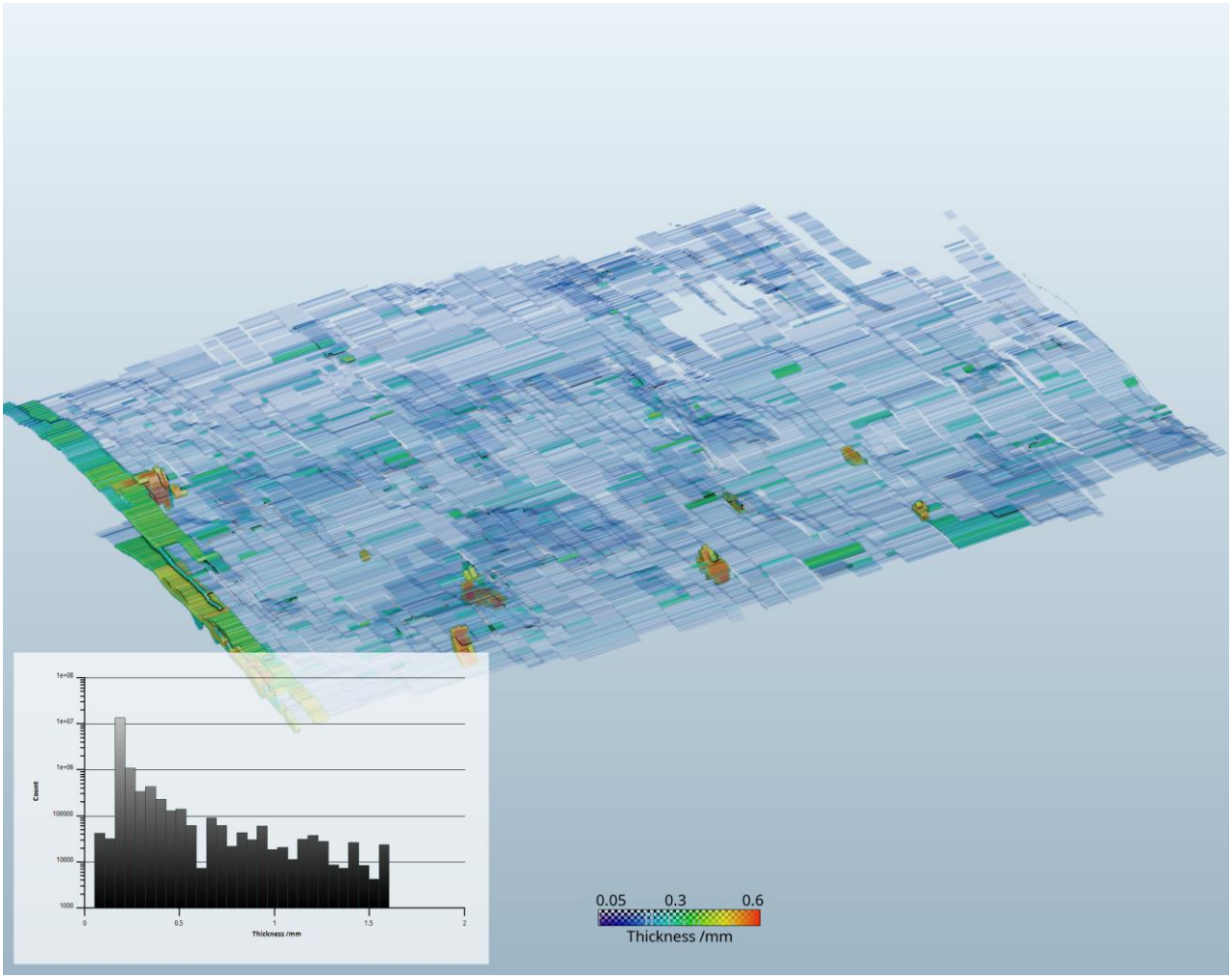

Figure 5-21: Thickness map of segmented fracture geometry (Mrakotin granite, MSVJ2) with histogram of width distribution of all fracture sections. Due to the limitation of spatial resolution in the analysis of the large sample geometry, there are uncertainties in the reconstruction of the fracture geometry of the large field of view. For this reason, smaller sample geometries were additionally analysed with respect to the fracture geometry with µCT, cf. Fig. 5-22.

Due to the limited spatial resolution in the analysis of the large specimens, uncertainties arise in the reconstruction of the fracture geometry of the large field of view. For this reason, smaller specimen geometries were analysed with a focus on fracture geometry using µCT, cf. **Fig. 5.22**., in addition to the global picture provided by the µCT overview (**Fig. 5.21**).

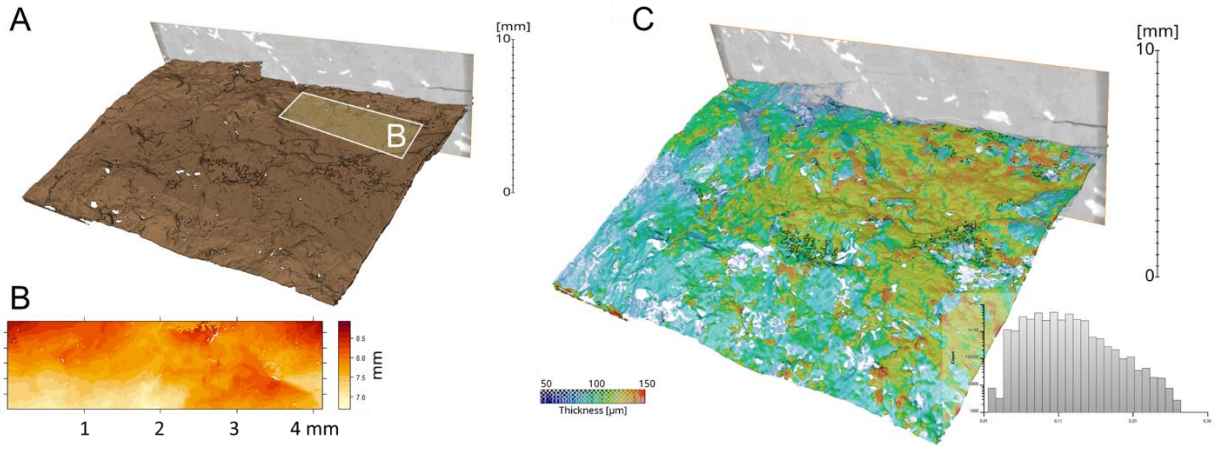

Figure 5-22: (A) Segmented fracture of the small Mrakotin granite, MSVJ2, resolution ca. 10 µm. (B) Calculated surface topography, used for roughness analysis (Fig. 5-19). (C) Thickness map (aperture distribution) of the small sample.

Advective transport of the tracer F-18 through the en échelon fracture geometry over a maximum period of 450 minutes is shown in Figure 5.23. Advective flow occurs from left to right, forming individual preferential flow channels on the fracture surfaces. After 60 minutes, one channel is almost fully developed, while the formation of other channels is not completed until 180 minutes. This picture changes only slightly thereafter at 360 min. and 450 min., respectively. Thus, the observed channel formation appears to be stationary after 180 min. We calculated the local velocity distribution from the PET data sets for advective tracer transport, cf. flow rate data in Figure 5.24.

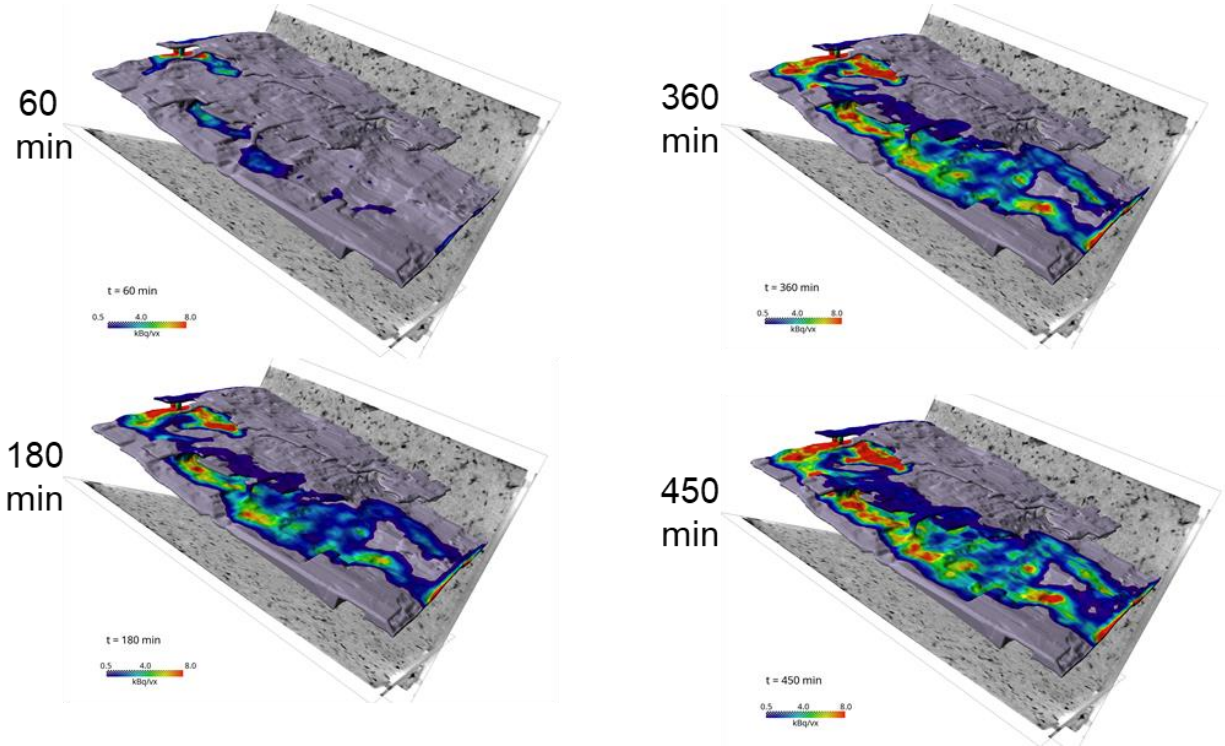

Figure 5-23: Advective transport (Mrakotin granite, MSVJ2) of the tracer F-18 through the en échelon fracture geometry (µCT data) over a maximum period of 450 minutes, shown in four time slices. The distribution of tracer transport on different sections of the complex fracture geometry is reconstructed from the PET data. The colour scale indicates a maximum activity per voxel of 8 kBq.

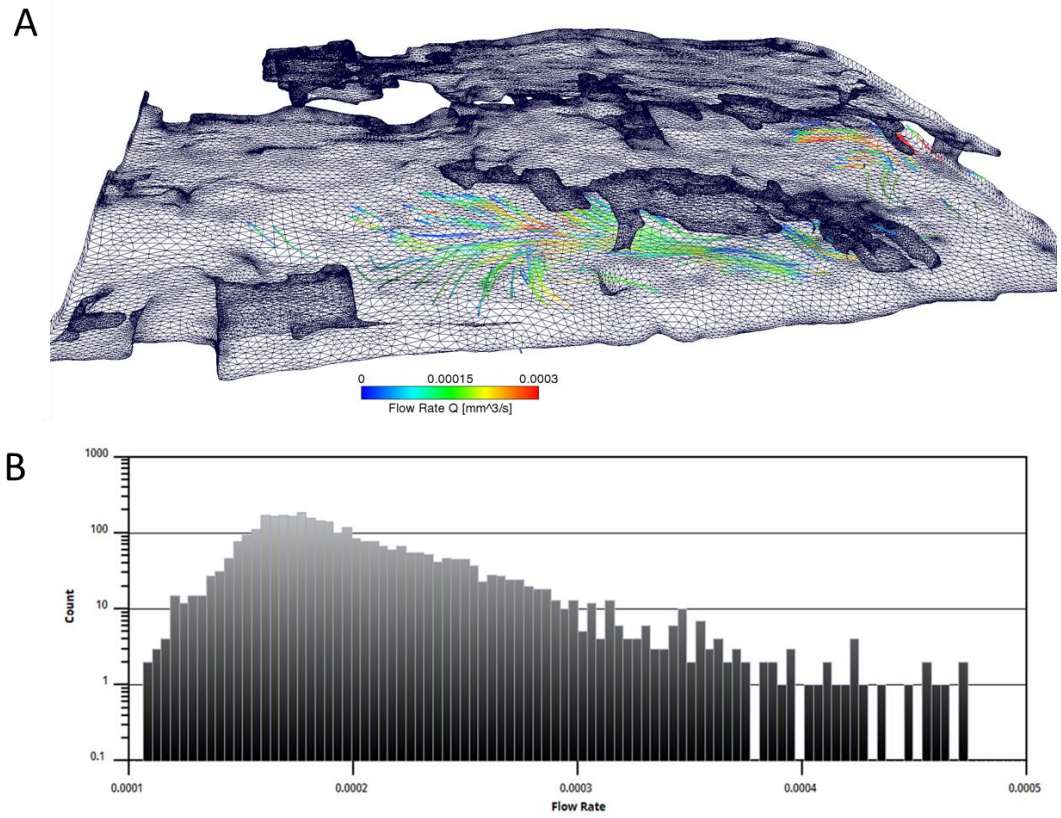

Figure 5-24: (A) Flow rate vector field derived from PET images visualized on µCT geometry (Mrakotin sample, MSVJ2). Flow channels dominate the transport behaviour. For visualization, the maximum value has been set to 0.003 mm^3/s. (B) The asymmetric distribution of the flow rate ranges up to more than 0.004 mm^3/s.

We have developed a method to map the maximum exposure amplitude of the tracer and contact time to the surface based on the PET data. This is used to quantify the effective surface area (Table 5-3) where solid-liquid interactions are likely to occur. The surface area affected is a function of the amplitude threshold and the residence time during which that amplitude is maintained (Fig. 5-25). Assuming a minimum amplitude of 3% of the maximum amplitude, 32% of the segmented surface is exposed to the tracer (Table 5-3).

Table 5-3. Analysis of the effective surface area of the Mrakotin granite (MSVJ2) fracture for fluid-solid interactions derived from the PET tracer contact, cf. Fig. 5-25 for visualization.

Maximum activity [kBq]	Maximum activity [%]	Surface area portion [%]
2	7	6
4	13	10
8	27	12

30	100	4
		Σ 32

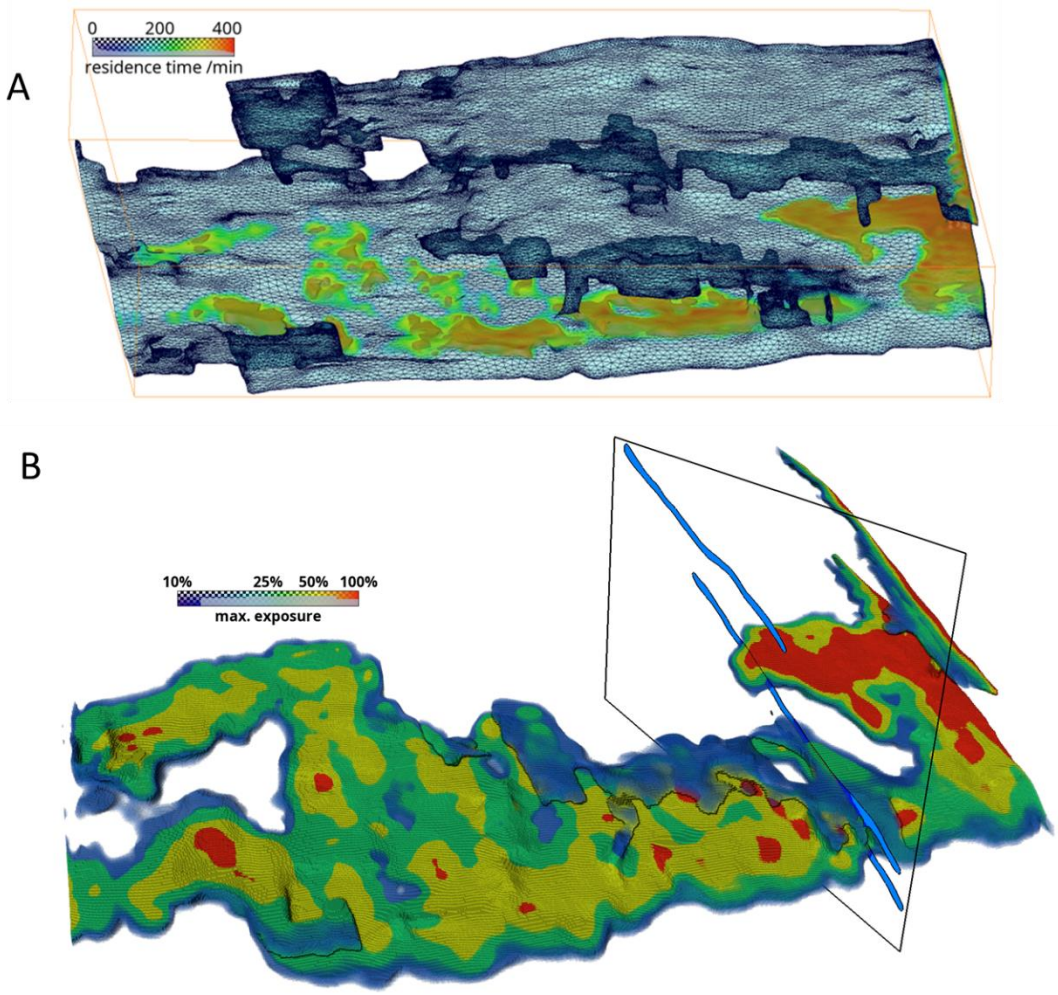

Figure 5-25: (A) Spatial distribution of residence time (Mrakotin granite, MSVJ2) with significant tracer concentration per voxel and (B) maximum activity during this period. The localized activity data are used to quantify the effective surface area (Table 5-3) where solid-liquid interactions are likely to occur.

5.4.3.2 BUKOV URF; BZ8_1

Based on CT data with only single, isolated fracture surfaces, advective transport was considered unlikely. Several generations of calcite precipitates exist in the rock, completely filling the fractures. A complex formation of different generations of fissure-filling calcite mineralization was inferred from the CT data (Fig. 5-26). Note the spatial distribution of calcite precipitates, indicating multiple generations, cf. arrows in Figure 5-26 (upper left: 3D visualization). Despite the low contrast of the gray values in this figure (upper right: horizontal cross section, lower section: vertical cross sections), the homogeneous appearance of the calcite material in contrast to the more granular structure of the host rock CT data allows lidentification of calcite material. Because of the apparently very low permeability of the material, we decided to perform a diffusion experiment without any applied pressure gradient to be analysed using PET techniques. To investigate the influence of complex geometries of calcite mineralization on transport, the tracer was introduced into a reservoir hole (V = 1 mL) within a comparatively thick volume of calcite precipitates as the initial volume for diffusive flow. Further calcite generations crossing this sample section can thus be investigated in their influence on a potential modification of the initial

diffusive transport (Fig. 5-27). There are continuous sections of fracture-filling calcite precipitates. Their transport behaviour, especially at their interfaces with the host rock was the focus of our investigations. The combined visualization on the bottom right in Fig. 5-27 shows the µCT image of the sample and the infilled PET tracer at the beginning of the transport experiment with high activity (bright colors) in the tracer reservoir. The sample was preconditioned (7 days) with synthetic groundwater plus 0.01 mol/L NaI. During this time, a loss of approximately 1.5 mL was observed by suction, which was replenished. The conditioning fluid was then replaced by the labelled solution: [124I]NaI + synthetic groundwater. PET analysis was performed over a total period of 18 days.

Preliminary PET data reconstruction and visualization was performed. As usual, corrections are based on the acquired µCT data of the core volume. A time-resolved sequence of PET data frames is available and can be used, for example, to validate subsequent simulation calculations of transport in such complex materials (Fig. 5-28).

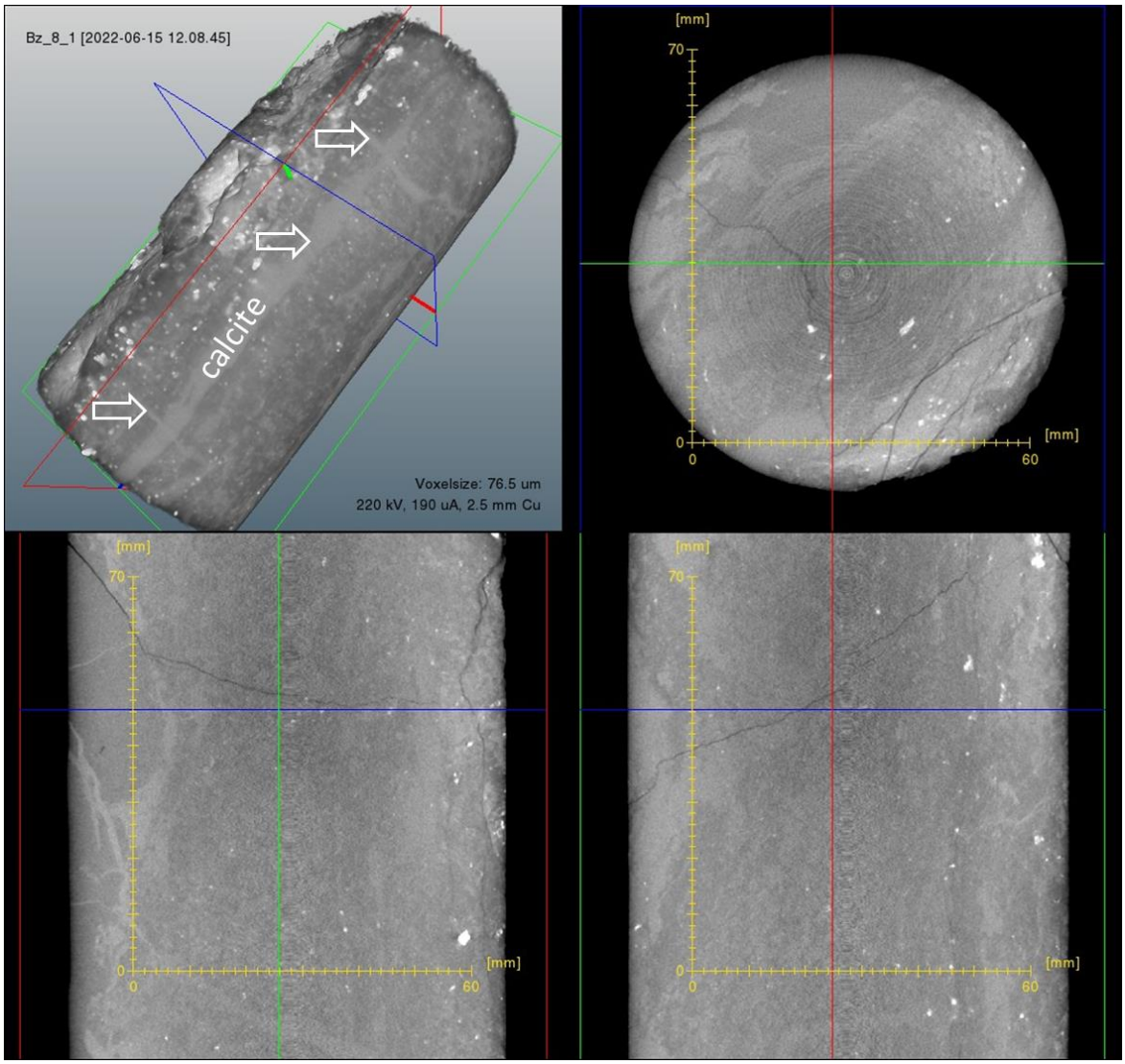

Figure 5-26: Structural analysis of BUKOV sample BZ8_1. A µCT analysis of the whole core sample (d = 80 mm) has been performed, showing open fractures and several generations of calcite precipitates (arrows) in fractures. Note the presence of individual granular minerals of high density (ores).

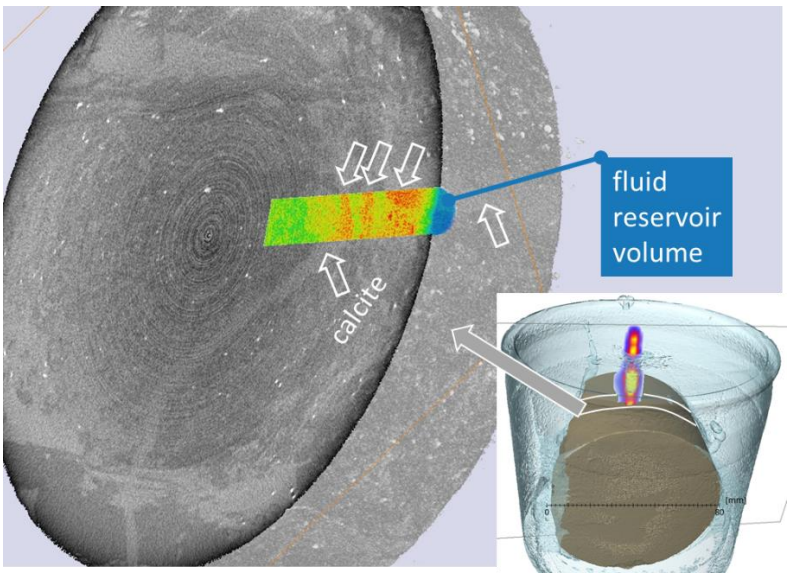

Figure 5-27: The positioning of the drill hole for the tracer acquisition for diffusive transport (BUKOV BZ8_1) was made in a zone without fractures according to µCT findings.

The qualitative transport result from the PET measurements collected here is a complex superposition of suction and diffusion processes. Overall, the flow was highly inhomogeneous, e.g., the flow front was locally stopped at a fracture surface (**Fig. 5.29**). There is no evidence of retention of the tracer by sorption, i.e., no local accumulation of the tracer. It can be concluded that the I-124 tracer used is inert in this complex multi-mineral material. This is another important conclusion for application-related studies of such multi-mineral host rock lithologies.

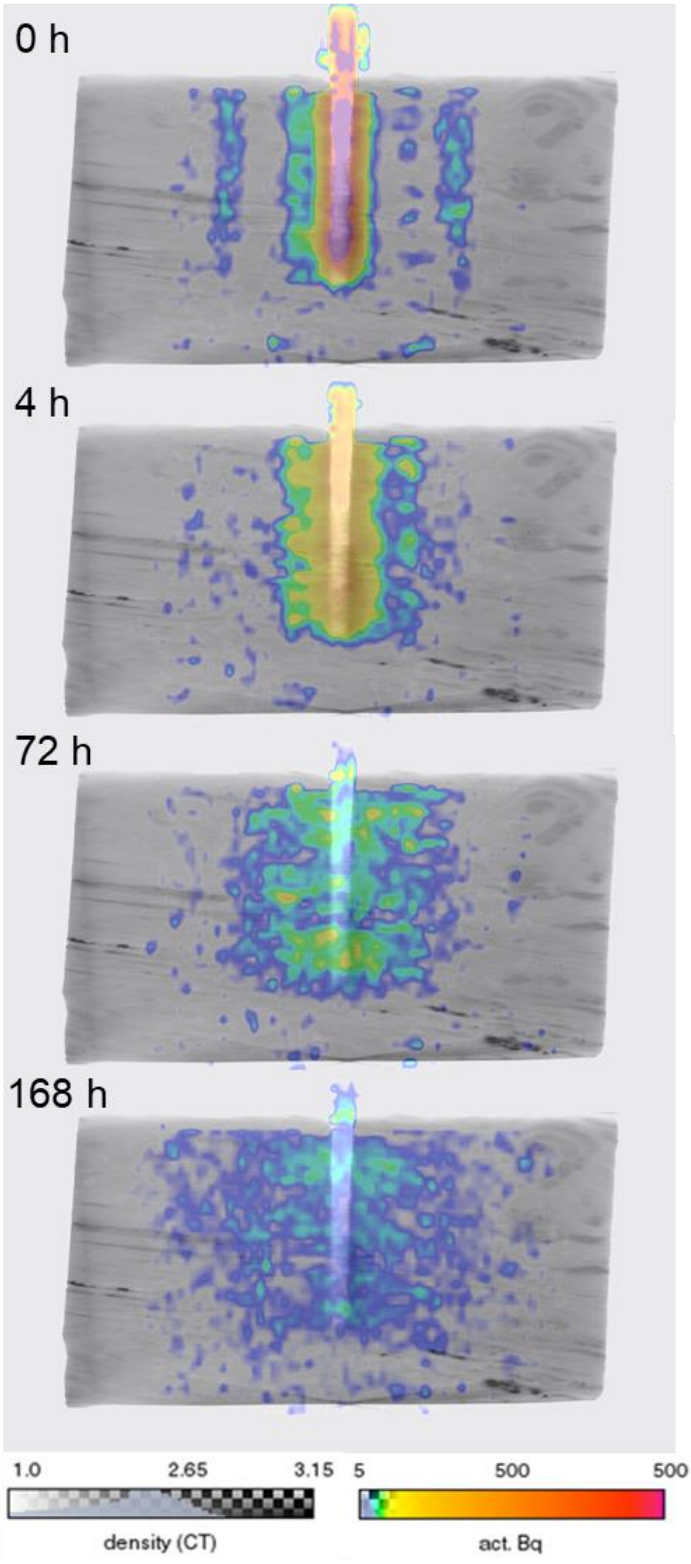

Figure 5-28: PET dataset of low permeability transport in calcite-bearing sample BUKOV BZ 8_1, over a total period of one week, time steps: 0 h, 4 h, 72 h, 168 h. In the start image (top), the high local activity amplitude in the well causes scattering artefacts outside the tracer reservoir. These artefacts disappear in subsequent data sets. Remarkably, the heterogeneity of activity that occurs in PET datasets of 4 h and beyond appears disk-like in the cross-section of the 3D dataset (Fig. 5-29). The images are overlain with µCT data. These data can serve as a basis for validating complex simulation calculations based on the density data and associated regions of effective diffusivity.

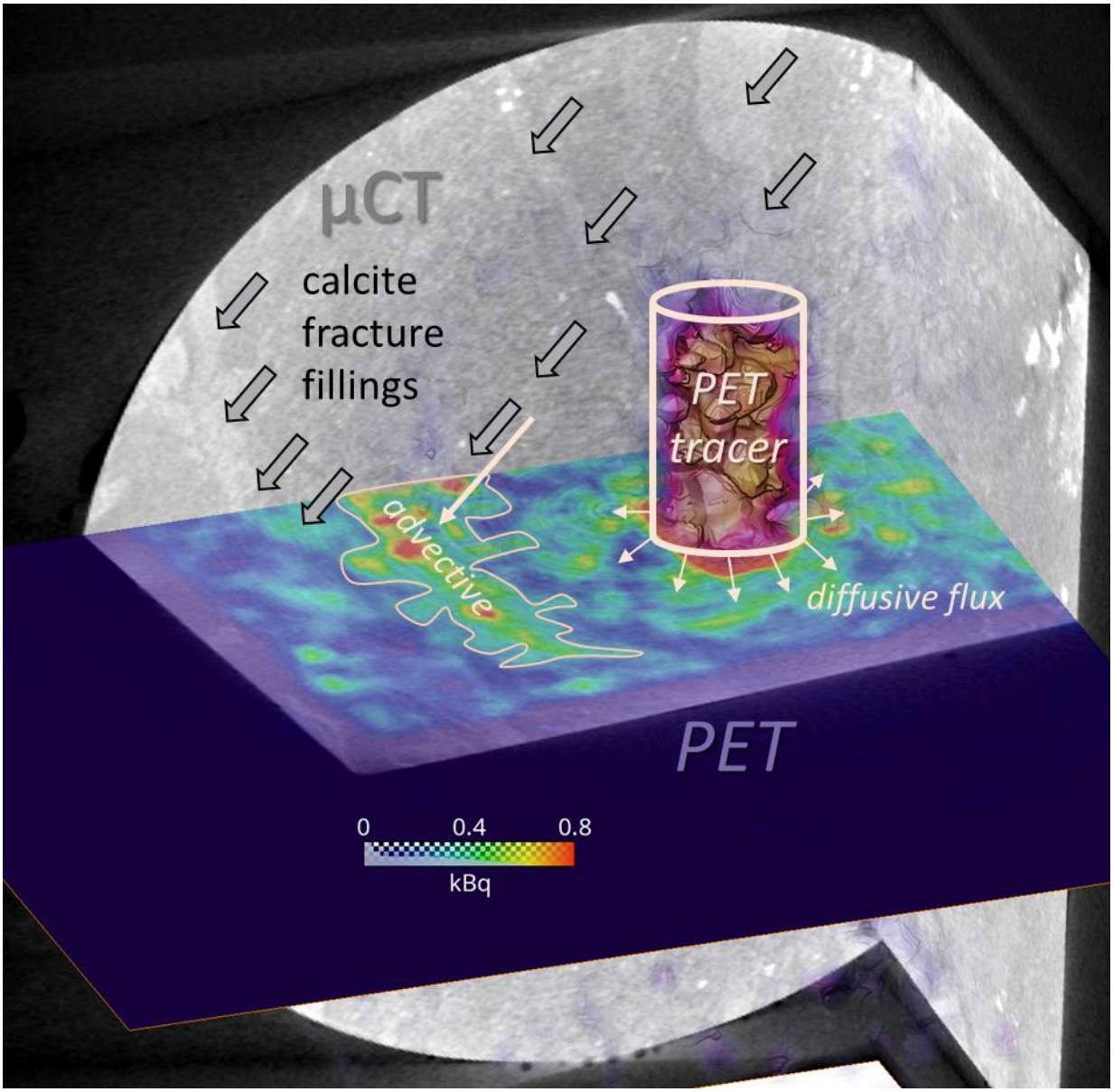

Figure 5-29: PET dataset of sample BUKOV BZ 8_1 combined with µCT cross sections after diffusive flux of 264 h (11 days). The PET data set shows a dichotomy of tracer concentration: PET tracer activity is detected around the reservoir, which is due to diffusive flux of the tracer. However, on the left side of the figure there is an isolated area of increased tracer concentration. This finding indicates that there is a residual pathway in the healed fractures (calcite precipitates) that could be responsible for advective transport (isolated area: "advective").

5.4.3.3 BUKOV URF; S36/5

The entire core was scanned in an overview µCT dataset for subsequent PET data reconstruction. The resulting spatial resolution was 52 µm. Two smaller sections with higher spatial resolution (voxel size: 29 µm) were scanned for further quantitative investigations. A thickness distribution (aperture map) of the open fracture was calculated from the data (Fig. 5-30).

The sample was prepared and preconditioned by UJV. A breakthrough curve from this work at UJV is available and serves as a comparison. A PET analysis was performed using a 0.01 mol/L [^{18}F]KF

solution. The flow rate was 0.017 mL/min. PET data were processed and are available as time-resolved sequences. The flow rate vector field was calculated for the analysis of the flow properties. These data can provide valuable support for the validation of numerical analyses.

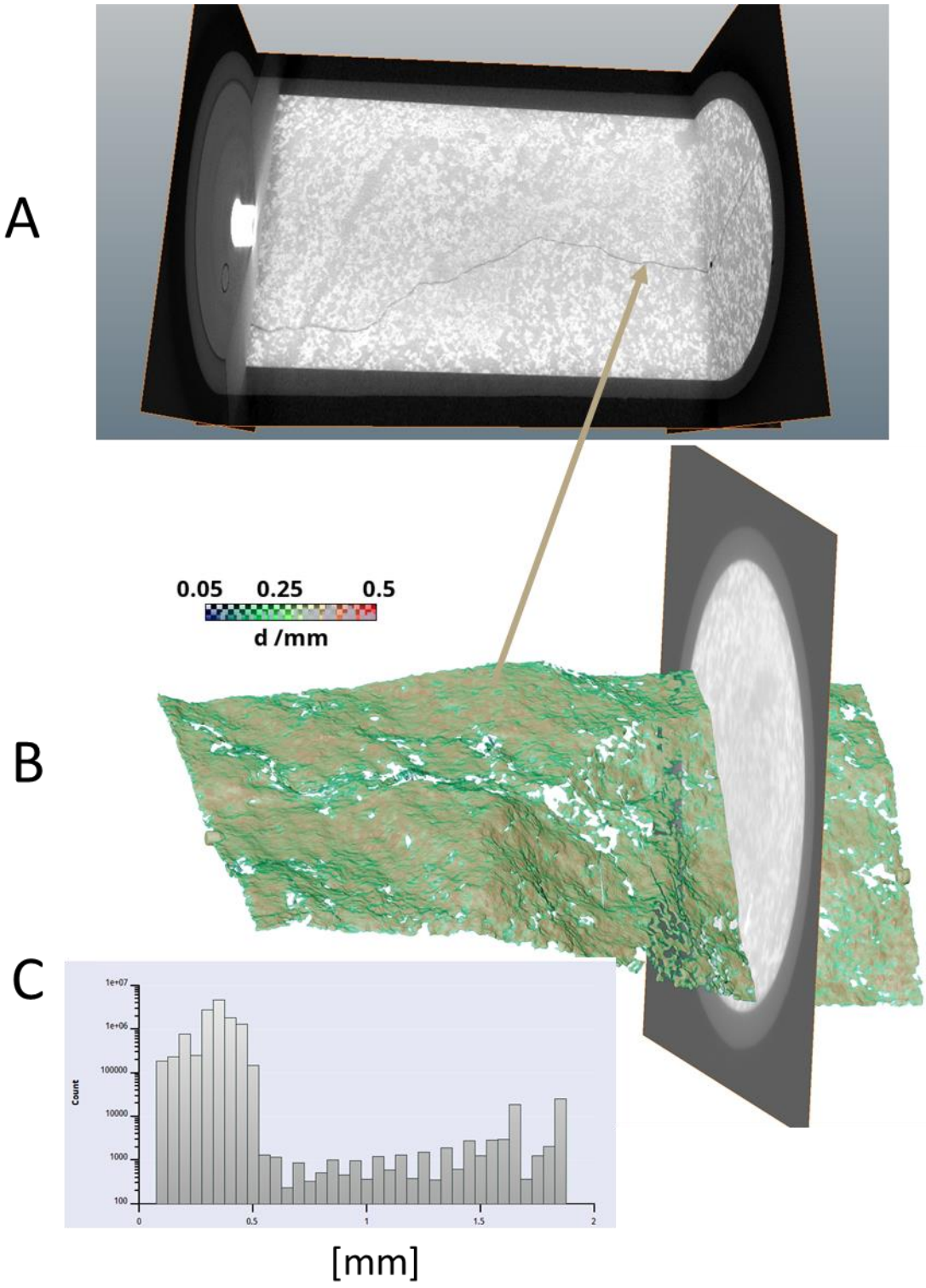

Figure 5-30: Analysis of the fracture geometry of BUKOV S36_5 sample, based on µCT data. The sample was cast in epoxy resin and prepared for PET analysis of the flow through experiment. (A) Overview image with open fracture (arrow). Sample diameter is 7.5 cm. (B) Fracture aperture segmentation with thickness mapping and (C) histogram of aperture width.

A flow experiment was conducted for a period of 5 hours in total (Fig. 5.-31). The flow behaviour was analysed with PET and the flow field evolution was calculated. The data set is available for an application to transport simulations. The heterogeneity of the flow field indicates that local channelling occurs during flow. Initially, tracer activity can be seen near the inlet (right). After about 100 minutes, a flow pattern is established in the first two fifths of the observed sample, indicating the formation of complex channel patterns due to the different tracer concentrations. As the experiment progresses, after 180 minutes, flow channels are formed up to the left edge where the outlet is located. After 300 minutes, most of the tracer has left the sample. Only a few isolated sections indicate that residual tracer has remained. However, most of the tracer has been washed out of the fracture system with its channel structure.

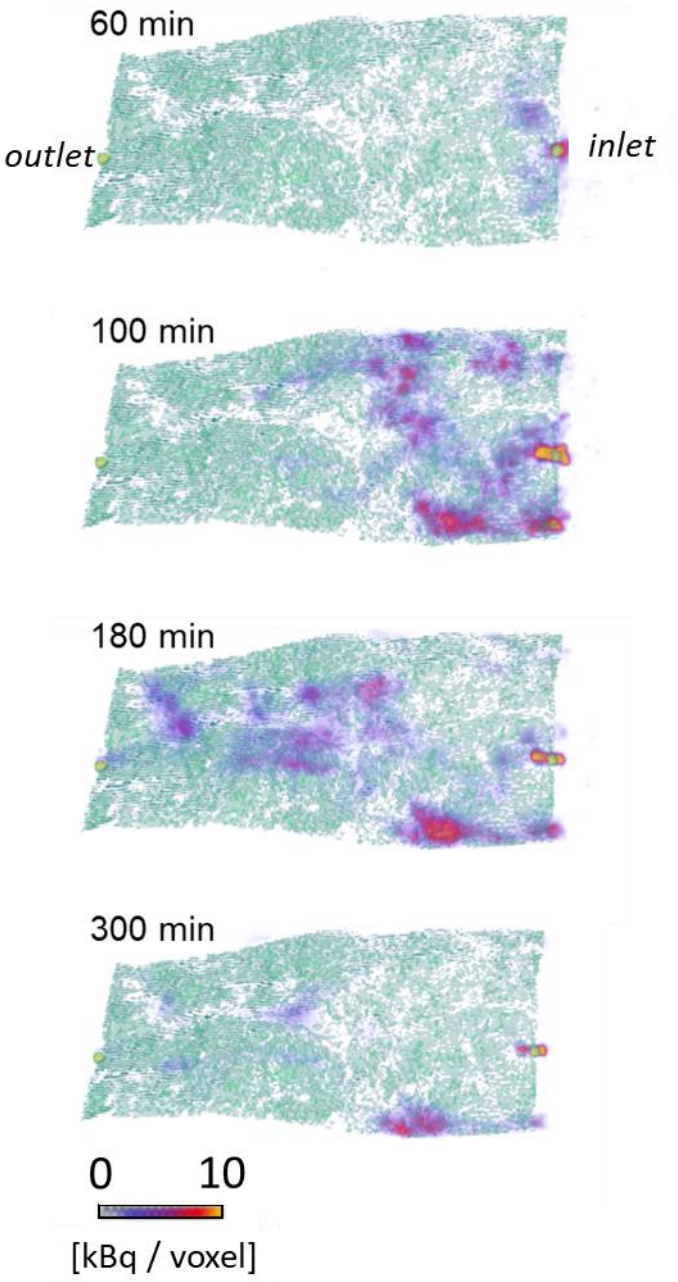

Figure 5-31: Combined PET data and µCT-based aperture width distribution map of BUKOV S36_5 sample. Four time steps of the PET dataset are shown, i.e., after 60 min (1 mL), 100 min (1.7 mL), 180 min (3 mL), and 300 min.

The vector field of flow rate was derived from the PET data set. The histogram shows the contributions to the total rate in their frequency distribution (Fig. 5-32).

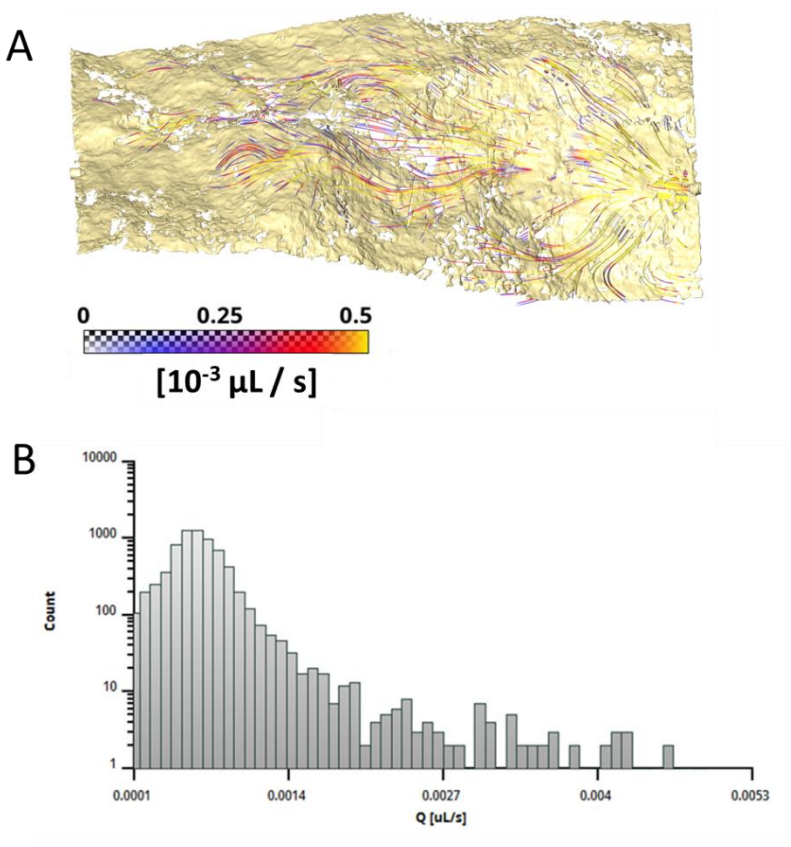

Figure 5-32: Combined flowrate vector field (A) derived from PET datasets and flow rate histogram (B) of BUKOV S36_5 sample.

5.4.3.4 ONKALO; OLKR5

A µCT analysis of the whole core (voxel size 62 µm) was performed. Higher spatial resolution µCT data (voxel size 16 µm) was generated for analysis of fracture geometry and fracture fill, and a higher resolution µCT data set was also generated for analysis of fracture geometry (Fig. 5-33). The fracture fill contains high density grains (ore grains) at µm to mm scale. The calcite and chlorite-bearing fracture-filling materials are clearly distinguishable from the host rock in the CT dataset. The lighter cloudy artefact that appears as a reflection of the denser fracture fill is caused by the necessary correction of ring artefacts. Segmentation of the intermittent open areas of the fracture is difficult even on the higher resolution images. The pore size of the fracture minerals is less than 60 µm, with several mm-sized open voids. Preliminary segmentation and analysis of the smaller sample shows a bimodal volumetric pore distribution with a maximum at 100 µm and a second at 300 µm.

A Visualization (CT image) of the sample installation in the sample holder, prepared for performing the flow experiment and the accompanying analysis of the flow field in the fracture with PET analytics is shown in **Figure 5.34**.

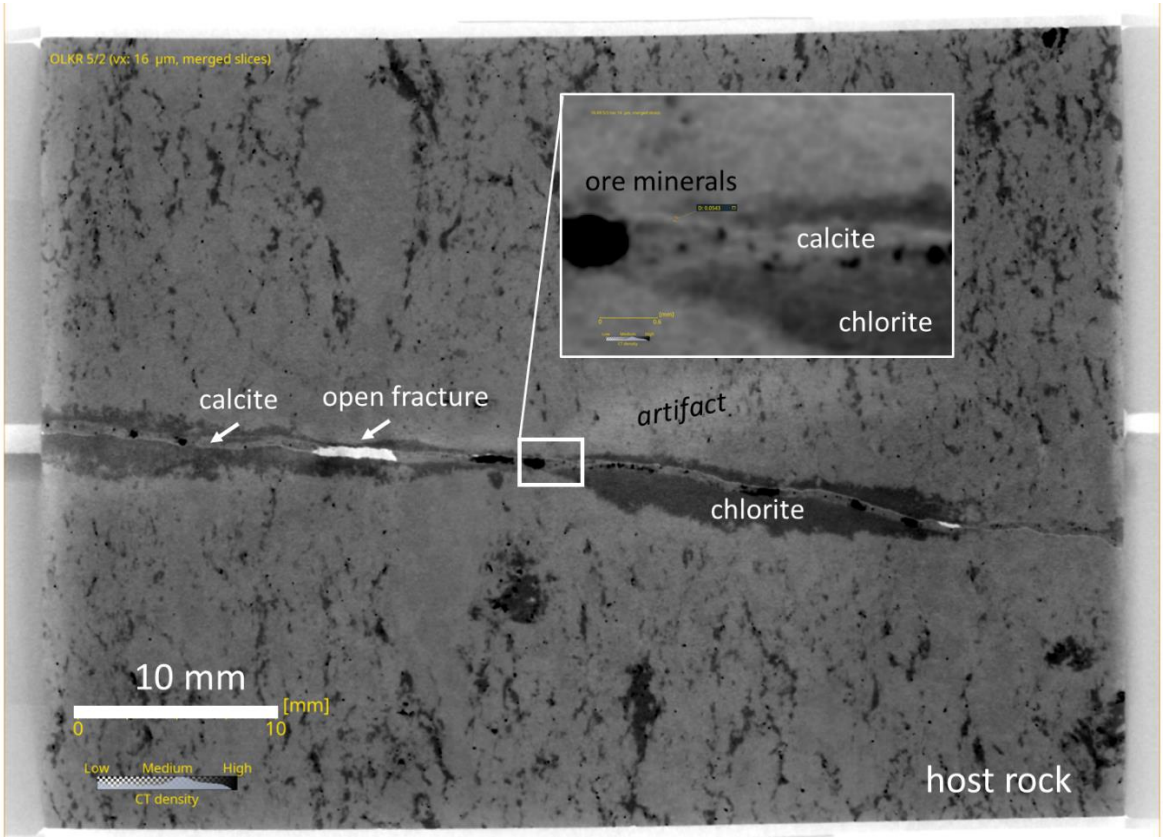

Figure 5-33: Merged high-resolution µCT images with a voxel size of 16 µm of the entire drill core (ONKALO; sample OLKR5). Dense material is shown in black, grey zones are fracture fill (chlorite and calcite), white is open volume of fracture.. Inset: Enlarged section showing the complex structure of the fracture and the position of the different fracture mineralisation.

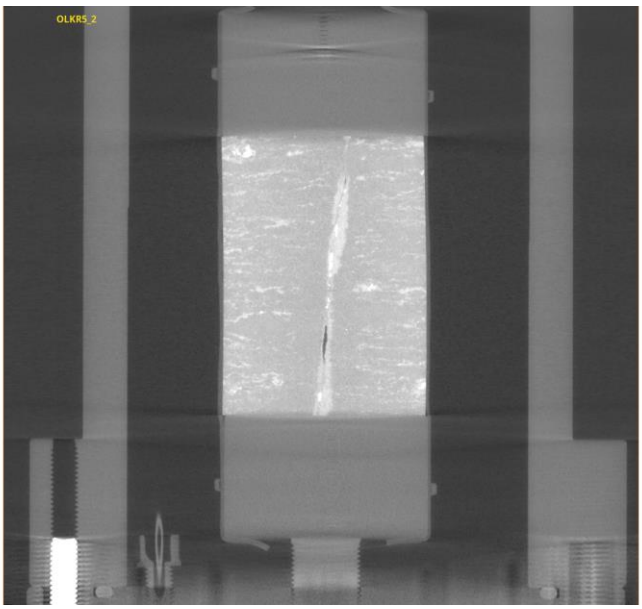

Figure 5-34: Visualization (CT image) of the sample installation in the sample holder (ONKALO; sample OLKR5).

A flow experiment using F-18 as a PET tracer was performed (Fig. 5-35). The results show that the mineralized fracture allows advective flow despite the secondary minerals. The tracer pulse has already

reached the outlet of the sample volume after a few minutes of flow. However, a complex flow geometry occurs, reflecting the complex fracture filling geometry.

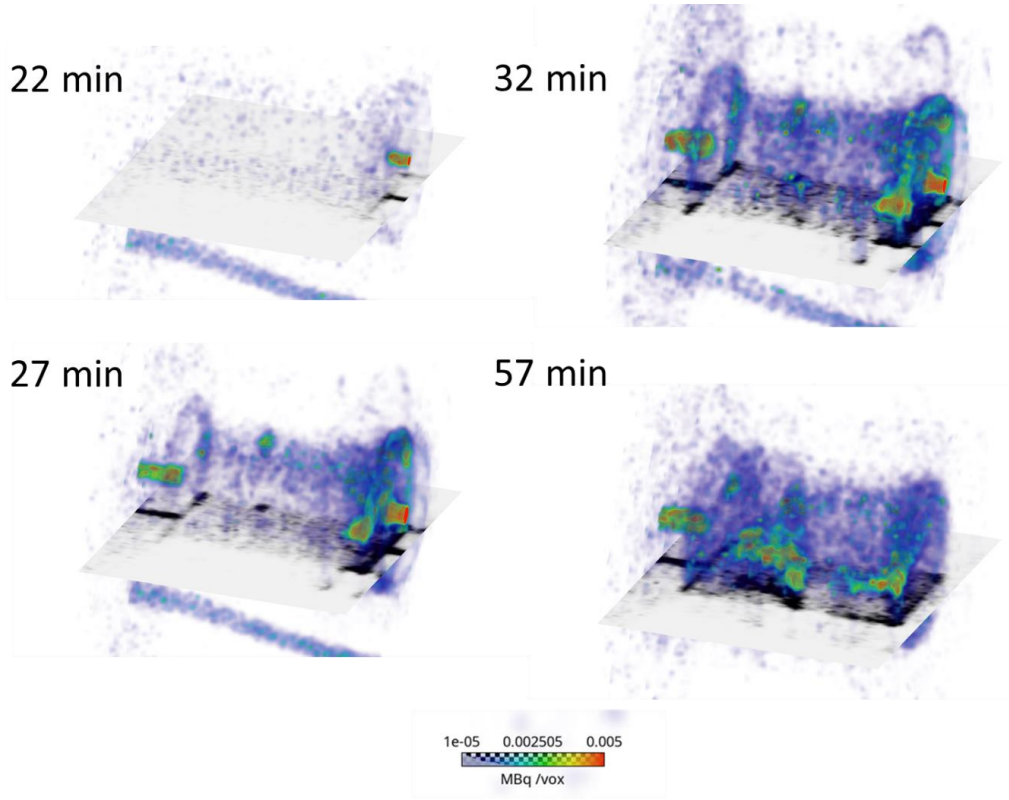

Figure 5-35: Time steps of the flow experiment (ONKALO; sample OLKR5), using the ^{18}F PET tracer, to visualize the flow (from right to left direction). Four time steps are shown, respectively at 22, 27, 32, and 57 min after the tracer pulse entered the sample. At 27 minutes after injection, the tracer already reached the outlet (left). At the bottom of the visualization, the activity of the injection tube can be seen.

The use of ^{18}F as a radiotracer may be error-prone due to its potential reactivity with calcium in calcite fillings. However, this depends on the overall crystal surface reactivity and fluorine concentration. For this reason, the PET experiments were subsequently performed using ^{124}I as the tracer, since the latter is considered a conservative tracer (not shown here).

In the ^{18}F experiment, the sample was preconditioned for 4 days with 0.001 mol/L KF solution at a flow rate of 0.03 mL/min. The driving pressure was 0.8 bar. PET measurement was performed at the same flow rate and drive pressure. No significant evidence of CaF_2 (retention or local accumulation) was observed. The different residence times of the labeled fluid in this fracture are explained by different permeabilities of the overall fracture system. Note that the upper channel in Figure 5-35 feeds the outlet after 27 minutes. The lower channel shows almost no activity at this time. The first sections of this lower channel are visible at 32 minutes of tracer injection and it is completely passed at 57 minutes.

The ^{124}I experiment was performed one month later. The sample was preconditioned with 0.01 mol/L NaI solution for one day, starting with the same flow rate and pressure as above. The pressure increased during preconditioning after injection of 9.4 mL of the solution. Therefore, the flow rate was reduced to 0.007 mL/min during the PET experiment. For 3 hours, the pressure remained stable below 5 bar and then increased above the 5 bar limit. Therefore, the experiment was continued under constant pressure conditions.

It can be assumed that narrow areas of the fracture became clogged during the second experiment, which was not expected after the constant conditions of the first experiment. A potential reason could

be the mobilization of particles at the higher flow rate or the swelling of the pore-filling material some time after contact with the solution. Further analysis of the second transport experiment is complicated by the unstable conditions. The passing of the ^{18}F tracer through the sample was extremely short (only 5 min, i.e., velocity of 0.2 mm/s). This short exposure time is probably the reason why no F-retention is observed. It also complicated the analysis of the PET data, as the fast progress requires a very short image duration. This leads to noisy images.

5.4.4 Transport modeling [HZDR]

Originally, no numerical work was planned in our work package. However, to take advantage of the time of Corona-related laboratory closures, transport modelling was performed on a sample or fracture geometry that was already available. The motivation was sensitivity analyses on the influence of aperture width variability and wall roughness variability. This has application-related relevance, since these data are strongly dependent on the spatial resolution of the methods. High spatial resolutions can only be achieved by costly additional measurements. We wanted to answer the question of what effort is actually necessary for the user when analysing fractured host rocks.

5.4.4.1 Mrakotin

The sensitivity of a transport model using Comsol FEM software to the aperture variation (extension vs. compression) of the fracture and to the different levels of detail of the microstructure of the fracture wall were investigated (Fig. 5-36). The bifurcation of the flow field and the activity time curves were reproduced by the model, but not the exact structure of the flow field. Also, the patchy distribution could not be reproduced. The best approximation in terms of activity pattern was obtained from the model with added microstructure, but with only gradual difference from the unmodified model. The simulated propagation of the tracer pulse always covers the entire surface, which is in contrast to the PET observations.

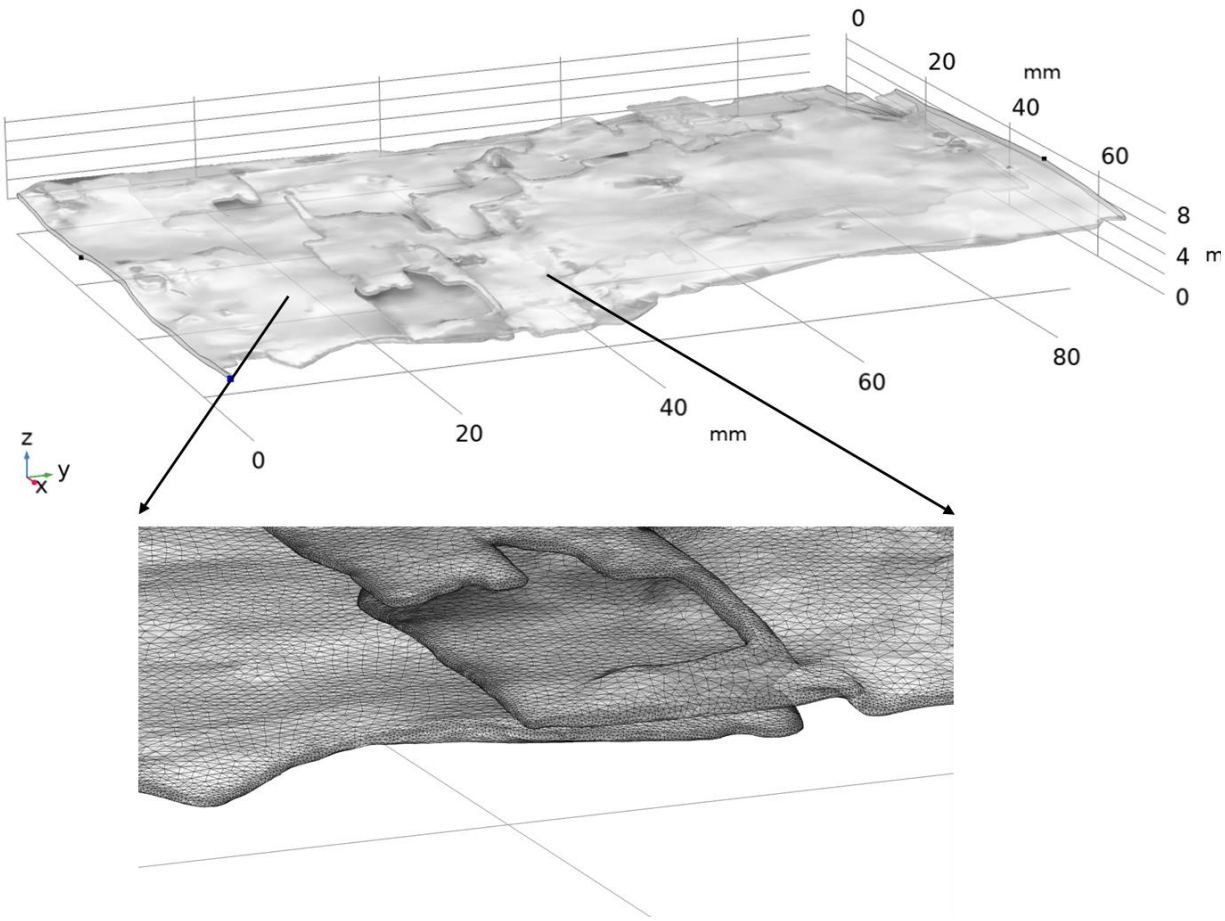

Figure 5-36: Geometric finite element model (Mrakotin fracture, MSVJ2) after extensive manual post-processing of the segmented image using a combination of Avizo watershed segmentation, Simpleware, Meshlab and Comsol. Detail of the FEM mesh is shown below.

After providing the µCT-based geometry (Fig. 5-36, Fig. 5-37a), it was refined by additional data sets from surface microscopy (confocal microscopy). For this purpose, fracture surface components were measured, evaluated and the roughness information was generically modulated onto the µCT data (Fig. 5-37b-d).

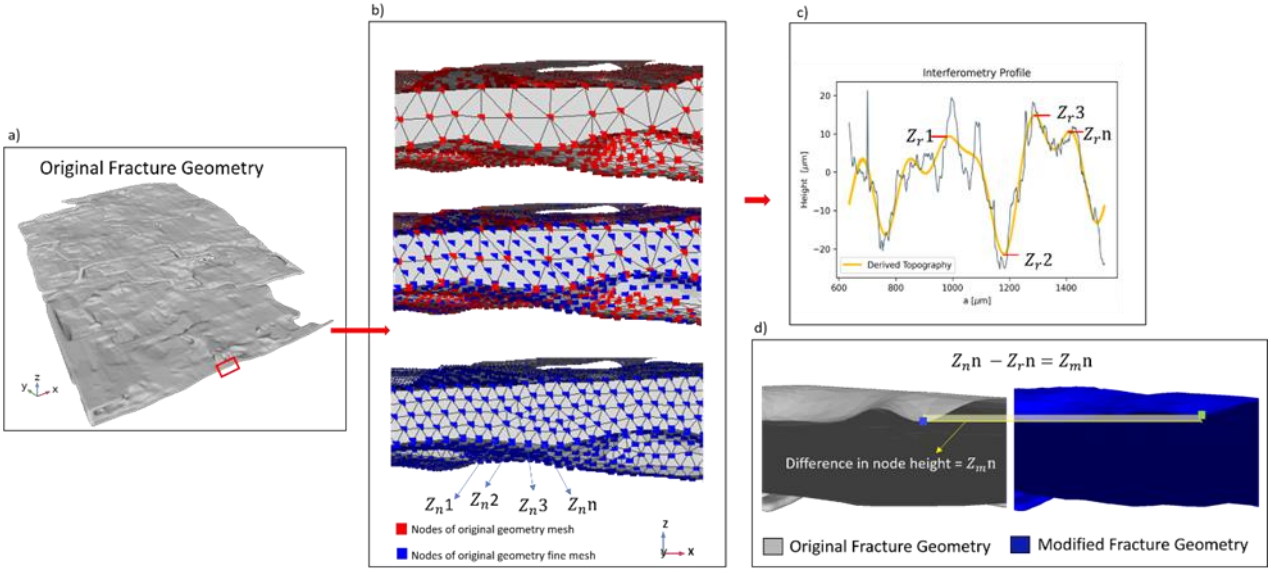

Figure 5-37: Workflow of geometric integration of the different measured topographies of a 3D fracture geometry (Mrakotin granite, MSVJ2), thus testing the sensitivity of the model results with respect to additional surface roughness. For this purpose, the mesh of the original geometry (a) was refined (b), the roughness data was extracted and analysed from additional confocal microscopy data (c), and the small-scale (high spatial frequency) amplitude variations missing in the CT data were merged with the CT data (d).

The Figure 5.38 shows how the surface elements are blended to increase the resulting depth of detail to be used in transport simulation calculations.

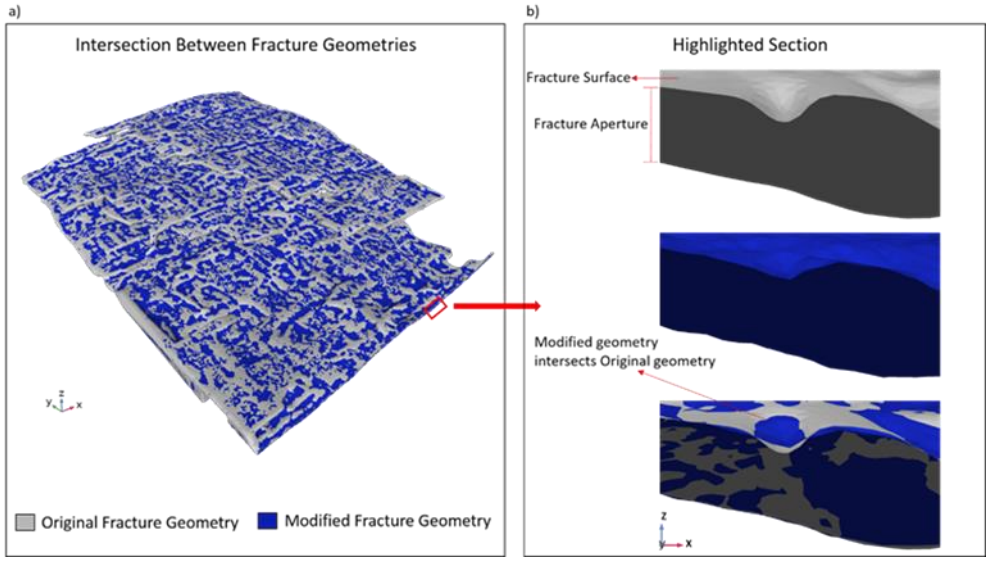

Figure 5-38: Visualization of the comparison of the original fracture geometry (grey) and the modified geometry (blue), which contains the small-scale (high-frequency) surface asperities (Mrakotin granite, MSVJ2). (a): entire domain, (b): close-up view.

Finally, a comparison is performed, which is a sensitivity analysis of the transport simulation with respect to the aperture width and surface roughness parameters. For this purpose, the original FEM model is firstly refined with the roughness data and secondly the aperture width is reduced. This is of interest because the ratio of aperture width and maximum roughness is important for the resulting cross-sectional area of the fissure. These three different approaches to transport simulations are compared with experimental flow data analysed with PET (Fig. 5-39). The result overview is shown for three different snapshots of the transport process at t = 60 min, 180 min, and 360 min.

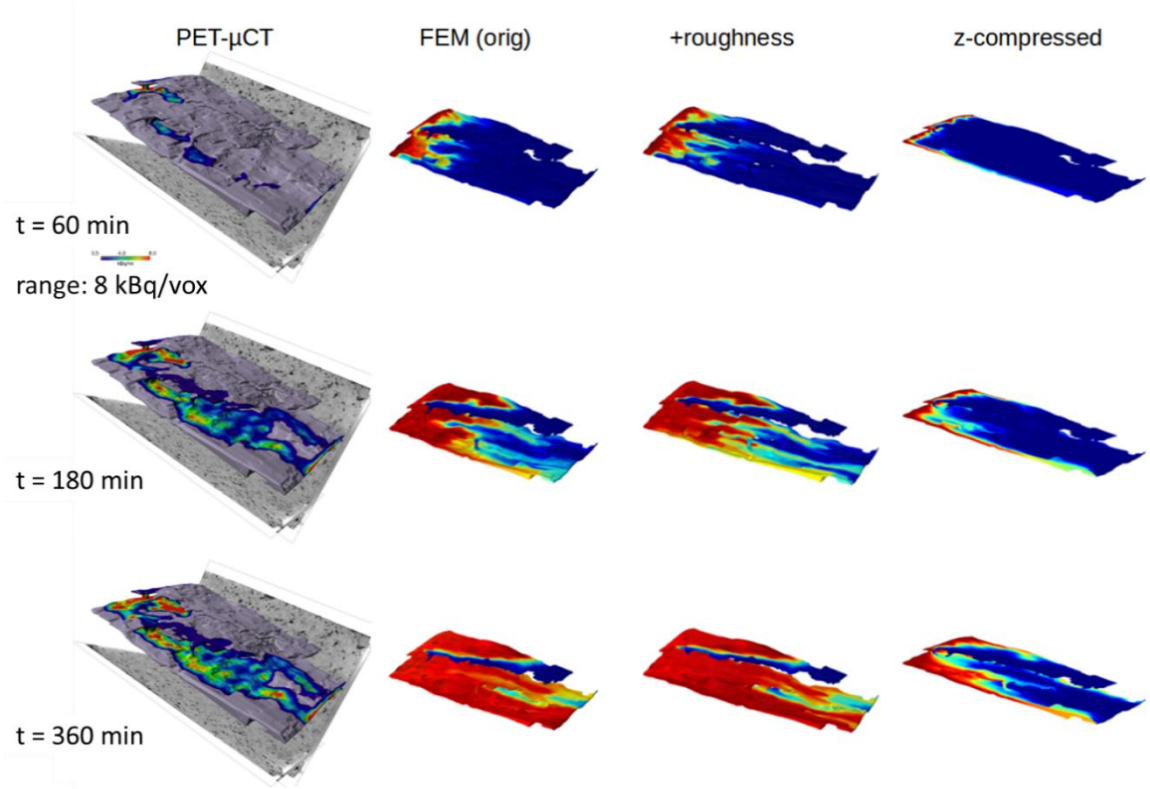

Figure 5-39: Measured PET activity distribution (left: 3 time steps) compared to simulation results of transport in the original fracture model (second column from left), the modified model with added roughness (third column from left), and a compressed model with reduced aperture width (right column); Mrakotin granite fracture (MSVJ2). Transport is from left to right.

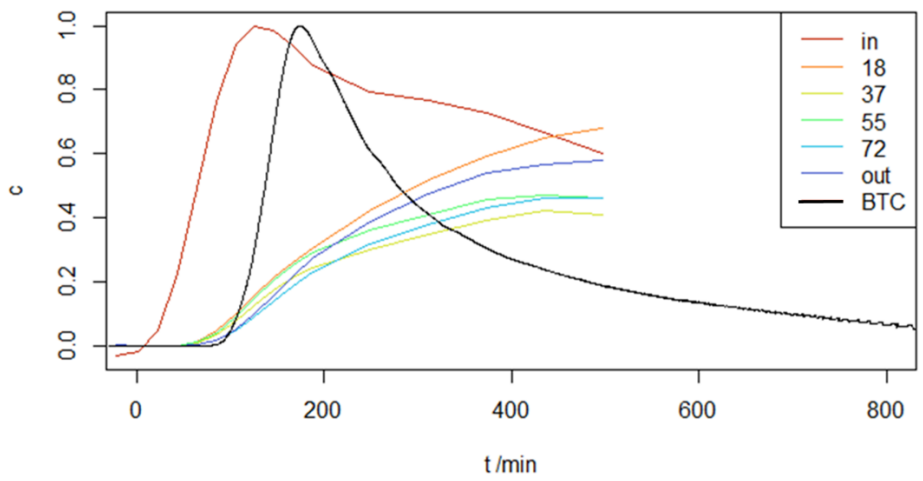

Figure 5-40: Activity-time curves derived from PET analytical data (Mrakotin granite, MSVJ2). These are calculated from activity sums over transaxial slices along the sample at distances of 0, 18, 37, 55, 72, 78 mm from the entrance plane. The curves are normalized to improve visibility. The breakthrough curve measured with a flow counter is coloured black. The input signal of the tracer is marked in red.

Site-specific breakthrough curves can be extracted from the PET data set (Fig. 5-40). These can be calculated from integrated activities of sample sections. For complex flow paths, as in the Mrakotin granite with en échelon geometry, these partial breakthrough curves may not be intuitively interpretable. Nevertheless, they give an impression of the signal evolution over the sample length. The input signal already has a long tail (retardation) because it was extracted from the first PET voxel layers. It shows the complexity of distributing a well-defined input signal over a complex fracture geometry. This already partially retarded input signal is further modified during transport and in particular further local retardations (additional tailing) are characteristic.

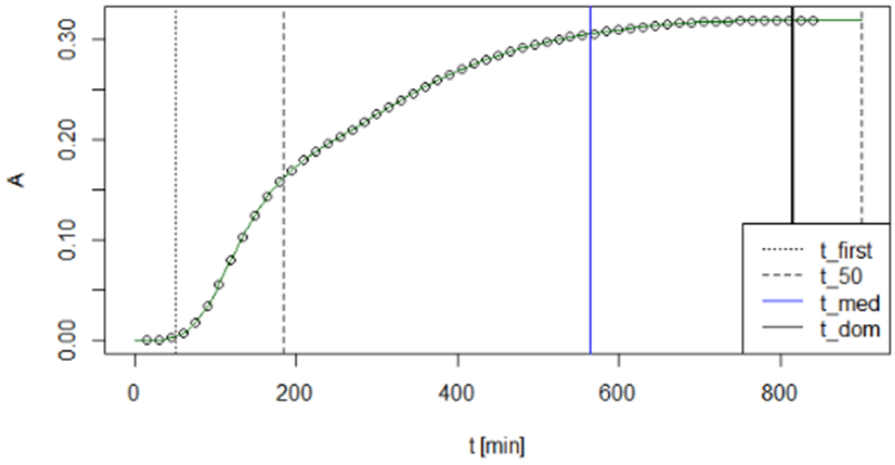

Figure 5-41: Parameterization of the activity-time curves for further evaluation and comparison (Mrakotin granite, MSVJ2). The first arrival and rise time (t_50 - t_first) are further used for comparison of the measured data with the model results.

The changed flow behaviour of the different model approaches (Fig. 5-39) requires the identification of comparison parameters in order to quantify the changes in a statistically comprehensible way. This is

done via the temporal development of the breakthrough curve, cf. Fig. 5-41. This time period (Δt := [rise time, first arrival time]) is further used for comparisons.

The comparison of the resulting breakthrough and rise times as a function of the aperture width of the fracture model when using the modified (rough) aperture is shown in Fig. 5-42. Surprisingly, the dependence on the aperture width is not a monotonic function. This is probably due to the complex en échelon geometry, which causes different local efficiencies for tracer transport of the fracture surface sections as a function of aperture width in a nonlinear situation.

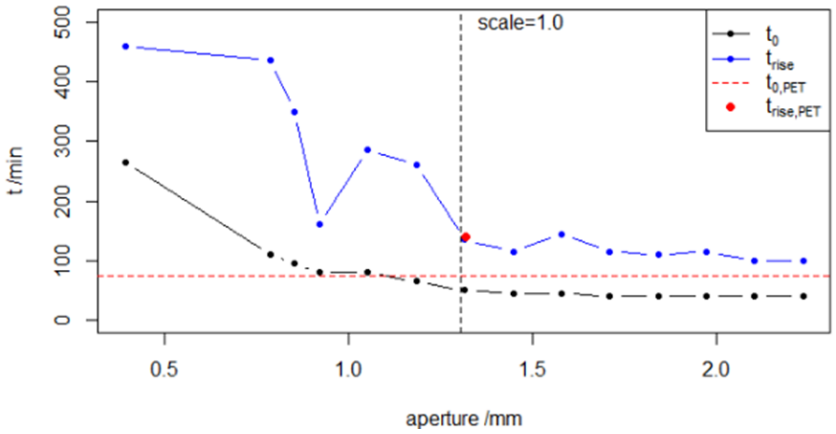

Figure 5-42: Breakthrough time t_0 and rise time t_{rise} as a function of the aperture width of the fracture model, using the modified (microrough) aperture. The vertical line represents the original width (comparison of compression vs. widening, left vs. right). The measured data (PET) of the real fracture are shown for comparison.

5.4.4.2 Comparison to the fractured Soultz-sous-Forêts granite

In a comparative study (Pingel et al., 2023), we investigated the fluid flow field in a fractured granite core sample from Soultz-sous-Forets. Again, sequential imaging with positron emission tomography (PET) allowed direct reconstruction of flow streamlines, providing a direct comparison with previously published numerical results (Stoll et al., 2019). Pulse migration experiments using the positron-emitting radionuclide $^{18}F^-$ as a tracer were performed on a fractured granitic drill core obtained from a depth of 1958 m at the Enhanced Geothermal System (EGS) reference site in Soultz-sous-Forêts, France. The flow field was analysed as a function of inlet and outlet positions in the fracture and applied flow rates. Different flow path characteristics were identified. Both fracture opening variation and fracture surface topography affect the flow field with implications for flow channelling and preferred flow paths. In addition, the pulse migration experiments were also numerically simulated with a 2.5D model using COMSOL Multiphysics® (Fig. 5-43).

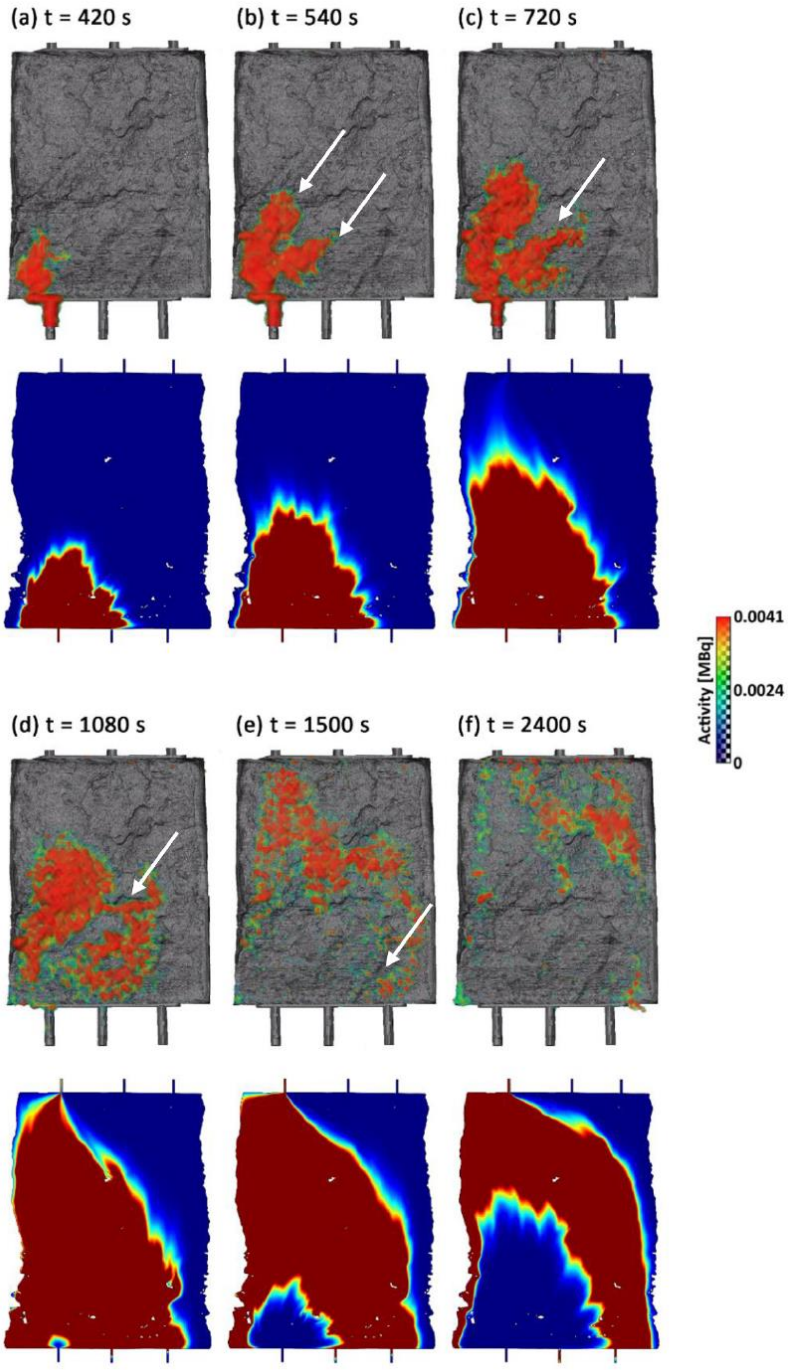

Figure 5-43: Comparison of the different stages during the flow-through experiment analysed by PET techniques and the numerical simulation (COMSOL) (Pingel et al., 2023). Starting at an early stage of the experiment, (a) shows the onset of injection of the radiotracer into the fracture at t = 420 [s]. Figures (b) to (d) illustrate the splitting of the tracer front, see arrows. (e) is the time at which the tracer reaches the outlet in the upper left corner of the flow cell, continued at (f). The white arrows highlight some of the more important flow paths (e.g., channelling behaviour or shadow zones) that can be observed in all experiments and differ from the numerical predictions.

While the higher flow velocity experiments show a broader and stronger dispersion of the flow path, a lower velocity results in a more localized flow and channelling behaviour (Pingel et al., 2023). This type of study therefore provides improved experimental insight into the hydrodynamics of fracture-related flow and its relationship to the rough structure of the fracture wall. It helped validate model simulations and experimentally determine hydrodynamic parameters needed for modelling reactive transport that would otherwise be estimated with a high degree of uncertainty.

5.5 Summary, conclusions, and outlook

The migration of radionuclides in fractured crystalline rocks has been studied intensively in the past. The range of investigations covers the migration of non-sorbing nuclides (e.g., Park et al., 1997; Vandergraaf et al., 1997), the migration behaviour of different sorbing nuclides (e.g., Missana et al., 2006) and the particle-dominated transport via colloids (e.g., Schafer et al., 2004; Vilks and Baik, 2001). Nevertheless, important gaps in the knowledge of the transport properties of radionuclides were identified and motivated the EURAD FUTURE work package, subtask: transport in crystalline rocks. For this, a number of overarching objectives have been formulated in the FUTURE project proposal. As part of these overarching objectives, the following objectives related to transport processes in fractured crystalline host rocks were specifically addressed in this subchapter:

- The role of microstructures on transport in crystalline rocks
- The impact of pore size variability and heterogeneity on the mobility of chemical species
- Refined understanding of the relation between fracture/ pore structures and transport as well as the feedback of mineral reactions (dissolution/precipitation, clogging) on pore structure and connectivity

Of particular importance for hydrodynamics and transport behaviour are the topographic microstructures that characterize the fracture walls in crystalline rocks (e.g., Deng et al., 2018; Deng et al., 2022; Noiriel and Soulaine, 2021; Zhou et al., 2023). An important motivation for WP FUTURE was to move away from previous simplistic fracture and fault models that considered smooth and/or simplified regular geometries (cf. discussions in, e.g., Huber et al., 2021; Jia et al., 2022; Kurotori et al., 2023; Zhou et al., 2023). This previous simplification motivated the continued use of a very conservative approach to transport predictions. In fact, the potential small-scale heterogeneity of the hydrodynamics was often not considered in the previous approaches. This, of course, has consequences for the upscaling of hydrodynamic model results from the laboratory or core scale to the system or field scale. In the past, tracer pulse breakthrough curve shapes in crystalline rock fractures have been subject of analysis and discussion. However, the specific mechanisms responsible for possible tracer retardation remained often unclear in the interpretation of the BTC tailings. In the absence of specific interpretations, the scope for subsequent applications is limited in predictability. WP FUTURE provides datasets in this direction, and with the results presented here, has been able to improve the quality of the predictive capability, thus making a significant contribution to subsequent upscaling strategies in transport behaviour and migration.

In particular, two specific foci were treated to address the above points and to prepare guidelines for application:

Firstly, the influence of (partially) fracture-filling precipitates on transport properties was investigated. In addition to geochemical variability, i.e. mineral-specific sorption efficiencies, such diverse precipitates also modify the micro-topography, i.e. the surface roughness of the fracture wall. Different types of mineralization, such as calcite and phyllosilicates, are dominant in the studied host rocks from the Czech Republic and Finland. Such fracture fillings further modify the advective flow field by locally increasing the fluid residence time and increasing the heterogeneity of the fluid-rock interface.

We now have a practical tool and an exemplary dataset by using Power Spectral Density (PSD) analysis of fracture wall surfaces to provide a cross-scale analysis of surface topography variability. This approach also illustrates how this initial dataset can be complemented with respect to other types of fracture mineralization and infiltration. The demonstrated trend of specific changes in surface microtopography due to multiple materials is a valid starting point for future comparisons of different types of fracture systems in crystalline rocks. This can serve as an important input parameter for

subsequent sensitivity analysis of numerical transport approaches. Overall, this helps to support the quantitative comparison (wrt. hydrodynamics) of different types of fractured host rocks.

The fracture wall geometry is only one of two important parameters that characterize the fracture geometry and thus constrain the resulting hydrodynamics. The aperture width variability is another critical parameter related to flow field propagation. The above effect of fracture wall topography variability is superimposed by the effect of fracture aperture width and distribution. Due to the concurrent effects of the two parameters, they must be considered in combination to avoid misleading interpretations. In this respect, the WP FUTURE contributed to a better understanding by using a specific analytical method of flow field tomography.

Secondly, studies on the tomographic analysis of the flow field in fractures were central to our work. Positron emission tomography has been applied to various fracture types in crystalline rocks and characteristic flow field heterogeneities have been derived. A remarkable number of tomograms of advective flow fields is now available; this was a specific goal that we pursued with the WP FUTURE. These flow field data can either provide parameterizations for further transport simulations or validate the simulation calculations based on specific geometric constraints, see above explanation on surface topography and aperture width. First own numerical results are presented which aim at the quantitatively determining the influence of the two geometric parameters, aperture width and wall roughness. The numerical results were compared with flow tomographic results and the sensitivity of the geometric parameterization was explained. These results are currently being summarized in a manuscript and will be submitted soon. A further comparison in this regard was made on another type of fractured granite and the influence of flow path channelization was quantified. These results have been published (Pingel et al., 2023). In general, the results contribute to a more realistic view of radionuclide migration in complex systems to overcome the current over-conservative consideration of heterogeneities such as fracture planes, mineral fills and porosity networks. The activities were carried out in close cooperation between the participating institutions.

As a specific outlook, positron emission tomography (PET) flow field data from fractured crystalline host rocks are available from the investigations in WP FUTURE. The unique data cover a range from non-mineralized complex fractures to weakly to strongly mineralized fractures with calcite and phyllosilicates. The frequently occurring hydrothermal mineralized fractures show extremely complex flow fields with diffusive and advective contributions. The flow fields have been studied with non-sorbing, i.e., conservative tracers (F-18, I-124) to provide insight into the flow field behaviour. The key question is: How does the transport behaviour of non-sorbing tracers converge in these different systems so that a robust parameterization of model sizes above the laboratory scale can be achieved? This remaining question can be answered by using the flow field data now available.

Existing µCT and porosity data can be used to build transport models for further investigation. Based on this, breakthrough curves can be calculated from the simulation results and the PET data sets can be used for validation. The sensitivity of variability in fracture geometry, fracture roughness, and mineralization distribution on breakthrough behaviour can also be analysed. The goal is to obtain generalizable types of breakthrough curves, and this can be achieved by using the data sets developed in the FUTURE WP. This allows to develop strategies for upscaling radionuclide transport in mineralized fractures, similar to the dual porosity situation, with clear improvements in the predictive capability of transport models.

Voxel-specific BTC analysis of PET datasets is another open issue derived from the results of the FUTURE WP presented here. Positron emission tomography (PET) data provide an excellent means of validating transport models. Such complex flow data sets are increasingly used for this purpose. However, there is still no way to interpret such flow data sets in a fully mechanistic way. This currently limits their generalized use for parameterization of transport models, although the large amount of data

in flow datasets is very attractive for this purpose. To solve this problem, we expect a systematic analysis of existing PET datasets of well-defined systems for the parameterization of transport models. The time-resolved data yield a large number (typically several hundred thousand) of voxel-specific breakthrough curves (BTCs). Their propagation along the pressure gradient is responsible for the only continuum-scale BTC currently used to interpret transport simulation results. In the future, we expect to use the hydrodynamic information from the large number of voxel-specific BTCs to identify their contributions to the overall (integrated) "classical" BTC. Thus, the mechanistic influence of pore-scale heterogeneities on the overall hydrodynamic behavior will be identified and mechanistic predictability will be enabled. For this purpose, PET data sets as well as complementary tomographic compositional data sets from investigated host rocks will be used in the future. Spatially registered series of experimentally altered (local dissolution reactions, local porosity increase) host rocks are also available. These additional datasets contain clusters of locally altered BTCs induced by the targeted experimental alteration. The identification of specific changes in the large datasets and their inheritance to the resulting BTCs opens another avenue to provide a generalizable parameterization of transport models.

5.6 References of chapter 5

References

Bollermann, T., Yuan, T., Kulenkampff, J., Stumpf, T., Fischer, C., 2022. Pore network and solute flux pattern analysis towards improved predictability of diffusive transport in argillaceous host rocks. Chemical Geology, 606: 120997.

Deng, H., Molins, S., Trebotich, D., Steefel, C., DePaolo, D., 2018. Pore-scale numerical investigation of the impacts of surface roughness: Upscaling of reaction rates in rough fractures. Geochimica et Cosmochimica Acta, 239: 374-389.

Deng, Y. et al., 2022. Research on the influence of roughness on solute transport through 3D self-affine fractures by lattice Boltzmann simulation. Arabian Journal of Geosciences, 15(5): 393.

Huber, F.M. et al., 2021. Impact of rock fracture geometry on geotechnical barrier integrity – A numerical study. International Journal of Rock Mechanics and Mining Sciences, 142: 104742.

Jia, S. et al., 2022. Uncertainty quantification of radionuclide migration in fractured granite. Journal of Cleaner Production, 366: 132944.

Kulenkampff, J., Gründig, M., Zakhnini, A., Lippmann-Pipke, J., 2016. Geoscientific process monitoring with positron emission tomography (GeoPET). Solid Earth, 7(4): 1217-1231.

Kurotori, T., Zahasky, C., Gran, M., Kovscek, A.R., Benson, S.M., 2023. Comparative Analysis of Imaging and Measurements of Micrometer-Scale Fracture Aperture Fields Within a Heterogeneous Rock Using PET and X-ray CT. Transport in Porous Media, 147(3): 519-539.

Missana, T., García-Gutiérrez, M., Alonso, U., Mingarro, M., 2006. On radionuclide retention mechanisms in fractured geologic media. Journal of Iberian Geology, 32(1): 55-77.

Noiriel, C., Soulaine, C., 2021. Pore-Scale Imaging and Modelling of Reactive Flow in Evolving Porous Media: Tracking the Dynamics of the Fluid–Rock Interface. Transport in Porous Media, 140(1): 181-213.

Park, C.-K., Vandergraaf, T.T., Drew, D.J., Hahn, P.-S., 1997. Analysis of the migration of nonsorbing tracers in a natural fracture in granite using a variable aperture channel model. Journal of Contaminant Hydrology, 26(1): 97-108.

Pingel, J.L. et al., 2023. In-situ flow visualization with Geo-Positron-Emission-Tomography in a granite fracture from Soultz-sous-Forêts, France. Geothermics, 111: 102705.

Schafer, T., Geckeis, H., Bouby, M., Fanghanel, T., 2004. U, Th, Eu and colloid mobility in a granite fracture under near-natural flow conditions. Radiochimica Acta, 92(9-11): 731-737.

Stoll, M. et al., 2019. Experimental and numerical investigations on the effect of fracture geometry and fracture aperture distribution on flow and solute transport in natural fractures. Journal of Contaminant Hydrology, 221: 82-97.

Vandergraaf, T.T., Drew, D.J., Archambault, D., Ticknor, K.V., 1997. Transport of radionuclides in natural fractures: some aspects of laboratory migration experiments. Journal of Contaminant Hydrology, 26(1): 83-95.

Vilks, P., Baik, M.H., 2001. Laboratory migration experiments with radionuclides and natural colloids in a granite fracture. Journal of Contaminant Hydrology, 47(2-4): 197-210.

Zhou, J.-Q., Guo, L.-G., Jiao, J.J., Luo, X., 2023. Geometry-Based Prediction of Solute Transport Process in Single 3D Rock Fractures Under Laminar Flow Regime. Journal of Geophysical Research: Solid Earth, 128(3): e2022JB025542.

6 The Long Term in situ test (LIT) at the grimsel test site [KIT]

In this section we report on the results of the in-situ radionuclide tracer test conducted at the Grimsel Test Site (GTS) in Switzerland, provided as an in-kind contribution to the FUTURE final technical report. A detailed description of such experiment as well as its outcomes are described in the forthcoming NAGRA technical report NTB 23-10 [1]. The corresponding funding entities are listed at the end of the actual contribution.

The LIT experiment consisted in a packer-system containing 16 FEBEX bentonite rings - four of them spiked with radionuclide (RN) tracers - emplaced in the crystalline rock of the GTS intersecting a water-conducting shear zone [2]. The saturation of the bentonite with the Grimsel groundwater (GGW) from the shear zone, its consequent swelling with possible release of bentonite colloids, and the diffusion of RNs through the bentonite followed by their transport/retention through the granodiorite shear zone under advective conditions were investigated for a duration of 4.5 years.

6.1 Description of the work

The Grimsel Test Site groundwater is a Na^{+}/Ca^{2+} -HCO_3^{-} -SO_4^{2-} type with a pH of 9.6, an Eh(SHE) of ca. -220 mV and an ionic strength 1.2 mM, providing conditions for high stability of bentonite colloids [3]. The geochemical conditions established in the saturated bentonite source were estimated with calculations undertaken using PHREEQC v.3.5 and PhreePlot v.11 [4]. Water samples were collected from two near field boreholes (5.6 cm from the bentonite source). In these samples, composed of bentonite pore water mixing with GGW from the shear zone, the concentration of the radioactive tracers ^{99}Tc, ^{233}U, ^{237}Np, ^{242}Pu and ^{241}Am as well as that of the conservative fluorescent tracer Amino-G (AGA) was analysed. The RN tracers were introduced into a bentonite block as Tc(VII), U(VI), Np(V), Pu(III) and Am(III). Depending on the redox state establishing in the course of the experiment, the RNs behave as weakly (e.g. Tc(VII)) or relatively strongly (e.g. Pu(IV) and Am(III)) sorbing elements for which a slow diffusion through bentonite is expected. Consequently, ultra-trace levels are expected in the LIT water samples.

Such analytical challenge was faced with AMS that provides extremely high sensitivity for ^{99}Tc and actinide nuclides. In particular, actinide tracers were analysed at the 3 MV tandem accelerator of VERA, while ^{99}Tc at the 14 MV tandem accelerator of TUM, enabling quantification at the level of ca. 7×10^4 atoms/sample and ca. 1×10^6 atoms/sample, respectively [5, 6].

A further challenge consisted in the possible background of the shear zone from previous *in situ* RN tracer tests [3, 5]. In order to estimate such shear zone background and identify RNs originating from the LIT, an analysis of the RNs originating from previous in-situ RN tracer tests was undertaken in GGW samples collected before the emplacement of LIT and from the tailing of the tests in 2012 and 2013 [5].

6.2 Results

Extremely low concentrations of the RN tracers were determined in the LIT water samples, for example for ^{99}Tc with values spanning from a maximum of $(1.2 \pm 0.6) \times 10^9$ atoms/mL at 206 days and down to $(4.5 \pm 1.2) \times 10^6$ atoms/mL at 1600 days after the start of the experiment. Similar trends are observed for ^{233}U and ^{237}Np with a possible maximum in the first phase of LIT and decreasing levels towards the end, while ^{242}Pu shows a more or less flat concentration profile. Levels higher than detection limits for ^{241}Am are determined in samples collected up to ~900 days with concentrations generally lower than $(8.3 \pm 5.5) \times 10^4$ atoms/mL. The initial elution curve shapes of all the RNs could be ascribed to the inhomogeneous swelling in the early phase of bentonite saturation with the GGW [2], possibly opening preferential transport pathways for the RNs and AGA. At the same time, redox conditions in the bentonite varied due to oxygen consumption that may have an impact mainly on the speciation of Tc and Np. This is supported by the observation that the signal of the conservative tracer was already detected after 20 days, reached its maximum between 400 and 750 days and decreased by 60% due to the increase of the extraction rate of the water samples from 20 to 50 µl/min at 750 days. The decrease in the concentration of ^{99}Tc was much higher than 60% and cannot be explained only with a dilution effect due to the mixing of bentonite pore water with a higher volume of GGW. Notably for Tc at least a partial

reduction from mobile TcO_4^- to strongly adsorbing reduced Tc(IV) species can be expected which actually will prevail under the given geochemical conditions in the saturated bentonite. Based on those analytical data collected over ~4.5 years, the fraction of RN tracers in LIT water samples relative to the emplaced inventory corresponds to ~8.5×10^{-5} for ^{99}Tc, 3.4×10^{-4} for ^{233}U, 1.9×10^{-5} for ^{237}Np, 6×10^{-5} for ^{242}Pu and 2.4×10^{-5} for ^{241}Am (with AGA recovery equal to ~ 3.7×10^{-2} [2]).

The present results can be interpreted assuming an adaption of the initial oxidation states of the applied RN tracers to repository conditions and allow further understanding of the in-situ RN tracers diffusion through compacted bentonite and consequent migration through a water-conductive feature in granodiorite rock over the time span of 4.5 years.

Further investigations are ongoing with the post-mortem analysis of the LIT after a cylinder of granodiorite rock enclosing the bentonite source and containing a portion of the granodiorite shear zone was over cored.

6.3 References of chapter 6

[1] NAGRA technical report NTB 23-10 (2023).

[2] Kollorado-e2 Final Report. *KIT publications*, Editors: Noseck, U. and Schäfer, T. (2019).

[3] Geckeis, H., T. Schäfer, W.Hauser, Th. Rabung, T. Missana, C. Degueldre, A. Möri, J. Eikenberg, Th. Fierz and W. R. Alexander (2004). Radiochim. Acta. 92: 675−674.

[4] Montoya, V., U. Noseck, F. Mattick, S. Britz, I. Blechschmidt, T. Schäfer (2022) Radionuclide geochemistry evolution in the Long-term In-situ Test (LIT) at Grimsel Test Site (Switzerland) J. Hazard. Mat., 424 127733.

[5] Quinto, F., I. Blechschmidt, C. Garcia Perez, H. Geckeis, F. Geyer, R. Golser, F. Huber, M. Lagos, B. Lanyon, M. Plaschke, P. Steier and T. Schäfer (2017). Multiactinide Analysis with Accelerator Mass Spectrometry for Ultratrace Determination in Small Samples: Application to an in Situ Radionuclide Tracer Test within the Colloid Formation and Migration Experiment at the Grimsel Test Site (Switzerland). Anal. Chem. 89: 7182−7189.

[6] Quinto, F., C. Busser, T. Faestermann, K. Hain, D. Koll, G. Korschinek, S. Kraft, P. Ludwig, M. Plaschke, T. Schafer and H. Geckeis (2019). Ultratrace Determination of ^{99}Tc in Small Natural Water Samples by Accelerator Mass Spectrometry with the Gas-Filled Analyzing Magnet System. Anal. Chem. 91: 4585-4591.